UNIVERSITAT POLITÈCNICA DE CATALUNYA
INSTITUT D'ESTUDIS ESPACIALS DE CATALUNYA

THERMAL DIAGNOSTICS EXPERIMENTS FOR LISA PATHFINDER

FERRAN GIBERT GUTIÉRREZ

BARCELONA, NOVEMBER 2015

THESIS SUBMITTED FOR THE DEGREE OF
DOCTOR OF PHILOSOPHY

ADVISOR: DR. MIQUEL NOFRARIAS I SERRA

TUTOR: DR. ADRIANO CAMPS CARMONA

DEPARTAMENT DE FÍSICA

PHD PROGRAM IN AEROSPACE SCIENCE AND TECHNOLOGY

A la memòria del Prof. Alberto Lobo (1953-2012)

Truth, of course, must of necessity be stranger than fiction, for we have made fiction to suit ourselves.
—G.K. Chesterton, *Heretics*

Il faut toujours connaître les limites du possible. Pas pour s'arrêter, mais pour tenter l'impossible dans les meilleures conditions.
—Romain Gary, *Charge d'âme*

Alguna cosa deixarem a mitges.
—Miquel Pairolí, *Octubre*

Agraïments

A vegades les aventures no comencen de la manera que més t'agradarien. És de justícia i per mi un orgull començar aquest escrit amb el record de l'Alberto, amb qui vaig fer els primers passos a l'institut. Apassionat de les petites coses que, posades l'una al costat de l'altra, acaben conformant un projecte de la complexitat del LISA Pathfinder i sense perdre la tenacitat i coratge en moments tothora compromesos, a ell li dec l'entusiasme que em va embarcar, ara fa uns anys, en el que ha acabat sent aquesta tesi. Pel primer *raiz de Hercio*, gràcies Alberto.

La segona reconeixença se la mereix el Miquel. A ell he d'agrair la motivació que m'ha ajudat a tirar endavant aquests anys trepidants i la confiança que m'ha acabat fent sentir partícep d'aquest projecte. Al cap de poc d'haver tornat de Hannover et vas trobar en un moment incert i delicat que necessitava empenta i decisió, i no vas dubtar en llençar-t'hi. Gràcies per l'energia que m'has transmès al llarg d'aquests anys i per tot el que he pogut aprendre de tu.

Amb especial il·lusió, vull agrair també la companyia de viatge que ha suposat el grup LISA Pathfinder de l'institut. Al Nacho, Lluís, Víctor, Miquel, Daniel, Fran, Ivan i Carlos per tots aquests anys viscuts on n'hem passat de tots colors, sempre amb un somriure. Gràcies Nacho per totes les hores al Nexus i discussions *variopintes* i també al Nikos, amb qui he pogut compartir moltes estones divertides de meetings i viatges. També pel Juan Pedro, tot i que no hem pogut coincidir gaire temps.

Fa temps que vaig arribar a l'institut, però encara recordo els que em van ajudar a fer-me una mica la idea del *tinglado* que tenia el davant: moltes gràcies Pep, Marc i altre cop al Nacho pel vostre temps i explicacions. També a la resta de companys dels primers anys al Nexus, l'Alberto, el Markus, la Júlia i la Pris, i a l'administració de l'IEEC –Pilar, Anna i Eva per totes les seves gestions. Una abraçada ben inofensiva pel Josep Guerrero.

La vida al nou despatx a l'ICE, amb vistes al claustre del que ha acabat sent aquest particular convent amb *scriptorium*, també ha sigut un entorn fantàstic des d'on poder treballar, escriure, discutir i arreglar el món, sempre amb l'orella posada per si calia fer cafès o comentaris d'emergència. Així doncs, gràcies Padu i de nou, Daniel i Fran.

I moltes gràcies també a la resta d'estudiants i investigadors de l'institut amb qui he pogut compartir tants cafès, dinars a l'etse, *hores del iogurt*, partits de futbol-patxanga, etc. Ha sigut poc temps però tot un plaer que he pogut gaudir. La llista aquí és massa llarga, així que gràcies a tots!

Pointing now to L1, it is time to extend my gratitude to the whole LISA Pathfinder data analysis collaboration. Though being sometimes tough and even exhausting, all the meetings have been interesting opportunities where to learn and boost my enthusiasm for the project. Exciting times are coming now, I hope I can share them with you all. Special thanks to Martin, Paul, Dave, Michele, Mauro and Luigi for your patience and for replying so many bothersome emails.

In the last year of my PhD I had the opportunity to meet the *trentinian* group of the collaboration. For three months I could enjoy working with a great team and approaching the project from a completely different point of view. Special thanks to Rita, Stefano, Bill, Paolo, Daniel, Valerio, Antonella, Andrea, Giuliana, Roberta, Karine and Li. Also to

C.D. for all his useful comments and contributions. Ci vediamo presto!

No tot han sigut *commits* al llarg d'aquest temps, així que també vull agrair als que han contribuït a fer d'aquesta travessa una etapa més humana. Gràcies doncs a tota la gran colla d'amics de Manresa, *aquella gent* que quasi sou com una segona família. I a tots els altres amics i companys d'excursions i viatges que han fet més amena aquesta aventura: gràcies Jordi, Laia, Ignasi, Albert i Uri. Una abraçada molt especial per la Núria també, sense la qual res haguera sigut el mateix.

Sens falta també, pel que m'és més proper i que *sempre ha sigut allà*. Així, he d'agrair també especialment tota l'ajuda que he rebut al llarg d'aquests anys per part dels meus pares, a vegades en forma de paciència i tantes vegades en forma de carmanyola. Moltes gràcies a tu també Marta per, des de la distància —que algun dia s'escurçarà!— ser-hi sempre que ha calgut.

Finalment, a la Maria, per aguantar-me durant tot aquest temps d'escriptura i per tot el que ens queda per compartir.

A tots, de nou, moltes gràcies!

Manresa, novembre del 2015

Prologue

The LISA Pathfinder project is an ESA/NASA technology demonstrator mission that must test the critical instrumentation required for a future space-borne gravitational wave observatory based on the LISA design. The satellite, to be launched by the end of 2015, carries two free-floating test masses and an interferometer that measures the relative distance between them. The main objective of the satellite is to demonstrate that the residual acceleration noise between the masses is lower than $3\cdot 10^{-14}\,\mathrm{m\,s^{-2}\,Hz^{-1/2}}$ in the band between 1–30 mHz. In terms of displacement, a sensitivity of picometers in the same frequency band is required. To achieve such a high sensitivity, the instrument is provided with an accurate control system that allows to sense and actuate on 15 degrees of freedom of the system composed of the two test masses and the spacecraft, avoiding interference with the scientific measurements. The whole instrument is called the LISA Technology Package (LTP).

At such low frequencies, the system is exposed to a broad list of external perturbations that eventually limit the sensitivity of the instrument. Amongst them, temperature fluctuations at different spots of the satellite can end up distorting the motion of the masses and the interferometer readouts through different mechanisms. In order to measure these fluctuations and to characterise their contribution to the system sensitivity, the satellite is equipped with a thermal diagnostic subsystem composed of a series of heaters and high precision temperature sensors. Three different kind of thermal perturbation mechanisms are to be studied with such a subsystem: (1) thermal effects inducing direct forces and torques to the test masses due to the presence of temperature gradients, (2) thermo-elastic distortion due to temperature fluctuations in the structure hosting the test masses and the interferometer, and (3) thermo-optical distortion of two optical parts located outside the ultra-stable optical bench. This thesis focuses on the design of the experiments aimed to study the first two mechanisms. These experiments essentially consist in the injection of a series of heat loads near each of the thermal-sensitive locations in order to stress their associated thermal mechanism. The induced perturbation is visible with high signal-to-noise ratio (SNR) at both the optical measurements and the nearby temperature sensors and allows to derive coupling coefficients for each of the effects or, at least, bound their contribution to the acceleration noise.

The analysis of the impact of forces and torques on the test masses has followed two approaches: firstly, a simulator environment has been designed and implemented to estimate the impact of any kind of heat signal applied close to the test masses and, secondly, a test campaign has been carried out by means of a LTP-test mass replica installed in a torsion pendulum facility. Regarding the simulator, a state-space model has been developed including a thermal system of the whole spacecraft and a specific design for each of the mechanisms that generate forces and torques from temperature gradients: the radiometer effect, the radiation pressure effect and asymmetric outgassing. This model has been integrated into a general simulator of the whole LTP performance, what has allowed to simulate the whole chain between the heater activation and the final impact to the closed-loop performance of the LTP. In parallel, the experimental campaign by means of a torsion pendulum facility of the University of Trento has enabled to characterise the impact of each of the effects on different scenarios of absolute temperature and pressure.

On the other hand, the analysis of thermo-elastic noise in the LTP is based on the results obtained during a spacecraft Thermal Vacuum test campaign. In this test, a series of heater activations in the suspension struts that attach the LTP core assembly to the satellite structure allowed to bound the impact of temperature fluctuations at these locations and to characterise the main mechanical distortion mode associated to them.

The work presented here, as a continuation of other thesis on the same topic [1, 2], and with parallelisms with [3], is therefore intended to provide the framework and the tools for the definition and analysis of two of the thermal diagnostics experiments to be carried out by the LTP on board LISA Pathfinder.

Contents

Acknowledgements **iii**

Prologue **vi**

Table of Contents **ix**

Acronyms **xi**

1 Introduction **1**

- 1.1 Gravitational waves . . . 1
  - 1.1.1 Gravitational waves detection concept . . . 2
  - 1.1.2 Gravitational wave detectors . . . 4
  - 1.1.3 Space-based GW detectors . . . 8
- 1.2 LISA and eLISA: a project for a space-based GW observatory . . . 9
- 1.3 The LISA Pathfinder mission . . . 13
  - 1.3.1 The LISA Technology Package . . . 17
  - 1.3.2 LTP performance . . . 24
  - 1.3.3 LISA Pathfinder operations . . . 31
  - 1.3.4 Status of the project . . . 34
- 1.4 Structure of the thesis . . . 36

2 Thermal Diagnostics subsystem **37**

- 2.1 Temperature-induced noise sources in LISA Pathfinder . . . 38
  - 2.1.1 Temperature-related noise effects on the Inertial Sensors . . . 38
  - 2.1.2 Structural thermo-elastic noise distortion . . . 44
  - 2.1.3 Thermo-optical distortion of the optical parts . . . 46
  - 2.1.4 Other thermal effects of interest . . . 46
- 2.2 Thermal Diagnostics on board LISA Pathfinder . . . 47
  - 2.2.1 Temperature Measurement System . . . 48
  - 2.2.2 Heat injection system . . . 54
- 2.3 Thermal experiments . . . 56

3 Thermal Model of the LPF **59**

- 3.1 Thermal model implementation . . . 59
  - 3.1.1 Heater model . . . 60
  - 3.1.2 ESATAN Thermal Model . . . 63
- 3.2 Thermal model validation . . . 69
  - 3.2.1 The Inertial Sensor Housing thermal correlation test . . . 71
  - 3.2.2 Thermal model validation during the OSTT . . . 74
  - 3.2.3 Validation test discussion . . . 76
- 3.3 A model for the thermal effects . . . 77

3.3.1 Radiative model 77
3.3.2 Implementation into LTPDA 89
3.3.3 Model verification 90
3.4 Summary 92

4 Electrode Housing thermal experiment: design and simulation 97
4.1 Experiment concept 97
4.2 Thermal coefficient measurement 98
4.3 Analysis of errors 99
4.3.1 Estimation of the global thermal coefficient 101
4.3.2 Estimation of the individual thermal effects 105
4.4 Input definition 108
4.5 End-to-end simulation 110
4.5.1 Data analysis 110
4.5.2 Results 112
4.5.3 Thermal coefficients 112
4.5.4 Noise projection to the interferometer 114
4.6 Summary 116

5 On-ground testing of the Inertial Sensor thermal effects 117
5.1 The GRS prototype of the 4-mass torsion facility 117
5.1.1 Electrostatic sensing and actuating system 119
5.1.2 Additional displacement sensors 119
5.1.3 Thermal items on the pendulum setup 121
5.2 Torsion pendulum performance 123
5.3 Experiment design 127
5.3.1 Measurement of the thermal coefficient 127
5.3.2 Modulation frequency 128
5.3.3 Measurement duration 130
5.3.4 Environmental stability requirements 130
5.3.5 Experiment procedure 131
5.4 Experimental results 132
5.4.1 Linearity check test 132
5.4.2 Pressure-dependent radiometer effect characterisation 133
5.4.3 Asymmetric outgassing vs. radiation pressure 136
5.4.4 Phase delay in the thermal modulations 138
5.5 Conclusions and heritage to LISA Pathfinder 140

6 Thermo-elastic noise in the LISA Technology Package 143
6.1 Struts experiment design 145
6.2 The LISA Pathfinder Thermal Balance and Thermal Vacuum campaign . . 148
6.2.1 Subsystems in the LISA Pathfinder Core Assembly 148
6.2.2 Thermal experiments during the campaign 149
6.3 Thermo-optical characterisation of the LISA Pathfinder Core Assembly . . 151

6.3.1 Temperature environment characterisation 152
6.3.2 Response of the x_1 and x_{12} interferometers to heat inputs 153
6.3.3 Response of the static interferometers to heat inputs 154
6.4 Projection of thermo-elastic induced phase noise 159
6.5 Summary 162

7 Summary and conclusions 163

A Data analysis tools for thermal systems 169
A.1 Introduction 169
A.2 Spectral Density 169
A.3 Thermal system modelling 170
A.3.1 Transfer function of a LTI system 170
A.3.2 Digital filtering 171
A.3.3 State-Space Model representation 172
A.4 Data analysis tools for LTI systems 175
A.4.1 Transfer function estimate 175
A.4.2 Coherence 176
A.4.3 Noise projection 176
A.5 Demodulation process 176

B Data analysis pipelines for the thermal experiments 179
B.1 Electrode Housing thermal experiment pipeline 180
B.2 Strut thermal experiment pipeline 183

C Outgassing fit: expressions of interest 187
C.1 Asymmetric outgassing approximation to second order Taylor expansion . 187
C.2 Propagation of errors in outgassing fit curve 189

D Measurement of pressure in the 4-mass vacuum chamber 193
D.1 Residual gas composition 193
D.2 Pressure system schematic 195
D.3 Pressure gas non linearities 196
D.4 Conclusions 198

E Thermal characterisation of the pendulum EH prototype 199
E.1 Single heater transfer functions 199
E.2 Temperature gradient transfer function from direct measurements 201

F Thermal transfer function of the LCA struts 203
References 205

Acronyms

AC	Autocollimator. 126
ADC	Analog-to-Digital Converter. 38, 50–54, 152, 153
AO	Analysis Object. 33, 34
ASD	Astrium Deutschland/Germany. 63, 203
CFRP	Carbon-fiber-reinforced polymer. 44, 45, 144, 158, 166, 203
CGS	Compagnia Generale per lo Spazio, former Carlo Gavazzi Space. 15, 63, 71, 72, 75, 200
CMB	Cosmic Microwave Background. 4, 8
CPSD	Cross-Power Spectral Density. 169
CRB	Crámer-Rao Bound. 100, 102, 106, 108
CVM	Cage and Vent Mechanism. 20, 21
DAC	Digital-to-Analog Converter. 122
DAU	Data Acquisition Unit. 51, 55, 71, 76, 122
DDS	Data Management and Diagnostics Subsystem. 24, 47, 71
DFACS	Drag-Free Attitude and Control System. 19, 24, 26–28, 181, 184
DMU	Data Management Unit. 22, 24, 50, 51, 55, 56, 71, 72, 76, 110, 122, 149, 151
DOF	Degrees Of Freedom. 17, 19, 20, 24–27, 90, 118, 119, 145
DPS	Differential Power Sensing. 22
DRS	Disturbance Reduction System. 13, 31
DWS	Differential Wavefront Sensing. 22, 35, 156, 158, 159
EGSE	Electrical Ground Support Equipment. 71
EH	Electrode Housing. 14, 15, 20, 21, 39, 40, 42, 78, 84, 89, 90, 94, 95, 97, 98, 137, 181, 185, 196, 199
eLISA	*evolved*-LISA. 1, 12, 13, 36, 166
EM	Engineering Model. 163
EQM	Engineering Qualification Model. 35, 69, 72, 74
ESA	European Space Agency. v, 1, 9, 12, 13, 18, 31
ESAC	European Space Astronomy Centre. 35, 110
ESATAN	ESA Thermal Analyser. 60, 63, 79, 80, 83–85, 89, 109, 163, 200
ESOC	European Science and Operations Centre. 31, 35, 67
ESTEC	European Space and Technology Centre. 63
FEE	Front-End Electronics. 19, 20, 24, 119, 125
FEM	Finite Element Method. 63
GEF	Generic Exchange Factor. 83–85, 87, 89

GPRM	Grabbing, Positioning and Release Mechanism. 21
GRS	Gravitational Reference Sensor. 14, 17, 20–22, 24, 26, 27, 33, 34, 43, 92, 117, 119, 121, 122, 125–127, 139, 140, 142, 150
GW	Gravitational Waves. 1–9, 14
HIS	Heat Injection System. 47, 54
HR	High Resolution. 20, 126
IFO	Interferometer. 21, 24, 38, 153, 184, 185
IS	Inertial Sensor. 17, 19, 119, 184, 185
ISH	Inertial Sensor Housing. 35, 69, 71, 72, 74
LCA	LTP Core Assembly. 17, 18, 23, 44, 45, 47, 48, 54, 63, 74, 144, 145, 147–150, 152–155, 158, 159, 162, 166, 203
LISA	Laser Interferometer Space Antenna. v, ix, x, 1, 4, 9–14, 17
LPF	LISA Pathfinder. 1, 14–16, 22, 23, 33, 35, 38, 39, 43, 53, 59, 60, 63, 110, 128, 140, 147
LSB	Least Significant Bit. 53
LTI	Linear Time-Invariant. 59, 89, 169–172
LTP	LISA Technology Package. v, vi, 13, 15, 17, 18, 22–27, 30–34, 36, 38, 42–48, 54, 57–60, 63, 92, 110, 116, 117, 121, 143, 145, 148, 150, 159, 162–165, 169, 170, 175, 176, 179, 203
LTPDA	LTP Data Analysis. 33, 34, 59, 60, 64, 65, 67, 89, 90, 110, 112, 164, 169, 170, 175, 179
LUT	Look-Up Table. 56
MOC	Mission Operations Centre. 31, 50
NASA	National Aeronautics and Space Administration. v, 1, 9, 12, 13, 31
NTC	Negative Temperature Coefficient. 48–50, 54–56, 60–62, 102, 121, 199
OB	Optical Bench. 17, 21, 143, 155, 185
OBC	On-Board Computer. 24, 50, 71, 151
OG	outgassing. 39, 83, 94
OMS	Optical Metrology System. 17, 21, 24–27, 30, 33–36, 38, 57, 58, 111, 143–145, 147, 149, 151, 153–155, 159, 160, 162, 169, 176
OPD	Optical Pathlength Difference. 155, 156
OSE	Offline Simulations Environment. 110
OSTT	On-Station Thermal Test. 34, 35, 52, 69, 74, 145, 148, 150–152, 158, 162
OW	Optical Window. 46, 58, 185
PSD	Power Spectral Density. 54, 125, 152, 169
REF	Radiative Exchange Factor. 79–85, 89

RM	radiometer. 39, 83, 94
RP	radiation pressure. 39, 83, 94
SNR	Signal-to-Noise Ratio. v, 32, 100, 108, 175
SOVT	Science Operations Verification Tests. 35
SSM	State-Space Model. 59, 60, 64, 65, 67, 72–74, 76, 77, 89, 90, 97, 102, 116, 128, 129, 172, 173, 199, 201
STC	Stiffness Compensator. 119, 121
STOC	Science and Technology Operations Centre. 35, 110
STR	Strut. 185
TC	Telecommand. 55, 110
TDS	Thermal Diagnostics Subsystem. 47
TM	Test Mass. 14, 15, 20–22, 33, 39, 40, 42, 44, 78, 84, 88, 89, 94, 97, 137
TMS	Temperature Measurement System. 47, 48, 52, 149, 152
TOQM	Thermo-Optical Qualification Model. 34, 74
TS	Temperature Sensor. 90, 185
ULU	Ultraviolet Light Unit. 20, 33, 44
UTN	University of Trento. 117, 119, 120, 122
VF	View Factor. 79
WB	Wheatstone Bridge. 50
WR	Wide Range. 20

CHAPTER 1

Introduction

The road to the detection and observation of Gravitational Waves (GW) requires a massive scientific and technological effort. In the particular case of *low-frequency* gravitational wave detection in the milli-Hertz range, expected to be rich in strong and constant sources, the challenge also includes placing the observatory in space with the increased complexity that this represents in terms of design, construction and operation.

Current designs for this kind of observatories are based on establishing laser links between *free falling* test masses, separated by distances of the order of millions of kilometres, in order to measure their relative motion with high precision interferometers. Eventual Gravitational Waves passing by are expected to ripple their relative distance.

As of today, the most mature project able to carry out such an enterprise is the *evolved*-LISA (eLISA) proposal for an European-lead gravitational wave observatory [4]. Based on the well-known Laser Interferometer Space Antenna (LISA) mission concept [5], eLISA demands extraordinarily quietness conditions with very low noise perturbations affecting their critical systems, essentially composed by the inertial sensors and the optical measurement systems. Testing and characterising them in realistic space conditions is the ultimate purpose of LISA Pathfinder (LPF), a mission from the European Space Agency (ESA) with collaboration from the National Aeronautics and Space Administration (NASA) aimed to demonstrate the feasibility of key systems for eLISA. Already in an advanced stage of integration at the time of writing these lines, LISA Pathfinder is expected to be launched late in 2015.

1.1 Gravitational waves

Gravitational radiation was predicted by Albert Einstein (1879-1955) in the framework of the General Theory of Relativity [6], as the mechanism to explain how perturbations in the gravitational field propagate through space in concordance with the casualty law. Before that, gravity had been understood for centuries as an instantaneous-propagating force since the *Classic Mechanics* formulation by Isaac Newton in 1687.

Gravitational Waves are generated by *any* massive system, composed by one or more bodies whose mass distribution varies with time in a specific manner —with non-zero quadrupole momentum. Any asymmetric orbiting system or spinning asymmetric object may become a gravitational wave source. Gravitational waves propagate at the speed of light by rippling the spacetime geometry and, according to General Relativity, have two polarisation modes ('+' and '×') as shown in Figure 1.1. As transverse waves, their perturbation is perpendicular to the direction of propagation.

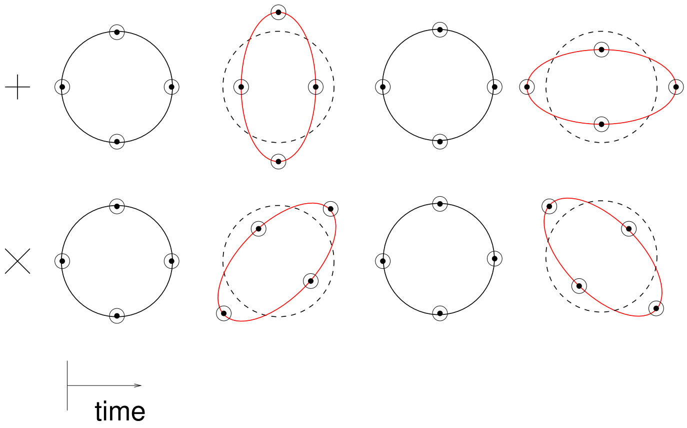

Figure 1.1: In General Relativity, GW present two possible polarisations that perturb the space in the plane perpendicular to the direction of propagation. In the example, the GW direction is perpendicular to the paper and the possible polarisation modes '+' (*top*) and '×' (*bottom*) are shown [2].

Extremely massive events or scenarios like merging black holes, neutron stars coalescence or galactic binaries are believed to be powerful GW emitters. However, GW have never been *directly* detected mainly because of their small incidence on Earth and the so far unavailable instrumental sensitivity required.

From an astrophysics point of view, the detection of GW would open a new window to the universe observation. GW barely interact with matter, so they can propagate across environments that are completely opaque to electromagnetic waves. In effect, establishing a parallelism with the electromagnetic spectrum exploration, the observation of the GW spectrum may yield unimaginable information from sources so far invisible to us.

Experimental evidence of the existence of GW was proved by Russell A. Hulse and Joseph H. Taylor *Jr.* in 1978 [7] after observing the loss of energy of a neutron star binary pulsar —the pulsar PSR B1913+16, later known as the *Hulse-Taylor* pulsar— and fitting it to General Relativity predictions. Such work was awarded with the Nobel Prize in Physics in 1993.

1.1.1 Gravitational waves detection concept

The fundamental concept of GW detection is based on the fact that any *massive* object or system exposed to gravitational radiation is geometrically distorted as a gravitational wave passes by. In effect, a system composed of two objects exposed to a GW will experience a distortion along the perpendicular wave direction as schematized in Figure 1.2.

Such a distortion caused by a GW is measured in terms of strain h, defined as

$$h = \frac{\Delta L}{L} \tag{1.1}$$

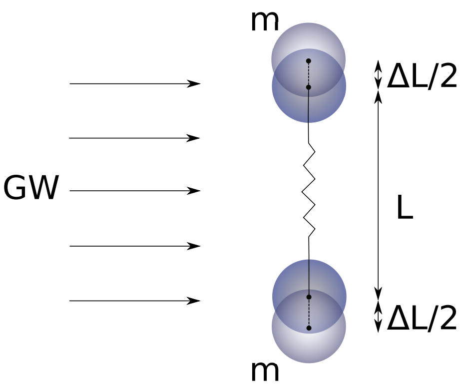

Figure 1.2: Distortion experienced by a system of two masses m exposed to a GW.

where L is the nominal distance between the masses.

Still, such a relative change in distance between two unbounded free-falling bodies as a consequence of a GW interaction is severely tiny. The strength of the strain as measured from the Earth scales with [8]

$$h \propto \frac{M}{R}\frac{M}{l}\left(\frac{v}{c}\right)^{\alpha} \varepsilon \tag{1.2}$$

where M is the source mass at a distance R, l is a characteristic length of the source, v/c is a characteristic speed inside the source and ε accounts for its asymmetry. The ratio M/l can be understood as the compactness of the source. In consequence, the strongest signals may come from compact, fast and asymmetric sources like for example supernovae, neutron stars or black holes, or eventual systems between them.

Depending on the spin or orbital speed of the emitting system —actually, the second derivative of the quadrupole moment—, the consequent measured strain oscillates at a different frequency. Thus, supernovae GW signals are expected at the range of $\sim$100 Hz, compact binary coalescences between 1 Hz and 1 kHz, and much heavier systems like black hole mergers of galactic binaries induce strain at a much lower frequencies, i.e. $\sim$1 mHz. Such a broad range of frequencies actually opens an extended spectrum to observe, from 10^{-18} Hz up to $\sim$kHz defining the ranges summarized in Table 1.1 [9].

Accordingly, several kind of GW detectors have been developed, focusing on particular bands and using different techniques. Still, the strain to be measured is in any case dramatically small. Take for instance the following approximation which provides an upper limit for the strain [10]

$$h \leq \frac{1}{R}\frac{1}{l}\left(\frac{GM}{c^2}\right)^2 \tag{1.3}$$

where G and c are the gravitational constant and the speed of the light, respectively[1]. This bound already states that an eventual strong GW emission by a supernovae with a

---

[1] $G = 6.67 \cdot 10^{-11}\,\mathrm{m^3\,kg^{-1}\,s^{-2}}$ and $c = 3 \cdot 10^{8}\,\mathrm{m\,s^{-1}}$

Name	Range [Hz]	Main sources
Ultra low frequency band	$10^{-18} - 10^{-13}$	Stochastic background from inflation phase (CMB)
Very low frequency band	$10^{-9} - 10^{-7}$	Millisecond pulsars, unresolved coalescing binary black holes
Low frequency band	$10^{-5} - 1$	Neutron stars (essentially pulsars) merging binary black holes, stochastic background from phase transitions
High frequency band	$1 - 10^{4}$	Compact binaries, supernovae, pulsars and transitions

Table 1.1: Summary of the gravitational radiation bandwidths of interest and their main sources [9].

mass $1M_\odot$ in our galaxy produces a strain of $h \leq 10^{-18}$. However, such a detection results improbable since events of this kind occur just a few times per century or even less. In order to have approximately one event per month it is necessary to expand the scope up to 10 Mpc to include the Virgo cluster of galaxies, but then the limit is reduced to $h \leq 10^{-21}$ [10]. In a system composed of two bodies separated 1 km such a level of strain would induce variations of distance already in the order of 10^{-18} m. Many techniques aiming to measure such small perturbations have succeed in achieving such sensitivities, as explained in the following sections.

1.1.2 Gravitational wave detectors

Sophisticated detectors able to measure characteristic strains in the order of 10^{-22} have been developed an operated along the last decades. Research on the high frequency band is carried out by means of resonant bars [11] and interferometry-based on-ground detectors [12, 13]. The band between 10^{-9} and 10^{-6} Hz is covered by Pulsar Timing arrays [14, 15, 16] and the trace of GW at the lower edge of this band is being sought by detectors measuring the polarization of the cosmic microwave background [17]. Finally, interferometer-based space observatories are planned to inspect the milli-Hertz band, following the LISA concept proposed at the end of the last century [4]. Figure 1.3 presents a variety of detectors and their measurement bandwidths together with their expected main sources.

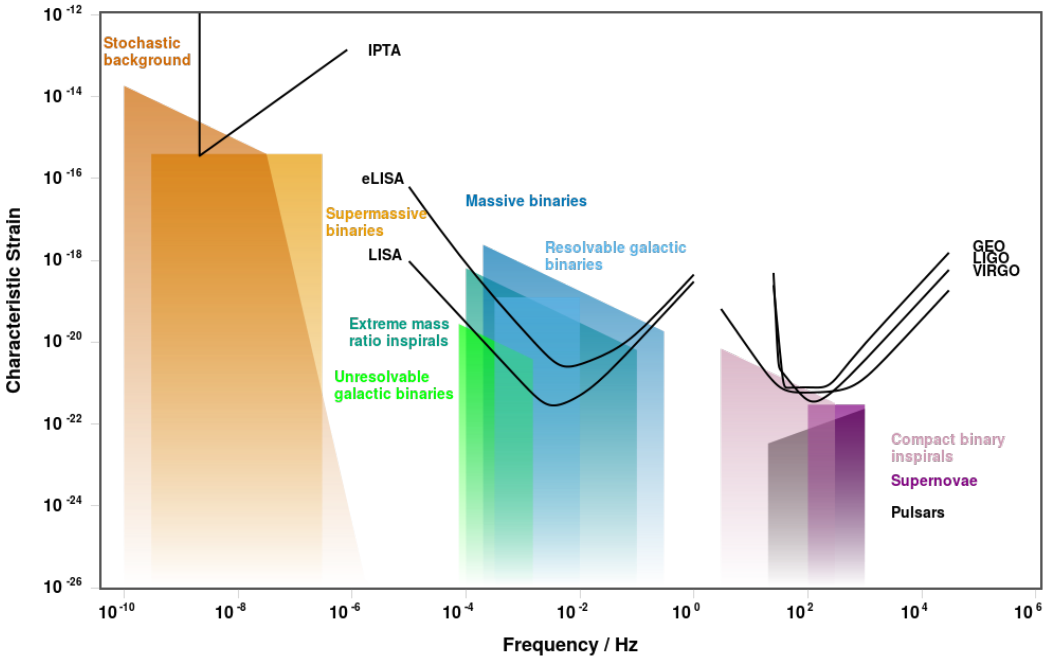

Figure 1.3: Characteristic strain h from main GW sources together with the sensitivity of some detectors, excluding the *ultra-low frequency* band. Resonance spikes have been removed from the sensitivity of some detectors. Credits: [18, 19].

1.1.2.1 Resonant mass detectors

The very first attempts to detect GW were based on resonant masses and started in the 1960s by the physicist Joseph Weber [20]. The measurement principle states that eventual high frequency GW passing by could excite the natural vibration modes of an isolated body, what can be measured by means of several kind of deformation sensors. Weber's designs consisted of resonant cylindrical bars with a high mechanical quality factor Q, i.e. with a low energy dissipation when oscillating at specific frequencies. With different setups which included bars of approximately 1 m and piezoelectric sensors, he managed to measure a strain of the bar down to 10^{-16} at the frequency of ~1 kHz, what actually means stunning variations of $\sim 10^{-16}$ m [11].

Despite it was demonstrated that Weber's bars were unable to measure GW [21], his inventor claimed he had actually observed gravitational radiation, what generated major controversy at the time [22, 23]. In any case —no matter the results he obtained—, the GW community has always recognized him as the father of gravitation wave detection and his reports encouraged several groups to start working on the field [11].

Over the last decades, the sensitivity of this kind of sensors has been largely improved by modern detectors using cryogenic techniques like ALLEGRO [24, 25], AURIGA [26, 27], EXPLORER [28] at CERN, Niobe [29] and NAUTILUS [30, 28]. Other similar designs include resonant spheres or polyhedron geometries rather than resonant cylinders, as MiniGRAIL [31], TIGA [32] and Mario Schenberg [33]. Strain sensitivities down to $10^{-22}\,\mathrm{m\,Hz^{-1/2}}$ have been achieved with this kind of detectors, always for frequencies higher than 100 Hz and reduced bandwidths ~10 Hz.

1.1.2.2 Interferometric detectors

In the 1970s, the development of laser interferometry techniques to measure distance fluctuations pushed interferometer-based detectors as an alternative to the resonant bars. Replacing the one single vibrating mass by an optical arm between separated masses allowed to widen the operational bandwidth and to relax the length fluctuation requirements to measure similar kind of strains.

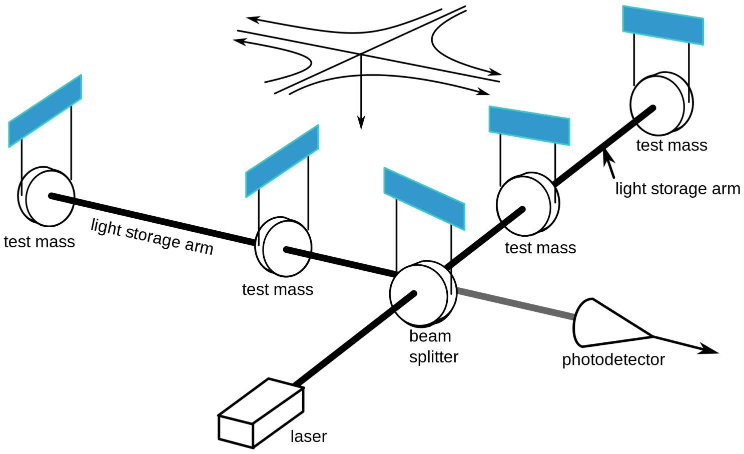

Figure 1.4: Schematic of an on-ground laser interferometer gravitational wave detector. Credits: LIGO Laboratory.

Instead of measuring the distortion of a single body, this kind of detectors measure the distance fluctuation between two separated bodies by means of laser interferometry. In order to distinguish a GW from other eventual perturbations, at least two arm-links are required. Figure 1.4 shows a schematic of a generic laser interferometer detector. As observed, the laser is split in two beams that are injected in two optical arms. If properly oriented, an eventual GW passing by squeezes one arm while stretches the other, what is sensed by recombining the beams coming from the two arms and evaluating their respective phase shift. For the simplified case of a GW impinging perpendicularly on the interferometer's place, the phase variation is determined by [34, 3]

$$\delta\phi = 2\frac{\omega_L}{\Omega_{\mathrm{GW}}}\, h_+ \sin\frac{\Omega_{\mathrm{GW}}\,\tau}{2} \tag{1.4}$$

where ω_L is the angular laser frequency and Ω_{GW} the angular frequency of the GW inducing a polarised strain h_+ aligned with the arms of the interferometer. Finally, τ is the time it takes to the beam to complete twice the distance that separates the masses of a single arm L, $\tau = 2L/c$. Such an expression leads to the optimum arm-length L for a given GW frequency:

$$L_{\mathrm{opt}} = \frac{\pi c}{2\,\Omega_{\mathrm{GW}}} = \frac{\lambda_{\mathrm{GW}}}{4} \tag{1.5}$$

where λ_{GW} is the wavelength of the GW. By using Fabry-Pérot cavities as resonators, the effective length L is amplified a factor ∼100. Such a scheme is commonly combined with power recycling techniques that allow to confine in the arms light power ∼1 kW, though the laser source is ∼10 W.

On-ground detectors with arm-lengths of ∼1 km and measurement bands > 1 Hz were developed in the 1990s, like GEO600 (600 m, [35, 36]), TAMA (300 m, [37]), Virgo (3 km, [38]) and LIGO [39], the latter being actually composed by two detectors of 4 km. Figure 1.5 shows the sensitivity of some of them.

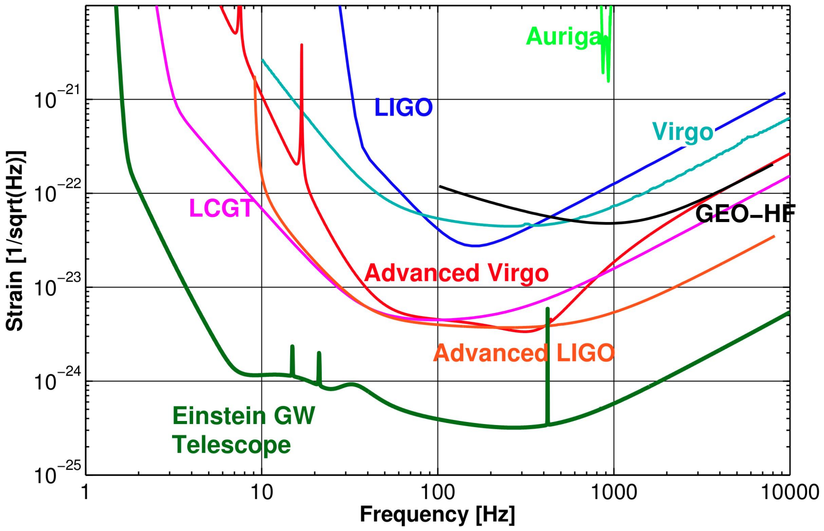

Figure 1.5: Sensitivity curves for a variety of on-ground gravitational wave detectors. LCGT is the former name for the Japanese KAGRA detector. Credit: [40].

The most important perturbation that strongly limits the sensitivity of this kind of detectors around 1 Hz is the Earth seismic noise. In order to minimize this effect, most of the optical parts need to be suspended by complex damping structures consisting of a series of mechanical filters in cascade. On the other hand, the sensitivity at the higher edge of the band is limited by the quantum noise, actually a combination of shot noise —sensing noise— at high frequencies and photon radiation pressure noise at low frequencies [41, 40].

Campaigns carried out so far have not yet captured evidence of GW measurement, but have been useful to set upper limits to the expected signals induced by some sources [42]. All of them have relied on statistically-expected sources but without unequivocal candidates. Nevertheless, the development of the forthcoming generation of on-ground detectors is expected to improve their sensitivity at least one order of magnitude: *advanced*-LIGO (aLIGO, [43, 13]), *advanced*-Virgo (aVirgo, [44, 12]) and a possible detector in India similar to aLIGO, namely IndIGO [45]. At the moment of writing these lines, first measurements are expected by the end of 2015 and according to estimated statistics of potential sources in the new available range after the upgrade, first GW could be detected along 2016, possibly from a binary of neutron stars [46, 47].

Finally, third-generation detectors are already in their way. Placed underground to reduce the impact of seismic noise and using cryogenic mirrors to minimise thermal noise, KAGRA detector [48] is expected to be fully operative by 2018 with strain sensitivity of $\sim 10^{-24}\,\mathrm{m\,Hz^{-1/2}}$ at 100 Hz. Meanwhile, the Einstein Telescope (ET) project [49] is being designed in Europe, with a strain sensitivity target $\sim 10^{-25}\,\mathrm{m\,Hz^{-1/2}}$ at 100 Hz. The expected sensitivity curves for both ET and KAGRA —formerly known as the Large-Scale Cryogenic GW Telescope (LCGT)— are shown in Figure 1.5.

1.1.2.3 Pulsar Time Arrays

Pulsar Time Arrays (PTA) observatories track radio signals emitted by several millisecond pulsars in order to detect pulse rate fluctuations caused by interaction with GW. Indeed, eventual GW emitted by massive sources like merging black hole binaries in two coalescing galaxies imprint delays in the observed pulse rates, estimated of the order ~10 ns along periods from weeks to decades.

The main PTA detectors are the Australian Parker's PTA (PPTA, [15]), that started operations in 2005, the European PTA (EPTA [14, 16]) and the American NANOGrav [50]. All of them have joint into a single collaboration in the International PTA (IPTA, [51]). Current estimations expect to make detections of supermassive black holes or cosmic strings no later than 2020 [52], though some optimistic predictions state that first prediction could already take place in 2016 [53].

1.1.2.4 Cosmic Microwave Background detectors

Some experiments aimed to observe the polarization of the Cosmic Microwave Background (CMB) may report as well proof of gravitational wave detection at some point in the following years. Their main objective is to prove cosmic inflation by observing the B-mode polarization of CMB. Since ultra-low frequency GW may arise from inflation, the B-mode polarisation map could eventually contain a quadrupole signature imprinted by this kind of GW. BICEP1 [54] and BICEP2 [55] have been leading these observations, the latter claiming in March 2014 a possible detection of GW from the very early universe (10^{-16} Hz) [56]. Unfortunately, a posterior joint analysis with data from Planck [57] attributed the candidate signal to an excess of interstellar dust in the region observed by BICEP2, discarding any possibility of having observed GW [17].

Nevertheless, more accurate CMB detectors have been developed to pursue their objective: the improved Keck Array [58] and BICEP3 [59], already operative and observing.

1.1.3 Space-based GW detectors

The GW detectors presented so far have operative bandwidths far from the milli-Hertz band, a region expected to host many of the most abundant sources. As already stated, seismic noise limits on-ground observation for frequencies below 1 Hz. So, a direct alternative is to place the whole detector in space. In effect, laser interferometry between satellites hosting test masses in quasi-free fall conditions would cancel this kind of noise. In addition, the arms-length can be much longer, even in the order of $\sim 10^9$ m.

The idea of placing a Michelson laser interferometer in space arose in the 1980s with LAGOS (Laser Gravitational Observatory), a proposal from P.L. Bender and J. Faller from the JILA[2] [5]. Such a detector consisted on placing a constellation of three satellites with laser links between them, orbiting directly around the Sun.

Such an initial idea evolved to the definition of LISA, proposed in the 1990s as a shared mission between ESA and NASA in response to the ESA's *Call for Mission Proposals* for the third Medium-Size Project (M3). Since then, the mission has been refined and has competed in different mission proposals from ESA. In parallel, the Japanese detector DECIGO [60, 61] was proposed in 2001, a project with similarities to LISA but including more satellite constellations and observing in the band 0.1–1 Hz.

The technical challenges —and the associated risk and cost of money— have always prevented a serious implementation of any of them. Nevertheless, a call for a LISA-like mission to be launched by the ~2030s is expected after *The Gravitational Universe* topic was selected by ESA [4, 62].

In parallel, lots of effort have been directed on the development of technologies that must ensure the feasibility of an eventual space observatory. Indeed, technology-demonstrator satellites are being developed for both LISA-based and DECIGO space detectors: LISA Pathfinder [63], to be launched at the end of 2015 and the main concern of this thesis, and DECIGO Pathfinder [64], with similar objectives and to be launched between 2016-2017 with even a small chance of detecting GW [65].

Finally, the Big Bang Observer (BBO) [66], a more complex space-based detector that would include more than one satellite constellations, has already been proposed for a post LISA mission.

1.2 LISA and eLISA: a project for a space-based GW observatory

The Laser Interferometer Space Antenna (LISA) design is a classic proposal for a space-borne gravitational wave detector in the bandwidth between 10^{-4} and 1 Hz [4]. This measurement band is expected to be rich in sources emitting powerful and regular signals, like massive black holes and different kind of binaries involving either neutron stars, white dwarfs or even black holes. In addition, the scope envisaged already includes some *verification binaries* that are well-known white dwarf binaries whose signal must be in any case detected as a proof of performance.

---

[2] JILA: Joint Institute for Laboratory Astrophysics, Boulder, Colorado (USA).

Since their abundance in the scope envisaged for LISA is already proved, their detection by LISA once operative should be reasonably straightforward.

The detector itself consists of three satellites in a triangular constellation of $5 \cdot 10^6$ km each arm, as shown in Figure 1.6. Laser links between each pair of satellites allow a performance similar to a Michelson interferometer with a third arm providing information of wave polarisation and system redundancy. The light beam is an infra-red laser of 1064 nm.

The whole constellation orbits around the Sun at 1 AU with 20° of delay with respect to the Earth and a constellation-plane inclination of 60° with respect to the ecliptic plane —see Figure 1.6. During a whole orbit around the Sun, the satellite constellation also completes a whole rotation around its center.

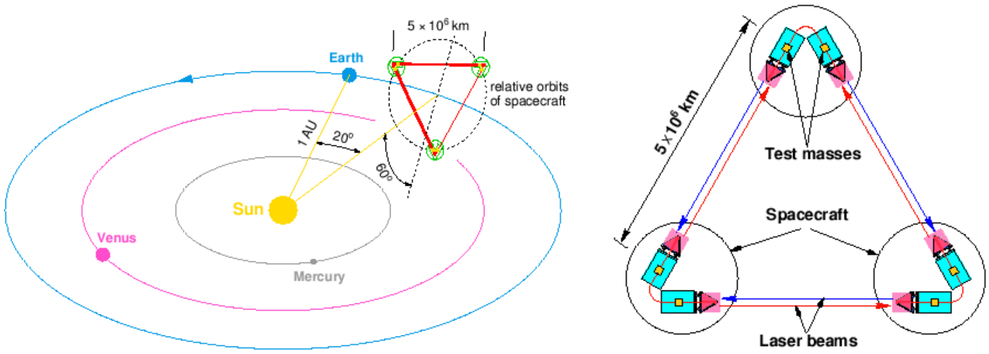

Figure 1.6: *Left:* LISA constellation orbit around the Sun. *Right:* LISA classic configuration.

The strain to be measured is $\sim 10^{-20}\,\mathrm{Hz}^{-1/2}$ in the milli-Hertz band, what represents an associated length fluctuation of $\sim 50\,\mathrm{pm\,Hz}^{-1/2}$ in each LISA arm. However, the spacecrafts are exposed to strong perturbations coming mainly from the Sun —i.e. solar radiation pressure and solar wind— that induce jitter and net forces to the spacecraft that jeopardise the Test Masses quietness. The solution is found by measuring the fluctuations between Test Masses kept inside the spacecrafts, protected from external perturbations. These Test Masses —actually platinum-gold cubes of 46 mm per edge— operate as end mirrors for the interferometers and need to be released inside vacuum enclosures in quasi free fall conditions.

Many noise sources present significant contributions to the motion of the Test Masses at this level of required precision. Roughly, external perturbations like magnetic field fluctuations and high energy particles passing by, and different satellite self-induced perturbations, induce effects deriving to stray forces and torques to the masses. Therefore, the Test Masses need to be somehow controlled and centred in their nominal locations with respect to the satellite without inducing excessive noise to the science measurements. This is achieved by carefully measuring the position of each Test Mass with respect to the satellite by means of capacitive sensors and a sophisticated electrostatic control of their attitude, leaving only certain degrees of freedom in free-fall conditions in the bandwidth of interest while the others keep actuated. In parallel, direct spurious forces on the spacecraft are compensated by means of high precision thrusters so the satellite keeps centred on the Test Masses.

The measurement of relative displacement between masses differs from the Michelson classic interferometer in the sense that there is no destructive recombination of the beams, what in on-ground detectors is achieved by imposing equal arm-lengths. In addition, there is not a single laser source but one for each of the six masses, emitting the beam to be impinged to its opposed mass $5 \cdot 10^6$ km away. All in all, in LISA there is an important contribution of laser noise, and therefore alternative techniques to measure the phase difference are needed. The solution is found by combining the phasemeter outputs of the different beams by means of a post-processing technique known as Time-Delay Interferometry (TDI) that consists on properly time-shifting and linearly combining independent Doppler measurements [67]. Such a technique must also cope with the fact that the absolute distance between satellites is expected to oscillate 10^3 km per year.

The sensitivity in the classic LISA design is determined by three main factors:

- *Antenna frequency response*: The highest part of the band (10^{-2}–1 Hz) is dominated by the roll-off of the antenna transfer function, which decreases with the frequency —thus, the noise increases with the frequency ω. The cut-off frequency of this transfer function is defined by the length L of the arms and the angle between them [2].
- *Shot noise*: The sensitivity in the central part of the band (10^{-3}–10^{-2} Hz) is limited by the shot noise or the noise associated to the photon rate fluctuations in the beam. The effect is a noisy path difference δL inversely proportional to the squared root of the received laser power. This kind of noise can be reduced by increasing the beam power —i.e. increasing the rate of photons— or by using larger telescopes.
- *Acceleration noise*: The band $f < 10^{-3}$ Hz is limited by the direct spurious forces that appear on the Test Masses and includes residual gravity effects, cross-talks from electrostatic actuation noise, temperature and magnetic field fluctuations, Test Mass random charge, etc. Assuming a certain spectral distribution for these forces $S_F^{1/2}(\omega)$, the induced noise in the strain is found by

$$S_{\Delta h}^{1/2}(\omega) = \frac{2}{m\,L} \frac{S_F^{1/2}(\omega)}{\omega^2} \tag{1.6}$$

The final required sensitivity curve of LISA is defined in terms of residual differential acceleration (Δa) spectral density between each pair of opposed Test Masses as

$$S_{\Delta a}^{1/2}(\omega) \leq 3 \cdot 10^{-15} \left[1 + \left(\frac{\omega/2\pi}{3\,\text{mHz}}\right)^2\right] \text{m s}^{-2}\,\text{Hz}^{-1/2} \tag{1.7}$$

what in terms of equivalent displacement noise is

$$S_{\Delta x}^{1/2}(\omega) = \frac{S_{\Delta a}^{1/2}(\omega)}{\omega^2} \tag{1.8}$$

both in the band from 10^{-4} to 0.1 Hz. In order not to affect the precision of the measurements, the capacitive sensors of electrostatic control require a precision of $\sim 10\,\mathrm{nm\,Hz^{-1/2}}$, while the thrusters require a precision $< 1\,\mu\mathrm{N\,Hz^{-1/2}}$ in the band of interest.

The eLISA proposal

Though the LISA design achieved an important level of maturity [5], it never transferred to an advanced development stage. Nevertheless, its initial concept has been an inspiration source for more realistic proposals —in terms of budget and space agency's programmes— that have competed in different mission calls. In this sense, the New Gravitational Observatory (NGO) was presented in 2012 [68] to compete in the ESA's L1 mission slot call, while further studies were being addressed by NASA [69]. After some years with no success in any mission call, ESA selected the *Gravitational Universe* as the topic to be studied by the upcoming L3 call for a large mission (*L-class*). Such a mission should set a space-based gravitational wave detector by 2034, and the LISA-like proposal called *evolved*-LISA (eLISA) [4] is undoubtedly the best positioned for such a mission. Figure 1.7 shows the satellite constellation and Figure 1.8 the expected strain sensitivity of eLISA. Notice that the current proposal includes only two arm links of 10^6 km, though such a feature may vary in future reviews of the design. Also, the arms proposed are shorter than those planned for LISA, what reduces the sensitivity in the lower edge of the bandwidth —see Figure 1.8.

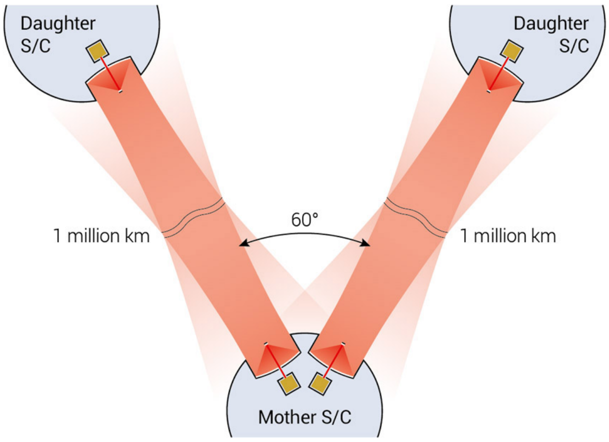

Figure 1.7: eLISA satellite constellation (not to scale). Credits: [4].

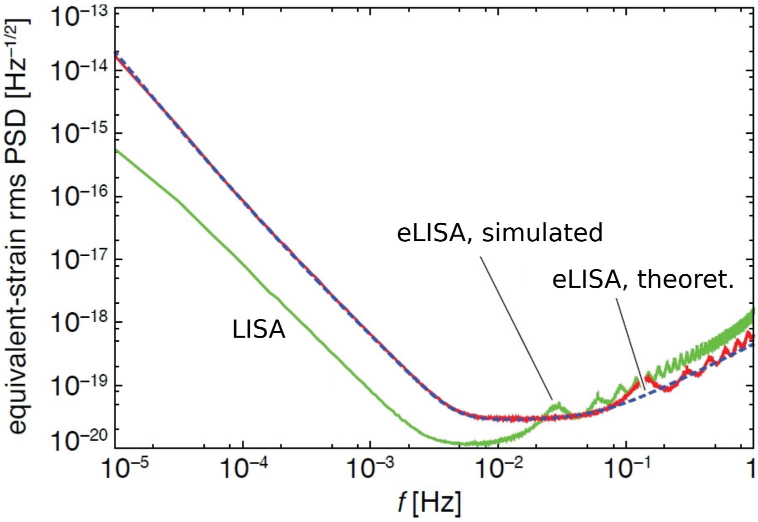

Figure 1.8: Estimated sensitivity curves for eLISA with respect to classical LISA. Credits: [70].

A technology demonstrator for LISA

In front of the need to develop and validate the challenging technologies required by the initial LISA proposal, both ESA and NASA decided to previously launch a technology demonstrator mission to test the different aspects of LISA that cannot be proved on-ground, excepting some mechanical design issues such as the laser pointing between satellites. In this sense, the noise sources involved with the *length* of the LISA arms and the Time-Delay Interferometry can be tested on-ground, leaving a contribution of residual laser frequency noise of 5% in the band above 8 mHz and negligible below this frequency [71]. Also, the local interferometer noise affecting the same upper band can be tested in the laboratory as well, leaving only the need to evaluate the acceleration noise on the Test Masses. This kind of noise in LISA limits the sensitivity in the band around 1 mHz and can only be fully reproduced in zero-gravity environments. Fortunately, spurious forces on the Test Masses are vastly induced by local effects. Thus, they can be proved in one satellite by squeezing enough a LISA arm. That is the purpose of LISA Pathfinder.

1.3 The LISA Pathfinder mission

LISA Pathfinder is thus a medium-class mission of ESA with contribution from the NASA to test the key elements for a future LISA-based gravitational wave observatory that cannot be tested on-ground, essentially: the suppression of force disturbances on the free-falling Test Masses. To do so, the satellite itself contains a simplified version of a whole LISA arm with two Test Masses. In order to fit in a single spacecraft, the relative distance between masses is reduced to just few tenths of centimetres. The mission aims to validate the in-space performance of different subsystems, such as a picometer resolution interferometer, two types of μN-resolution thrusters, specific drag-free controllers and environment diagnostics equipment, amongst others. The satellite hosts two *payloads*: the LISA Technology Package (LTP) [72, 73] from ESA with collaboration of several state members, and the Disturbance Reduction System (DRS) [74] from NASA, the latter providing an alternative controller and a dedicated set of μN-thrusters but using the Test Masses and interferometers from the former.

As in LISA, the LISA Pathfinder top requirement is expressed in terms of maximum residual differential acceleration spectral density between Test Masses:

$$S_{\Delta a}^{1/2}(\omega) \leq 3 \cdot 10^{-14} \left[1 + \left(\frac{\omega/2\pi}{3\,\mathrm{mHz}}\right)^2\right] \mathrm{m\,s^{-2}\,Hz^{-1/2}} \tag{1.9}$$

in the band between 1–30 mHz, as shown in Figure 1.9. Notice that such requirement is similar to the LISA main one but relaxed one order of magnitude and the band is squeezed to focus just on the milli-Hertz region. This request is specifically envisaged to test the free-fall quality of the Test Masses, but certainly prevents any GW detection since its arm-length is reduced to 38 cm.

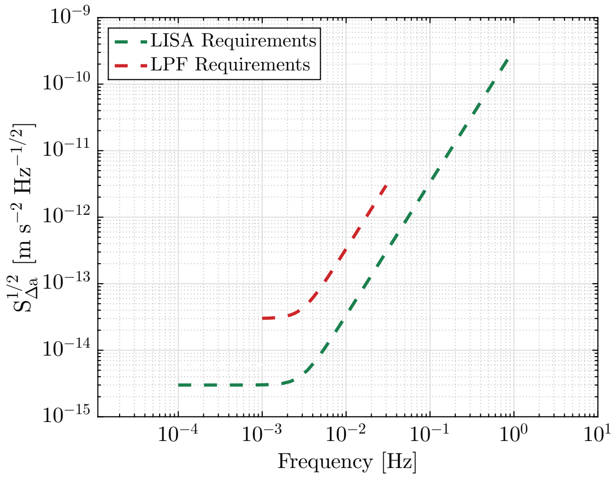

Figure 1.9: LISA Pathfinder acceleration sensitivity requirements vs. classic LISA specifications.

The LPF Test Masses are cubes of 46 mm of edge, made of an alloy of platinum and gold (27%–73%) with a total weight of 1.96 kg per mass. Each Test Mass (TM) is located inside an Electrode Housing (EH). Each Electrode Housing is made of molybdenum and is equipped with a series of electrodes on all its internal walls that allow to measure the relative position of its Test Mass with respect to the satellite by means of capacitive measurements. Each EH-TM system composes the essential part of each of the two Gravitational Reference Sensors (GRS) onboard —see Figure 1.10. Figure 1.11 shows one Flight Model of the Electrode Housing.

The requirement in Equation 1.9 needs to be met *only* on the axis that joins the Test Masses, namely the x axis. The instrument responsible for this differential measurement is a picometer resolution interferometer that traces the relative displacement

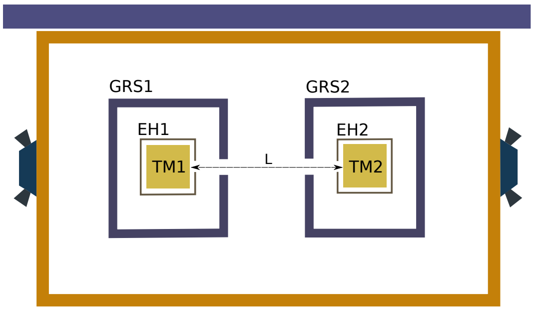

Figure 1.10: Simplified draft of the LTP. Each Test Mass (TM) is located inside an Electrode Housing (EH). Each EH hosts a series of electrodes that provide electrostatic sensing and control of the position and attitude of the TM with respect to the satellite. At the same time, series of precision thrusters control the attitude of the spacecraft.

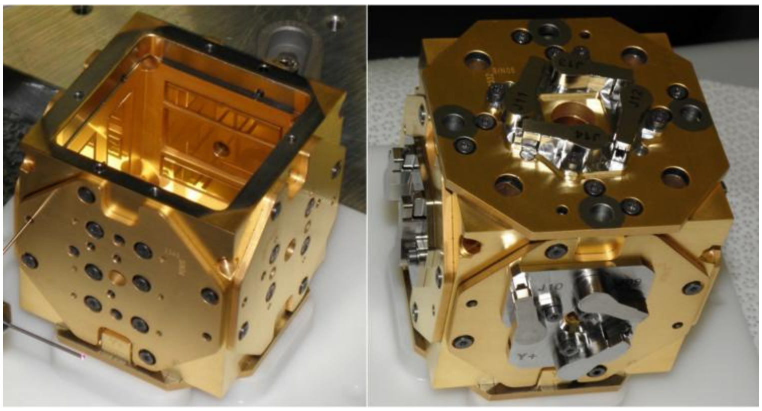

Figure 1.11: Flight model Electrode Housing. Credits: CGS SpA.

between the two Test Masses and the relative motion between one Test Mass and the spacecraft, amongst other measurements.

From a technical point of view, LPF is aimed to provide a test bench where to develop the following activities:

- *Demonstrate free-fall performance*: Long measurements of acceleration noise between the Test Masses need to ensure that the acceleration requirement in Equation 1.9 is fulfilled. This demands a smooth performance of the different control loops that keep both the satellite and the masses in their consigned positions without inducing excessive jitter to them [73].

- *Demonstrate noise suppression*: Several kinds of noise sources —external and self-induced— can eventually perturb either the Test Masses directly or the optical instrumentation. The kinds of noise sources are diverse: high energy particles passing by, magnetic or temperature fluctuations, Brownian noise from the different subsystems, laser noise, etc. LPF is designed in order to minimise them, however residual fluctuations are still expected. The main ones already have an apportioned gap in the global noise budget of the experiment, and series of sensors and auxiliary readouts must ensure that their noise limits are not exceeded [75].

- *Characterise critical noise sources*: A further step in the experiment is to directly characterise the mechanisms that induce some noise contributions by means of dedicated experiments, allowing the possibility to later subtract them from the measurement [76]. In this sense, LPF turns into an ideal space-based testing platform. Precisely, LPF is equipped with a series of heaters and coils to induce thermal and magnetic signals aimed to characterise the impact of temperature fluctuations and magnetic field noise by dedicated experiments [77].

Consequently, the LPF experiment ultimately consists on characterising all the noise sources detected with the eventual subtraction of some of them to achieve a sensitivity as good as possible in the milli-Hertz band.

The satellite is going to be launched by a Vega rocket, that will inject the spacecraft to an elliptic orbit around the Earth of around $200 \times 1600\,\mathrm{km}$ and an inclination of 63°. From there, a dedicated Propulsion Module will push the Science Module to achieve its final $500,000 \times 800,000\,\mathrm{km}$ Lissajous orbit around the Sun-Earth Lagrange point L1, where the satellite will operate. Since the Propulsion Module is equipped with liquid propellant tanks whose residual content could jeopardise the performance of the satellite's experiments, the Propulsion Module will separate from the Science Module at some point before achieving L1 —see Figure 1.12. Figure 1.13 shows a picture from the Science Module and the Propulsion Module in the launch configuration.

1.3.1 The LISA Technology Package

The LISA Technology Package (LTP) is the main scientific instrument on board LISA Pathfinder. It is composed essentially by the two Gravitational Reference Sensors (GRS), the Optical Metrology System (OMS), plus the different associated subsystems required to carry out the whole experiment. The two GRS and the Optical Bench (OB) of the OMS are located in the central part of the satellite, namely the LTP Core Assembly (LCA), while all the other equipment like the different control units, power management units, batteries, etc. are placed in the different compartments around —see Figure 1.14. The LCA is attached to the satellite structure by means of the eight Suspension Struts, as shown in Figure 1.15.

1.3.1.1 Gravitational Reference Sensors

Each Gravitational Reference Sensor is actually one independent Inertial Sensor (IS) that provides sensing and control for all the six DOF of its Test Mass. The measurements are provided by an accurate capacitive system that monitors the variation of electrical capacitance between pairs of electrodes and the Test Masses. Each Electrode Housing surrounding each Test Mass contains the layout of electrodes shown in Figure 1.16.

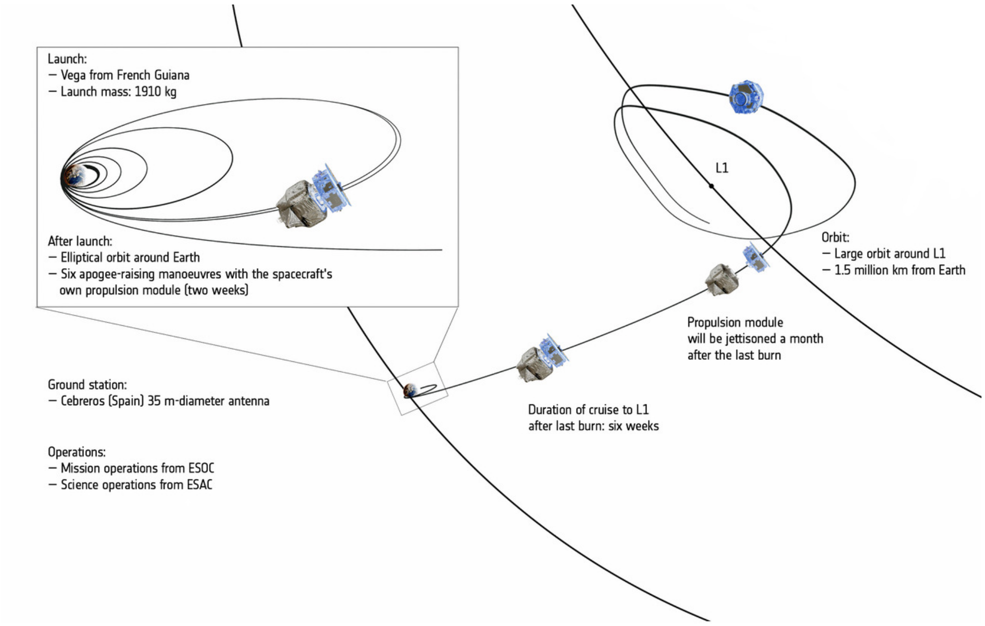

Figure 1.12: LISA Pathfinder transfer to the Lissajous orbit around L1. Credits: ESA/ATG medialab.

Figure 1.13: LISA Pathfinder at IABG's space test centre in Ottobrunn, near Munich, Germany, just few days before being shipped in its way to the launch site in Kourou, French Guinea. Credits: IABG/ESA

There are a total of eighteen sapphire gold coated electrodes attached on the inner walls of the Electrode Housing [78]: twelve of the electrodes are for capacitive sensing and actuation on all the DOF while six of them are used to induce bias voltage signals

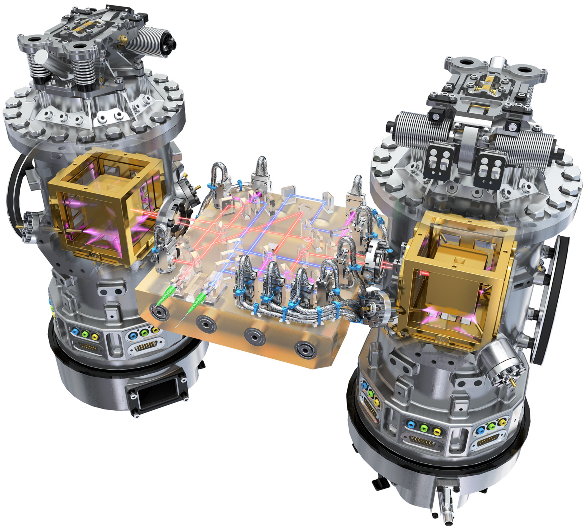

Figure 1.14: Artistic view of the two Inertial Sensors and the Optical Bench. Credits: ESA/Medialab.

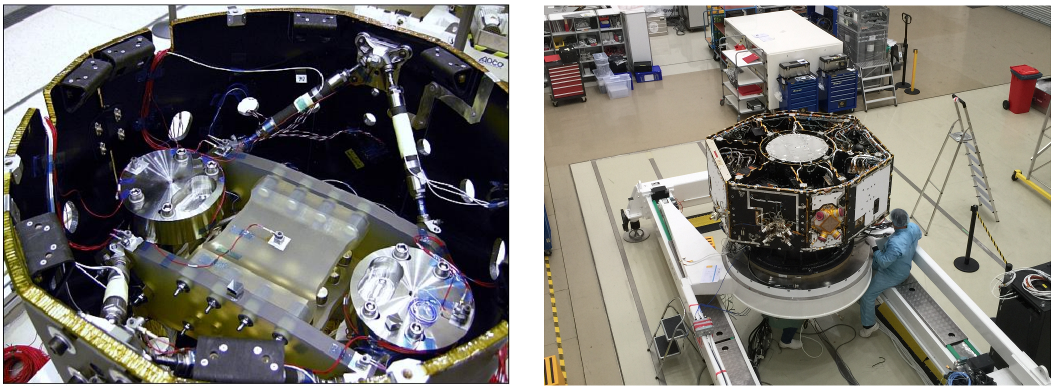

Figure 1.15: *Left*: LCA inside its thermal shield cylinder. Eight Suspension Struts attach the LCA to the satellite structure. *Right*: structure of the satellite during final integration. The LTP Core Assembly (LCA) is located inside the cylindrical thermal shield, at the central round section. Credits: Airbus Defence and Space.

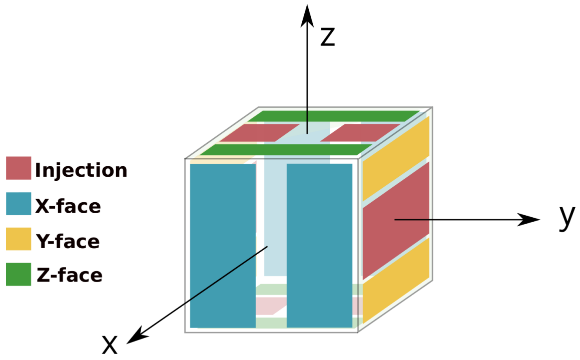

Figure 1.16: Layout of electrodes inside each Electrode Housing.

on the Test Mass. The capacitive measurement is done as follows: an oscillating 100 kHz bias voltage is injected on specific electrodes located on the $\pm z$ and $\pm y$ Electrode Housing walls, the *injection* electrodes. Such a bias signal induces modulated currents between pairs of opposed electrodes that are amplified and measured by the Inertial Sensor Front-End Electronics (IS-FEE) —see Figure 1.17. Since the bias signal applied is sinusoidal, no effective change of voltage is applied to the Test Mass.

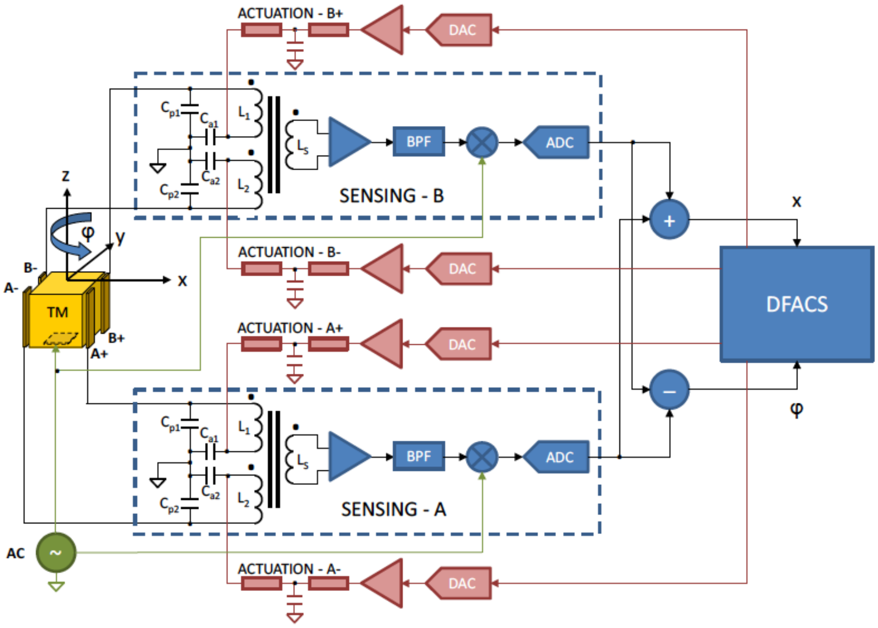

Figure 1.17: Schematic of the x and ϕ sensing and actuation by means of the FEE. The capacitive measurements on the two pairs of electrodes are sent to the DFACS controller, which generates the required control signals. The actuation on the other DOF follows identical procedures. Credits: [78].

Displacements are measured by averaging the readouts of both pairs of electrodes on each direction, while rotations are obtained by subtracting them. For example, the pairs of electrodes on the $\pm z$ faces of the Electrode Housing measure the η rotation as well as the z displacement. An accurate calibration of the different $\partial C/\partial x_i$ terms in all the pairs of electrodes is crucial to achieve coherent results. Such a calibration is performed on-ground.

On the other side, the electrostatic actuation is based on the fact that a voltage applied to a capacitor produces and attracting force between the two polarisations. For the case of the EH-TM system, this means that applying a certain voltage to one of the electrodes results into a *pulling* force to the Test Mass. The actuation procedure uses the same set of sensing electrodes and operates at different frequencies (~10–100 Hz) and phases to avoid cross talks between DOF [79]. For the case of x actuation, the voltage applied to the set of electrodes produces a force on the TM

$$F_{x,\mathrm{act}} = \frac{1}{2}\sum_i \frac{\partial C}{\partial x}\left(V_i - V_{\mathrm{TM}}\right)^2 \tag{1.10}$$

where V_i is the voltage applied to each electrode and the Test Mass voltage V_{TM} is defined as

$$V_{\mathrm{TM}} = \frac{Q_{\mathrm{TM}}}{C_T} + \frac{1}{C_T}\sum_j C_j V_j \tag{1.11}$$

where the term Q_{TM} is the total charge on the Test Mass, C_T the total capacitance of the EH-TM system and each C_j and V_j the nominal capacitances and voltage amplitude applied to each of the electrode pairs, respectively. Net, independent and uncorrelated forces and torques can be applied to any DOF at any time [80] by applying different patterns of sinusoidal signals to the collection of electrodes relevant to a given DOF.

One important consequence of this kind of actuation is that it originates a position-dependent force to the Test Mass. Indeed, the injection voltage induces an electrostatic stiffness to the EH-TM system whose consequences can be minimised by selecting a proper operation point for the Test Mass. Reducing the amplitude of the bias signal also reduces this kind of stiffness.

Also, Equation 1.11 suggests that it is desirable to null the charge of the Electrode Housing to cancel out its contribution to the applied force. Such an action requires first to estimate the Test Mass charge and then to discharge it by means of an Ultraviolet Light Unit (ULU) [81].

The FEE has two operation modes, the High Resolution (HR) and the Wide Range (WR). The High Resolution is the preferred mode during operations, with a sensitivity of 1.8 nm $\mathrm{Hz}^{-1/2}$ at 1 mHz per pair of electrodes (what implies measurements of 1.5 aF $\mathrm{Hz}^{-1/2}$) in a range of ±200 μm and an actuation authority of 5 nN. On the other hand, the Wide Range provides a greater sensing range up to 4 mm —approximately the size of the gap— and has an actuation authority of 8 μN. However, its sensing noise is few orders of magnitude worse [80].

The GRS also includes the caging and the grabbing mechanical systems that must keep the masses locked during the launch and the transfer phases. Once in L1, these systems must release the Test Masses with less than $5\,\mu\text{m}\,\text{s}^{-1}$ and $100\,\text{mrad}\,\text{s}^{-1}$ in order to allow a smooth transition to the free-fall condition [82]. Such step is carried out by two different mechanisms: a first one, the Cage and Vent Mechanism (CVM) that pulls back the eight fingers that cage the Test Masses during the high loads of the launch ($\approx$1200 N); and a second mechanism, the Grabbing, Positioning and Release Mechanism (GPRM) that grabs the Test Masses with two centred fingers on their $\pm z$ faces using a piezo-actuated mechanical system. While the first one is single-use, the second one is designed to operate multiple times [83].

Finally, the EH inner cavities are directly connected to the open space by a venting tube that evacuates the particles from residual outgassing fluxes in order to achieve a pressure as low as possible in the order of 10^{-6} Pa. This tube will remain closed until the Test Masses are un-caged by the CVM mechanism.

1.3.1.2 Optical Measurement System

The low-acceleration performance of the GRS is to be demonstrated by the Optical Metrology System (OMS), which is the instrument able to measure displacements within $\sim 10\,\text{pm}\,\text{Hz}^{-1/2}$ in most of the bandwidth of interest. The OMS essentially consists of a system of four Mach-Zender interferometers (IFO) [84] performing the following measurements —see Figure 5.7:

- o_Δ **interferometer**: the main measurement is the relative motion between the Test Masses along the x axis, namely $x_1 - x_2$. It also provides the relative angles between the two Test Masses in ϕ and η. In free-fall conditions this measurement will report the readouts with the lowest noise.

- o_1 **interferometer**: the channel o_1 senses the relative motion on the x axis between TM1 and the spacecraft —specifically, the Optical Bench (OB). As the previous case, it is also sensitive to relative angle motion in directions ϕ and η between TM1 and the spacecraft. Since it is sensitive to the spacecraft motion, such a channel is expected to be significantly noisier than the previous.

- **Reference interferometer**: this interferometer is sensitive to environment perturbations and pathlength noise originated outside the Optical Bench. This readout is subtracted from the rest of the interferometers readouts by default to remove common-mode disturbances and increase their sensitivity.

- **Frequency interferometer**: this interferometer is similar to the *reference* interferometer but with an intended 38 cm pathlength mismatch which makes it specifically sensitive to laser frequency fluctuations. This readout is used as the control signal for the Reference Laser Unit.

The laser beam is a near-infrared 1064 nm Nd:YAG with power ≈ 25 mW at the end of the injection fibres [1]. The TM displacement associated to a phase variation is computed as

$$\delta x = \frac{1}{2}\frac{\lambda}{2\pi\cos\alpha}\delta\phi \tag{1.12}$$

where λ is the laser wavelength, α the angle of incidence (nominally 4.5°), ϕ the measured phase and the term 1/2 already accounts for the beam reflection on the TM. The dynamic range of the longitudinal measurements is ±0.1 mm [85].

The photodiodes implemented are actually quadrant photodiodes, therefore they are also sensitive to displacements and angular fluctuations of the beams. Such feature allows to measure the Test Masses attitude around y (η_1, η_2) and z (ϕ_1, ϕ_2). Two different approaches are used to measure these angles [86, 87]:

- *Differential Power Sensing* (DPS) measurements, where beam displacements are measured on the quadrants and Test Mass angles inferred. Strictly, such measurement provides the average displacement of the two recombined beams on each quadrant photodiode.

- *Differential Wavefront Sensing* (DWS) measurements, where the Test Mass angles are obtained by measuring the relative phases between the two beams on each quadrant photodiode.

While the DPS technique has a wider dynamic range, the DWS is used as a measurement signal for the different control loops because of its better sensitivity.

For redundancy issues, each interferometer's measurement is performed by actually two quadrant photodiodes. Considering that there are as well two additional photodiodes to control the amplitude stability of each injected laser beam[3], a total of ten quadrant photodiodes are placed on the LTP Optical Bench —see Figure 1.18.

Beside the Optical Bench [84], which is located between the the two Gravitational Reference Sensors (GRS), the Optical Metrology System is also composed by the Reference Laser Unit, the Laser Modulator and the Phasemeter [86]. The whole instrument is managed by the Data Management Unit (DMU) [88].

1.3.1.3 Diagnostics Subsystem

The Diagnostics Subsystem is intended to study different external noise sources eventually critical for the sensitivity of the LTP performance [77]. The LTP is equipped with three different kind of diagnostics instrumentation:

- **Magnetic diagnostics**: Magnetic field fluctuations on the GRS induce direct forces and torques to the Test Masses by interacting with the magnetic remnant moment of the Test Masses and with the susceptibility of its material [88]. In consequence, a requirement for the magnetic field fluctuations and the magnetic field gradient fluctuations in the area of the Test Masses is set to 650 nT Hz$^{-1/2}$ and

---

[3] The amplitude detectors are single element photodiodes but, due to the lack of availability of convenient space-qualified single element photodiodes they are implemented as one element of a quadrant photodiode.

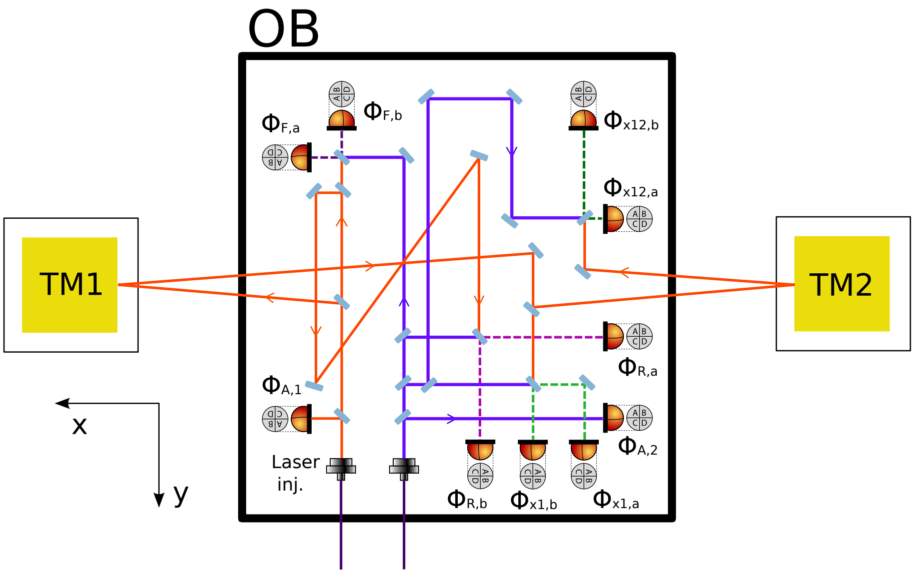

Figure 1.18: Schematic of the interferometer main measurements: Φ_{12} quadrant photodiodes measure relative displacement of TM1 with respect to TM2, and angular relative position on y and z axes between them. On the other hand, Φ_1 quadrant photodiodes measure the same displacements and angles on Test Mass 1 but with respect to the spacecraft. The final relative displacement measurements x_{12} and x_1 are obtained by subtracting the reference measurement Φ_R to both Φ_{12} and Φ_1, respectively. The suffixes *a, b* refer to each of the redundant photodiodes of each interferometer measurement, and the dashed lines represent the recombined beams for each measurement.

$250\,\mathrm{nT\,m^{-1}\,Hz^{-1/2}}$, respectively, in the LPF band [1]. A set of four Fluxgate magnetometers is responsible to ensure that the requirements are met, though careful extrapolation of their measurements is needed to estimate the magnetic field and the magnetic field gradient in the precise Test Mass locations [3]. The total contribution to the acceleration must be less than $1.2\cdot10^{-14}\,\mathrm{m\,s^{-2}\,Hz^{-1/2}}$ [75], what makes the magnetic field fluctuations one of the top contributors to the LTP noise, specially in the low edge of the band. Amongst the different sources of magnetic noise, this contribution is expected to be dominated by the interplanetary magnetic field fluctuations. In order to characterise the magnetic properties of the Test Masses, the LTP is also equipped with two coils aimed to inject accurate magnetic field signals to the Test Masses while their consequences are sensed by the interferometers and the magnetometers [3].

- **Thermal diagnostics**: Following a similar concept as in the previous case, the LTP is also sensitive to temperature noise through different mechanisms able to transduce temperature fluctuations to interferometer phase fluctuations. Consequently, there is a temperature stability requirement of $10^{-4}\,\mathrm{K\,Hz^{-1/2}}$ across the whole LPF bandwidth in the LCA environment. The LTP is equipped with a series of temperature sensors and heaters to measure in-situ different thermal couplings already identified [1, 2]. Such a subsystem is extensively described in Chapter 2 since it is the essential framework of this thesis.

- **Radiation Monitor**: Random charge of the Test Mass directly interacts with the GRS sensing and actuation system, degrading and eventually limiting their performance [89]. Such random charge comes from direct exposition of the spacecraft to the ionization radiations coming from the Sun and from the galaxy. Both sources emit high energy particles —mainly protons— that can eventually hit the Test Masses and transfer their charge. With the purpose of characterising such radiation and their potential effects to the Test Masses, the LTP is equipped with a radiation particle counter that identifies the number of particles with energy $> 70\,\mathrm{MeV}$, which is the approximate shielding that the spacecraft offers to the test masses [90]. In addition, for those particles appearing as coinciding events in the two diodes in telescope configuration, the monitor is able to classify their energy in 1024 energy bins [88].

1.3.1.4 Support equipment

Beside the main instruments and measuring subsystems on board LISA Pathfinder, there are some additional units of special interest to complete the whole data chain:

- The **Data Management Unit (DMU)** [88]: As part of the Data Management and Diagnostics Subsystem (DDS) together with the Diagnostics Subsystem, the DMU is the interface that coordinates most of the scientific instrumentation of the satellite. It hosts the electronics associated to the diagnostics subsystem operation: the acquisition circuits for the temperature sensors and magnetometers, the voltage sources for the heaters, etc. It also plays a crucial role in the OMS operation, since the DMU receives the IFO readouts from the Phasemeter, time-stamps the samples with its own clock, generates the feedback control signals to the laser control system and sends the OMS data to the DFACS.

- The **On-Board Computer (OBC)**: With direct connection to the DMU for data transfer and clock synchronisation, the OBC is the central unit that manages all the essential satellite activities. It controls all the basic satellite systems, such as the solar panel, batteries, thrusters, star-tracker, uplink/downlink communications and telecommand reception/transmission, amongst others. It also hosts the controllers associated to the LTP performance, so it is responsible for processing the GRS data from the FEE and the OMS data from the DMU to define the proper control signals to be sent back to the GRS or to the μN-thrusters.

1.3.2 LTP performance

The performance of the LTP is actually the combined performance of a three-body system composed by the spacecraft and the two Test Masses. It requires to sense and control 15 of the 18 total degrees of freedom of the system: all the DOF of both Test Masses and the attitude of the spacecraft. Figure 1.19 shows the reference frames and notation associated to each body.

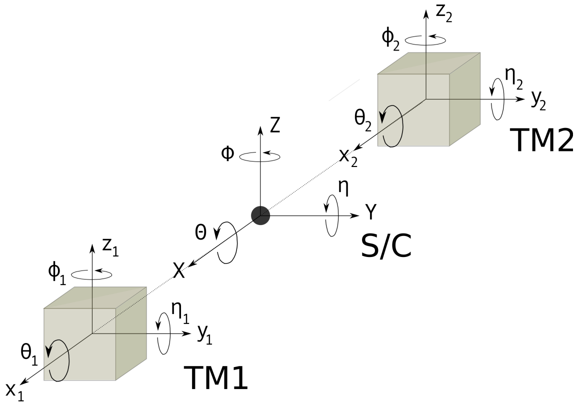

Figure 1.19: LTP reference frames.

The LTP performance is organized in different operational modes. Only the *Science modes* fulfil the free-fall conditions required for the differential acceleration measurements. In this section, we briefly introduce the main operational modes to then describe the dynamics associated to the principal scientific measurement. At the end of the section, we provide an overview to the different expected noise contributions to the measured acceleration.

1.3.2.1 Operational modes

The main operational modes of the LTP are the following ones:

- *Attitude Mode*: Only the attitude of the spacecraft is controlled in this mode, while the two Test Masses remain mechanically caged.
- *Accelerometer Mode*: In this mode, the motion of both Test Masses is subjugated to the spacecraft's motion by electrostatically caging the masses with high gain and bandwidth.
- *Normal Mode*: The drift on x of the primary mass is followed by the spacecraft, while the secondary mass directly follows the spacecraft with high bandwidth controllers and using the capacitive sensors as motion sensors.
- *Science Mode*: Both the spacecraft and the secondary mass follow the x motion of the primary mass. Two submodes of interest are found here:
  - *Science Mode 1.1*: Only capacitive readouts are used to sense the Test Masses motion.
  - *Science Mode 1.2*: Optical Metrology System (OMS) readouts used for the redundant measurements (x_1, x_2, η_1, η_2, ϕ_1 and ϕ_2), together with capacitive measurements for the remaining DOF.

Each mode can have multiple variations by defining different combinations of released and subordinated DOF and by setting the instrument used to sense each of the redundant magnitudes. The transition from an initial mode where the Test Mass are caged to the full science mode requires a long procedure with at least five intermediate modes [91].

The Science Mode 1.2 is the relevant one for the LTP scientific operation, where the condition of free-fall is achieved for the x trajectory of the primary mass (TM1). Once in this mode, the x motion of the primary mass rules over the remaining controlled degrees of freedom: the spacecraft follows the TM1 x motion by means of the μN-thrusters, while the secondary mass (TM2) follows the primary mass. The Drag-Free Attitude and Control System (DFACS) is responsible for this performance, and manages two important control loops:

- The High-Gain loop: A high bandwidth controller that actuates on both the spacecraft and any required DOF of the Test Masses. It is on charge of keeping the spacecraft well-centred around the primary mass.

- The Low-Frequency Suspension loop: This controller operates at a very low gain to minimize frequency components in the milli-Hertz band. It is used to control over the critical DOF whose actuation can perturb the main differential measurement —for example, the actuation on the x axis of the subordinated Test Mass, not the primary one.

In front of any observed deviation in given DOF, the actuation follows the scheme in Table 1.2, which assumes the reference systems defined in Figure 1.19.

The controllers require the position and attitude of both Test Masses as inputs. These measurements are provided by the GRS or, eventually, by the available OMS readouts. The attitude of the spacecraft is sensed by an autonomous star tracker *Terma HE-5AS* [93] —there are two of them for redundancy. It is mainly required to keep the medium gain antenna pointing to the Earth and it must cope with the rotation of the spacecraft of ≈2° per day. During nominal performance, the spacecraft attitude is not subordinated to the star tracker sensing, but it keeps active to put the spacecraft in save mode if the spacecraft eventually turns 5° away from the Sun direction.

The consequent requested *actuation* on the system is performed by electrostatic actuation on the Test Masses and by dedicated μN-thrusters for the spacecraft attitude. Specifically, the actuation on the spacecraft is carried out by sets of cold gas thrusters similar to the thrusters on board GAIA satellite [94]. Their performance with noise $\leq 0.1\,\mu\mathrm{N\,Hz}^{-1/2}$ has already been successfully tested [95]. Figure 1.20 illustrates the LTP closed loop.

1.3.2.2 x-axis acceleration

In the operational Science Mode 1.2, the magnitudes of interest are x_1, which is the relative distance between TM1 and the spacecraft, and Δx, which is the relative distance

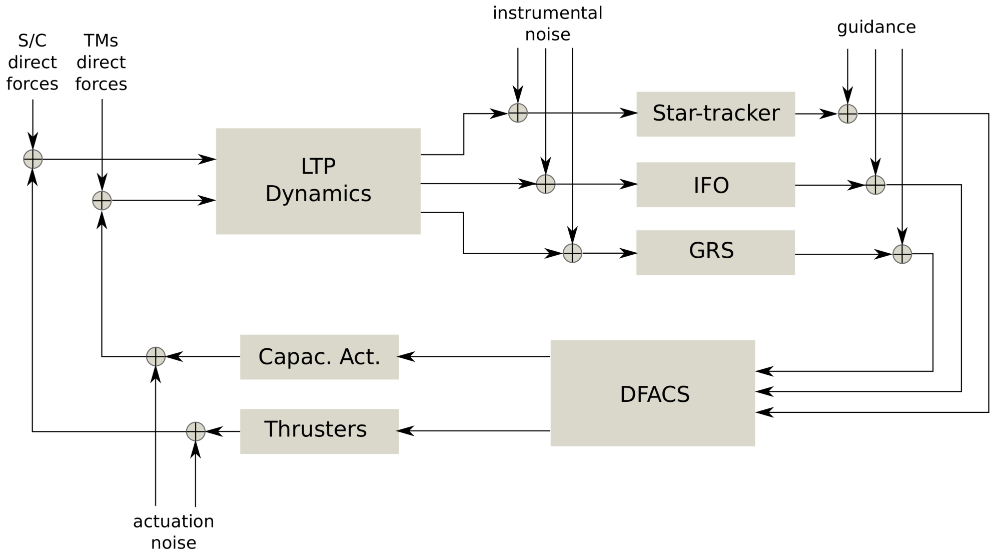

Figure 1.20: Schematic of the LTP closed loop. The *LTP Dynamics* block represents the acceleration to displacement/rotation conversion of the set of 15 controlled DOF. The outputs of this block are sensed by the star-tracker, the OMS and the GRS, whose signals are sent to the DFACS controller. This last block generates the control signals to be sent to the capacitive actuators and the μN-thrusters (represented by the *Capac. Act.* and the *Thrusters* blocks, respectively) which apply the commanded forces and torques to the system. The main noise inputs are represented by actuation and instrumental noise inputs in the schematic. Also, the *direct forces* terms are mostly contributed by noise like solar pressure exerted to the spacecraft and magnetic field noise perturbing the masses. Eventual thermal and magnetic input signals may be introduced through the *direct forces* channel as well. Finally, the input guidances enter the loop just before the DFACS block as *fake* sensor readouts for system characterisation purposes.

	θ_{SC}	η_{SC}	ϕ_{SC}	x_1	y_1	z_1	θ_1	η_1	ϕ_1	x_2	y_2	z_2	θ_2	η_2	ϕ_2
x_{SC}	–	–	–	H	H	H	–	–	–	–	H	H	–	–	–
y_{SC}	–	–	–	–	H	–	H	–	–	–	H	–	–	–	–
z_{SC}	–	–	–	–	–	H	H	–	–	–	–	H	–	–	–
θ_{SC}	–	–	–	–	H	H	H	–	–	–	H	H	–	–	–
η_{SC}	–	–	–	–	H	H	H	–	–	–	H	H	–	–	–
ϕ_{SC}	–	–	–	–	H	H	H	–	–	–	H	H	–	–	–
x_1	–	–	–	–	–	–	–	–	–	–	–	–	–	–	–
y_1	–	–	H	–	–	–	–	–	–	–	–	–	–	–	–
z_1	–	H	–	–	–	–	–	–	–	–	–	–	–	–	–
θ_1	H	–	–	–	–	–	–	–	–	–	–	–	–	–	–
η_1	–	–	–	–	–	–	–	L	–	–	–	–	–	–	–
ϕ_1	–	–	–	–	–	–	–	–	L	–	–	–	–	–	–
x_2	–	–	–	–	–	–	–	–	–	L	–	–	–	–	–
y_2	–	–	H	–	–	–	–	–	–	–	–	–	–	–	–
z_2	–	H	–	–	–	–	–	–	–	–	–	–	–	–	–
θ_2	–	–	–	–	–	–	–	–	–	–	–	–	L	–	–
η_2	–	–	–	–	–	–	–	–	–	–	–	–	–	L	–
ϕ_2	–	–	–	–	–	–	–	–	–	–	–	–	–	–	L

Table 1.2: DFACS actuation protocol in Science Mode. The top raw refers to the **sensed** motion on the different degrees of freedom, while the left column refers to the **actuated** degrees of freedom in front of a given observation. *H* stands for *High* gain actuation, while *L* stands for Suspension Loop actuation —with low gain, out of loop control responses. In order to minimize cross-talk effects, a complex sequence of actions involving many degrees of freedom is applied in front of certain deviations. Thus, for example, an observed TM2 motion along y (named y_2 in Figure 1.19) is compensated by actuating on the spacecraft, actually on x_{SC}, y_{SC}, θ_{SC}, η_{SC} and ϕ_{SC}. Amongst other effects, such an actuation induces an obvious deviation on ϕ_{SC}, which is corrected actuating on η_1 and η_2. Notice that in this mode there is no actuation on x_1 [92].

defined as $\Delta x = x_1 - x_2$. Neglecting the gravity gradient between Test Masses, the equations of motion along these magnitudes in the s-Domain[4] are essentially described, in terms of acceleration, by [2, 96]

$$\left(s^2+\omega_1^2\right) x_1 = \frac{f_1}{m} - \frac{F}{M} - H_{\mathrm{DF}} H_{\mathrm{th}}\, o_1 \tag{1.13}$$

$$\left(s^2+\omega_2^2\right) \Delta x + \left(\omega_2^2-\omega_1^2\right) x_1 = \frac{f_2-f_1}{m} - \frac{F}{M} - H_{\mathrm{lfs}} H_{\mathrm{el}}\, o_\Delta \tag{1.14}$$

---

[4] The s-Domain is the complex frequency domain resulting from the application of the Laplace Transform, similar to the Fourier transform but based on a complex variable.

where

- ω_1 and ω_2 are the total stiffness per unit of mass between each Test Mass and the spacecraft. Under nominal performance, both terms are dominated by actuation stiffness from direct actuation and actuation cross-couplings.
- o_1 is the readout associated to x_1. It is defined as $o_1 = x_1 + o_{\mathrm{n1}}$, where o_{n1} is the noise readout of the interferometer o_1.
- o_Δ is the readout associated to the differential readout between Test Masses. It is defined as $o_\Delta = x_2 - x_1 + o_{\mathrm{n}\Delta} + \delta s x_1$, where $o_{\mathrm{n}\Delta}$ is the noise readout of the interferometer o_Δ and δs is a cross-talk between both readouts.
- f_1 and f_2 are the stray forces on each Test Mass.
- F are all the forces acting on the spacecraft.
- M and m are the spacecraft and the Test Mass masses, respectively.
- H_{DF} and H_{lfs} are the control loop gains associated to the *Drag-Free* loop applied to the spacecraft and to the *low-frequency suspension* loop applied to the secondary Test Mass.
- H_{th} and H_{el} are the gains associated to the thruster actuation and to the electrostatic actuation, respectively.

The closed loop performance of both channels is presented in Figure 1.21. Neglecting the cross-talk δs under the assumption of ideal interferometer and considering that stray forces on the spacecraft are much larger than stray forces on TM1 —i.e. $F/M >> f_1/m$ [2]—, the transfer functions associated to the readouts o_1 and o_Δ are

$$\begin{aligned} o_1 &= \frac{1}{s^2+\omega_1^2+H_{\mathrm{DF}}H_{\mathrm{th}}}\frac{F}{M} \\ &+ \frac{\omega_1^2+s^2}{s^2+\omega_1^2+H_{\mathrm{DF}}H_{\mathrm{th}}}o_{\mathrm{n1}} \end{aligned} \tag{1.15}$$

$$\begin{aligned} o_\Delta &= \frac{1}{s^2+\omega_2^2+H_{\mathrm{lfs}}H_{\mathrm{el}}}\left(\frac{f_2}{m}-\frac{f_1}{m}\right) \\ &+ \frac{\omega_1^2-\omega_2^2}{(s^2+\omega_2^2+H_{\mathrm{lfs}}H_{\mathrm{el}})(s^2+\omega_1^2+H_{\mathrm{DF}}H_{\mathrm{th}})}\frac{F}{M} \\ &+ \frac{s^2+\omega_2^2}{s^2+\omega_2^2+H_{\mathrm{lfs}}H_{\mathrm{el}}}o_{\mathrm{n}\Delta} \\ &+ \frac{\left(\omega_1^2-\omega_2^2\right)H_{\mathrm{DF}}H_{\mathrm{th}}}{(s^2+\omega_2^2+H_{\mathrm{lfs}}H_{\mathrm{el}})(s^2+\omega_1^2+H_{\mathrm{DF}}H_{\mathrm{th}})}o_{\mathrm{n1}} \end{aligned} \tag{1.16}$$

The difference $\omega_1^2 - \omega_2^2$ is the differential stiffness $\Delta\omega^2$. Notice that in scenarios with $\Delta\omega^2 = 0$, the stray forces on the spacecraft are fully suppressed from the o_Δ readout.

The measured acceleration is thus determined by the transfer function between the differential acceleration a_Δ and the differential readout o_Δ. Since

$$o_\Delta = \frac{1}{s^2 + \omega_2^2 + H_{\mathrm{lfs}} H_{\mathrm{el}}} a_\Delta \tag{1.17}$$

thus,

$$\begin{aligned} a_\Delta &= \frac{f_2}{m} - \frac{f_1}{m} + \left(s^2 + \omega_2^2\right) o_{\mathrm{n}\Delta} \\ &+ \frac{\Delta\omega^2}{s^2 + \omega_1^2 + H_{\mathrm{DF}} H_{\mathrm{th}}} \frac{F}{M} \\ &+ \frac{H_{\mathrm{DF}} H_{\mathrm{th}} \Delta\omega_2}{s^2 + \omega_1^2 + H_{\mathrm{DF}} H_{\mathrm{th}}} o_{\mathrm{n}1} \end{aligned} \tag{1.18}$$

This equation already shows that any force applied to the the Test Masses is directly observed as a differential acceleration. Since the acceleration needs to be estimated from the differential readout, it is of high importance to carefully characterise the transfer function in Equation 1.17.

1.3.2.3 Noise breakdown

Most of the noise contributors to the sensitivity budget of the LTP present a frequency-dependent behaviour. The contribution from electrostatic actuation noise is expected to limit the sensitivity in the lower edge of the band with ~8 fm s^{-2} Hz$^{-1/2}$ at 1 mHz, while the upper band is limited by the OMS phase noise with ~4 pm s^{-2} Hz$^{-1/2}$ at 30 mHz. Figure 1.22 presents both the requirements and the best estimation noise breakdown, as expected from different test campaigns [97, 73]. Notice that the current expectation at 1 mHz is a factor three below the requirements.

During the drift mode experiment [73], the actuation is going to be switched off for some periods of time, partially cancelling the actuation noise contribution during segments of ~100 s. In that case, the performance at 1 mHz is expected to be directly limited by the contribution of the direct forces at ~7 fm s^{-2} Hz$^{-1/2}$. Amongst the different kind of direct forces, the magnetic field noise contribution is expected to dominate at the lower edge of the band with a contribution close to 7 fm s^{-2} Hz$^{-1/2}$, while above 3–4 mHz the white-shaped Brownian noise may dominate the direct force noise contribution with a level between 2–7 fm s^{-2} Hz$^{-1/2}$ depending on the residual pressure inside the Electrode Housing [98]. For an eventual worst-case scenario with too high pressure (~50 μP instead of the ~1 μP), Brownian noise could increase to ≈12 fm s^{-2} Hz$^{-1/2}$ and thus limit the sensitivity at a level even above the electrostatic actuation contribution.

Finally, other noise sources like stray voltages on the electrodes, laser radiation pressure noise, temperature fluctuations, self-gravity noise and charge noise present individual contributions of less than ∼1 fm $\mathrm{s}^{-2}\,\mathrm{Hz}^{-1/2}$.

1.3.3 LISA Pathfinder operations

After the launch and the commissioning period, the satellite will start the scientific phase where ESA will operate the spacecraft following the science team plan. This consist of three months of operations for the European LTP scientific team and three other months for the NASA DRS team.

Scientific operations need to follow a tight schedule to execute all the experiments planned. In addition, the satellite housekeeping requires a dedicated day per week. During such day, maintenance and control activities will have higher priority than the experiments, what leaves a satellite operational availability of six days per week.

Communications with the satellite during science operations will be performed by means of the 35-meter deep-space antenna at Cebreros, Spain, which will establish a communication link with the satellite of about 6–8 h per day and send it to the Mission Operations Centre (MOC) at European Science and Operations Centre (ESOC) in Darmstadt, Germany, from where the satellite is operated and the telemetry is preprocessed and stored in dedicated repositories.

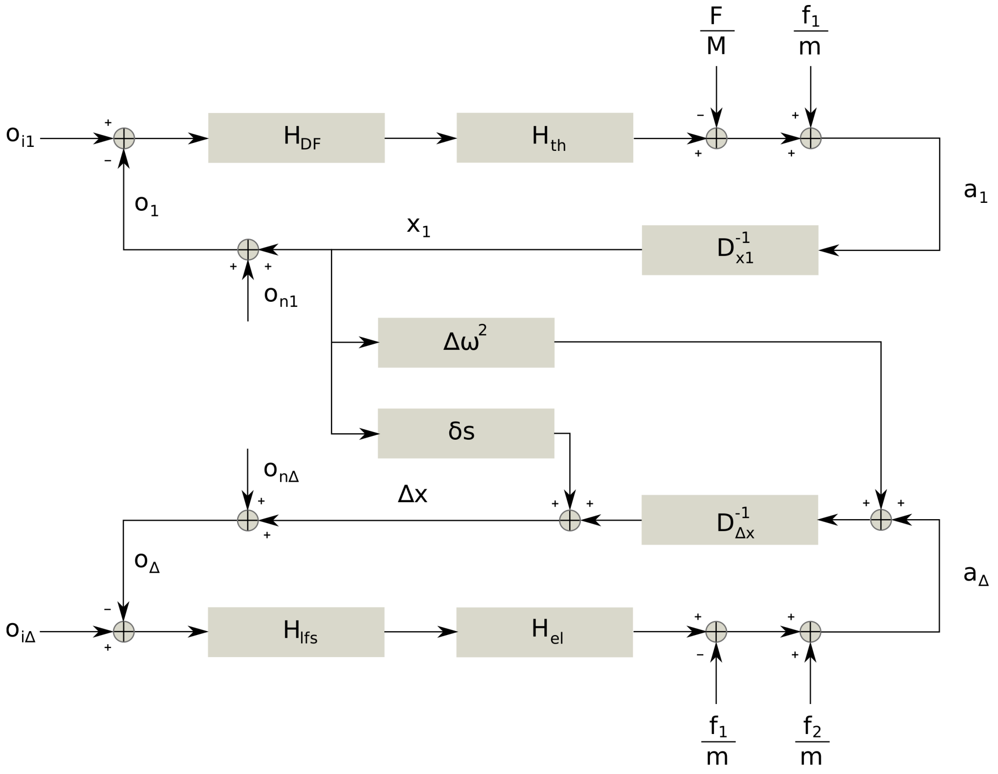

Figure 1.21: Schematic of the control loops representing the x-axis dynamics. The injection signals o_{i1} and $o_{i\Delta}$ are nominally null.

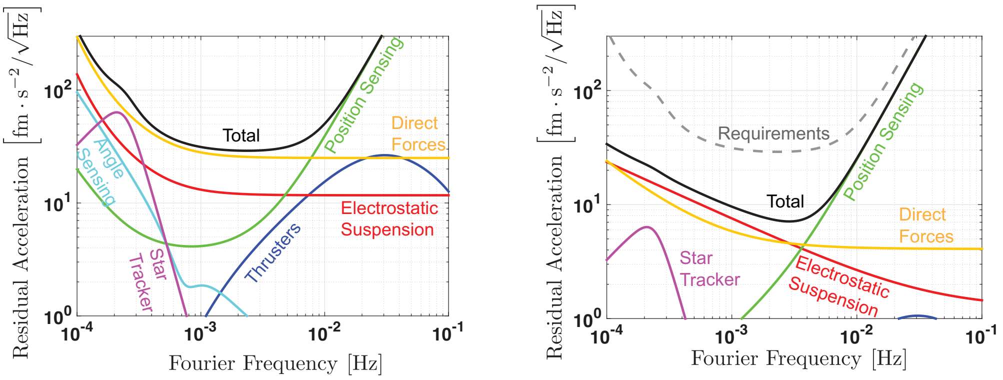

Figure 1.22: LTP sensitivity requirements (*left*) and best estimates (*right*). Credits: [73].

1.3.3.1 Experiments

The list of experiments to be executed during operations is long and variate [97]. Some of them are presented below:

- *Acceleration noise measurement*: The measurement of long segments of noise to calculate the residual acceleration is the cornerstone of the experiment. This experiment is to be repeated several times during the mission in different conditions of actuation stiffness, control modes, etc [99].

- *Dynamics system identification experiments*: These kind of experiments are aimed to estimate with as much precision as possible the key parameters of the system at a given condition of operations. By injecting either (1) fake guidance signals to the controllers or (2) real signals to the thrusters, high SNR responses of the system allow to identify, for example, the total stiffness of the system, the capacitive actuation gains, the thruster gains and other parameters of interest from the control loop [100, 101, 102].

- *Cross-talk experiments*: Similar to the previous kind of experiments, here the aim is to identify the contribution to the x axis from the actuation on the other degrees of freedom. Major contribution from ϕ with respect to the other ones is expected, since the actuation on this degree of freedom is carried out by the electrodes located on the $\pm x$ faces.

- *Free-fall experiments*: As commented above, the actuation noise is expected to limit the sensitivity of the measurement in normal performance. A long period without activation would make the Test Masses to drift due to residual gravity until crashing against the Electrode Housing walls. However, if the residual gravity is properly characterised, then series of short electrostatic kicks properly oriented can induce a parabolic trajectory to one Test Mass, letting it *free falling* without actuation in between the kicks. By doing so, series of periods ~350 s without actuation noise are obtained in this experiment, though it requires a careful data analysis to estimate the sensitivity in the milli-Hertz band after removing the effect of the kicks [73, 103].

- *Charge estimation experiments*: Random Test Mass charge is expected during operations, what can lead to malfunction of the capacitive sensors and actuators. This experiment provides an estimation of the Test Mass charge by applying sequences of DC voltages in some of the electrodes [104].
- *Thermal diagnostics experiments*: In this experiment, series of controlled heat signals are applied at different locations of the LTP to evaluate their contribution to the interferometer sensitivity[5].
- *Magnetic diagnostics experiments*: Similar to the previous, a controlled magnetic signal on the x axis is injected by means of two coils in the LTP to estimate the residual magnetic moment and susceptibility of the Test Masses [3].

Apart from this list of dedicated experiments, other activities need to be performed such as stability check of the Radiation Monitor, eventual charge/discharge compensation of the Test Masses by means of the ULU lamps, optimal TM positioning, analysis of the degradation of the TM reflectivity and of the photodiodes, estimation of the gains of the OMS control loops, estimation of the radiation pressure noise contribution to the phase, laser frequency noise characterisation, analysis of the stray potentials on the GRS, etc.

1.3.3.2 Data analysis

The *calibration* nature of the experiments to be run on board the satellite combined with the relatively short period of operations requires a rapid analysis of the data obtained the same day in order to optimise the scientific yield of each test. In addition, the complexity of the LTP performance, requiring the joint in-loop operation of multiple systems and instruments demands a complex data analysis environment able to provide a common language and understanding to all the data analysis team. The solution was found by creating a dedicated MATLAB® Toolbox [105], namely the LTP Data Analysis (LTPDA) Toolbox, which provides an object-oriented generic data analysis environment to be used in multiple kinds of data analysis projects[6]. The specific LPF analysis tools are added to the toolbox by means of an external module that is later appended to the environment. Both the toolbox and the external module are maintained by the LISA Pathfinder data analysis team [106].

The whole data analysis environment provides the tools to download all the relevant data from the official telemetry repositories together with the methods required for each of the analysis. The elemental class in the toolbox is the Analysis Object (AO), that is

---

[5] This thesis focuses precisely on two types of these experiments.

[6] The LTPDA Toolbox can be downloaded in `https://www.elisascience.org/ltpda/`

associated to a measurement and allows to keep track of the history of all the processes applied to an initial set of telemetry data. Such a feature enables any other analyst to easily track back the analysis chain and reproduce the same results.

In addition to the previous, the data analysis of each LTP experiment along the mission is carried out by dedicated *pipelines*. Roughly speaking, each experiment pipeline is a class that contains all the data analysis actions to be performed on a given subset of satellite telemetry parameters. The different packets of actions are grouped in pipeline *steps* whose execution order is already established in each pipeline class definition. Each step contains the calls to functions that can be specific for a given action or generic from the LTPDA toolbox, but with predefined function parameters that ease and speed up the whole execution.

A complete pipeline chain downloads its parameter subset, converts it to Analysis Objects (AOs) and returns a consolidated result together with the information of all the procedure applied, what allows to easily track-back all the actions applied —see Appendix B.

1.3.4 Status of the project

As of autumn 2015, the spacecraft has already been integrated and last operational tests have been carried out in the IABG facilities in Ottobrunn, close to Munich, Germany. It is currently being assembled into the launcher in Kourou (French Guiana). The expected launch is by the beginning of December.

Along these last years, the satellite has been exposed to different performance tests, achieving on-ground interferometry measurements with precision of $6.4\,\mathrm{pm\,s^{-2}\,Hz^{-1/2}}$ in the On-Station Thermal Test (OSTT). Such test campaign was held in the same IABG facilities in Autumn 2011 with the Thermo-Optical Qualification Model (TOQM) version of the satellite —see Figures 1.23 and 1.24, and detailed description in Chapter 6. This version already included the whole OMS but the GRS were missing and replaced by piezo-actuated mirrors [107].

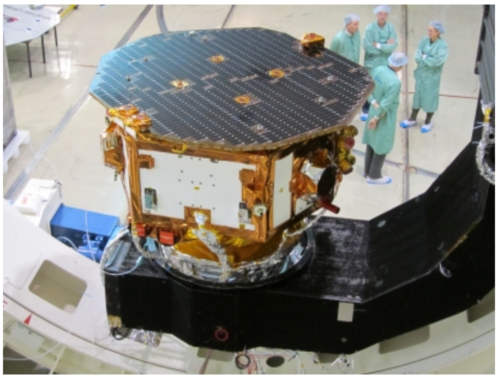

Figure 1.23: LISA Pathfinder during the On-Station Thermal Test (OSTT) in Autumn 2011. Credits: Airbus Defence and Space UK.

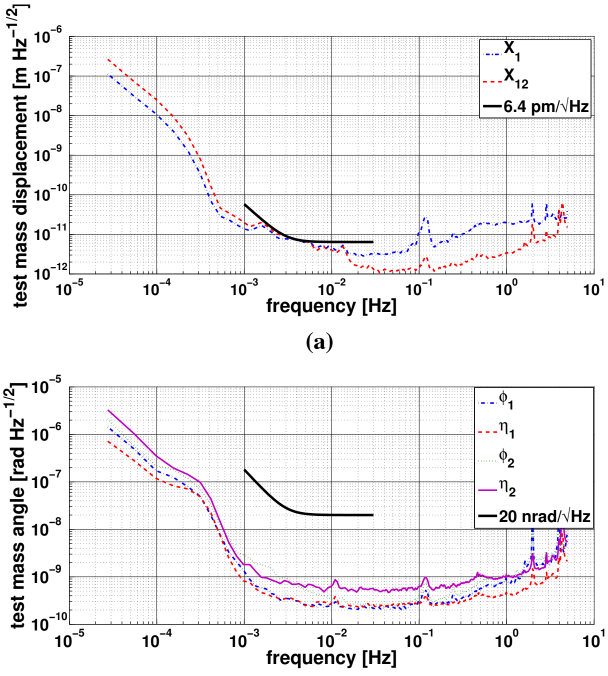

(a)

(b)

Figure 1.24: OMS performance at ~30 °C during the OSTT. On the top: Longitudinal displacement measurements. On the bottom: Angular fluctuation measurements (DWS). Credits: [107].

Regarding the diagnostics equipment, the performance of the actuation items has already been tested in several tests. Main ones include the thermal tests in the OSTT campaign [108], thermal tests with the Inertial Sensor Housing–Engineering Qualification Model (ISH–EQM), in 2013 [109], a proton irradiation test of the Radiation Monitor [90], etc.

Preparation for on-ground operations has already been progressing lead by LPF teams in ESAC and ESOC, who are responsible for the satellite control and operations and data downlink. In order to validate the whole telecommand chain, a realistic simulator of the whole satellite processes has been developed and is maintained in ESOC. Series of simulations campaigns with different levels of simulated data and real hardware have been carried out along the last two years in different Spacecraft Control Loop tests and Science Operations Verification Tests (SOVT).

In parallel, the scientific community has been optimising the experiments and preparing the data analysis tools required to follow the mission with daily analysis. Specific science simulators have been developed to validate the experiments and the analysis tools, together with the pipelines and procedures for each activity. Dedicated simulation campaigns, namely the Science and Technology Operations Centre (STOC) test campaigns, have been carried out to validate the data analysis associated to each experiment [110].

1.4 Structure of the thesis

In this first chapter we have introduced the background describing the framework of this thesis. The next chapters are organised as follows:

- **Chapter 2** introduces the Thermal Diagnostics Subsystem on board LISA Pathfinder and the different mechanisms that induce noise to the OMS due to the presence of temperature fluctuations. It also presents the bases of the thermal experiments aimed to characterise these mechanisms.

- **Chapter 3** is dedicated to the design and implementation of a thermal model for the LTP thermal diagnostics, providing as well a tool to simulate the effects of temperature gradients in the Electrode Housing.

- **Chapter 4** addresses the design of the Electrode Housing Thermal experiment in order to define proper inputs to the relevant actuation heaters in the Electrode Housing.

- **Chapter 5** presents the results of the on-ground experimental campaign carried out at the University of Trento to characterise the thermal effects by means of a torsion pendulum setup equipped with a LISA Pathfinder Test Mass replica.

- **Chapter 6** presents the results of the thermo-elastic thermal experiments carried out in a thermal campaign that included the whole satellite in an advanced level of integration. This chapter provides the first estimations of thermo-elastic couplings from the Suspension Struts to the OMS and extracts conclusions for the input signals to be applied in-flight.

- Finally, the **Conclusions** section provide an overview of the work and the main results obtained. Discussion on possible flight scenarios with the associated temperature noise contributions is followed by an outline of suggestions in terms of thermal design for a future gravitational wave observatory as eLISA.

The document is complemented by a series of Appendices providing additional information on specific topics:

- Appendix A sets the theoretical background required for the analysis of thermal systems, introducing tools both for the design of the experiments and for the associated data analysis.

- Appendix B introduces the data analysis pipelines that have been developed for the analysis of the thermal experiments during the mission.

- Appendices C, D and E support the experimental campaign described in Chapter 5.

- Appendix F provides an estimation of the thermal behaviour of the Suspension Struts.

CHAPTER 2

Thermal Diagnostics subsystem

Noise perturbations derived from temperature fluctuations play an important role in the design of many space applications. The ultimate origin of this kind of noise can be caused by many different sources: fast transitions from direct sunlight to Earth's shadow, satellite manoeuvres that modify the spacecraft attitude with respect to the Sun, Sun radiation fluctuations or fluctuations self-induced by the satellite's equipment performance, etc. The consequences of these fluctuations are commonly mitigated by using materials with low thermal-expansion coefficients and by protecting the instrumentation by means of thermal isolators, complemented by refined temperature control systems equipped with heaters, heat pipes, radiators, etc. However, in low frequency regimes ($< 1\,\mathrm{Hz}$), temperature fluctuations become pretty hard to passively attenuate, since unavailable amounts of mass and volumes are normally required.

Space-based experiments including inertial sensors are also extremely sensitive to temperature gradient fluctuations and their associated effects that can induce net forces and torques on their test masses. As discussed in [111], temperature stability and temperature gradients around test masses are of high importance to ensure proper measurements are taken. Missions like *Galileo Galilei* (GG) [112] and μSCOPE [113], both operating at room temperature as LISA Pathfinder, have addressed this kind of problems. Warnings have been raised for μSCOPE, to fly in 2016, as the temperature gradient induced radiometer effect could shape the target signal of an Equivalence Principle violation [114] if temperature gradients exceed $2.4 \cdot 10^{-9}\,\mathrm{K}$. On the other hand, GG —not yet approved— relies on reducing the temperature noise by spinning the spacecraft in order to average out the temperature gradients. Alternatively, STEP [115] operates at $1.8\,\mathrm{K}$, what reduces the radiometer effect by extremely lowering the molecular kinetic energy. It is also the case of G-Probe B [116], launched in 2004, that carried spinning test masses. In order to reduce thermal perturbations it operated at very low pressures ($\leq 2 \cdot 10^{-9}\,\mathrm{Pa}$) and cryogenic conditions, and used high thermal conductive materials to reduce temperature gradients around its spheric test masses. Some missions studying the variations of the Earth gravitational field also perform measurements in the milli-Hertz band. This is the case of GOCE [117], that measures in the band $5 - 100\,\mathrm{mHz}$ and carries a gradiometer that need to be stabilised to $\approx 85\,\mu\mathrm{K}$. In this case, the gradiometer is thermally decoupled from the satellite by means of passive shielding and has its own dedicated thermal control. In addition, an outer control loop keeps the outer layers at a very stable temperature while thermoelastic distortions are minimised by using ultra stable Carbon structures. Other missions with similar aims like GRACE and GRACE Follow-On [118, 119] spend a significant portion of the satellite power budget with the control system that regulates temperature fluctuations on the accelerometer, where temperature gradients must be in the order of 0.1 K.

The case of the LTP experiment is not an exception. The extremely high sensitivity required in the milli-Hertz band makes the system unavoidably exposed to temperature noise affecting not only the performance of its test masses, but also perturbing the system structure thermo-elastically and some of the optical components. Though an important effort has been done to attenuate the effects of external temperature fluctuations, their consequences will still be perceived. This already justifies the presence of a dedicated diagnostic subsystem on board to characterise the impact of this kind of perturbations: the Thermal Diagnostics Subsystem.

The Thermal Diagnostics subsystem is consequently intended to provide precise temperature fluctuation measurements at different thermal-sensitive spots of the LTP to be correlated with the perturbations observed mainly in the OMS. Furthermore, a subset of heaters is strategically distributed to inject controlled heat signals, allowing to characterise the different thermal-induced distortion mechanisms. In addition, the electronics acquisition system associated is specially designed to reduce the impact of noise sources as Johnson noise, ADC noise and other effects.

In this chapter we first introduce the different thermal effects relevant in the LTP performance and provide an approach to their estimated contribution. After that, the whole LPF Thermal Diagnostics Subsystem is described to finally introduce the thermal experiments to be carried out on board the satellite.

2.1 Temperature-induced noise sources in LISA Pathfinder

Different phenomena in the LTP system transduce temperature fluctuations to perturbations on the IFO readout phase [1]. The Thermal Diagnostics subsystem is intended to characterise the most important three of them:

1. Thermal effects in the Inertial Sensors, induced by temperature gradient fluctuations on the Electrode Housings.

2. Thermoelastic distortions of the Optical Bench as a consequence of temperature fluctuations on the LTP mechanical structure.

3. Thermo-optical distortions of optical parts outside the Optical Bench, i.e in the Optical Window.

The effects of residual temperature fluctuations at any of these locations are individually assessed in the following subsections.

2.1.1 Temperature-related noise effects on the Inertial Sensors

The free-floating Test Masses are exposed to different kinds of temperature-dependent noise sources that end up generating spurious direct forces on them. Two type of contributors are distinguished here: (1) thermal effects causing forces and torques due to the presence of temperature gradients around the Test Masses, and (2) effects like Brownian noise whose noise contribution is a function of the absolute temperature —not the temperature fluctuation itself.

2.1.1.1 Effects due to temperature gradients in the Electrode Housing

Asymmetric distribution of temperature around the Test Masses —i.e. temperature gradients in the EH— induce net forces and torques to them caused essentially by the following effects:

1. Asymmetric outgassing (OG)
2. Radiation pressure effect (RP)
3. Radiometer effect (RM)

Since all of them present a force $F \propto \Delta T$, their contribution is described by terms of thermal coefficients α_i, hence

$$F = \left(\alpha_{\mathrm{OG}} + \alpha_{\mathrm{RP}} + \alpha_{\mathrm{RM}}\right)\Delta T \tag{2.1}$$

All of them have already been extensively studied [120]. Nevertheless, their specific contribution is difficult to predict since they strongly depend on the final pressure and remnant particles in the Electrode Housing cavities. In addition, they are also dependent on the system geometry and the final treatments applied to the surfaces, like polishing or baking out.

Asymmetric outgassing

Any surface exposed to an atmosphere at a given pressure presents an interchange of particles with the environment which is highly dependent on the temperature and the kind of particles. At low pressures, the flux is dominated by outgoing particles defining the so called *outgassing rate* Q. Irregularities in the surface may lead to different outgassing rates at a local scale. Also, in stable conditions the outgassing rate tends to decrease with time. The time scales of such decreases are months or even years, so this effect is notable on all surfaces that experience pressure reductions, such as any vacuum chamber in a laboratory or space instruments assembled at typical Earth pressure. The latter is clearly the case for LPF's Electrode Housings.

For the case of the EH-TM system, asymmetric distributions of outgassing rates at the inner surfaces induce different pressure distributions that can lead to net forces and torques over the Test Masses. The outgassing rate, Q_{rate}, of a given molecule is defined by an outgassing prefactor, Q_0, and an activation temperature, Θ_{OG}, as

$$Q_{\mathrm{rate}}(T) = Q_0 \exp\left(-\frac{\Theta_{\mathrm{OG}}}{T}\right) \tag{2.2}$$

Theoretically, each of the species in the environment presents different outgassing parameters depending upon its molecular properties. However, it is a usual approximation to assume averaged outgassing parameters. Therefore, a difference in the outgassing rates at both sides of the Test Mass induce a difference in the pressure expressed as

$$\Delta P = \frac{\Delta Q_{\text{rate}}(T)}{C_{\text{eff}}} \tag{2.3}$$

where C_{eff} is an equivalent conductance including the conductances between both sides of the Test Mass and through the Electrode Housing venting holes [120]. After linearising, the force caused by a temperature gradient is expressed as

$$F_{\text{OG}} = A_{\text{TM}} \frac{Q_{\text{rate}}(T_0)}{C_{\text{eff}}} \frac{\Theta_{\text{OG}}}{T_0^2} \Delta T \tag{2.4}$$

where A_{TM} is the area of one face of the Test Mass. Therefore, the outgassing thermal coefficient is written as

$$\alpha_{\text{OG}} = A_{\text{TM}} \frac{Q_0 e^{-\frac{\Theta_{\text{OG}}}{T_0}}}{C_{\text{eff}}} \frac{\Theta_{\text{OG}}}{T_0^2} \tag{2.5}$$

Exact values of Q_0 and Θ_{OG} are difficult to predict on ground and will not be revealed until first measurements are taken on board the satellite. The Electrode Housings and the Test Masses have been baked out to minimize the outgassing contribution. Such a treatment is basically focused on removing the water particles deposited during the integration.

The average activation temperature is expected to be between 3000 and 30000 K, slightly increasing with time since particles with lower activation temperature will be outgassed faster than those with higher activation temperatures. Regarding the flow prefactors, values of the order 1–10 nJ s^{-1} are expected. Finally, a first estimation for the outgassing contribution at 293 K was experimentally set to 40 pN K^{-1}, assuming a Θ_{OG} of 30000 K [120].

Radiation pressure effect

The pressure exerted by electromagnetic radiation from the surfaces inside the EH-TM system induces net forces on the Test Masses when exposed to asymmetric temperature distributions. Starting from the simple case of an infinite plate, under the black-body assumption, a surface at a given temperature, T, produces an associated pressure described by the Stefan-Boltzmann Law:

$$P_{\text{RP}} = \frac{2}{3}\frac{\sigma}{c} T^4 \tag{2.6}$$

where σ is the Stefan-Boltzmann constant[1] and c the speed of light. The coefficient 2/3 is the result of projecting the net radiation flux contribution on the direction perpendic-

---

[1] $\sigma = 5.67 \cdot 10^{-8}\,\text{W}\,\text{m}^{-2}\,\text{K}^{-4}$

ular to the surface.

Linearising the effect both the force and the thermal coefficient in the Electrode Housing are defined as

$$F_{\mathrm{RP}} = \frac{8}{3}\frac{\sigma}{c} k_{\mathrm{RP}} A_{\mathrm{TM}} T_0^3 \Delta T \tag{2.7}$$

$$\alpha_{\mathrm{RP}} = \frac{8}{3}\frac{\sigma}{c} k_{\mathrm{RP}} A_{\mathrm{TM}} T_0^3 \tag{2.8}$$

The coefficient k_{RP} added here accounts for both the optical properties of real surfaces —emissivity, absorptivity and reflectivity— and for the geometry relations between surfaces that include the view factors between a Test Mass face and the emitting Electrode Housing surface.

The estimated radiation pressure contribution is $27 k_{\mathrm{RP}}\,\mathrm{pN\,K^{-1}}$, as reported in [120]. Different values for k_{RP} are proposed there, though the assumption of a specular surface leading to a $k_{\mathrm{RP}} = 0.32$ is recommended. The coefficient k_{RP} is lower than 1 because the radiation pressure effect is dominated by the reflections between surfaces inside the Electrode Housing.

Radiometer effect

The radiometer effect appears only in rarefied atmospheres where particles have a mean free path longer than the characteristic dimensions of the system, as it is the case of the famous Crookes's light mill radiometer analysed by Maxwell and Reynolds already in 1879 [121, 122, 123] —as reported in [124]. Under such conditions, collisions between particles are infrequent and most of them keep bouncing from one surface of the system directly to another. The dimensionless Knudsen number sets a limit for these conditions:

$$\mathrm{Kn} = \frac{\lambda}{L} \tag{2.9}$$

where λ is the mean free path of the particle and L is the characteristic length scale of the system. An eventual region with $\mathrm{Kn} = 1$ is representative of the transition between continuum and molecular free regimes. The Knudsen number is equivalently written as

$$\mathrm{Kn} = \frac{K_B T}{\sqrt{2}\pi d^2 P L} \tag{2.10}$$

where the Knudsen number appears as a function of the system temperature T, the total pressure P and the averaged diameter d of the particles. The radiometer effect is observed for $\mathrm{Kn} > 0.01$ and becomes prominent at ≈ 10 [125]. In the case of LISA Pathfinder's Electrode Housing, a pressure $P \approx 10^{-6}\,\mathrm{Pa}$ yields $\mathrm{Kn} \sim 1000$, clearly out of the continuous regime and still with a strong radiometer contribution. In this kind of environments there is no homogeneous pressure and particles hitting a surface bounce back with a velocity v_p defined by the temperature of the surface that is hit [1]:

$$v_p = \sqrt{\frac{3K_B T_{\text{surf}}}{m}} \tag{2.11}$$

where T_{surf} is the surface temperature, m the mass and K_B the Boltzmann constant[2].

In this kind of environment, the pressure between two parallel, *infinite* plates at different uniform temperatures T_1 and T_2, and separated by a negligible distance compared to their dimensions, is written as [120]

$$P_{pl} = \frac{P}{2}\left(\sqrt{\frac{T_1}{T_0}} + \sqrt{\frac{T_2}{T_0}}\right) \tag{2.12}$$

where P and T_0 are the pressure and temperature in equilibrium with a particle reservoir. Integrating this pressure over the area of one Test Mass, and assuming small temperature and pressure variations with respect to the equilibrium parameters, we reach the following expression for the force

$$F_{\text{RM}} = \frac{1}{4}\frac{P}{T_0}\Delta T \tag{2.13}$$

Therefore, including a geometrical coefficient k_{RM} to account for the specific case of the EH-TM system, we write the thermal coefficient for the radiometer effect as follows

$$\alpha_{\text{RM}} = k_{\text{RM}}\frac{1}{4}\frac{P}{T_0} \tag{2.14}$$

where a scenario with $k_{\text{RM}} = 1$ would represent the case of two infinite parallel plates. In [120], a $k_{\text{RM}} = 1.25$ is proposed to account for the shear effects of the molecules on the lateral walls of the Test Masses —those aligned with the x axis—, which increase the effective momentum transmitted to the masses. A total contribution of $18 k_{\text{RM}}\,\text{pN}\,\text{K}^{-1}$ at $P = 10^{-5}\,\text{Pa}$ and $T = 293\,\text{K}$ was estimated experimentally.

The radiometer effect is the only thermal effect that is directly related to the pressure. The final pressure in the Electrode Housing is estimated to be around $10^{-6}\,\text{Pa}$, what would hide the radiometer effect contribution behind the other thermal effects. Still, the worst case of $10^{-5}\,\text{Pa}$ must be considered. Unfortunately, the LTP is not equipped with pressure sensors, so no direct measurement of the pressure will be available. In addition, the pressure is not going to be constant during the mission: as explained in Section 1.3.1.1, each Electrode Housing cavity is connected to the space by means of a

---

[2] $K_B = 1.38064852 \cdot 10^{-23}\,\text{m}^2\,\text{kg}\,\text{s}^{-2}\,\text{K}^{-1}$

venting pipe that will be opened just after releasing the Test Masses. Such a connection should help to evacuate the residual particles and the outgassing flux outside the Electrode Housing cavity, so the pressure inside is expected to decrease during the mission. However, some parts exposed to the pipe conduction, including most of the caging system, are not baked out and could induce a temporal pressure increment inside, just after de-caging the Test Masses.

Total temperature gradient noise contribution

Considering total correlation between the thermal effects described, the temperature gradient noise contribution to the acceleration in the GRS is expressed as

$$S^{1/2}_{a,\mathrm{GRS}}(\omega) = \frac{A_{\mathrm{TM}}}{m}\left(\frac{1}{2}k_{\mathrm{RM}}\frac{P_0}{T_0} + \frac{8}{3}\frac{\sigma}{c}k_{\mathrm{RP}}T_0^3 + \frac{Q_0 e^{-\frac{\Theta_{\mathrm{OG}}}{T_0}}}{C_{\mathrm{eff}}}\frac{\Theta_{\mathrm{OG}}}{T_0^2}\right)S^{1/2}_{\Delta T,\mathrm{GRS}}(\omega) \tag{2.15}$$

The total expected thermal contribution under nominal conditions $T_0 = 293\,\mathrm{K}$ and $P_0 = 10^{-5}\,\mathrm{Pa}$ yields a global thermal coefficient of $\approx 85\,\mathrm{pN\,K^{-1}}$. The final number will mainly depend on the residual outgassing flux and the efficiency of the venting tube that must evacuate the residual particles in the Electrode Housing to open space —thus reducing the pressure as much as possible.

2.1.1.2 Brownian noise

Residual particles in the Electrode Housing cavity present a random, Brownian noise that contributes to damping of the Test Mass motion [98]. Such a damping effect is consistent with the fluctuation-dissipation theorem [126], which establishes a relation between a generic impedance and associated fluctuations with that value. For the particular case of a Test Mass, the mechanical impedance will induce a force noise given by:

$$S_{\mathrm{Brownian}} = 4K_B\,T\,\mathrm{Re}\Big\{Z(\omega)\Big\} \tag{2.16}$$

where K_B is the Boltzmann constant, T the system absolute temperature and $Z(\omega)$ the mechanical impedance. Concerning LPF's Test Masses, the mechanical impedance turns into a viscous and frequency independent β term for each degree of freedom. It has been demonstrated by means of torsion pendulums [98] that such a viscous term is proportional to pressure and, as stated in Section 1.3.2.3, in an eventual LPF scenario with pressure higher than $10^{-5}\,\mathrm{Pa}$, Brownian noise could arise as the factor limiting the LTP sensitivity.

The final contribution to the acceleration is written as [98]

$$S_a^{1/2} = 1.3\cdot 10^{-15}\left(\frac{P}{10^{-6}\,\mathrm{Pa}}\right)^{1/2}\ \mathrm{m\,s^{-2}\,Hz^{-1/2}} \tag{2.17}$$

2.1.1.3 Other thermal effects in the Inertial Sensor

In addition to the effects described so far, other temperature-dependent minor effects in the Inertial Sensors include:

- Test Mass surface reflectivity reduction: reflection properties of the TM will decrease during the mission. At the beginning of the mission, 1% of the 2 mW of the laser beam is transferred to the Test Mass. A variation of this proportion with time would imply heat flux changes on the Test Mass of $\sim 10\,\mu$W. This effect is to be studied in-flight through dedicated experiments by measuring the decay of the beam intensity in the photodiode.

- Thermal expansion of the Electrode Housing modifies the relative position between the electrodes and the Test Mass. These displacements modify the capacitances between the TM and each electrode, causing variations in the stiffness of the system. The consequences of this effect are however considered negligible [1].

2.1.2 Structural thermo-elastic noise distortion

Residual temperature fluctuations in the LTP Core Assembly (LCA) structure induce mechanical distortions that affect the optical pathlength of the interferometers. Such a temperature noise is expected to be dominated by external temperature fluctuations. Heat sources inside the LTP in normal performance —considering that no heaters and no coils are active and no ULU activity is going on— include basically the dissipation of heat from the laser beams at the different optical parts and the dissipation from the currents in the electrodes and in the photodiodes. Their total contribution in terms of temperature noise is considered negligible with respect to the fluctuations coming through the Suspension Struts that attach the LCA to the structure of the spacecraft. In this sense, the eight struts are the main conductive links between the LCA —neglecting wires and optical fibres— and arise as the only mechanisms able to significantly contribute to the thermo-elastic distortion of the LTP. Each of the struts has a central part of Carbon-fiber-reinforced polymer (CFRP) of 9.95 cm and a Titanium end fitting at both sides of the strut, 2.9 cm each one, ending up to a total strut length of ~16 cm. Figure 2.1 shows a representation of the LCA with the eight struts.

The thermal shield surrounding the LTP Core Assembly is intended to attenuate external temperature fluctuations leaving just $\leq 10^{-4}\,\mathrm{K\,Hz^{-1/2}}$ in the struts. A first estimation of the effect of such noise is obtained by assuming simple thermo-elastic free elongation of a heated bar with nominal length L and uniform temperature distribution. In that case, the elongation is given by

$$\delta x = L\alpha\delta T \tag{2.18}$$

where α is the thermal expansion coefficient of its material. For the case of the struts, considering $\alpha_{\mathrm{CFRP}} = 8.3\cdot 10^{-7}\,\mathrm{K^{-1}}$ and $\alpha_{\mathrm{Ti}} = 8.6\cdot 10^{-6}\,\mathrm{K^{-1}}$, the free elongation noise $S_{l,\mathrm{free}}$ of one strut in front of a certain spatially-averaged temperature noise $S_{T_{\mathrm{av}}}$ is

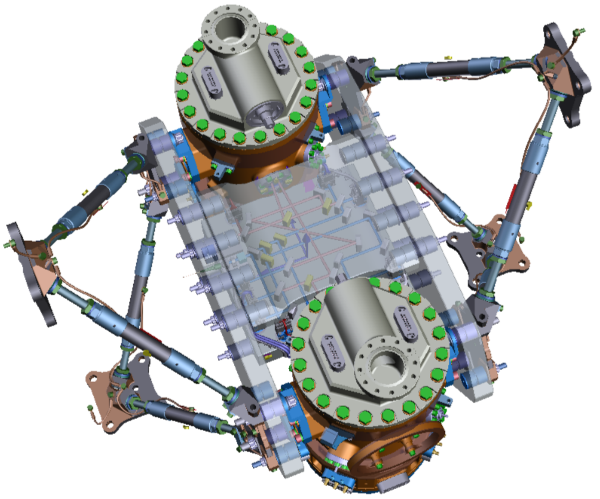

Figure 2.1: LTP Core Assembly (LCA) with the eight Suspension Struts. Credits: Airbus Defence and Space.

$$S^{1/2}_{l,\mathrm{free}}(\omega) = \left(L_{\mathrm{CFRP}}\,\alpha_{\mathrm{CFRP}} + L_{\mathrm{Ti}}\,\alpha_{\mathrm{Ti}}\right) S^{1/2}_{T_{\mathrm{av}}}(\omega) \tag{2.19}$$

where L_{CFRP} and L_{Ti} are the total lengths of the CFRP and Titanium parts respectively. For an averaged strut temperature noise of $10^{-4}\,\mathrm{K\,Hz^{-1/2}}$, the free displacement at the edge of the strut is $60\,\mathrm{pm\,Hz^{-1/2}}$. However, the fact that each strut cannot freely elongate but is actually attached to an hyperstatic structure significantly reduces this possible elongation. The *constrained* displacement noise of the strut edge, $S^{1/2}_{l,\mathrm{const.}}(\omega)$ is written as

$$S^{1/2}_{l,\mathrm{const.}}(\omega) = K\, S^{1/2}_{l,\mathrm{free}}(\omega) \tag{2.20}$$

where K is a parameter to describe the constrain. Some observations must be done at this point:

- A first assumption considers that the stress induced by the heated strut must be at last absorbed by the remaining struts —assuming no distortion of the LCA. This yields a first reduction factor of 1/8 to the theoretical free elongation.

- The elasticity associated to the Zerodur® material that compound the plates of the Optical Bench structure is similar to that of the materials used in the struts. The fact that the Zerodur® plates are much thicker and robust than the struts significantly reduces the stiffness of the LCA. We associate a reduction factor of ~10 to this effect.

These considerations lead to an estimated damping coefficient of $K \sim 1/80$ with respect to the free elongation of one strut at 1 mHz, leading already to the ~$1\,\mathrm{pm\,Hz^{-1/2}}$ level. The noise budget document of the LTP [75] allocates a total of $3\,\mathrm{pm\,Hz^{-1/2}}$ to all the thermo-elastic effects excluding the effects in the Optical Windows of the Vacuum Enclosures. An experimental estimation of the total contribution provides coupling factors in the order of 1 nm K^{-1}. This is further addressed in Chapter 6 [108].

2.1.3 Thermo-optical distortion of the optical parts

Another kind of thermal distortion that requires a dedicated treatment is the effect of temperature fluctuations in the different optical parts of the LTP. At a local level, apart from eventual thermo-elastic displacements of the optical components that clearly modify the pathlength between them, temperature variations in the optical parts induce optical path noise through residual thermal expansion of the glass. The effective optical length s of a glass slab of thickness b and refractive index n is defined by [1]:

$$s = nb - b \tag{2.21}$$

The derivative with respect to the temperature leads to

$$\frac{ds}{dT} = b\frac{dn}{dT} + \frac{db}{dT}(n-1) \tag{2.22}$$

Both the index of refraction and the thickness of the glass can actually vary with temperature. Including now the thermal expansion coefficient of the glass, $\alpha = \frac{1}{b}\frac{db}{dT}$, and the pathlength to phase conversion $\phi = \frac{2\pi}{\lambda}s$, being λ the laser wavelenght, the final phase dependence on temperature is expressed as

$$\frac{d\phi}{dT} = \frac{2\pi b}{\lambda}\left[\frac{dn}{dT} + \alpha(n-1)\right] \tag{2.23}$$

Amongst all the optical parts that conform the different interferometer readouts, only the Optical Windows (OW) on the Vacuum Enclosures have been considered critical in terms of thermo-optical noise. The main reason lays in the fact that they are the only optical parts placed outside the ultra-stable Optical Bench, therefore exposed to higher thermo-elastic stress. Specifically, they are clamped on the Vacuum Enclosures to let the laser beam access the Electrode Housings. Such enclosures, actually metallic tanks, are far less stable in terms of thermo-elasticity than the Zerodur® Optical Bench. The contribution of 40 rad K^{-1} at 1 mHz has been experimentally determined in [127].

2.1.4 Other thermal effects of interest

The LCA is obviously not the only system in the LTP sensitive to temperature. In first place, the different electronic units are sensitive to temperature through the already known Johnson-Nyquist white noise caused by the thermal agitation of the charge carriers that increase with temperature. This kind of noise is responsible of the sensitivity limit of many measurements, including the diagnostics sensors themselves [2]. Temperature noise at low frequency can also induce variations in the oscillators of the different clocks and affect the gains and phases of some of the devices. Though most of the units are equipped with local temperature sensors, their low resolution will allow just to check their performance rather than characterising their consequences onto the LTP performance. In any case, though electronic units are located outside the LCA and therefore exposed to higher temperature noise, all this equipment has been designed to not limit performance assuming a temperature stability of $10^{-3}\mathrm{K Hz}^{-1/2}$.

2.2 Thermal Diagnostics on board LISA Pathfinder

As part of the Data Management and Diagnostics Subsystem (DDS) equipment of the satellite, the LTP is equipped with series of temperatures sensors and heaters aimed to stress and characterise the main thermal perturbation mechanisms identified in the Section 2.1. The whole layout of thermistors, heaters and associated electronics is grouped in the Thermal Diagnostics Subsystem (TDS). The main objectives of the TDS are:

1. Sense with very high precision ($<10^{-5}\mathrm{K Hz}^{-1/2}$) temperature fluctuations at various places in the LTP.
2. Characterise and quantify any thermal-related effect that impacts on the main scientific measurement.

To cope with that the TDS system is composed by:

1. A Temperature Measurement System (TMS) with 24 temperature sensors spread around the Electrode Housing, the Optical Window, the Struts and other spots of interest.
2. A Heat Injection System (HIS) with a layout of 18 physical heaters distributed close to the thermal-sensitive parts, in order to stress the different thermal perturbation mechanisms.

More specifically, there are 2 heaters and 2 sensors at each $\pm x$ side of each Electrode Housing, 2 heaters and 3 temperature sensors close to each Optical Window and a heater and a sensor on 6 of the 8 struts. Finally, 4 additional sensors are attached to the edges of the Optical Bench, without heaters associated. The complete layout of thermal diagnostics items is schematized in Figures 2.2 and 2.3. Details on each of them are found in the following subsections.

2.2.1 Temperature Measurement System

The Temperature Measurement System (TMS) gathers the set of 24 thermistors distributed around the LCA, as shown in Figures 2.2 and 2.3, together with their associated

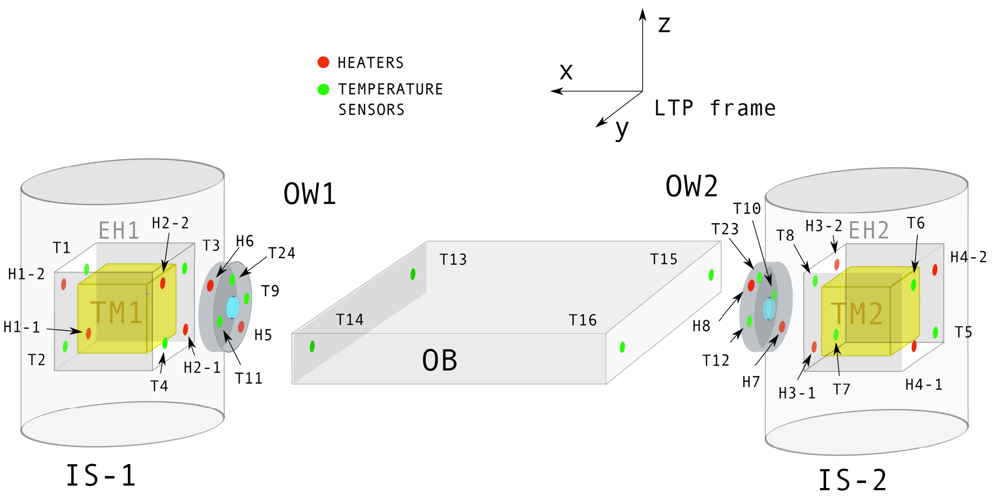

Figure 2.2: Schematic of the temperature sensors and heaters layout inside the LTP Core Assembly.

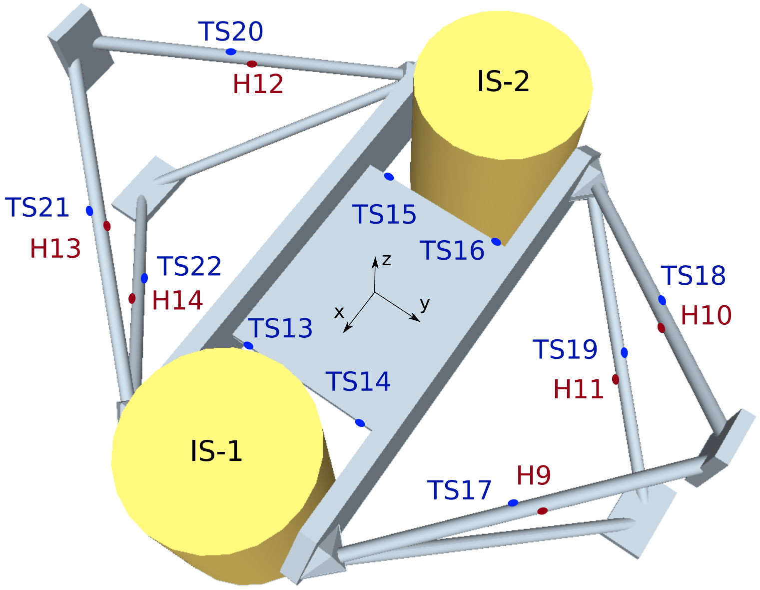

Figure 2.3: Schematic of the temperature sensors and heaters layout on the struts that attach the LTP Core Assembly to the satellite structure.

front-end electronics [2]. The thermistors used are Negative Temperature Coefficient (NTC) sensors with a nominal resistance of 10 kΩ, model BetaTherm-G10K4 [128]. The operational range is from 7.7 °C to 32 °C [2]. Their performance in terms of precision is much better than alternatives such as Platinum sensors. In effect, their sensitivity around $0.04\,\mathrm{K}^{-1}$ in the range of interest is an order of magnitude greater than the equivalent for the Platinum sensors [2]. A direct trade-off, however, is the lose of accuracy, since the chosen NTC devices have an accuracy of ±0.5 K in the absolute temperature measurement, far worse than other space-qualified Platinum-based alternatives with ±0.01 K.

The sensitivity function of NTC devices is exponential. The temperature dependence on the resistance follows the Steinhart-Hart model [129]:

$$\frac{1}{T} = A_S + B_S \ln R(T) + C_S \ln^3 R(T) \tag{2.24}$$

where A_S, B_S and C_S are the characteristic coefficients. Regarding the sensors on board LISA Pathfinder, an experimental campaign to validate each sensor and measure their Steinhart-Hart coefficients was done in [130]. The final values to be used during operations are presented in Table 2.1. Figure 2.4 shows some of the temperature sensors already integrated to the Flight Model Optical Bench and on one Optical Window.

Parameter	**Value [K^{-1}]**
A_S	$1.142 \cdot 10^{-3}$
B_S	$2.193 \cdot 10^{-4}$
C_S	$2.402 \cdot 10^{-7}$

Table 2.1: Nominal Steinhart-Hart coefficients to be used for the flight model NTC sensors [130].

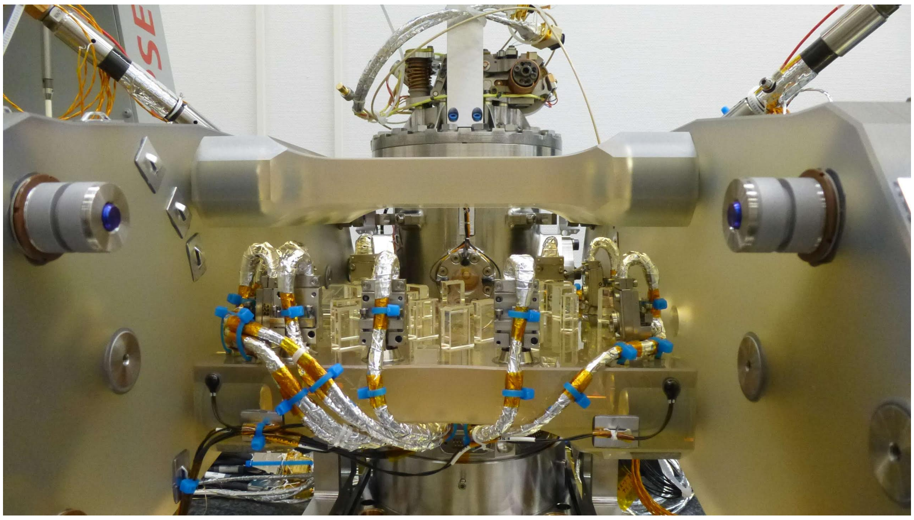

Figure 2.4: Flight model Optical Bench with visible thermal items on the bench itself and on the Optical Window. Credits: Airbus Defence and Space.

2.2.1.1 Measurement principle

The principle of measurement is the Wheatstone Bridge (WB) measurement of an unknown resistance [2]. In this kind of circuits, maximum sensitivity is met when the two resistances being compared —the actual thermistor and a nominal resistance— present similar values. However, the sensitivity decays exponentially with the difference of the resistances being compared and the temperature. So, in order to maximise the sensitivity, the whole range is divided into six different scales. By using different nominal resistances at each scale, associated to different NTC temperatures, a sensitivity of $\sim 6.5\,\mathrm{mV\,K^{-1}}$ is preserved across the whole range. Furthermore, hysteresis margins at the limits between the range of each scale minimize fluctuations between scales if the temperature fluctuates around one of the limits —see Table 2.2 [131].

Scale	R_0 [kΩ]	T_{min} [°C]	T_{max} [°C]
0	17.5	7.70	13.86
1	15	13.55	17.88
2	12.5	17.55	21.62
3	11	21.32	24.36
4	10	24.08	26.74
5	9	26.72	32.25

Table 2.2: Table summarizing the hysteresis margins for the different scales in the temperature range.

The output voltage of the Wheatstone Bridge is sampled by the Analog-to-Digital Converter providing 8000 initial samples, 4000 in positive polarisation and 4000 in negative polarisation to remove offset effects. These samples are accumulated into a 32-bit signed integer [132] whose average value provides a single temperature measurement in *counts*.

The information associated to absolute temperature measurements is therefore divided into time series of sampled ADC *counts* and time series of the *scale* associated to each sample. These time series are encapsulated as independent telemetry parameters, that are packed by the DMU and sent to the OBC, where they are stored until being requested for download by the MOC.

Once on-ground, the number of *averaged* counts per sample ($C_{\mathrm{A/D}}$) is first determined from the 8000-accumulated readout D_{acc} [132, 2]

$$C_{\mathrm{A/D}} = \frac{D_{\mathrm{acc}}}{8000} \tag{2.25}$$

Following that, considering the 10 V scale range of the 16-bit ADC, the measured voltage is determined by

$$V_\text{o} = \frac{10}{2^{16}} C_\text{A/D} \tag{2.26}$$

The equivalent thermistor resistance associated to the measurement of the absolute temperature is given by:

$$R_\text{out} = R\left[\left(\frac{V_\text{o}}{G V_\text{b}} + \frac{R_\text{ref}}{R + R_\text{ref}}\right)^{-1} - 1\right]^{-1} \tag{2.27}$$

where:

- $R = 10\,\text{k}\Omega$
- $V_\text{b} = 0.6201\,\text{V}$ is the Wheatstone Bridge voltage supply.
- $G = 198.6$, corresponding to the gain of the instrumentation amplifier.
- R_ref is the resistance associated to the current scale —see Table 2.2.

The equivalent absolute temperature in °C is finally obtained by applying the Steinhart-Hart equation using coefficients from a dedicated calibration:

$$T_\text{TSx} \quad = \quad \frac{1}{\alpha + \beta \ln R_\text{out} + \gamma \ln^3 R_\text{out}} - 273.15 \tag{2.28}$$

In addition to this *absolute temperature measurements*, the Temperature Measurement System performs two other kind of measurements:

- *Differential measurements*: These measurements are obtained by replacing the scale resistance by another temperature sensor, what allows to cancel out the influence of the common environment temperature fluctuation.
- *Reference measurements*: in this case the electronic noise of the system is directly sampled by replacing the thermistor in the Wheatstone Bridge by a high stability resistance. This measurement provides an estimate of the sensitivity of each Wheatstone Bridge.

The electronics performing all these temperature measurements are distributed in two Data Acquisition Units (DAU) located in the DMU. Each DAU contains three sets of Wheatstone Bridges, four sensors per bridge. Different multiplexers are in charge of selecting each thermistor and connecting it to a 16-bit ADC. Since the multiplexers switch each 200 ms and there is one multiplexer per group of six sensors, the final sampling frequency on board for each temperature sensor is 0.833 Hz. Still, due to downlink telemetry constraints, the temperature data needs to be on board downsampled a factor

4, resulting into a final rate on-ground of 0.208 Hz. This is performed by a Butterworth filter of third order with a cut-off frequency of 80 mHz [2].

2.2.1.2 Temperature Measurement System performance

Figure 2.5 shows the Power Spectral Density from a noise measurement as measured by two sensors during one integration test —TS9 and TS11 in the OSTT test campaign. The sensitivity above 2 mHz is kept around 10^{-5} K Hz$^{-1/2}$, limited by system electronic noise, while below this frequency the system is affected by residual environmental noise. More details on this test campaign are found in Chapter 6.

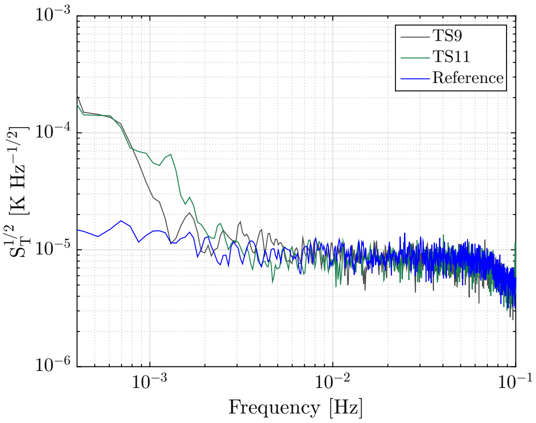

Figure 2.5: Power Spectral Density of two absolute temperatures measured by TS9 and TS11 during one noise measurement test together with their reference measurement.

2.2.1.3 Post-process issues

Two aspects of the TMS and the downlink chain induce two relevant issues that affect the post-process and the forthcoming data analysis: a conflict related to the downsampling filter and the scale changes on one hand, and an expected ADC non-linear error on the other hand.

Scale changes

The filter applied for the downsampling process explained in Section 2.2.1.1 is directly applied to the data stream. However, at each change of scale there is one meaningless sample of *counts* that is actually the 8000-times averaged value of a sequence of measurements including the *previous* scale and the *new* scale. Such a sample is actually seen as a step input by the filter, which responds imprinting a visible spike to the data associated consistent with the step response of the filter. Such an effect needs to be carefully removed once on-ground. Figure 2.6 shows an example of the feature and the result after being processed.

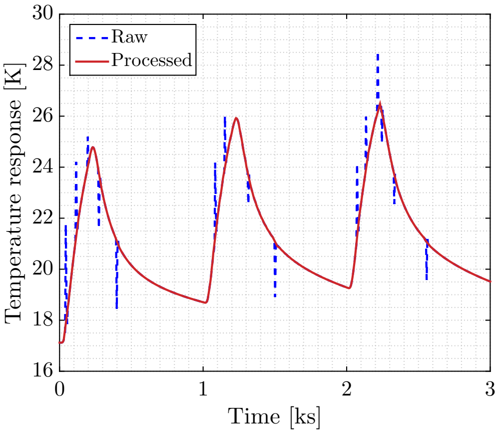

Figure 2.6: Comparison between raw temperature and processed data cleared from spikes.

ADC non-linear error

Too high temperature drifts induce a non-linear error associated to imperfections in the voltage comparators of each bit in the Successive Approximation Register (SAR) ADC [133]. Such a small-scale effect can be amplified in low noise environments if the temperature drifts keep approximately constant during enough time. The frequencies associated depend on the imperfect bit affected and the current temperature drift. Each bit contribution —as a voltage error— is frequency-dependent and it can be expressed as [133, 134]:

$$|q_k(\omega)| = \Delta \sum_{n=-\infty}^{\infty} \frac{\sin \frac{n\pi\varepsilon_k}{2^{k+1}\Delta}}{n} \frac{\sin \frac{n\pi}{2}}{\sin \frac{n\pi}{2^{k+1}}} \delta\left(\omega - \frac{\pi n|b|}{2^k \Delta}\right) \tag{2.29}$$

where:

- b is the temperature slope, in $\mathrm{K\,s^{-1}}$.
- Δ is the ADC quantization step in V.
- k is the binary digit, increasing from 0 to 15 —from the least significant bit to the most significant one.
- ε_k is the relative error associated to each bit, as a fraction of Δ.

For the LPF temperature sensors such an effect has been repeatedly observed [133, 108], as shown in Figures 2.7. The bumps that appear in the power spectra of some temperature sensors are individually associated to integral non-linearities of specific bits. In Figure 2.7 the affected frequencies clearly oscillate close to 3 mHz and 6 mHz, which is consistent with a bit mismatch at the 2^{nd} and 3^{rd} Least Significant Bit (LSB) of the ADC in front of a drift around $6\,\mu\mathrm{K\,s^{-1}}$, considering a system sensitivity of $1.35\,\mathrm{K\,V^{-1}}$.

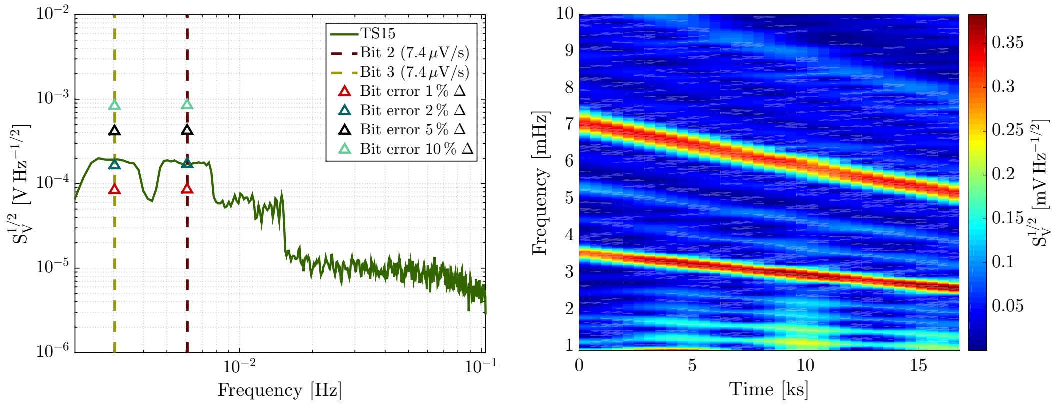

Figure 2.7: *Left*: PSD of the noise at TS15 at specific segment where the ADC non-linear effects create two bumps around 3 mHz and 6 mHz caused by bit errors at bits 2 and 3 and a voltage drift around 7.4 μV s^{-1}. *Right*: Spectrogram of the voltage during chosen segment. The reddish lines show the affected frequencies varying within the time, due to the variation of temperature drift.

The noise level introduced, around $2\cdot 10^{-4}$ K Hz$^{-1/2}$, clearly exceeds the ambient level by a factor two.

Limits to the temperature drift can be obtained from this analysis. Since the amplitude of the bumps depends only on the Δ parameter which cannot be modified, the highest-frequency bump must be shifted down in the bandwidth of interest. In this sense, in order to shift the highest frequency affected in Figure 2.7 (8 mHz) to 1 mHz, the temperature drift should be therefore reduced to 1/8 of the measured value, i.e. to 0.75 μK/s.

2.2.2 Heat injection system

The Heat Injection System (HIS) consists of a set of 18 heaters distributed around the LCA plus the associated electronics that allow to apply precise heat signals as requested by dedicated telecommands.

Two kinds of diagnostics heaters are found in the LTP: constant-resistance heaters with nominal resistance of 45 Ω and negligible dependence with temperature are found on each Optical Window and on the Struts, while NTC thermistors acting as heaters are located on the external walls of the Electrode Housing —see Figures 2.2 and 2.3. Though there are eight *physical* NTC heaters at the two Electrode Housings, they are actually commanded by pairs. Indeed, each pair of heaters on each $\pm x$ side of each Electrode Housing (H1-1, H1-2, H2-1, H2-2, ..., H4-2) is considered one *logical* heater, leaving just four operative heaters (H1 to H4) in the Electrode Housings. Table 2.3 summarizes the notation associated to each heater and its type.

The reason why heaters on the Electrode Housings are not like the other ones is caused by their need to be placed inside the Inertial Sensor Housings. Indeed, requirements in terms of cleanliness are so stringent that impede using any kind of Kapton

Heater	Type
H1 to H4	NTC thermistors
H5 to H14	Constant-resistance heaters

Table 2.3: Heaters classification.

heaters as those used on the Struts and on the Optical Windows. However, since the power requirements in the Electrode Housings are much smaller, NTC thermistors acting as heaters arose as suitable alternatives. The models chosen for the NTC devices acting as thermistors have a nominal resistances of 2 kΩ [135], five times smaller than the NTC temperature sensors. Still, some of the NTC devices presented a too high residual magnetic moment. An extensive screening campaign was carried out to find a proper set of complying items.

Heater activation telecommands

The telecommands (TC) sent to the satellite are received and managed by the DMU [136]. A same TC can request independent signals for up to four heaters —two per Data Acquisition Unit (DAU), though each DAU can only control half of the available heaters. Each signal is a square wave defined by the parameters shown in Figure 2.8. *Level-1* and *Level-2* stand for requested power levels, since the conversion to final voltage is carried out by the DMU software. The shape of the final TC considering all the possible fields is as shown in Table 2.4.

ID Heater 1 DAU 1	**Number of cycles**	**Period (secs)**	**Duty cycle (255 = 100%)**	**Level 1**	**Level 2**	**Phase relation**
Enum	Unsigned Integer	Unsigned Integer	Unsigned Integer	Unsigned Integer	Unsigned Integer	Unsigned Integer

ID Heater 2 DAU 1	**Number of cycles**	**Period (secs)**	**Duty cycle (255 = 100%)**	**Level 1**	**Level 2**	**Phase relation**
Enum	Unsigned Integer	Unsigned Integer	Unsigned Integer	Unsigned Integer	Unsigned Integer	Unsigned Integer

ID Heater 1 DAU 2	**Number of cycles**	**Period (secs)**	**Duty cycle (255 = 100%)**	**Level 1**	**Level 2**	**Phase relation**
Enum	Unsigned Integer	Unsigned Integer	Unsigned Integer	Unsigned Integer	Unsigned Integer	Unsigned Integer

ID Heater 2 DAU 2	**Number of cycles**	**Period (secs)**	**Duty cycle (255 = 100%)**	**Level 1**	**Level 2**	**Phase relation**
Enum	Unsigned Integer	Unsigned Integer	Unsigned Integer	Unsigned Integer	Unsigned Integer	Unsigned Integer

Table 2.4: Parameters to be defined in the telecommand to activate a group of heaters. The telecommand ID is TC(8,1).56 *Switch on heaters* [136, 137].

When feeding two heaters with the same DAU, the average power supplied per heater is half of the power commanded since the system keeps multiplexing between the two output heaters at 2 Hz .

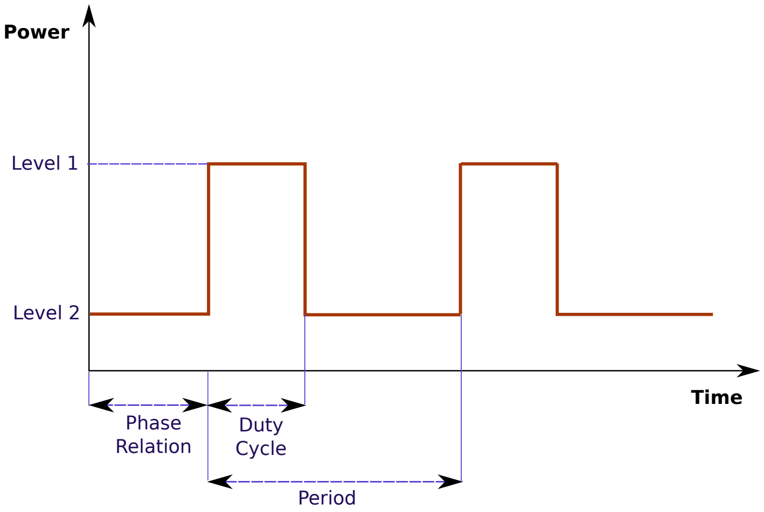

Figure 2.8: Parameters to be defined in the heater activation command.

The wave generator is based on a voltage source with a maximum voltage amplitude of 10 V. With such a voltage, heat pulses of up to 2.2 W can be applied to resistive heaters. On the other hand, the maximum power available for the NTC thermistors acting as heaters is 45 mW per *physical* heater, i.e. 90 mW per *logical* heater [137]. This is the power achieved when applying the maximum voltage at a nominal temperature of ≈18°C. Nevertheless, due to their NTC nature, the total power applied strongly depends on the local temperature. At temperatures lower than 18°C, the available power starts to decrease until it reaches a power of ≈60 mW in the lowest edge of the range. In the opposite case, too high temperatures could lead to unstable behaviour with power higher than 90 mW, so a maximum operational limit at this power is imposed for temperatures higher than 18°C.

In addition, the final steady-state power delivered by the NTC heaters needs to account for the self-heating effect, that is the resistance reduction when the heater is activated at a constant voltage due to the local temperature increment. This effect implies that for a same commanded voltage different steady-state power amplitudes are obtained depending on the initial temperature. Fortunately, such an initial temperature can be measured by the temperature sensors located nearby. Therefore, in order to apply a certain power, the system needs to first measure the temperature and solve the inverse of the Steinhart-Hart equation, what allows to predict the voltage required. Such last step also requires to have a good estimate of the thermal coupling between the heater and the surface where it is attached [2]. With the purpose of easing such a process, the DMU includes series of Look-Up Tables (LUT) that directly reports the approximated voltage to be applied for a requested power and measured temperature [137].

2.3 Thermal experiments

In order to characterise the different thermal effects introduced in Section 2.1 by means of the Thermal Diagnostics Subsystem described in Section 2.2, three kinds of thermal experiments are considered:

1. Electrode Housing thermal experiments.
2. Strut thermal experiments.
3. Optical Window thermal experiments.

The aim of all of them is to apply controlled heat signals by means of the diagnostic heaters to specific thermal-sensitive points in the LTP and measure both the temperature response in the heated spots and eventual disturbances on other LTP subsystems, fundamentally the OMS. The product of them should be in terms of coupling factors between either temperature fluctuations or temperature gradient fluctuations and other physical quantities like forces and torques on the Test Mass, Optical Window pathlength variation and laser beam disruption, depending on the case. Since most of the scientific readouts in the LTP are generally in terms of Test Mass displacements and rotations, careful conversions from the readouts to the magnitudes of interest affected are required.

Finally, the ultimate purpose of such analysis is to estimate the contribution of temperature fluctuations to the general performance of the LTP. This is to be carried out by performing temperature noise measurements during general acceleration noise measurements and computing the contribution by applying the estimated coefficients. However, these couplings are obtained in scenarios with temperature distributions strongly dominated by the activated heaters, while temperature distributions during temperature noise measurements may present different patterns —usually more homogeneous than in the experiments. Such a difference may require additional assumptions before applying the measured coefficients to the noise measurement case.

Electrode Housing thermal experiments

The Electrode Housing thermal experiments are aimed to identify the thermal coefficient that couples the temperature gradient on the main sensitive axis of the OMS —the x axis, in LTP notation— to the direct forces induced through the main thermal effects described: radiation pressure, radiometer effect and outgassing effect.

In order to stress the contribution of such effects, a square wave heating signal is applied by alternating the activation of both heaters on a same Electrode Housing, hence inducing a significant temperature gradient signal across the Electrode Housing modulated at the frequency of the input signal. The consequences of such a heat pattern are observed in x_{12}, no matter the role of the heated mass at the moment (primary or secondary). The consequences on x_1 are expected to be imperceptible due to the spacecraft jitter noise.

If such heater sequences are carried out at different averaged temperatures, the global thermal coefficient varies according to the temperature dependence of each thermal effect, what eventually allows to disentangle the contribution of the different effects.

In addition, since there is no way to directly measure the pressure in the Inertial Sensor cavities, an eventual identification of the radiometer effect would allow to set an upper limit to the pressure. This is of much interest in order to assess the contribution of Brownian noise, that could be critical in scenarios with higher residual pressure as expected.

A significant part of Chapter 3 is dedicated to the definition of a model to simulate these experiments. Chapter 4 addresses the design of the experiments in order to define proper inputs, while Chapter 5 provides an experimental approach to the identification of the three thermal effects that depend on the temperature gradient.

Strut thermal experiments

The experiments on the Struts are aimed to apply a controlled thermo-elastic distortion to the whole LTP Core Assembly, with clear consequences on the OMS channels since most of the laser beams are likely to be distorted from their nominal positions. To accomplish that, and also to distinguish eventual asymmetries, series of pulses are individually applied to each heater in the struts.

The deformation of the structure, consistent with the thermal expansion of each strut, must be related to the different perturbations observed in the OMS. No frequency dependence on the couplings observed should be detected at the bandwidth of interest. Chapter 6 is devoted to the analysis of this experiment.

Optical Window thermal experiments

The Optical Window (OW) thermal experiments are intended to induce a significant pathlength variation in the OMS readouts by directly heating the titanium flanges of the Optical Windows. In this experiment, sequences of pulses are applied simultaneously to both heaters on the same Optical Window, what produces visible consequences on the OMS channels, mainly on x_{12}. An extensive experimental campaign to model the effects of this experiment was already carried out in [1, 127]. Therefore the study of this effects are kept out of the scope of this thesis.

CHAPTER 3

Thermal Model of the LPF

In order to design and optimize the yield from thermal experiments, it is of high interest to develop a tool that predicts how heat fluxes propagate across a system and how temperature at specific spots responds to certain heat inputs. Nowadays, there is a wide variety of thermal-oriented software, based on the Finite-Element Method (FEM), that allows to model complex systems and to simulate their thermal behaviour in several kinds of thermal environments. Still, these models need to be somehow validated by real tests. Since in space projects it is pretty expensive to carry out extensive test campaigns with flight model parts, it is a recurrent option to partially test them by using equivalent systems where missing parts are replaced by dummy, thermal-representative masses.

Concerning the LISA Pathfinder satellite, a detailed thermal model has been built for thermo-mechanical design purposes. Such a model can also play a role in the scientific analysis since it allows us to simulate the temperature responses at different spots of the LTP when applying different heat signals on the heater locations. In addition, since ensuring total thermal isolation between the different parts becomes infeasible at low frequencies, such a simulation tool is also pretty helpful to detect eventual cross-couplings and unexpected heat exchanges between subsystems.

Still, the existing LPF thermal model does not include models for the thermal effects inside the Electrode Housing described in Section 2.1.1. This arises the need to develop a dedicated algorithm for them. The outputs of such an algorithm —actually the forces and torques on the Test Masses induced by temperature gradients— can be lately included in a general simulator of the whole LTP, allowing to estimate the impact of certain heat activations to the whole system.

In the following sections, a thermal model of the satellite is first adapted to the LTP experiment needs and implemented by means of State-Space Models (SSMs) in the LTPDA simulation environment. Following that, the model is compared to real data obtained in different test campaigns which allows its reliability to be checked. Finally, at the end of the chapter, the thermal model is enhanced with an extension that enables to simulate the forces and torques induced on the Test Masses due to asymmetric temperature distributions on the Electrode Housing. Such an extension requires an accurate analysis of the reflections between the different surfaces inside the Electrode Housings.

3.1 Thermal model implementation

Heat transfer problems are usually modelled under the assumption of Linear Time-Invariant (LTI) systems —see Appendix A for more details. Such a strong assumption allows to represent thermal systems by series of first order differential equations that can be expressed in several different ways, such as transfer functions, partial fractions or State-Space Model objects, amongst other. Concerning the LPF thermal experiments, it is of special interest to represent them as SSMs —see Section A.3.3— so they can be easily integrated to the models of the whole LTP. The desired thermal model needs to have the different heaters as inputs and the temperature responses at the different locations of interest as outputs. The thermal model implemented here is divided in two blocks to distinguish between two kinds of heat fluxes: the heat conduction from the heater devices to its surface and the heat flux distribution from the surface to any other location in the satellite. Thus, we have

1. The **Heater model block**: Some of the diagnostics heaters, actually the NTC ones, present a transient after the activation that needs to be modelled —see Section 2.2.2 for more details. This block contains the information regarding the time response of such devices, i.e. it simulates the *applied* power by the heaters to the surface as a function of the *commanded* power.

2. The **ESATAN model block**: It contains the information of how the heat is transferred across the spacecraft, i.e. it simulates variation of temperature at different output points when certain power is applied to the heater locations.

Both of them are implemented as SSM objects by means of the available LTPDA modelling tools. Two types of outputs are considered here:

1. Outputs representing the temperature sensor readouts: the temperature sensors in the model are considered ideal devices represented by single thermal nodes. The readout features from the signal acquisition and preprocess like the scale changes associated spikes are not included in the model.

2. Outputs representing the temperature at other spots of interest: in order to achieve an accuracy as good as possible in the modelling of the thermal effects, it is of interest to estimate the temperature response in the Electrode Housing. Therefore the thermal model must also provide the temperature responses at specific nodes of the Electrode Housing.

3.1.1 Heater model

As stated in Section 2.2.2, there are two types of heaters in the LTP: **constant-resistance heaters** in the six Suspension Struts and in the two Optical Windows, and **NTC heaters** in the two Electrode Housings, the latter presenting a non-linear dependence on temperature [2]. In the model, the inputs to all of them are defined in terms of power. However, each type requires a different modelling to account for their differences.

3.1.1.1 Constant-resistance heaters

With negligible temperature dependence, these heaters are assumed to present an ideal resistive behaviour, i.e their nominal resistance is constant and the delivered power is directly determined from the power commanded. Neglecting the thermal contact and the losses by radiation [138], the *real* applied power on the surface is expressed as

$$P_{\text{applied}}(t) = P_{\text{commanded}}(t) \tag{3.1}$$

3.1.1.2 NTC thermistors as heaters

Negative Temperature Coefficient (NTC) thermistors are more complex and require special consideration in the modelling. The main reason is that their electric resistance varies with temperature, and the latter keeps increasing during the experiments what makes the actual injected power vary with time. In addition, the thermal contact between the thermistors and the surface where they are attached is determinant to define the equilibrium temperature achieved and must also be modelled. Finally, the amount of power delivered at a certain voltage depends as well on the temperature at the beginning of the pulse [2]. All in all, the activation of the device introduces a small transient at the beginning of each new pulse, actually much shorter than the expected length of the pulse itself. The transient period is around few seconds and depends basically on the thermal capacitance and resistance of the heater.

The power expression for NTC thermistors that includes these effects is written as

$$P_{\text{applied}}(t) = \frac{1}{R}\left[T_{\text{heater}}(t) - T_{\text{surface}}(t)\right] = \frac{1}{R}\Delta T_{\text{heater}}(t) \tag{3.2}$$

where $T_{\text{heater}}(t)$ is the heater temperature, $T_{\text{surface}}(t)$ is the temperature of surface where the heater is attached and R is the thermal resistance between the surface and the heater. The temperature response to an eventual power step signal —or heater *switch on* command— is expressed as [137]

$$\Delta T_{\text{heater}}(t) = T_{\text{surface}}(t) + \frac{P_{t=0,\,\text{heater}}}{aC}\left(1 - e^{-at}\right) \tag{3.3}$$

where a is the inverse of the time constant of this system, defined as

$$a = \frac{1}{C}\left[\frac{1}{R} - P_{t=0,\,\text{heater}}\frac{\beta}{T^2_{t=0,\,\text{heater}}}\right] \tag{3.4}$$

The parameters $T_{t=0,\,\text{heater}}$ and $P_{t=0,\,\text{heater}}$ refer to the temperature and the power dissipated at the beginning of the pulse, while C is the thermal capacitance of the heater and β is a characteristic parameter of the thermistor. The initial temperature is directly obtained from the readout of any of the two temperature sensors close to each heater in the Electrode Housing just before the pulse. Table 3.1 provides values for β, the capacitance C and the thermal contact R. $P_{t=0,\,\text{heater}}$ is determined as

$$P_{t=0,\,\text{heater}} = \frac{V^2_{\text{heater}}}{R_{t=0,\,\text{heater}}} \tag{3.5}$$

where V_{heater} is the voltage applied and $R_{t=0,\,\text{heater}}$ is found from an approximation of the Steinhart-Hart equation described in Section 2.2.1:

$$R_{t=0,\,\text{heater}} = R_0 \exp\left[\beta\left(\frac{1}{T_{t=0,\,\text{heater}}} - \frac{1}{T_0}\right)\right] \tag{3.6}$$

with the nominal values $R_0 = 2000\,\text{k}\Omega$ and $T_0 = 298\,\text{K}$. Consequently, the expression for the power applied is written as

$$P_{\text{applied}}(t) = \frac{P_{t=0,\,\text{heater}}}{aRC}\left(1 - e^{-at}\right) \tag{3.7}$$

Parameter	Value	Units
β	3499	K
R	100	$\text{K}\,\text{W}^{-1}$
C	0.01	$\text{J}\,\text{K}^{-1}$

Table 3.1: Nominal values for the NTC heaters [130, 135].

Opposite to the switch on case, the applied power after switching off the heater is expressed as

$$P_{\text{applied}}(t) = \frac{1}{R} T_{\text{peak}}\, e^{-\frac{t}{RC}} \tag{3.8}$$

where T_{peak} is the highest temperature achieved during the previous pulse, i.e. the temperature reached before the voltage applied was discontinued.

Finally, switching from a power level to an other requires a recalculation of the parameters a and $P_{t=0,\,\text{heater}}$ that lead to a new equilibrium temperature in the NTC device. Such a feature is expressed as

$$P_{\text{applied}}(t) = P_{\text{prev}} + \left(\frac{P_{t=t',\,\text{heater}}}{aRC} - P_{\text{prev}}\right)\left(1 - e^{-at}\right) \tag{3.9}$$

where P_{prev} is the last value of P_{applied} before changing to the new power level at time $t = t'$.

The resolution of each transient is determined by the time step value Δt compared to the time constant of the system, $\tau = 1/a$. Since $\tau \sim 1\,\mathrm{s}$, for sampling frequencies lower than 0.1 Hz it is not necessary to include this feature.

3.1.2 ESATAN Thermal Model

There are two relevant thermal models in relation to LISA Pathfinder: a general model of the whole spacecraft developed by ASD and coded in ESATAN [139], and a more detailed model of just the LCA coded in Thermica© and maintained by CGS [140]. A merged version of both models, coded in ESATAN, is maintained by ESTEC.

Both thermal software tools use FEM algorithms based on the Lumped Parameter method that divide systems —in these cases, the whole LCA or the LPF— into many thermal representative nodes. Specific properties such as volume, geometry and thermal capacity need to be set for each node, together with their interaction towards the other nodes in terms of node-to-node thermal couplings. As an example, Figure 3.1 partially shows how the inner surfaces of the Electrode Housing are discretised in the model.

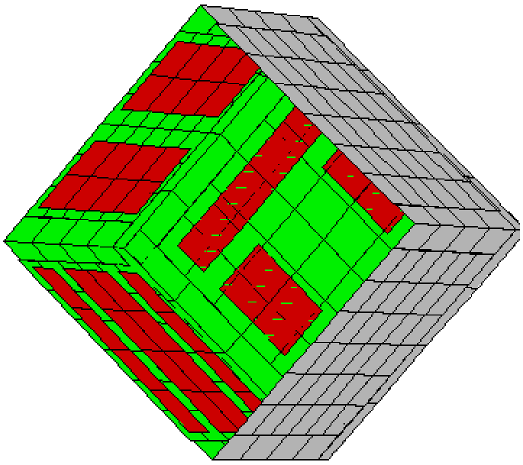

Figure 3.1: Electrode Housing inner surfaces discretisation in the LTP thermal model. Red nodes account for the molybdenum electrodes while green nodes represent the sapphire surfaces [140]. Credits: CGS SpA.

An important feature of ESATAN is that given a thermal model, the software is able to compute transfer functions from one arbitrary node to another, where the inputs are the heat flux applied and the outputs the temperature responses at specific locations. Indeed, series of transfer functions describing the temperature responses in front of heater activations are obtained by identifying the nodes representing the heaters and the temperature sensors.

In this sense, we used the model from ESTEC. We were provided with a subset of requested transfer functions whose inputs where the nodes of the 16 physical heaters and the outputs the locations of the 24 sensors and 176 nodes representing the electrodes inside the Electrode Housing, the latter being of special interest to map the temperature distributions on the inner walls of the Electrode Housings. At the moment of writing this manuscript, however, the version of the thermal model implemented slightly differs from the final Flight Model version, since the latest modifications of the Electrode Housing are not yet available as SSM objects. Nevertheless, as addressed in Section 3.2.1, no major differences are expected between the implemented model and the final Electrode Housing.

3.1.2.1 Transfer function fitting

The transfer functions provided consist of 16 inputs × 200 outputs, i.e. 3200 lists of gains and phases at 100 log-spaced frequencies between 10^{-7} and 1 Hz. In order to adapt them to a suitable format, in this case as SSM objects, the following steps are required:

1. Fit the gain and phases in complex domain to get continuous transfer functions in s domain. The frequency domain fit is carried out by a version of the **Vector Fitting** algorithm [141, 142] implemented in the LTPDA environment. The order of the fitted transfer functions is variable, though most of the transfer function required at least an order ~8 [138]. For the particular case of heaters in the Electrode Housing (heaters H1 to H4), since each logical heater is actually composed of two physical heaters (H1 is actually H1-1 + H1-2) with a 8-order transfer function each, the final order of transfer function representing the activation of one of these logical heaters is 16. The transfer function for a heater h and an output temperature point m represented in series of partial fractions is written as

$$H_{h\to m}(s) = \sum_{k=1}^{N} \frac{r_{hm,k}}{s - p_{hm,k}} \tag{3.10}$$

   where $r_{hm,k}$ and $p_{hm,k}$ are the zeros and poles of the transfer function (8 or 16 depending on the input heater), specific for each combination of heater h and output m.

2. After the fit, it is necessary to built a continuous SSM object from each s-domain transfer function, following the procedure described in Section A.3.3. The number of system variables —actually, *states*— is equal to the order of its original transfer function. Consequently, the transfer function between a physical heater and a temperature output is represented by a SSM with 8 states variables —SSMs whose $[A]$ matrices size 8×8.

3. Once all the SSM individual objects are built, they are assembled to a multiple-input multiple-output SSM object. Since $16 \times 8 \times 200 = 25600$, the size of the global

thermal SSM presents the following shape:

$$\underset{25600\times 1}{\begin{bmatrix} \dot{x}_i \end{bmatrix}} = \underset{25600\times 25600}{\begin{bmatrix} \quad A \quad \end{bmatrix}} \underset{25600\times 1}{\begin{bmatrix} x_i \end{bmatrix}} + \underset{25600\times 16}{\begin{bmatrix} \quad B \quad \end{bmatrix}} \underset{16\times 1}{\begin{bmatrix} q_h \end{bmatrix}} \tag{3.11}$$

$$\underset{200\times 1}{\begin{bmatrix} T_m \end{bmatrix}} = \underset{200\times 25600}{\begin{bmatrix} \quad C \quad \end{bmatrix}} \underset{25600\times 1}{\begin{bmatrix} x_i \end{bmatrix}} + \underset{200\times 16}{\begin{bmatrix} \quad D \quad \end{bmatrix}} \underset{16\times 1}{\begin{bmatrix} q_h \end{bmatrix}} \tag{3.12}$$

where q_h is the input power to each heater and T_m the output temperature.

4. Finally, the SSM object is discretised to a desired sampling frequency, as explained in Section A.3.3.

Once the previous steps are implemented, the LTPDA infrastructure allows to simulate any kind of heat input to the heater locations. Figure 3.2 shows a subset of transfer functions for different combinations of heaters and temperature sensors.

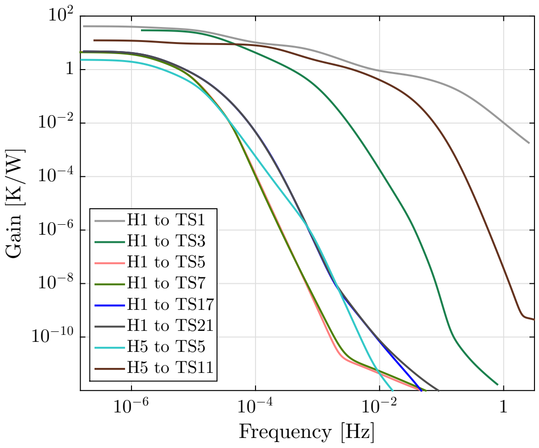

Figure 3.2: Amplitude gains for a subset of transfer functions. The whole model includes 3200 transfer functions.

Transfer functions representing strong thermal couplings like *input* heaters close to *output* sensors —e.g. the case of H1 to TS1— are normally composed of pure real filter coefficients. However, imaginary terms appear in some cases with weak thermal couplings due to a particularity of the fitting method in cases of high uncertainty. This feature arises when sharp slopes in the gain of the original frequency responses are fitted with a double pole represented by two complex conjugate numbers. In that case, the imaginary components can achieve magnitudes close to the real components. However, due to their complex-conjugate nature, the final imaginary components numerically cancel out. Nevertheless, this characteristic must be included in the filtering process to avoid residual rippling in the output. In addition, weak couplings between nodes distant to each other are also specially sensitive to the precision of the coefficients obtained — 16 significant digits in our case—, which must be kept in order to avoid extra offsets. Figure 3.3 shows some of these effects in an extreme case for just testing purposes: in the *left* plot, the same 1 mHz input signal with 1 W amplitude is applied to H1 while tracking TS1, representing a high gain transfer function, while in the *right* plot the signal is applied to H5 and the observed sensor is TS5, representing a weak coupling. While in the former case the precision and the imaginary terms do not play any observable role, for the latter case both features significantly distort the expected temperature.

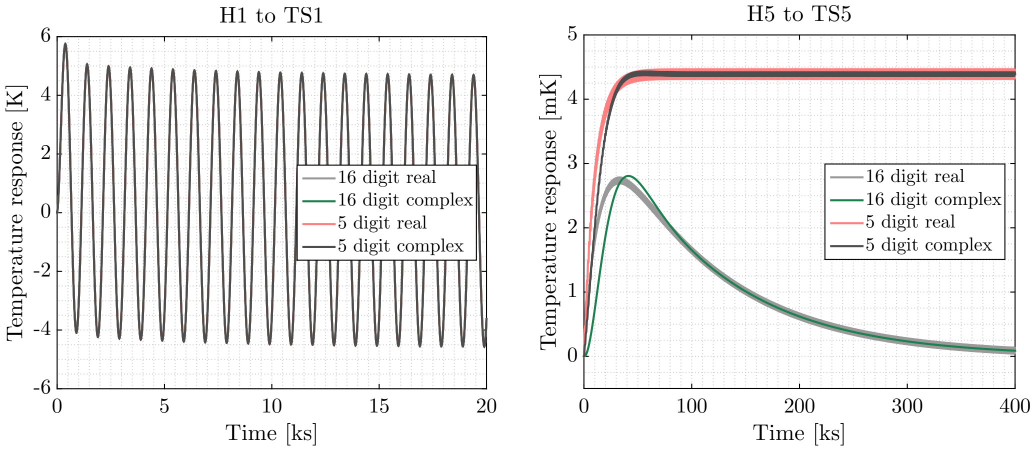

Figure 3.3: *Left:* Temperature responses on TS1 when applying a 1 mHz, 1 W sinusoid to H1 and considering different processes to the filter coefficients. Since the thermal coupling between H1 and TS1 is large, no significant differences arise after truncating and neglecting the imaginary components. *Right:* Temperature response on TS5 after applying the same input to H5. In this case the differences are notable: while truncating the precision of the coefficients shifts the equilibrium points, discarding the imaginary terms adds a rippling pattern to the signal.

3.1.2.2 SSM infrastructure verification

In order to test the whole infrastructure and as a proof of performance, a simulation with inputs to all the heaters is considered here. The following series of three pulses at maximum power are applied to the different heaters:

1. Electrode Housing heaters: Pulses of 90 mW, period 1000 s and 50% of duty cycle to heaters H1-H4.

2. Optical Window heaters: Pulses of 2 W, period 1000 s and 20% of duty cycle to heaters H5-H8.

3. Strut heaters: Pulses of 2 W, period 1000 s and 20% of duty cycle to heaters H9-H14.

The following Figures 3.4, 3.5 and 3.6 show the temperature responses at all the diagnostic sensors for the different heat injections described. In general, time steps of ~1 s are enough for such long simulations.

Such a simulation allows to identify the temperature responses at different parts when their closest heaters are activated, what is of interest for the design of the different thermal experiments. However, they also provide an estimation of eventual cross-couplings. The main temperature increments are summarized in the following lines:

- The activation of the Electrode Housing heaters (Figure 3.4) with the proposed heating pattern produces temperature increments up to ≈500 mK in the closest thermistors and temperature increments of ≈150 mK in the opposed face of the Electrode Housing. The Optical Window presents a temperature response of ~10 mK, while both the struts and the sensors in the Optical Bench show an accumulated temperature increase of less than ~10 mK.

- The activation of the Optical Window heaters (Figure 3.5) induces a local temperature increment of ≈8 K. Accumulated temperature increments of ≈200 mK are perceived in the closest Electrode Housing, while the total temperature increment in the Optical Bench and in the struts remains around ≈100 mK.

- The activation of the heaters in the struts (Figure 3.6) produces temperature increments in the heated struts of ≈9 K. The temperatures in the Optical Bench and in the Optical Window increase to ≈120 mK, while the accumulated temperature increment in the Electrode Housing is of ≈100 mK.

Notice that all the heater activations are perceived by all the temperature sensors. Though the accumulated temperature increments are quite significant, the components in the milli-Hertz band are strongly damped, leaving just slow temperature drifts that achieve their maximums around 15 ks after the last heater is switched off.

3.1.2.3 Partial fraction representation for the filters in the ESOC simulator

Apart from the implementation as SSM objects for the LTPDA simulators, a parallel version of the same thermal model has been developed as an extension of the official simulator of the satellite at ESOC. Such a model is coded in $C++$ and does not operate with SSM objects. Alternatively, partial fraction digital filters are implemented for each of the transfer functions described before. Their conversion to digital filters is done applying the bilinear transform described in Section A.3.2, hence each digital filter from a heater h to an output node m is expressed as

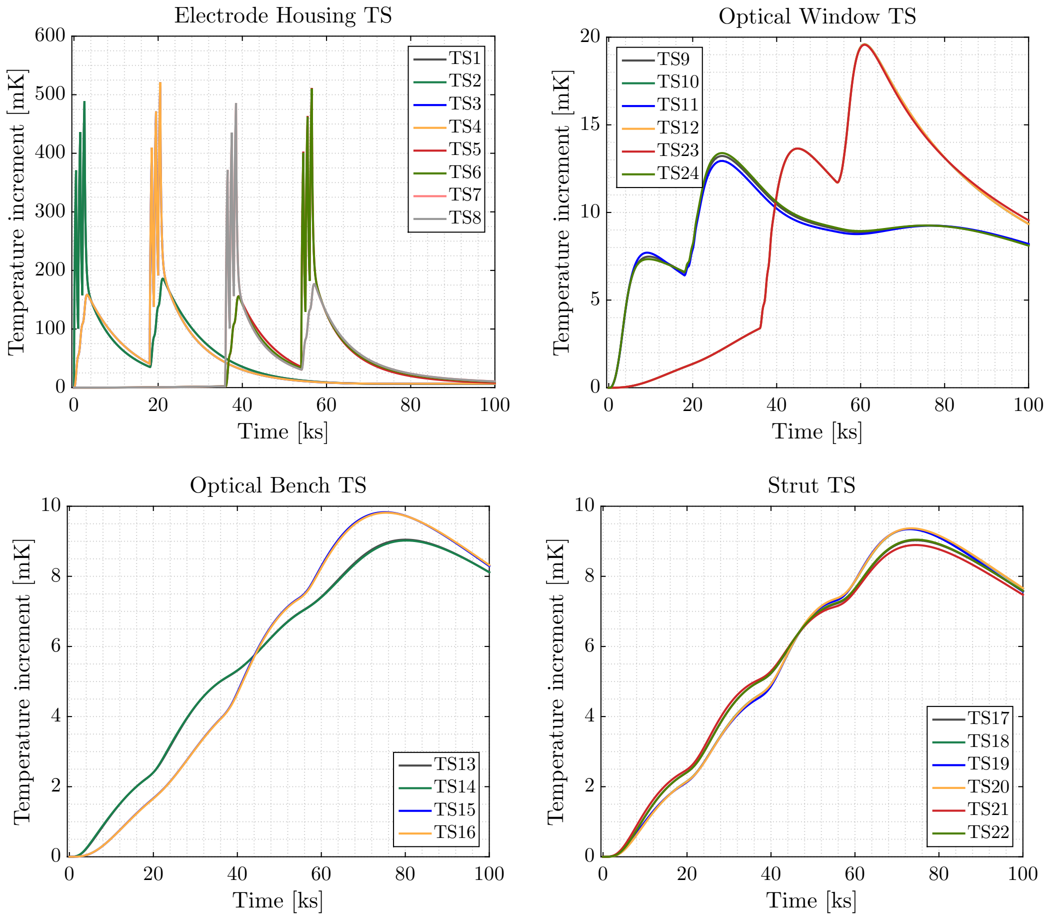

Figure 3.4: Temperature responses at the different sensor locations to inputs in the Electrode Housing heaters. The order of activation of the heaters is H1, H2, H3, H4.

$$H_{h\to m}[z] = \sum_{k=1}^{N} \frac{a_{0,k}}{1 + b_{1,k}\, z^{-1}} \tag{3.13}$$

where $a_{0,k}$ and $b_{1,k}$ are the coefficients defining every digital filter (8 or 16 depending on the heater) while the coefficients $b_{0,k}$ in Equation A.12 are forced to be 1. Figure 3.7 shows the execution algorithm for each first order filter in Equation 3.13.

Temperature responses at the different spots are obtained by filtering in parallel the input heat signal with each of the first order filters in Equation 3.13. The final temperature increment is found by adding the contributions from all the active heaters during a given experiment, as

$$T_m[z] = \sum_{h=1}^{H} H_{h\to m}[z]\, P_h[z] \tag{3.14}$$

where H is the total number of activated heaters during the exercise and $P_h[z]$ the power applied to each heater. The diagram in Figure 3.8 shows the sequence to be applied for

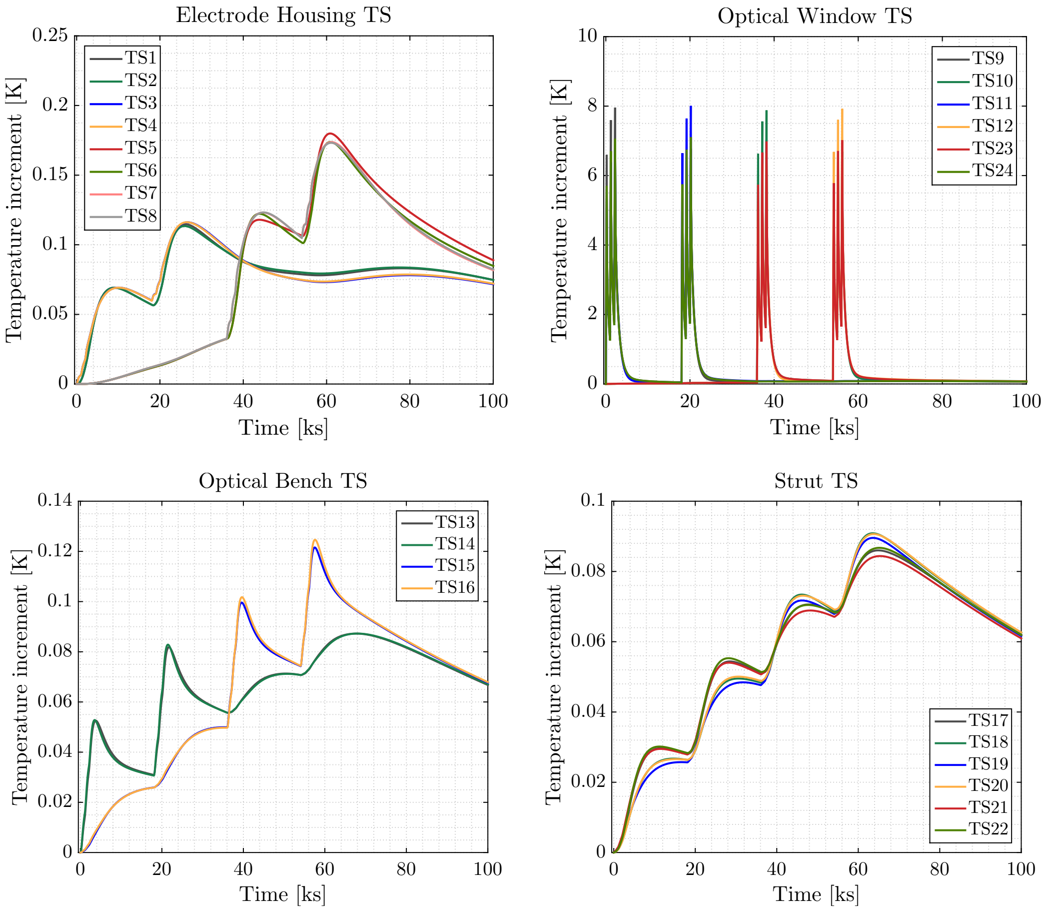

Figure 3.5: Temperature responses at the different sensor locations to inputs in the Optical Window heaters. The order of activation of the heaters is H9, H10, H11, H12.

each temperature increment.

3.2 Thermal model validation

The validation of the models implemented has been done through two test campaigns:

1. The Inertial Sensor Housing-Engineering Qualification Model (ISH-EQM) Thermal Correlation tests. In this campaign, series of heat telecommands were applied to the heaters in the Electrode Housing and in the Optical Window in a reduced setup.

2. The On-Station Thermal Test (OSTT), that included a nearly-complete version of the whole spacecraft. In this test, the strut heaters could be activated in an advanced level of satellite integration.

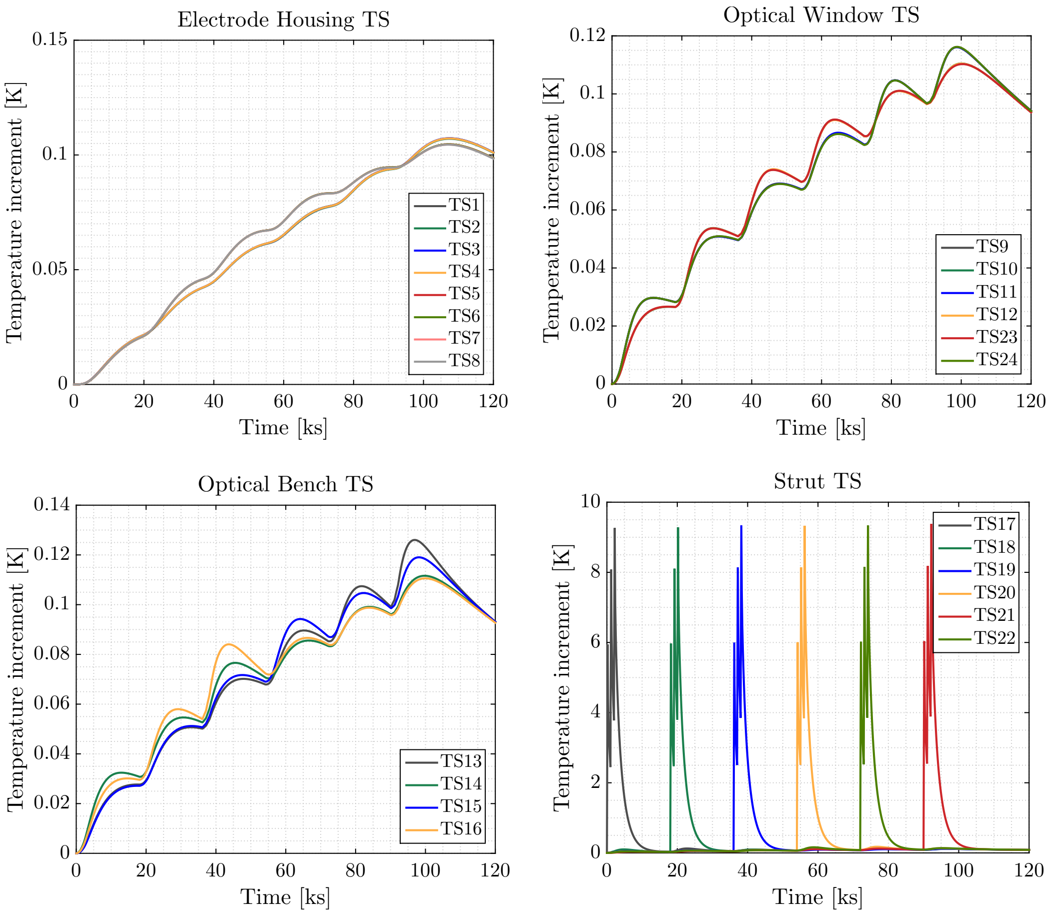

Figure 3.6: Temperature responses at the different sensor locations to inputs in the Strut heaters. The order of activation of the heaters is H9, H10, H11, H12, H13, H14.

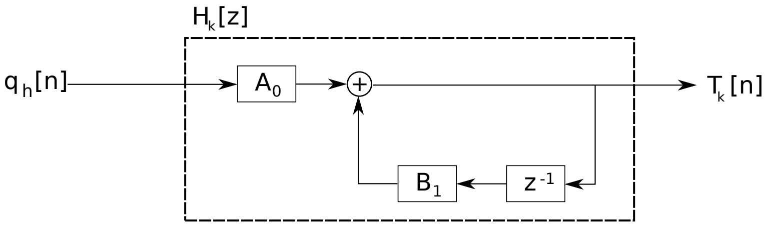

Figure 3.7: Single filter algorithm for each of the first order filters composing a partial fraction digital filter in the thermal model. 8 or 16 filters like this one are required to obtain a single temperature response.

Both tests are introduced in the following sections, where main results are reported and compared against the existing models.

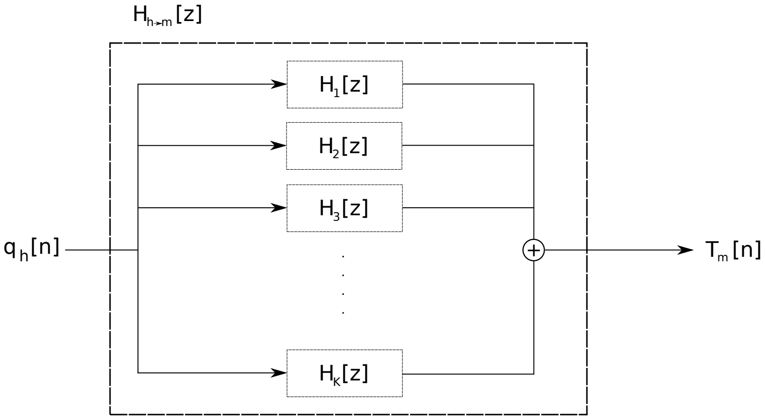

Figure 3.8: Filter process for each combination of heater h and temperature m. Each filter box $H_i[z]$ contains the specific filtering coefficients shown in Figure 3.7.

3.2.1 The Inertial Sensor Housing thermal correlation test

The Inertial Sensor Housing (ISH) thermal correlation tests took place at the facilities of Compagnia Generale per lo Spazio, former Carlo Gavazzi Space (CGS) in Tortona, Italy, during July and August 2013. The main objective of the campaign was to test the functionality of the different subsystems of the Inertial Sensor exposed to series of thermal cycles. The device used was the Engineering Qualification Model of one Inertial Sensor Housing after integration, which included a new version of the caging and grabbing mechanisms. Concerning the available thermal diagnostics items, the purpose was twofold:

1. Validate the telecommand execution of heater sequences on the Inertial Sensor and on the Optical Window.

2. Validate the thermal model of the Inertial Sensor Housing. In this test, this includes the sensors on the Electrode Housing and on the Optical Window.

The operative set of heaters and sensors available was that shown in Figure 3.10. This included a full set of heaters and sensors on one Optical Window and half of the items on the Electrode Housing. Such a setup was ideal to test the temperature response on the Optical Window, but allowed to heat and sense just half of the Electrode Housing, since the missing items on one full side prevented from measuring temperature gradients. Finally, the Electrical Ground Support Equipment (EGSE) was used to acquire the data from the DDS sensors and to command the heating sequences. It was composed of the Enginerring Model-1 of the DMU and of a PC running a minimal onboard simulation environment to control the DMU [109], properly configured to read out the OBC $<->$ DMU communications.

Some representative runs concerning the DDS heaters are summarized in Table 3.2 and shown in Figure 3.11. Since only one DAU (actually, the DAU2) was present, heaters

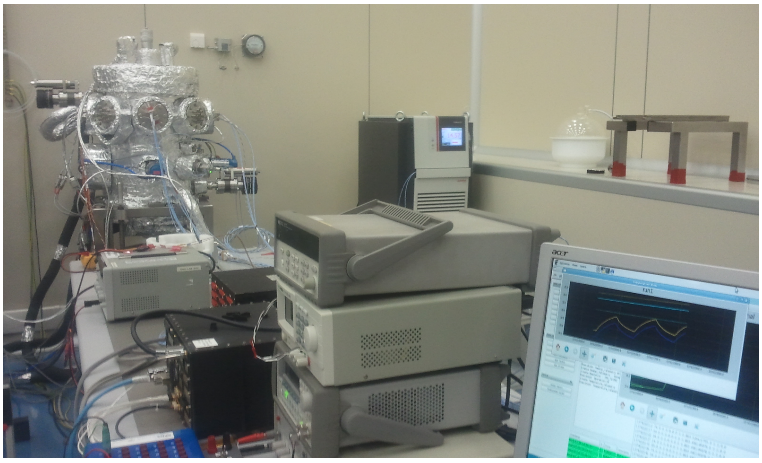

Figure 3.9: Experimental setup at the ISH-EQM during the thermal diagnostics tests at the CGS facilities in Tortona, Italy. The vacuum chamber containing the Inertial Sensor Housing was being monitored by one Engineering Model of the DMU. Some of the temperature measurements reported in Figure 3.11 are observed here being displayed in real time. Credits: CGS S.p.A.

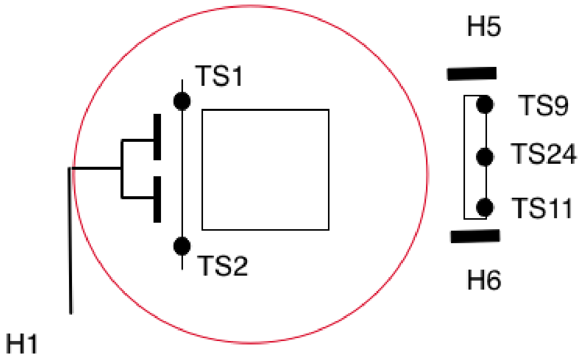

Figure 3.10: Schematic of the operative thermal diagnostics items during the ISH-EQM Thermal Correlation test.

H1 and H5 were rerouted to H2 and H8, respectively. Consequently, for the case of *Run 4*, it was unavoidable to multiplex when heat to two heaters was commanded.

The temperature responses in the Inertial Sensor were checked in *Runs* 1 and 2, reporting temperature increments around 430 mK and 105 K respectively, at the end of a pulses of 500 s and different power schemes. Both show fair enough consistency with the SSM, where the latter underestimates the measured value by just 12%. Indeed, the heating up due to H1 is pretty similar for both models and measurements despite some residual *high frequency* effects observed in *Run* 2, confirming a good agreement between the Electrode Housing thermal model and the real device.

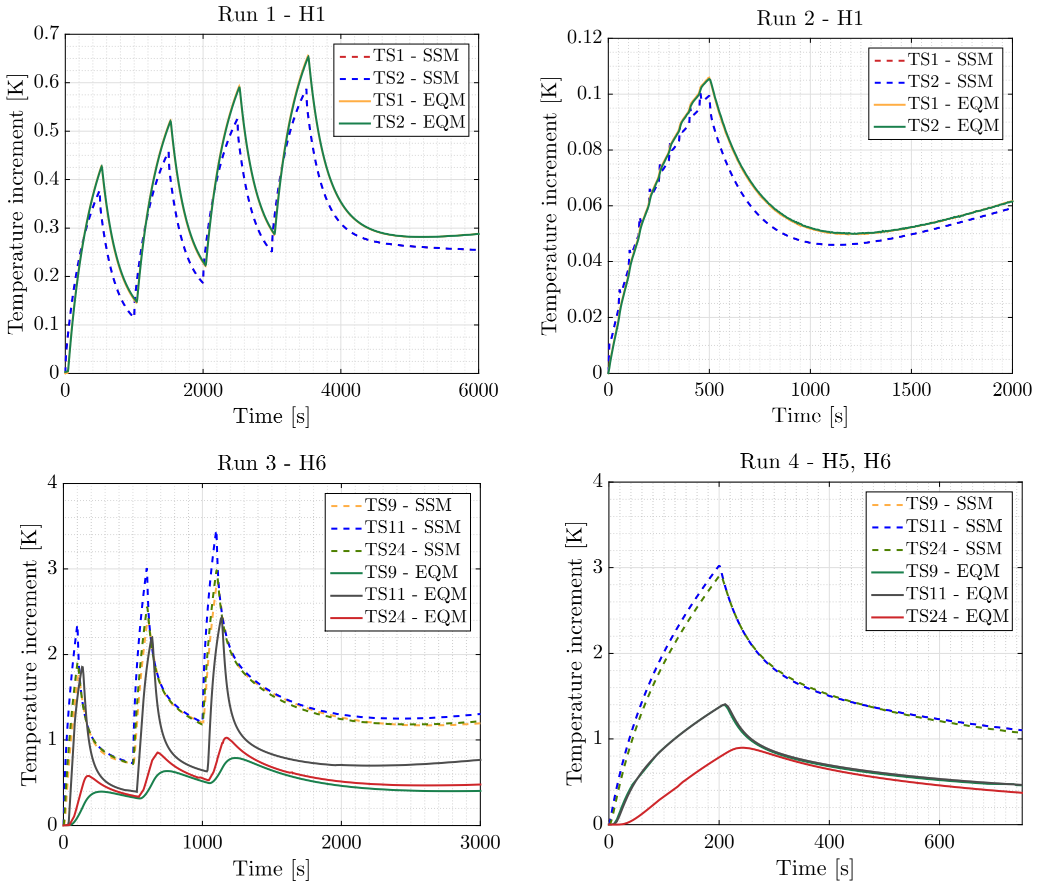

Figure 3.11: Temperature response for the different heater signals applied at the Inertial Sensor Housing test campaign (*continuous* lines), together with the equivalent thermal model expectations simulated by means of SSM objects (*dashed* lines). A linear slope has been removed to all the signals.

Run number	Active heater	Number cycles	Period [s]	Duty cycle	DC Power [mW]	Pulse Power [mW]	Phase	Dead Time [s]
1	H1	4	1000	50%	0	90	0	2000
2	H1	10	50	10%	20	40	0	2000
3	H6	3	500	20%	0	1000	0	2000
4	H5, H6	2	1000	20%	0	1000	0	–

Table 3.2: Commanding sequences applied during the ISH-EQM test campaign.

With respect to the heating of the Optical Window —*Runs* 3 and 4—, temperature increments of 1.8 K and 1.4 K are achieved at the sensors located close to the activated heaters. The effect of multiplexing is clearly observed in *Run* 4, where the same power is commanded but the amplitude achieved at, for example, $t = 100\,\mathrm{s}$ is approximately half of the power achieved at same point in *Run* 3. These plots also show the temperature response in the sensor TS24, located at the top of the Optical Window flange, far from the activated heaters. As observed in *Run* 4, at $t = 200\,\mathrm{s}$ the temperature increase of this sensor is around 60% of the temperature increment in the sensors TS9 and TS11, which are located close to the activated heaters. This difference of temperature increments at this point, of around 0.5 K, provides an idea of how long it takes to heat up the whole flange. Regarding the SSMs of the Optical Window, here the models clearly overestimate the temperature increments during multiplexing mode —see *Run* 4. Differences of up to a factor 4 with respect to TS9 and TS11 and up to a factor 8 with respect to TS24 are observed in this plot. Still, in *Run* 3 the agreement between the measured temperature in TS11 and the model seems quite realistic, though in this case the model also estimates a quite homogeneous heating of the flange, which is not observed in the measurements. Such a mismatch could be attributed to an inaccuracy of the model due to the low discretisation level applied in the modelling of these parts. Indeed, Figure 3.12 shows that the titanium flanges of each Optical Window are modelled by just 8 nodes and that the heaters and two of the sensors are actually linked to the same structural nodes.

3.2.2 Thermal model validation during the OSTT

The On-Station Thermal Test (OSTT) was an important milestone in the integration of the satellite. It took place late in 2011, when an advanced version of the satellite —namely the Thermo-Optical Qualification Model (TOQM)— was exposed to series of heat loads to test its performance at different temperatures. Since the spacecraft and the LCA were present with almost all of their flight model parts —excepting the Inertial Sensors—, and since the interferometer and most of the diagnostics items were operative, it was actually a precious platform where to test the strut experiments for the first time. Later on in this thesis, Chapter 6 provides a detailed description of the setup and the experiments carried out. For the purpose of this section, it is just fair focusing on the fact that the whole system was thermically equivalent to the real satellite. Therefore,

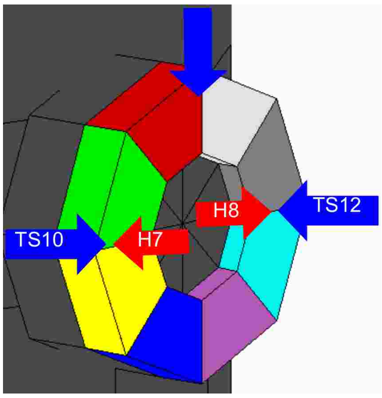

Figure 3.12: Discretisation of the OW2 in the thermal model [140]. Credits: CGS SpA.

the measured temperatures responses are of high interest and can be checked against the model.

Regarding the inputs, the applied heat signals were different combinations of struts heater activations. The two more relevant sequences in terms of thermal validation are reported here:

1. At an individual strut level, series of three pulses of 2 W at 1 mHz and a duty cycle of 20% are applied to each strut heater. The temperature response at each closest sensor was practically identical in all the struts, so only one case is plotted here —see Figure 3.13, where the temperature response in TS18 during the activation of H10 is shown. Temperature increments around 6–7 K are observed for both the model and the measurements, with about 20% of mismatch between them.

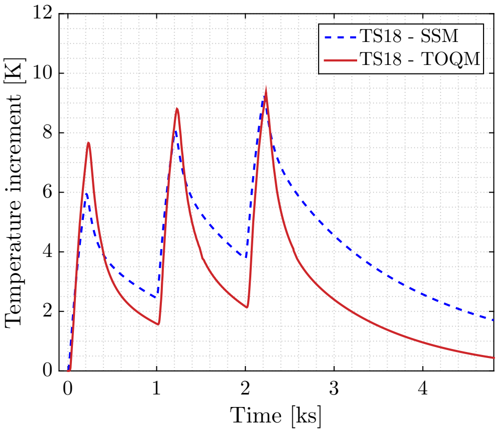

Figure 3.13: Temperature response of TS18 in front of a sequence of three pulses in H10. The period is 1 mHz with a duty cycle of 20% and a power of 2 W during the pulse.

2. Another case of interest is shown in Figure 3.14 (*left*), where a total effective power of 1 W is applied during 20 h to H9 and H11 to evaluate the long term heating of the system. Since both heaters belong to the same DAU, the multiplexing pattern is mandatory here requiring an actual commanded power of 2 W per heater. In this case, the total temperature increment in the model presents a deviation of 60% with respect to the measurements, though such a difference does not affect the band of interest. This sequence reported the dysfunction that can be observed in the closest view in Figure 3.14 (*right*). In effect, a zoom in the temperature readouts at TS17 and TS19 showed an irregular pattern, symmetric between the sensors, that lasted until the same command was resent ~50000 s later, after which the irregularity vanished. This issue, that actually raised a Non-Conformity Report, was extensively investigated in [143]. The fact that the time constants of the small exponential transients were similar to the time constant of the step response at the beginning of the whole sequence allowed to identify a feature in the multiplexing sequence. In phases of high stress in the DMU, this feature induced periodic delays in one of the heater transitions of the multiplexing scheme. As a result, repeated power deviations in the order of 1% from one heater to the other for periods of some minutes were enough to induce the observed ripples. This issue could be fixed in the following version of the application software.

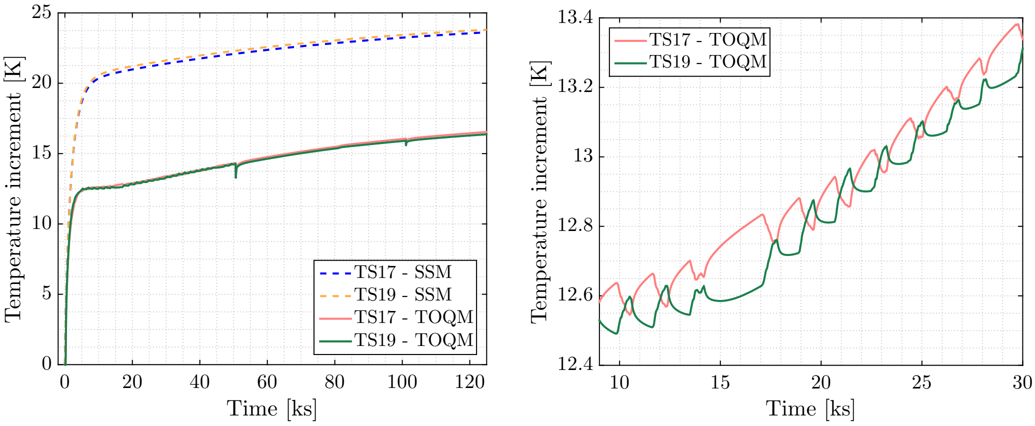

Figure 3.14: On the *left*, temperature response at sensors TS17 and TS19 in front of a heat pulse of 1 W. The predicted steady-state increment of temperature exceeds the measurement by 60%. On the *right*, a zoom on the feature observed, caused by repeated power deviations of ~1% from a heater to the other.

3.2.3 Validation test discussion

The SSMs reported here have shown a reasonable good agreement with the Electrode Housing and the strut heaters in the bandwidth of interest. For the particular case of the struts, the response out of band presents a significant deviation from the measurements that must be taken into account to calibrate the model in future simulations.

Regarding the Optical Window, the measurements suggest that the thermal conductance across the window clamp is lower than expected by the model. Such a feature can be attributed to the low discretisation level of the Optical Window itself or to the redesign of some parts of the Inertial Sensor during the last development stages, which have not yet been included into the model —the version of the thermal model used dates 2010. These redesigns could also affect the thermal behaviour of the Electrode Housing. Hopefully, an updated version of the thermal model is going to be implemented before temperature experiments take place onboard.

Moreover, as previously mentioned none of the measurements was carried out with the complete flight model satellite, so some of the discrepancies could be attributed to differences between the SSM system and the different setups.

Finally, not all the desired heat links could be tested due to project constraints. Indeed, the cross-heating test in the Electrode Housing that could have reported important information of expected temperature gradients inside the Electrode Housing has not yet been tested with flight model parts. In any case, the chance of applying some test cases during the flight commissioning phase may report substantial information in order to refine the optimal heat amounts to be applied in the experiments.

3.3 A model for the thermal effects

The main aim of this block is to simulate the expected forces and torques on all the axes of the Test Masses induced by the presence of asymmetric temperature distributions inside the Electrode Housing. In first place, it is necessary to discretise the inner surfaces in a grid of nodes able to represent differences in temperature distributions on a same wall of the Electrode Housing. Eventual temperature differences between opposed subsets of temperature nodes composing this new discretisation —named *facets* from now on— can be understood as thermal gradients, so individual force contributions between them can then be calculated. Nevertheless, such a procedure requires to previously define a radiative model to account for the interactions of each thermal effect and the system geometry.

3.3.1 Radiative model

First of all, the evaluation of the different thermal effects between areas at different temperatures must be done at a level smaller than the size of a surface from the Test Mass, otherwise it would be no option to calculate torques. In consequence, it is required to divide the mass surfaces into more than one subsection where to compute the different force contributions and obtain the final torque from the differences between the non-centred global force contributions.

Secondly, in order to model radiation reflection effects in the Electrode Housing it is necessary to develop a multi-reflection model for our specific system, detailing how reflections can take place and which is the amount of energy hitting one surface as a consequence of the reflection(s) from any other surface. Such treatment requires, in any case, to know how a given surface at a certain temperature interacts with another one.

Starting with the case of the radiation pressure propagation across a system, the energy rays moving across the inner walls of the Electrode Housing do not get totally absorbed in the impacting surface but most of it is reflected away. There are two models to describe this reflection effect:

- **Diffuse reflection**, when the energy from an incoming ray is distributed in all directions (Figure 3.15, *left*).
- **Specular reflection**, when the ray from an incoming direction is reflected into a single outgoing direction, as a perfect mirror. (Figure 3.15, *right*).

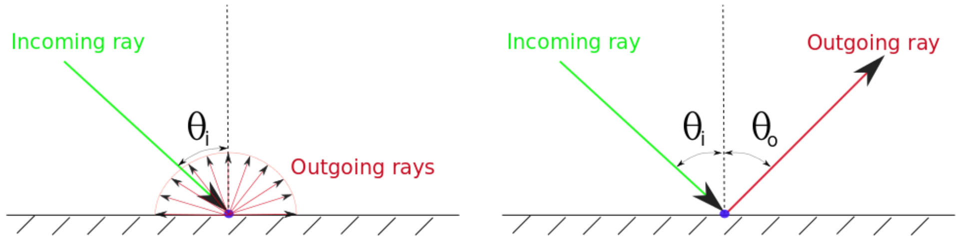

Figure 3.15: Types of reflections. *Left:* Example of diffuse reflection case. *Right:* Example of specular reflection, in this case $\theta_o = \theta_i$.

Real surfaces tend to present components of both types of reflections, and in all cases, part of the energy of the incoming ray is absorbed. The proportion of incoming energy reflected is defined by the different reflectivity coefficients, which depend on the surface material and is different for each type of reflection (diffuse or specular). The assumption of full diffuse reflection is adopted here for simplicity. Such an assumption strongly reduces the computation time since the routines do not need to keep memory of the direction of the incoming beam to calculate the outcoming beam. The surface reflection coefficients are introduced in Table 3.3.

Coefficient	Symbol	Value
Diffuse radiation reflectivity EH	$\rho^{D}_{\mathrm{RP,EH}}$	0.95
Diffuse radiation reflectivity TM	$\rho^{D}_{\mathrm{RP,TM}}$	0.98

Table 3.3: Surface reflectivity values considered in the model. The diffuse reflectivity of the Electrode Housing inner surfaces is an average between the inner walls made of molybdenum and the sapphire electrodes diffuse reflectivity.

3.3.1.1 Geometric elements

At this point it is worth reviewing some concepts extensively used in radiation heat transfer problems regarding the system geometry:

1. The **View Factors (VF)**, V_{ij}, which describe the proportion of radiation directly coming from a surface i and reaching another surface j.

2. The **Radiative Exchange Factors (REF)**, B_{ij}, which define the amount of energy coming from surface i being absorbed by surface j including any possible combination of bouncing and reflection.

These coefficients contain the information on how heat, and for extension energy, flows between surfaces and therefore how radiation pressure can be computed. In addition, the model must include the possibility of generating not only pressures but also shear forces on the Test Mass surfaces to account for the observations made in Trento with a torsion pendulum [120]. Such condition requires the calculation of all force contributions coming from the different surfaces in a *vectorial* way, so the different resulting components can be disentangled on each surface. In other words, we need a vectorial treatment for each Radiative Exchange Factor.

The expansion to the vectorial treatment of the geometric factors requires a previous introduction on how they are computed.

Vectorial view factors

The View Factor (VF) from a surface i to a surface j, V_{ij}, is defined as the fraction of radiation emitted from a surface i that directly hits another surface j, without reflecting at any other surrounding surface. Consequently, view factors are determined only by the geometry of the system, and they do not depend on the optical properties of the different surfaces. The identity $A_i V_{ij} = A_j V_{ji}$ is always applicable (where A_i is the area of surface i). Programs like ESATAN calculate the view factors through Ray-Tracing Monte Carlo techniques [144], where view factors from a specific surface are obtained by emitting particles in random directions and statistically assessing the number of particles received at the other surfaces.

Furthermore, since the aim is to calculate as well the direction of the forces on each Test Mass, we must consider the view factors in a vectorial way, where the norm of the vector is the value of the scalar view factor and its direction is that of an unitary vector $\bar{u}_{ij}$ coming from the centre of surface i to the centre of surface j [145]:

$$\bar{V}_{ij} = V_{ij}\bar{u}_{ij} \tag{3.15}$$

Though the Test Mass obviously moves in relation with the Electrode Housing, its motion does not significantly modify its relative position. Since the Test Mass is expected to oscillate with amplitudes $<<$ 1 mm while the gap between the mass and the Electrode Housing is of the order of mm, the assumption of constant view factors is applied, avoiding the need to recalculate the view factors at each iteration.

Radiative Exchange Factors

The Radiative Exchange Factor (REF) from a surface *i* to a surface *j*, B_{ij}, is defined as the fraction of energy emitted by a surface *i* that is finally absorbed at a surface *j*, including potential multi-reflections, i.e:

$$B_{ij} = \frac{q^{\text{absorbed at } j \text{ from } i}}{q^{\text{emitted at } i}} \tag{3.16}$$

and it only depends on the system geometry and the optical properties of its surfaces.

The main point concerning Radiative Exchange Factors (REFs) is that they provide information of the different paths (either direct or involving multi-reflection) that *emitted* energy from a surface follows before getting absorbed on another surface. Since in our case the interest is not focused on the total *absorbed* energy on a surface but on the total *incident* energy on a surface, the final coefficient that is going to be used is the quotient between the different REFs and their absorption coefficient of the *final* surface.

3.3.1.2 Vectorial REFs for the radiation pressure effect

ESATAN software computes REFs through two different methods, the matrix method [144, 146] and the Monte Carlo method [144]. However, they all provide *scalar* values and not their *vectorial* amount as it is required here. In addition, since individual vectors pointing to a same surface may come from different directions as shown in Figure 3.16, the final vectorial REF will usually present partial cancellation of the shear components, what is defined here as *vector cancellation*. Both effects are not considered by the available software. Fortunately, REFs can be alternatively calculated following a variation of Gebhart's Method [147]. From [144], scalar REFs are expressed as

$$B_{ij} = \varepsilon_j V_{ij} + \sum_{n}^{N_S} V_{in} \rho_n^D B_{nj} \tag{3.17}$$

where

- B_{ij} is the REF from surface *i* to surface *j*.
- ε_j is the emissivity of surface *j*, under Kirchoff's law of thermal radiation ($\alpha = \varepsilon$).
- V_{ij} is the View Factor from surface *i* to surface *j*.
- N_S is the total number of surfaces in the system.
- ρ_n^D is the diffuse reflectivity coefficient of surface *n*.

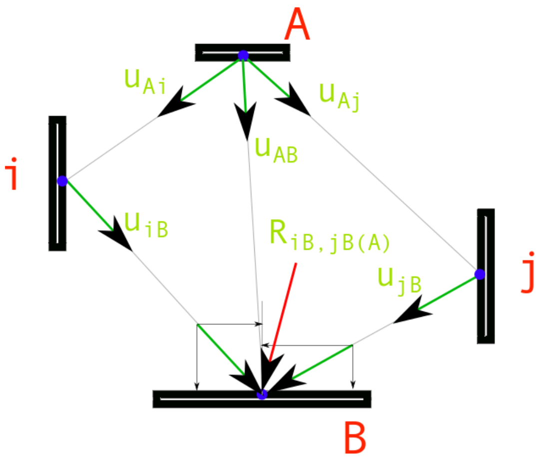

Figure 3.16: Example of vector cancellation in vectorial REFs. Shear components of vectors u_{iB} and u_{jB} are reduced by *vector cancellation*, as some of the components of the incoming vectors from surfaces i and j present opposite directions. Vector $R_{iB,jB(A)}$ shows approximately the resulting direction of the addition of the reflections from i and j.

This expression is solved with[1]:

$$\mathbf{B} = \left(\mathbf{I} - \mathbf{V}_\rho\right)^{-1} \mathbf{V}_\varepsilon \tag{3.19}$$

where **I** is the identity matrix and V_ρ and V_ε are two matrices whose components are defined as $V_{\rho,ij} = \rho_j V_{ij}$ and $V_{\varepsilon,ij} = \varepsilon_j V_{ij}$.

In order to clarify the notation, Equation 3.19 is extended here:

$$\mathbf{B} = \begin{pmatrix} B_{11} & \cdots & B_{1N} \\ \vdots & \ddots & \vdots \\ B_{N1} & \cdots & B_{NN} \end{pmatrix} = \begin{pmatrix} 1 - V_{11}\rho_1 & \cdots & -V_{1N}\rho_N \\ \vdots & \ddots & \vdots \\ -V_{N1}\rho_1 & \cdots & 1 - V_{NN}\rho_N \end{pmatrix}^{-1} \begin{pmatrix} V_{11}\varepsilon_1 & \cdots & V_{1N}\varepsilon_N \\ \vdots & \ddots & \vdots \\ V_{N1}\varepsilon_1 & \cdots & V_{NN}\varepsilon_N \end{pmatrix} \tag{3.20}$$

This procedure followed for the determination of scalar REFs is also extensible to vectorial REFs, always under the assumption of diffuse reflectivity. Vectorial REFs can

---

[1] This expression can also be written as

$$\mathbf{B} = \left(1 + \mathbf{V}_\rho + \mathbf{V}_\rho^2 + \mathbf{V}_\rho^3 + \ldots + \mathbf{V}_\rho^k\right) \mathbf{V}_\varepsilon \tag{3.18}$$

where k is the total number of reflections considered.

be written as

$$\bar{B}_{ij} = \varepsilon_j \bar{V}_{ij} + \sum_{n}^{N_S} V_{in} \rho_n^D \bar{B}_{nj} \tag{3.21}$$

where the only difference with the scalar Equation 3.17 is that $\bar{B}_{ij}$ is the vectorial REF from surface *i* to surface *j*, and V_{in} is the scalar View Factor from surface *i* to surface *n*.

Now, the solutions is expressed as

$$\bar{\mathbf{B}} = \left(\mathbf{I} - \mathbf{V}_\rho\right)^{-1} \bar{\mathbf{V}}_\varepsilon \tag{3.22}$$

where **I** is again the identity matrix, $\mathbf{V}_\rho$ is the same from Equation 3.19 and $\bar{\mathbf{V}}_\varepsilon$ is here a matrix of vectors defined as $\bar{V}_{\varepsilon,\,ij} = \varepsilon_j \bar{V}_{ij}$.

Expanding the expression as in the scalar case,

$$\bar{\mathbf{B}} = \begin{pmatrix} 1 - V_{11}\rho_1 & \cdots & -V_{1N}\rho_N \\ \vdots & \ddots & \vdots \\ -V_{N1}\rho_1 & \cdots & 1 - V_{NN}\rho_N \end{pmatrix}^{-1} \begin{pmatrix} \bar{V}_{11}\varepsilon_1 & \cdots & \bar{V}_{1N}\varepsilon_N \\ \vdots & \ddots & \vdots \\ \bar{V}_{N1}\varepsilon_1 & \cdots & \bar{V}_{NN}\varepsilon_N \end{pmatrix} \tag{3.23}$$

For each *vectorial* component:

$$\mathbf{B}_x = \begin{pmatrix} 1 - V_{11}\rho_1 & \cdots & -V_{1N}\rho_N \\ \vdots & \ddots & \vdots \\ -V_{N1}\rho_1 & \cdots & 1 - V_{NN}\rho_N \end{pmatrix}^{-1} \begin{pmatrix} V_{x,\,11}\varepsilon_1 & \cdots & V_{x,\,1N}\varepsilon_N \\ \vdots & \ddots & \vdots \\ V_{x,\,N1}\varepsilon_1 & \cdots & V_{x,\,NN}\varepsilon_N \end{pmatrix} \tag{3.24}$$

$$\mathbf{B}_y = \begin{pmatrix} 1 - V_{11}\rho_1 & \cdots & -V_{1N}\rho_N \\ \vdots & \ddots & \vdots \\ -V_{N1}\rho_1 & \cdots & 1 - V_{NN}\rho_N \end{pmatrix}^{-1} \begin{pmatrix} V_{y,\,11}\varepsilon_1 & \cdots & V_{y,\,1N}\varepsilon_N \\ \vdots & \ddots & \vdots \\ V_{y,\,N1}\varepsilon_1 & \cdots & V_{y,\,NN}\varepsilon_N \end{pmatrix} \tag{3.25}$$

$$\mathbf{B}_z = \begin{pmatrix} 1 - V_{11}\rho_1 & \cdots & -V_{1N}\rho_N \\ \vdots & \ddots & \vdots \\ -V_{N1}\rho_1 & \cdots & 1 - V_{NN}\rho_N \end{pmatrix}^{-1} \begin{pmatrix} V_{z,\,11}\varepsilon_1 & \cdots & V_{z,\,1N}\varepsilon_N \\ \vdots & \ddots & \vdots \\ V_{z,\,N1}\varepsilon_1 & \cdots & V_{z,\,NN}\varepsilon_N \end{pmatrix} \tag{3.26}$$

where $V_{x,\,ij}$, $V_{y,\,ij}$ and $V_{z,\,ij}$ are the respective three components of $\bar{V}_{ij}$.

3.3.1.3 Extension to Radiometer and Outgassing effects

In the previous section, a formalism to compute multi-reflection contributions for the radiation pressure has been introduced. The next step here is to adapt it to the remaining thermal effects in the Electrode Housing. The basic assumptions that we need to adopt to include them in our current framework are the following:

1. View Factors between surfaces computed by ESATAN are applicable to radiometer and outgassing effects.
2. The diffusive reflection approximation applies to the radiometer (RM) and asymmetric outgassing (OG) effects, as well as to radiation pressure (RP).

Under the previous assumptions, we can describe radiometer and asymmetric outgassing effects with three parameters analogous to the radiation pressure ones:

Absorption/Adsorption[2]: $\alpha^{\mathrm{RP}} \to \alpha^{\mathrm{OG}}, \alpha^{\mathrm{RM}}$

Emission: $\varepsilon^{\mathrm{RP}} \to \varepsilon^{\mathrm{OG}}, \varepsilon^{\mathrm{RM}}$

Reflection: $\rho^{\mathrm{RP}} \to \rho^{\mathrm{OG}}, \rho^{\mathrm{RM}}$

This will allow us to write down three equivalent expressions for the three effects. However, to keep in mind that we extended an approach originally thought for radiation to effects were gas molecules are involved, we will name the resulting values as Generic Exchange Factors (GEFs), G_{ij}, instead of REFs, B_{ij}. Thus, according to the previous assumptions, the equations for the radiation pressure, the radiometer effect and the outgassing are:

$$
\begin{aligned}
\bar{B}_{ij}^{\mathrm{RP}} &= \varepsilon_j^{\mathrm{RP}} \bar{V}_{ij} + \sum_n^N V_{in} \rho_n^{\mathrm{RP}} \bar{B}_{nj}^{\mathrm{RP}} && (3.27)\\
\bar{G}_{ij}^{\mathrm{RM}} &= \varepsilon_j^{\mathrm{RM}} \bar{V}_{ij} + \sum_n^N V_{in} \rho_n^{\mathrm{RM}} \bar{G}_{nj}^{\mathrm{RM}} && (3.28)\\
\bar{G}_{ij}^{\mathrm{OG}} &= \varepsilon_j^{\mathrm{OG}} \bar{V}_{ij} + \sum_n^N V_{in} \rho_n^{\mathrm{OG}} \bar{G}_{nj}^{\mathrm{OG}} && (3.29)
\end{aligned}
$$

where ρ and ε refer respectively to reflectivity and emissivity for the different effects.

The previous expressions can be rewritten as

$$
\bar{\mathbf{B}}^{\mathrm{RP}} = \left(\mathbf{I} - \mathbf{V}_\rho^{\mathrm{RP}}\right)^{-1} \bar{\mathbf{V}}_\varepsilon^{\mathrm{RP}} \tag{3.30}
$$

---

[2] Notice that we need to consider α^{OG}, α^{RM} as *adsorption coefficients*, since molecules are *adsorbed* (not absorbed) by surfaces.

$$\bar{\mathbf{G}}^{\mathrm{RM}} = \left(\mathbf{I} - \mathbf{V}_{\rho}^{\mathrm{RM}}\right)^{-1} \bar{\mathbf{V}}_{\varepsilon}^{\mathrm{RM}} \tag{3.31}$$

$$\bar{\mathbf{G}}^{\mathrm{OG}} = \left(\mathbf{I} - \mathbf{V}_{\rho}^{\mathrm{OG}}\right)^{-1} \bar{\mathbf{V}}_{\varepsilon}^{\mathrm{OG}} \tag{3.32}$$

where

$$V_{\rho,ij}^{\mathrm{RP}} = \rho_j^{\mathrm{RP}} V_{ij} \tag{3.33}$$

$$\bar{V}_{\varepsilon,ij}^{\mathrm{RP}} = \varepsilon_j^{\mathrm{RP}} \bar{V}_{ij} \tag{3.34}$$

$$V_{\rho,ij}^{\mathrm{RM}} = \rho_j^{\mathrm{RM}} V_{ij} \tag{3.35}$$

$$\bar{V}_{\varepsilon,ij}^{\mathrm{RM}} = \varepsilon_j^{\mathrm{RM}} \bar{V}_{ij} \tag{3.36}$$

$$V_{\rho,ij}^{\mathrm{OG}} = \rho_j^{\mathrm{OG}} V_{ij} \tag{3.37}$$

$$\bar{V}_{\varepsilon,ij}^{\mathrm{OG}} = \varepsilon_j^{\mathrm{OG}} \bar{V}_{ij} \tag{3.38}$$

3.3.1.4 System discretisation

The EH-TM inner cavity is composed by a cube of 46 mm-side for the Test Mass and a parallelepiped of 55.4 × 55.4 × 52.7 mm representing the Electrode Housing. The mass is supposed to be centred in the middle of the Electrode Housing. The vectorial geometric factors defined —both REFs and GEFs— need to be applied in a proper discretisation of this system to allow a correct computation of the different surface-to-surface calculation of the thermal effects. Such a discretisation must fulfil as well some requirements regarding the simulation of thermal forces and torques:

1. Non-centered forces on the Test Mass must be possible to compute in order to simulate eventual torques.
2. The Electrode Housing discretisation must allow representing asymmetric distributions of temperatures on a same surface.
3. The *real* temperature at different spots on the same facet of a discretised surface should not vary within a reasonable small margin in order to apply the assumption of isothermal facets.

From (1), a minimum number of 4 facets per TM surface is found. The same minimum number is ascertained for inner walls of the Electrode Housing. Though the discretisation of the ESATAN thermal model contains approximately 30 nodes per Electrode Housing surface, such a level of detail is not necessary for our model. In consequence, the discretisation of the system into 48 facets as shown in Figure 3.17 is adopted. Such a discretisation leaves temperature differences smaller than ≈3 mK between adjacent thermal nodes in a same facet in front of an input signal like the ones in Section 3.1.2.2 [145]. The notation considered is represented in Figure 3.17. Both EH1 and EH2 follow an identical discretisation.

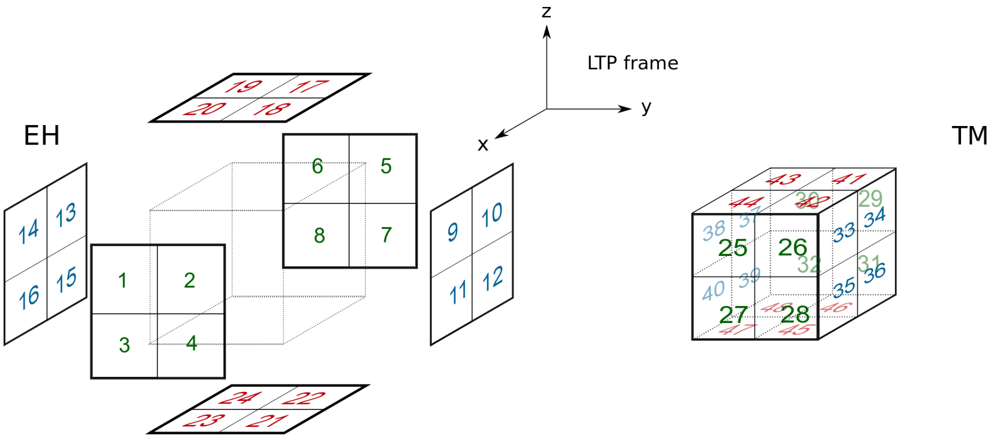

Figure 3.17: Discretisation considered for the temperature distribution in the inner faces of the Electrode Housing (exploded view, *left*) and on the Test Mass (*right*) with the numeration of the facets.

In the Electrode Housings, the temperature of each facet is determined by a representative selection of ESATAN thermal nodes inside, actually all the nodes characterizing the electrodes. Their averaged temperature is therefore the temperature associated to each facet, as shown in Figure 3.18 [145].

Regarding the Test Mass, the assumption of isothermal surfaces for all the parts is adopted here. This is accepted due to its low thermal coupling with the Electrode Housing —just by radiation— that implies a transient time much longer than its thermalisation time. Such a strong assumption is also of high convenience since it notably simplifies the algorithm.

The calculation of the REFs and GEFs between all the possible combinations of pairs of facets starts with the computation of the unit vector linking the centres of pressure of each combination of facets, which can be considered to be the geometric centres or centroids of the facets. As it is assumed that both Electrode Housings have identical geometries, this leads to the elaboration of a single matrix of $48 \times 48 = 2304$ vectors. However, some pairs of facets present partial visibility and their vectorial view factor need to be recalculated taking into account the unit vectors between the centres of pressures of their fractions with total visibility, as shown in Figure 3.19. Other more complicated pairs of facets, as for example the case of two perpendicular, adjacent Electrode Housing facets are more difficult to approximate since the pair of *subfacets* with total visibility is not so evident. However, these cases only appear between Electrode Housing facets, and fortunately we are just interested in vectors pointing to facets of the Test Masses.

3.3.1.5 Single facet-to-facet force contribution

The equations for the forces between each pair of facets pointing to a facet in the Electrode Housing shown below are the same expressions presented in Section 2.1.1 but including now the new development for the vectorial treatment between facets. The implementation presented here models the geometrical factors of the radiometer and the

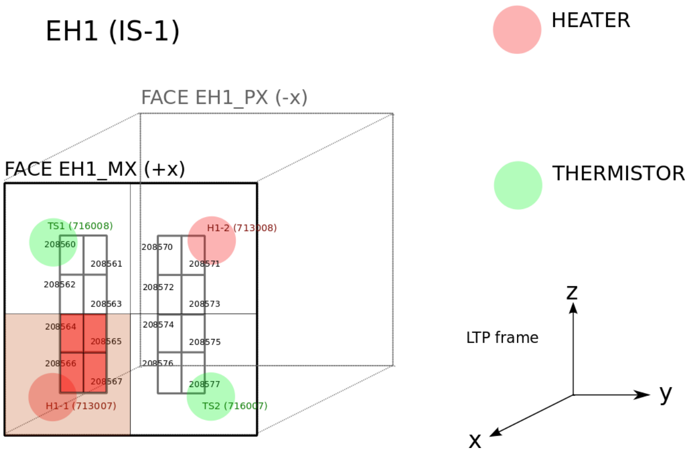

Figure 3.18: Example of a surface partition or *facet* and its representative nodes. The temperature of each facet is considered to be the average of temperatures of its representative nodes.

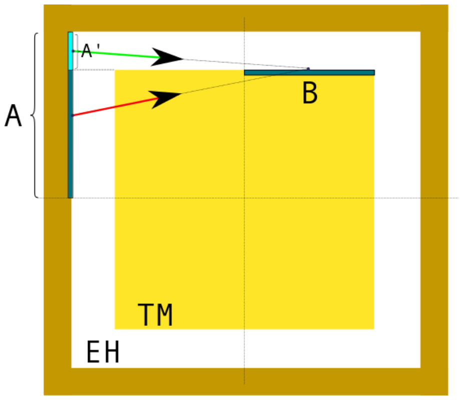

Figure 3.19: Example of corrections to the vectorial view factors. The unit vector associated to the View Factor V_{AB} would initially be defined by the direction between the geometric centres of facets A and B, but since there is an obstacle between the geometric centres of both facets —the Test Mass itself— the associated unit vector must be defined according to the geometric centres of the subsections A' and B. Roughly, the *red* vector must be replaced by the *green* vector when defining the vectorial view factor V_{AB}.

outgassing effects in a similar way as the radiation pressure, i.e. accounting for bouncing phenomena, visibility issues and expected shear effects.

Radiation pressure effect

The final expression of the vectorial *facet-to-facet* force contribution due to radiometer effect is

$$\bar{F}_{ij}^{\mathrm{RP}} = \frac{8}{3}\frac{\varepsilon_i A_j \sigma T^3}{c}\frac{\bar{B}_{ij}^{\mathrm{RP}}}{\varepsilon_j}\Delta T_{ij} \tag{3.39}$$

where the system geometry coefficient k_{RP} from Equation 2.8 is replaced by the quotient between the Radiative Exchange Factor $\bar{B}_{ij}^{\mathrm{RP}}$ and the emissivity ε_j, which can be considered as the amount of total heat flux hitting surface j including multi-reflections under the assumption of only diffuse reflections. The emissivity ε_j results from the Kirchoff's law of thermal radiation equivalence ($\alpha_j = \varepsilon_j$), while the emissivity ε_i of the emitting surface is also included to account for the emission efficiency with respect to an ideal black surface emission.

Radiometer effect

The final expression of the vectorial *facet-to-facet* force contribution due to radiometer effect is written as

$$\bar{F}_{ij}^{\mathrm{RM}} = \frac{1}{4}\frac{A_j p}{T}\frac{\bar{G}_{ij}^{\mathrm{RM}}}{\alpha_j^{\mathrm{RM}}}\Delta T_{ij} \tag{3.40}$$

where the geometric coefficient k_{RM} from Equation 2.14 is replaced by the relation $\bar{G}_{ij}^{\mathrm{RM}}/\alpha_j^{\mathrm{RM}}$, being $\bar{G}_{ij}^{\mathrm{RM}}$ an appropriate vectorial GEF parameter which contains information about the possible reflections under the assumption of only diffuse reflections. The parameter α_j^{RM} is an equivalent absorptivity to gather the amount of adsorbed molecules on surface j.

Outgassing effect

The *facet-to-facet* expression for the outgassing effect is

$$\bar{F}_{ij}^{\mathrm{OG}} = A_j \frac{Q_0 \Theta_{\mathrm{OG}} e^{-\frac{\Theta_{\mathrm{OG}}}{T_0}}}{C_{\mathrm{eff}} T_0^2}\frac{\bar{G}_{ij}^{\mathrm{OG}}}{\alpha_j^{\mathrm{OG}}}\Delta T_{ij} \tag{3.41}$$

where as in the radiometer case the geometric coefficient S_{ij}^{OG} from Equation 2.5 has been replaced by the relation $\bar{G}_{ij}^{\mathrm{OG}}/\alpha_j^{\mathrm{OG}}$, being $\bar{G}_{ij}^{\mathrm{OG}}$ a specific GEF and α_j^{OG} an equivalent adsorbity on surface j.

3.3.1.6 Total force computation

The total force at each axis, determined as the weighted addition of all the *facet-to-facet* force contributions, is expressed as

$$\bar{F} = \sum_{i}^{N_S} \sum_{j}^{N_{\mathrm{TM}}} \bar{F}_{ij}^{W} \tag{3.42}$$

where N_S is the total number of facets of the system, N_{TM} is the total number of TM facets and $\bar{F}_{ij}^{W}$ is the weighted facet-to-facet final force contribution that includes all the effects in a vector form.

These weighted forces are considered to introduce the possibility of distinguishing between pressure and shear forces for each thermal effect, and to cancel any of them if necessary. Therefore, the total force at each TM is calculated as

$$\begin{aligned}\bar{F}_{ij}^{W} = {} & w_n^{\mathrm{RM}}\left(\bar{F}_{ij}^{\mathrm{RM}} \cdot \bar{n}_j\right)\bar{n}_j + w_s^{\mathrm{RM}}\left(\bar{F}_{ij}^{\mathrm{RM}} - \left(\bar{F}_{ij}^{\mathrm{RM}} \cdot \bar{n}_j\right)\bar{n}_j\right) + \ldots \\ & \ldots + w_n^{\mathrm{RP}}\left(\bar{F}_{ij}^{\mathrm{RP}} \cdot \bar{n}_j\right)\bar{n}_j + w_s^{\mathrm{RP}}\left(\bar{F}_{ij}^{\mathrm{RP}} - \left(\bar{F}_{ij}^{\mathrm{RP}} \cdot \bar{n}_j\right)\bar{n}_j\right) + \ldots \\ & \ldots + w_n^{\mathrm{OG}}\left(\bar{F}_{ij}^{\mathrm{OG}} \cdot \bar{n}_j\right)\bar{n}_j + w_s^{\mathrm{OG}}\left(\bar{F}_{ij}^{\mathrm{OG}} - \left(\bar{F}_{ij}^{\mathrm{OG}} \cdot \bar{n}_j\right)\bar{n}_j\right)\end{aligned} \tag{3.43}$$

where

- w_n^{RM}, w_n^{RP}, w_n^{OG} are the weight coefficients corresponding to the normal components of each thermal effect force contribution.

- w_s^{RM}, w_s^{RP}, w_s^{OG} are the weight coefficients corresponding to the shear components of the force on the facet for each thermal effect force contribution.

- $\bar{F}_{ij}^{\mathrm{RM}}$, $\bar{F}_{ij}^{\mathrm{RP}}$, $\bar{F}_{ij}^{\mathrm{OG}}$ are each facet-to-facet force contribution of each thermal effect.

- $\bar{n}_j$ is the normal vector of each facet.

As can be observed from the last expression, the first term refers to all the *direct* or *normal* force contributions while the second term contains all the *shear* force contributions. The product "·" stands for the vector scalar (or dot) product.

3.3.1.7 Total torque computation

The total torque is determined directly by the addition of each torque contribution, obtained as

$$\bar{N} = \sum_{j}^{N_{\mathrm{TM}}} \left[\left(\sum_{i}^{N_S} \bar{F}_{ij}^{W}\right) \times \bar{d}_j\right] \tag{3.44}$$

where N_S, N_{TM} and F_{ij}^W have same meanings as seen in the previous section and $\bar{d}_j$ stands for the relative position of the centre of pressure of each facet j respect to the centre of masses of the Test Mass. The sign × stands here for the vector cross product. For more details of the model refer to [145].

3.3.2 Implementation into LTPDA

The scalar view factors have been calculated by the ESATAN radiative module after a proper discretisation of the inner surfaces of the EH-TM system. Following to that, the REFs and GEFs equations have been implemented in MATLAB®.

The coefficients required to compute forces and torques from temperature gradients are not time-dependent since they only depend on the system geometry and the surface properties. Therefore, at first glance there is no need to treat the forces and torques blocks as generic LTI systems. However, in practice, it is convenient to implement them into dedicated SSMs to facilitate its usage by the LTPDA simulator, though in any case their matrices A, B and C are just empty.

To summarize the whole process, the schematic of the algorithm is shown in Figure 3.20. The order of steps for a complete simulation is as follows:

1. Compute the actual applied power.
2. Compute the temperature responses at the sensor locations and inside the Electrode Housings.
3. Calculate the geometric factors (REFs and GEFs).
4. Compute the forces and torques on each Test Mass.

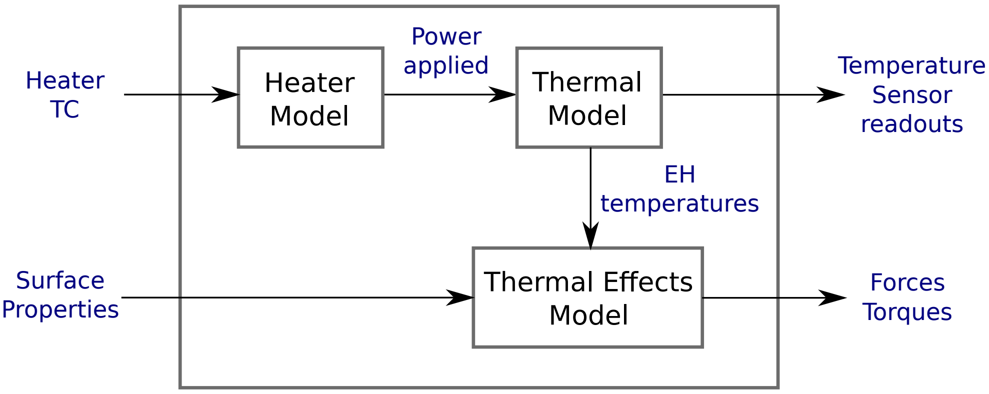

Figure 3.20: Block diagram of the algorithm to simulate forces and torques from the heater commands. Each block corresponds to an independent SSM that can be assembled to the other ones.

The dedicated models built are presented in Table 3.4.

Name	Description
`ssm_model_heater`	SSM of the real heat applied as a function of commanded heat.
`ssm_model_esatanTS`	SSM of the temperature responses on the TS locations due to real heat applied on the heaters.
`ssm_model_esatanEH`	SSM for the temperature responses on the EH facets due to real heat applied on the heaters.
`ssm_model_forcesAndTorques`	SSM of the forces and torques due to temperature gradients.
`ssm_model_TSdds`	SSM assembly to simulate temperature responses as function of commanded heat.
`ssm_model_EHdds`	SSM assembly to simulate forces and torques from commanded heat.

Table 3.4: SSMs developed in the LTPDA framework for the simulation of forces and torques on the Test Masses and temperature sensor readouts.

3.3.3 Model verification

A dedicated simulation is presented here in order to test the performance of the whole block. Figure 3.21 displays the temperature gradients in all the degrees of freedom (DOF) in front of a sequence of four pulses of 500 s and 90 mW —maximum power— applied alternatively to H1 and H2 at 1 mHz. The temperature gradients shown are obtained by averaging the temperature responses at each Electrode Housing wall and then computing the difference between averages. Since it is convenient that the sign of each temperature gradient keeps equal to the sign of the force or torque produced, the following convention is adopted for the translational degrees of freedom:

$$\Delta T_x = \frac{1}{4}\left(\sum_{i=1}^{4} T_{f_{i,-x}} - \sum_{i=1}^{4} T_{f_{i,+x}}\right) \tag{3.45}$$

$$\Delta T_y = \frac{1}{4}\left(\sum_{i=1}^{4} T_{f_{i,-y}} - \sum_{i=1}^{4} T_{f_{i,+y}}\right) \tag{3.46}$$

$$\Delta T_z = \frac{1}{4}\left(\sum_{i=1}^{4} T_{f_{i,-z}} - \sum_{i=1}^{4} T_{f_{i,+z}}\right) \tag{3.47}$$

where each $T_{f_{i,\pm q}}$ is the temperature of each of the four facets i on each $\pm q$ wall of the Electrode Housing, being q each translational degree of freedom x, y and z —see Figure 3.17. The rotational degrees of freedom are defined in a similar way, following the same convention:

$$\begin{aligned}\Delta T_\theta = &\frac{1}{2}\Big(\sum_{i=1}^{2} T_{f_i\,[-z,+y]} + \sum_{i=1}^{2} T_{f_i\,[+z,-y]} + \sum_{i=1}^{2} T_{f_i\,[+y,+z]} + \sum_{i=1}^{2} T_{f_i\,[-y,-z]} \\ &- \sum_{i=1}^{2} T_{f_i\,[-z,-y]} - \sum_{i=1}^{2} T_{f_i\,[+z,+y]} - \sum_{i=1}^{2} T_{f_i\,[+y,-z]} - \sum_{i=1}^{2} T_{f_i\,[-y,+z]}\Big)\end{aligned} \tag{3.48}$$

$$\begin{aligned}\Delta T_\eta = &\frac{1}{2}\Big(\sum_{i=1}^{2} T_{f_i\,[+x,-z]} + \sum_{i=1}^{2} T_{f_i\,[-x,+z]} + \sum_{i=1}^{2} T_{f_i\,[-z,-x]} + \sum_{i=1}^{2} T_{f_i\,[+z,+x]} \\ &- \sum_{i=1}^{2} T_{f_i\,[+x,+z]} - \sum_{i=1}^{2} T_{f_i\,[-x,-z]} - \sum_{i=1}^{2} T_{f_i\,[-z,+x]} - \sum_{i=1}^{2} T_{f_i\,[+z,-x]}\Big)\end{aligned} \tag{3.49}$$

$$\begin{aligned}\Delta T_\phi = &\frac{1}{2}\Big(\sum_{i=1}^{2} T_{f_i\,[+y,-x]} + \sum_{i=1}^{2} T_{f_i\,[-y,+x]} + \sum_{i=1}^{2} T_{f_i\,[+x,+y]} + \sum_{i=1}^{2} T_{f_i\,[-x,-y]} \\ &- \sum_{i=1}^{2} T_{f_i\,[+y,+x]} - \sum_{i=1}^{2} T_{f_i\,[-y,-x]} - \sum_{i=1}^{2} T_{f_i\,[+x,-y]} - \sum_{i=1}^{2} T_{f_i\,[-x,+y]}\Big)\end{aligned} \tag{3.50}$$

where $T_{f_i\,[\pm q,\pm p]}$ is the temperature of each of the two facets i located on the $\pm p$ side of the $\pm q$ wall of the Electrode Housing.

Back to Figure 3.21, ΔT_x is clearly dominated by the input signal, as expected. Regarding the other degrees of freedom, a notable gradient emerges along the z axis with a maximum difference of 80 mK which keeps increasing during the heater modulation. Meanwhile, the maximum temperature gradients achieved in the other degrees of freedom appear between 6000–9000 s after switching off the heater modulation and present maximum amplitudes below 10 mK.

For the case of ΔT_x, the reconstruction of the signal —by means of the simulated sensor readouts— has been added to the plot, showing a maximum difference between them of 45 mK. The temperature gradient measured by the sensors on the *external* walls of the Electrode Housing is approximately 15% larger than the temperature gradient on the electrodes inside. For sake of simplicity and to provide a better understanding of the temperature response in the Electrode Housing, the environmental noise has not been considered in these initial simulations. In the same way, the simulated temperature sensors do not include readout noise.

The induced forces and torques associated to these temperature gradients are simulated here with the parameters shown in Table 3.5. The results are presented in Figure 3.22, with the different contributions of each thermal effect disentangled. Notice from Table 3.5 that shear effects caused by the radiometer forces and by the radiation pressure have been considered, excluding any shear force from the outgassing effect. Temperature gradients in all the degrees of freedom contribute to the forces and torques on all the axes, with a clear incidence on the x axis. In this axes, a peak-to-peak force of 10 pN is observed, with the radiometer effect as the main contributor. In the z axis we observe an increasing force that achieves 2.5 pN at the end of the modulation. It is clearly proportional to the temperature gradient in z observed in Figure 3.21. Finally, the force on the y axis is much smaller and keeps below 0.1 pN during all the simulation. Since the expected resolution in the measurement of forces by the GRS is around tenths of pN at 1 mHz, the perturbations induced on the x and z axes could be observed, while the perturbation on y may remain unobservable. Regarding the torques, the effects are much more homogeneous with maximum increments below 1.2 fNm, but could still be unobserved since the expected resolution at 1 mHz is around 2.7 fNm.

3.4 Summary

In this chapter we have introduced a set of models that simulate the effects of applying heat signals to the diagnostics heaters in terms of:

- Temperature increments at different spots of interest of the LTP.
- Forces and torques on the Test Masses, induced by temperature gradients in all the degrees of freedom of the Electrode Housings.

An example case has been provided to show the effects of a simple heat modulation, while the thermal model used has been checked against data from different test campaigns.

The models presented in this chapter are intended to provide a support tool to assist the design of the different thermal experiments and to validate the heater activation telecommands before being sent to the satellite.

Nevertheless, due to the complexity of the systems concerned, their outputs need to be carefully evaluated. The validation of the thermal model through the thermal campaigns already spotted some important differences, that in some cases can achieve a

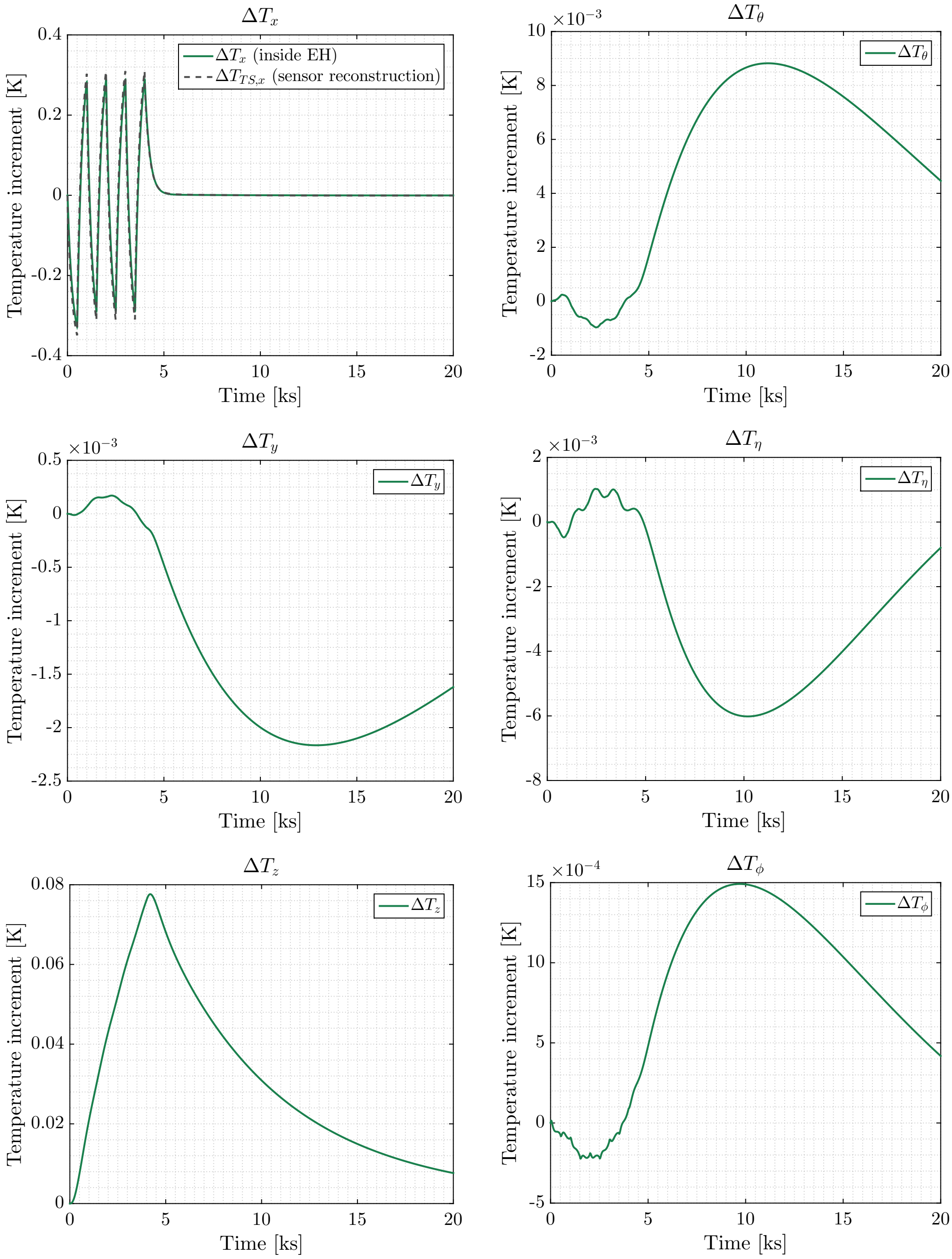

Figure 3.21: Simulation of the temperature gradients in all the degrees of freedom of the Electrode Housing. The input signal applied is a sequence of alternated pulses of 500 s and 90 mW to H1 and H2. A reconstruction of ΔT_x by means of the temperature sensor readouts is shown on the first plot (*dashed* line), with an amplitude excess of 15% of the amplitude inside. No environmental noise has been included in this simulation.

Parameter	Description	Value	Units
P	Pressure	10^{-5}	Pa
T_0	System temperature	293	K
Q_0	OG flow prefactor	$4.1e35$	$\mathrm{J\,s^{-1}}$
T_0	OG activation temperature	30000	K
$\rho_{\mathrm{D,RP,EH}}$	EH diffuse radiative reflectivity	0.95	–
$\rho_{\mathrm{D,RP,TM}}$	TM diffuse radiative reflectivity	0.98	–
$\rho_{\mathrm{D,RM,EH}}$	EH diffuse RM equivalent reflectivity	0.8	–
$\rho_{\mathrm{D,RM,TM}}$	TM diffuse RM equivalent reflectivity	0.8	–
$\rho_{\mathrm{OG,EH}}$	EH OG equivalent reflectivity	0	–
$\rho_{\mathrm{OG,TM}}$	TM OG equivalent reflectivity	0	–
$\varepsilon_{\mathrm{RP,EH}}$	EH radiative emissivity	0.05	–
$\varepsilon_{\mathrm{RP,TM}}$	TM radiative emissivity	0.02	–
$\varepsilon_{\mathrm{RM,EH}}$	EH RM equivalent emissivity	0.2	–
$\varepsilon_{\mathrm{RM,TM}}$	TM RM equivalent emissivity	0.2	–
$\varepsilon_{\mathrm{OG,EH}}$	EH OG equivalent emissivity	1	–
$\varepsilon_{\mathrm{OG,TM}}$	TM OG equivalent emissivity	1	–
$\alpha_{\mathrm{RM,EH}}$	EH RM equivalent absorptivity	0.2	–
$\alpha_{\mathrm{RM,TM}}$	TM RM equivalent absorptivity	0.2	–
$\alpha_{\mathrm{OG,EH}}$	EH OG equivalent absorptivity	1	–
$\alpha_{\mathrm{OG,TM}}$	TM OG equivalent absorptivity	1	–
$w_{\mathrm{RP,N}}$	RP normal component weight	1	–
$w_{\mathrm{RM,N}}$	RM normal component weight	1	–
$w_{\mathrm{OG,N}}$	OG normal component weight	1	–
$w_{\mathrm{RP,N}}$	RP shear component weight	1	–
$w_{\mathrm{RM,N}}$	RM shear component weight	1	–
$w_{\mathrm{OG,N}}$	OG shear component weight	0	–

Table 3.5: Table summarizing the parameters applied to the forces and torques block example test of Figure 3.22. Nominal values for the thermal effects have been selected, while the radiometer equivalent surface properties have been chosen so as the total contribution on x produces nominal effects.

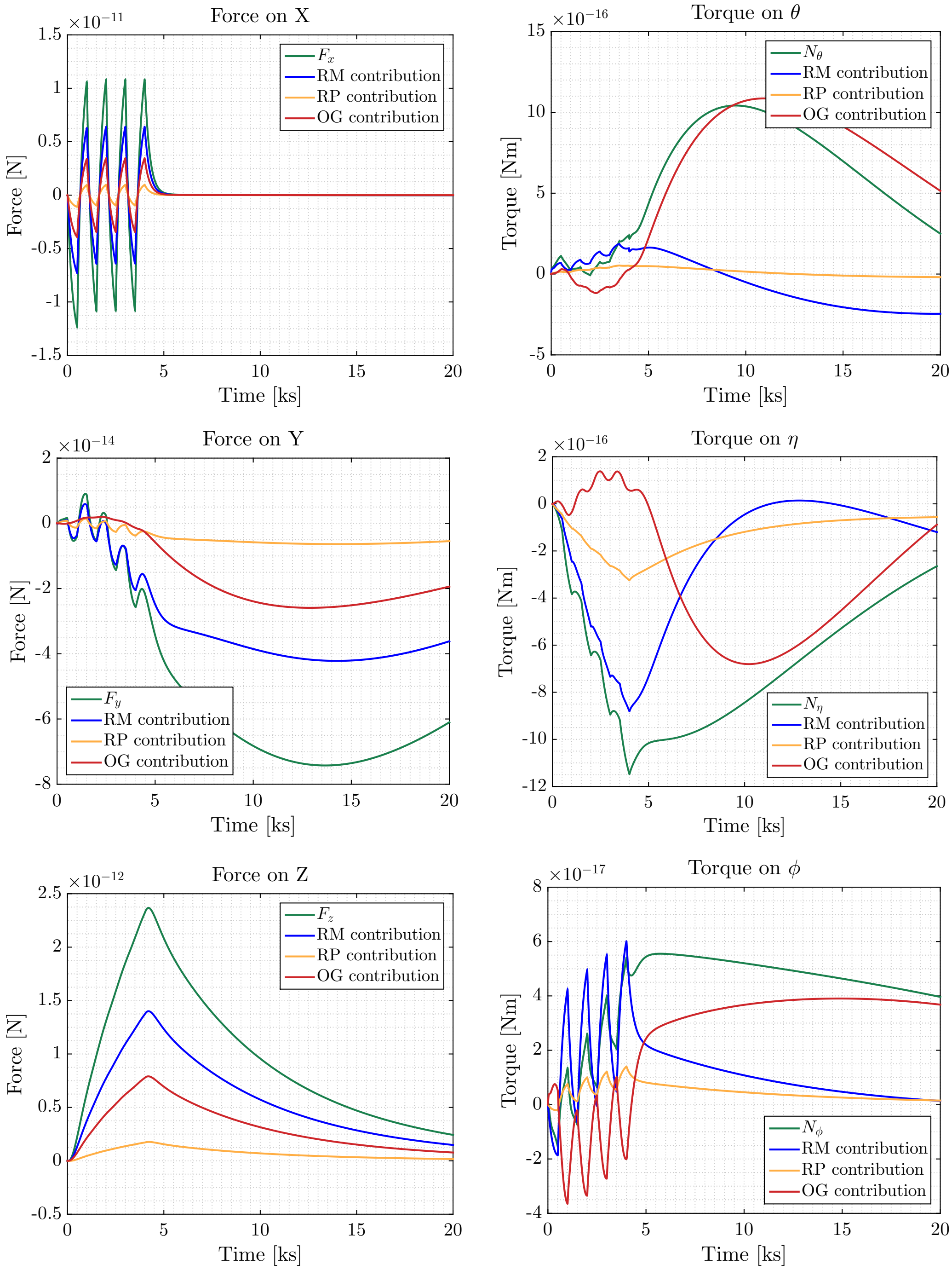

Figure 3.22: Force and torques on all the degrees of freedom of the EH. Neither environmental noise nor readout noise have been included in this simulation.

factor four with respect to the predicted amplitude. Still, the simulated temperature responses in the bandwidth of interest reasonably match all the measurements except for certain heat patterns applied to the Optical Windows.

Regarding the forces and torques block, no real validation can be done on-ground and only specific tests are available through torsion pendulum facilities. This kind of tests are assessed in Chapter 5 by means of a replica of the Electrode Housing installed in a torsion pendulum facility.

CHAPTER 4

Electrode Housing thermal experiment: design and simulation

The Electrode Housing thermal experiment is aimed to estimate the thermal couplings between temperature gradients in the Electrode Housing (EH) and direct forces on the Test Masses (TM). The definition of the heat signals requires a full understanding of the heat generation mechanism and how the heat transfers across the Electrode Housing system. It is also important to figure out the variety of possible scenarios and how environmental conditions like temperature and pressure noise can affect the experiment.

The procedure leading to the definition of the input signals needs to follow a series of steps: first, it is necessary to model the experiment and to extract the parameters of interest from the available measurements. In second place, an error analysis is required to derive a set of constraints needed to estimate the unknown parameters with the required precision. After that, the operational possibilities of the system are explored by means of the available simulators to finally derive proper input signals.

In this chapter, this procedure is followed leading to a final proposal of heat signal for the experiment. At the end, this same input signal is tested by means of the SSMs derived in Chapter 3.

4.1 Experiment concept

Due to the symmetry of the EH-TM system, the Electrode Housing thermal experiment is simplified to the measurement of the thermal-induced disturbances on the x axis. These perturbations are caused by the different thermal effects already introduced: the radiometer effect, the radiation pressure and the asymmetric outgassing. The heaters and sensors to carry out this experiment are located at the $\pm x$ external walls of the two Electrode Housings —see Figure 4.1.

The aim of this experiment is essentially double:

1. To measure the global couplings between thermal gradients on the x axis of the Electrode Housings and the differential channel x_{12} of the interferometer by applying heat signals that stress the different thermal perturbation mechanisms on the Inertial Sensors.
2. Disentangle the contributions of the different thermal effects from the global coupling. The only way to attempt such analysis is by taking advantage of the different temperature dependence of each thermal effect 2.1.1. This makes necessary to measure the variation of the thermal coupling in a sufficiently wide range

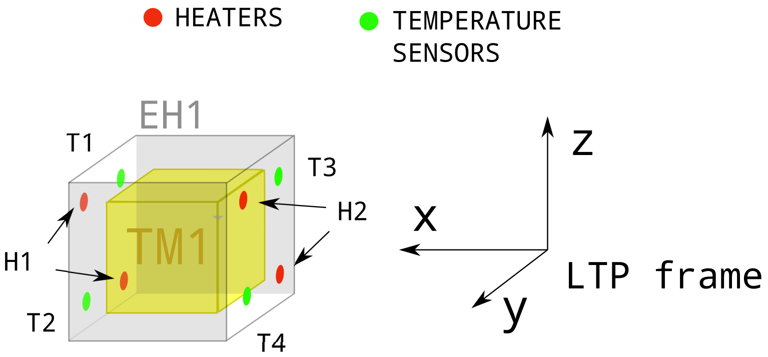

Figure 4.1: Heaters and sensors on the EH1. EH2 is equipped with an equivalent set —see Section 2.2.

of absolute temperatures. The purpose of this second goal is motivated by the need to estimate the pressure in the Electrode Housing cavity, as explained in Section 2.1.1.2.

The first point clearly demands a high Signal-to-Noise Ratio in the thermal perturbations induced to the interferometer. Since passive thermal systems behave as low pass filters, operating at low frequency bands is preferable in order to induce a ΔT signal as large as possible. Still, this approach requires an analysis of the cut-off frequencies of the model. In this sense, current predictions expect temperature noise below $\approx 10^{-4}\,\mathrm{K\,Hz^{-1/2}}$ around 1 mHz decreasing down to the sensing limit at $\approx 10^{-5}\,\mathrm{K\,Hz^{-1/2}}$ for frequencies higher than 10 mHz [108]. However, the real temperature noise shape cannot be fully tested on-ground and a nominal value of $10^{-4}\,\mathrm{K\,Hz^{-1/2}}$ along the whole band is assumed for design purposes [148].

4.2 Thermal coefficient measurement

The global thermal coefficient α along a given axis i is defined as

$$\alpha_i = \frac{F_i}{\Delta T_i} \tag{4.1}$$

where F_i is the applied force on the Test Mass along i axis and ΔT_i the temperature gradient on the same axis. For each Test Mass, temperature gradient signals are estimated from the readouts of the temperature sensor attached on the external walls of $\pm x$ faces of the Electrode Housing. Thus, for EH1 and EH2:

$$\Delta T_{x,\mathrm{EH1}} = \frac{T_3 + T_4 - T_1 - T_2}{2} \tag{4.2}$$

$$\Delta T_{x,\mathrm{EH2}} = \frac{T_5 + T_6 - T_7 - T_8}{2} \tag{4.3}$$

The criteria followed in both cases is that a positive temperature gradient must induce a positive force on the Test Mass.

In order to identify thermal forces amongst other kind of direct forces —like unavoidable magnetic forces or actuation forces—, the measurement of α is undertaken at a modulated frequency f_{mod}. A modulated temperature gradient signal is easily obtained by alternating the activation of the heaters on one side of the Electrode Housing with the activation of its opposed heaters at a certain f_{mod}.

The modulated amplitudes for both the force and the temperature gradient are recovered by demodulating the signals and applying a low pass filter to remove the high frequency components —for more details on this procedure refer to Appendix A. The quotient of the demodulated force over the demodulated temperature gradient provides one estimation of $\alpha_{f_{\mathrm{mod}}}$ per cycle. The final thermal coefficient $\alpha_{f_{\mathrm{mod}}}$ is computed by averaging the series of $\alpha_{f_{\mathrm{mod}}}$ coefficients for all the demodulated cycles. This is written as

$$\alpha_{f_{\mathrm{mod}}} = \frac{1}{N}\sum_{i}^{N}\left\{\frac{\mathrm{Im}\left(F_x[t_i]\,e^{j2\pi f_{\mathrm{mod}}(t_i - t_{\mathrm{delay},F})}\right)}{\mathrm{Im}\left(\Delta T_x[t_i]\,e^{j2\pi f_{\mathrm{mod}}(t_i - t_{\mathrm{delay},\Delta T})}\right)}\right\} \tag{4.4}$$

where $F_x[t_i]$ and $\Delta T_x[t_i]$ are the time series of N points of the estimated force on the x axis and the measured temperature gradient, respectively—the latter computed with Equation 4.2 or 4.3 depending on the heated Electrode Housing. Notice that either the delays $t_{\mathrm{delay},F}$ and $t_{\mathrm{delay},\Delta T}$ for the force and the temperature have been considered. The purpose of them is to arbitrarily center all the signal to one quadrature —in this case, the sine or *imaginary*, quadrature phase— to keep track of the information of the phase between signals. The fact of using different delays considers the possibility of having relative delays between them, what in fact has been experimentally observed —see Chapter 5.

Since the heat signal produced by the heater sequence is not a pure sinusoid at f_{mod} but actually a square wave, the demodulation procedure can be applied analogously to the immediate odd harmonics ($3f_{\mathrm{mod}}$, $5f_{\mathrm{mod}}$, $7f_{\mathrm{mod}}$, etc). Nevertheless, the low-pass behaviour of the Electrode Housing as a thermal system dramatically attenuates the heat flux components at frequencies higher than approximately 3 mHz, as shown later in Section 4.3.1.1.

In any case, since the thermal coefficient is expected to be constant across all the band, the value estimated at the modulation frequency is extended to all the band, thus $\alpha \approx \alpha_{f_{\mathrm{mod}}}$.

4.3 Analysis of errors

The error associated to the estimation of unknown parameters usually depends first, on the measurement duration and the precision, and second, on the dependence of the measured signal with respect to the parameter to be estimated. In this sense, the inverse of the Fisher matrix provides an estimator of the expected errors known as the Crámer-Rao Bound (CRB) that allows to define a minimum experiment length to achieve the desired level of precision in scenarios with relatively high SNR.

In general, the thermal experiments to be performed are approximated to

$$y[n] = \mathbf{H}(\Theta)x[n] + w[n] \qquad \text{for } n = 1, 2, ..., N \tag{4.5}$$

where $y[n]$ is each sample of the vector measurements $\mathbf{y}$, $\Theta = \{\theta_1, \theta_2, ..., \theta_n\}$ is the vector of parameters to estimate in the system model $\mathbf{H}$ and $x[n]$ are the samples of the vector of inputs $\mathbf{x}$. $w[n]$ is the external system noise. For systems modelled in this way, the likelihood function defines the probability to observe a measurement that depends on a known input, with certain levels of noise. Assuming white Gaussian distributed data, the likelihood function is written as [149]

$$p\left(\mathbf{y}|\Theta\right) = [2\pi\Sigma]^{-1/2} \exp\left\{-\frac{1}{2}\left[\mathbf{y} - \mathbf{H}(\Theta)\mathbf{x}\right]\Sigma^{-1}\left[\mathbf{y} - \mathbf{H}(\Theta)\mathbf{x}\right]^{\mathrm{T}}\right\} \tag{4.6}$$

where Σ is the covariance matrix of the channels considered.

The noise distribution must be *white* along the measurement bandwidth — *uncoloured*, otherwise the measured data $\mathbf{y}$ must be whitened. For the latter, the analysis must be done at a frequency bin level, considering the noise spectrum $S_y(\omega)$ associated to each frequency, which at the same time can be used as whitening filter for the measured data. The likelihood expression in this case is

$$p\left(\mathbf{y}|\Theta\right) = \int_0^{\infty} [2\pi S(\omega)]^{-1/2} \exp\left\{-\frac{1}{2S(\omega)}\left[Y(\omega) - \mathbf{H}(\Theta, \omega)\,X(\omega)\right]^2\right\} \mathrm{d}\omega \tag{4.7}$$

The best estimation of Θ is consequently associated to a maximisation of the likelihood function. For the sake of simplicity it is common to directly operate with the equivalent log-likelihood function. Assuming white noise on the measure data:

$$\log\left(p\left(\mathbf{y}|\Theta\right)\right) = \log(K) - \frac{1}{2}\left[\mathbf{y} - \mathbf{H}(\Theta)\mathbf{x}\right]\Sigma^{-1}\left[\mathbf{y} - \mathbf{H}(\Theta)\mathbf{x}\right]^{\mathrm{T}} \tag{4.8}$$

The Fisher information matrix is defined here as [2]

$$I_{ij} = \left\langle \left(\frac{\partial \log(p(\mathbf{y}|\Theta))}{\partial\theta_i}\right)^T \left(\frac{\partial \log(p(\mathbf{y}|\Theta))}{\partial\theta_j}\right)\right\rangle\Bigg|_{\theta=\theta_0} \tag{4.9}$$

from which we can extract the Crámer-Rao Bound bound, expressed as

$$\sigma^2_{\theta_i} \geq \left[\mathbf{I}^{-1}(\theta)\right]_{ii} \tag{4.10}$$

Such a boundary states that for given levels of noise in the measurements, the best estimates of the error of the parameters cannot be smaller than their respective diagonal terms in $\mathbf{I}^{-1}(\theta)$. This is of high interest for two main reasons: (1) allows to define appropriate inputs to achieve certain parameter precision and (2) allows to understand the impact on the precision of the different terms in the model, becoming a suitable tool to identify the limiting factors of the experiment.

As a general rule for White Gaussian noise signals, the Crámer-Rao Bound for single parameter models is equivalently expressed as [149]

$$\sigma_\theta^2 \geq \frac{\sigma_y^2}{\sum_{n=1}^{N} \left(\frac{\partial s[n,\theta]}{\partial \theta} \right)^2} \tag{4.11}$$

where $s[n,\theta]$ is the product of $\mathbf{H}(\theta) \cdot x[n]$, and σ_y^2 the variance in the measurement $\mathbf{y}$, i.e. the result of integrating the noise S_y across the whole bandwidth. Notice that accurate estimators are found in signals $s[n,\theta]$ that present a strong dependence on the parameters.

Furthermore, in case of a single input and single output system with a signal $s[n,\theta] = \theta\, x[n]$, if the input signal is a sinusoid, as

$$x[n] = A \sin(2\pi f t_n) \tag{4.12}$$

then, a recurrent approximation is

$$\sum_{n=1}^{N} \Big(A \sin(2\pi f t_n) \Big)^2 \approx \frac{A^2 N}{2} \tag{4.13}$$

which leads to the Crámer-Rao Bound as a function of the number of samples and the amplitude of the input signal

$$\sigma_\theta^2 \geq \frac{2\sigma_y^2}{A^2 N} \tag{4.14}$$

In the following lines, two models with unknown parameters are considered: (1) a model for the global thermal coupling and (2) a model with the individual contributions of each thermal effect.

4.3.1 Estimation of the global thermal coefficient

The preferred model when measuring the global thermal coefficient is a single channel system with a unique parameter α that gathers all the thermal effects. This implies the assumption of constant pressure and negligible temperature gradient amplitude with respect to the absolute temperature. Such a model is written as

$$F_x[n] = \alpha \Delta T[n] + w[n] \tag{4.15}$$

for $n = 1, 2, ..., N$. The modulated temperature gradient ΔT can be approximated to a sinusoid function of $f_{\rm mod}$ with a similar amplitude

$$\Delta T[n] \approx \Delta T \sin(2\pi f_{\rm mod} t_n) \tag{4.16}$$

Assuming now that the modulation frequency is much smaller than the sampling frequency and that the signal length is an integer number of its period, for a signal of N samples we compute the CRB by means of Equation 4.14

$$\sigma_\alpha^2 \geq \frac{2\sigma_F^2}{\Delta T^2 N} \tag{4.17}$$

The inverse quantity $\frac{\Delta T^2 N}{2\sigma_F^2}$ is actually an estimator of the Signal-to-Noise Ratio under the assumptions of stationary Gaussian random noise [2]. Equation 4.17 allows to derive minimum modulation times in order to achieve a desired precision. Assuming a noise in the force measurement of $5 \cdot 10^{-14}\,\mathrm{N\,Hz^{-1/2}}$ and a sampling frequency of 0.2 Hz, the deviation in the force measurement when integrating in the whole band is $1.6 \cdot 10^{-14}$ N. A list of integration times for different temperature gradient amplitudes and a desired precision of 0.1% over a worst-case $\alpha \approx 20\,\mathrm{pN\,K^{-1}}$ is presented in Table 4.1. The variation of the integration times upon the required precision is shown in Figure 4.2 (*left*).

ΔT [mK]	**Integration time [ks]**
1	6250
5	250
10	62.5
20	15.6
50	2.5
100	0.63
200	0.16

Table 4.1: Integration times required for the estimation of α within a 0.1% of error, assuming a worst-case $\alpha = 20\,\mathrm{pN\,K^{-1}}$ and sinusoidal input.

The maximum allowed temperature gradient amplitude across the Electrode Housing depends on the absolute temperature and varies within a range 60–100 mK, due to the NTC temperature-dependence described in Section 2.2.2. Consequently, integration times of at least 2000 s at maximum power should be envisaged for a good estimation of an unknown α.

Temperature gradients at different frequencies have been simulated by means of the SSMs to look for a suitable modulation frequency. The sequences obtained are shown in Figure 4.2 (*right*), where the low pass thermal behaviour is clearly observed. Indeed, the

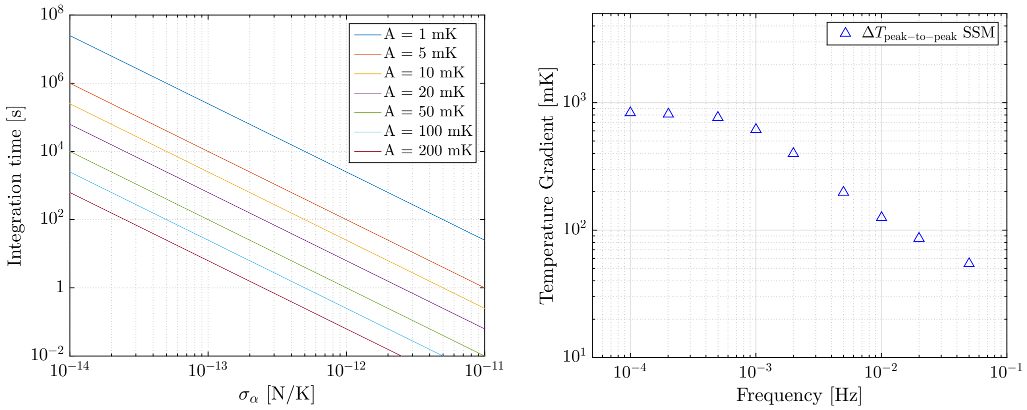

Figure 4.2: *Left:* Precision in the estimation of α for a subset of integration times and temperature gradient amplitudes. *Right:* Maximum peak-to-peak amplitudes of the temperature gradient across the Electrode Housings as a function of the frequency. In all cases, the amplitude of the square wave heating signal applied is 90 mW.

cut-off frequency observed at ~1 mHz sets an upper limit to the modulation frequency f_{mod} in order to optimise the temperature gradient applied. Since such a frequency is actually at the lower edge of the bandwidth of interest, a f_{mod} of 1 mHz arises as a reasonable option. Nevertheless, unexpected scenarios with a too high temperature noise at this band, or the requirement of performing the modulations in parallel with other experiments operating at 1 mHz, would recommend using a higher modulation frequency.

4.3.1.1 Multiple-frequencies content

The contribution of higher harmonics to the estimation of α is obtained by calculating the Fisher matrices associated to the temperature gradient amplitude at each harmonic and adding them to the main one, as if they were independent measurements:

$$\mathbf{I} = \mathbf{I}_{f_{\text{mod}}} + \mathbf{I}_{3f_{\text{mod}}} + \mathbf{I}_{5f_{\text{mod}}} + \mathbf{I}_{7f_{\text{mod}}} + \ldots \tag{4.18}$$

However, the improvement in the estimation is not significant since the amplitudes of the odd harmonics are progressively damped by the low-pass thermal filter effect —see Figure 4.2. Figure 4.3 shows the tiny precision improvements in α after considering different immediate harmonics from a measured temperature gradient signal of $\Delta T = 200\,\text{mK}$. A 1st-order exponential fit is used to bound the maximum improvement of expected σ_α that can be achieved by adding signal harmonics to the analysis, resulting in less than 1.5% when including all of them. In consequence, the information of the harmonics is not going to be considered in the analysis from this point on.

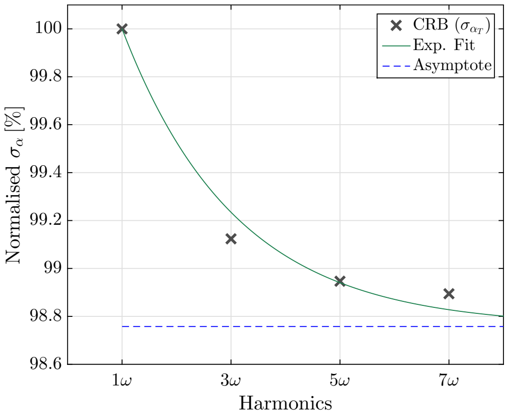

Figure 4.3: Cumulative contribution of the harmonics in the estimation of σ_α, normalised at the first harmonic (1ω), for a $\Delta T = 50\,\mathrm{mK}$ temperature gradient measurement of 5000 samples at 0.2 Hz. The 1st-order exponential fit (*green* line) applied bounds the maximum improvement of expected σ_α that can be achieved by including signal harmonics in the analysis. The *dashed* line indicates the limit corresponding to the maximum improvement.

4.3.1.2 Absolute temperature variation requirements

During the temperature gradient modulations, the absolute temperature may still present a residual drift due to environmental fluctuations or to the heater activations themselves. This temperature drift has an impact on the thermal coefficient, changing its value with the total temperature variation, what in the estimation of α appears as an additional error in the measurement. It is therefore important to assess the contribution of this error in order to define constraints to the maximum variation of temperature during a modulation segment. The total variation of α associated to a change of absolute temperature ΔT_{abs} is defined as

$$\Delta\alpha_{\Delta T\,\text{abs}} = \frac{\partial\alpha}{\partial T_{\text{abs}}}\Delta T_{\text{abs}} \tag{4.19}$$

with

$$\frac{\partial\alpha}{\partial T_{\text{abs}}} = 3\frac{\alpha_{\text{RP}}}{T_{\text{abs}}} - \frac{\alpha_{\text{RM}}}{T_{\text{abs}}} + \alpha_{\text{OG}}\left(\frac{\Theta_{\text{OG}}}{T^2_{\text{abs}}} - \frac{2}{T_{\text{abs}}}\right) \tag{4.20}$$

where the expressions for each effect defined in Section 2.1.1.1 have been applied to calculate $\partial\alpha/T_{\text{abs}}$. Thus, we define a limit on the variation of T_{abs} by imposing a maximum accepted variation equal to 10% of σ_α, as

$$\Delta\alpha_{\Delta T\,\text{abs}} \quad \leq \quad \frac{\sigma_\alpha}{10} \tag{4.21}$$

Considering the nominal contributions of each effect at 293 K as provided in [120], and a temperature activation $\Theta_{\mathrm{OG}} = 9000\,\mathrm{K}$, we get

$$\Delta T_{\mathrm{abs}} \leq 4.2\,\mathrm{mK} \tag{4.22}$$

where the effect of changing the nominal temperature across the measurement range, from 280 K to 303 K, modifies the constrain to 3.6 mK and 4.7 mK, respectively. Assuming modulation segments of ~6000 s, this constrain implies temperature drifts $\leq 0.7\,\mu\mathrm{K\,s^{-1}}$, what is difficult to achieve in flight since current predictions of residual drifts after stabilising at each temperature level are expected to keep around $1\,\mu\mathrm{K\,s^{-1}}$ at most. Such an scenario would actually limit the estimation of the parameter α to a $\sigma_\alpha \approx 0.2\%$ instead of the 0.1% imposed in the previous section. In order to evaluate such a restriction more carefully, we identify the contribution of each effect. Setting a limit for each requirement individually while keeping the imposition $\sigma_\alpha = 0.1\%$, we obtain

$$\Delta T_{\mathrm{abs,RP}} \leq 26\,\mathrm{mK} \tag{4.23}$$

$$\Delta T_{\mathrm{abs,RM}} \leq 71\,\mathrm{mK} \tag{4.24}$$

$$\Delta T_{\mathrm{abs,OG}} \leq 4.7\,\mathrm{mK} \tag{4.25}$$

where the outgassing effect is clearly *defining* the limit. As commented before, this bound has been calculated assuming an expected contribution of the outgassing effect with $\Theta_{\mathrm{OG}} = 9000\,\mathrm{K}$, where the outgassing effect would be dominant. It is of interest to note that, at a scenario of small outgassing contribution, i.e. $\Theta_{\mathrm{OG}} = 30000\,\mathrm{K}$, we require a $\Delta T\,\mathrm{abs} \leq 0.6\,\mathrm{mK}$. Such a total temperature request is clearly infeasible since would require drifts $\leq 0.1\,\mu\mathrm{K\,s^{-1}}$. In that case, the best estimate of α would present a $\sigma_\alpha \approx 1\%$.

4.3.2 Estimation of the individual thermal effects

Within the attempt to disentangle the contribution of the different thermal effects in the Electrode Housing, it is of high convenience to redefine the model to a single-channel system with parameters for each effect. This allows to keep apart the absolute temperature dependence of each effect. We recover here the general expression with linearised effects:

$$F_x[n] = \left[\rho_{\mathrm{RP}}\, T^3[n] + \rho_{\mathrm{RM}}\, \frac{1}{T[n]} + \rho_{\mathrm{OG}}\, \frac{e^{-\frac{\Theta_{\mathrm{OG}}}{T[n]}}}{T^2[n]}\right] \Delta T[n] + w[n] \tag{4.26}$$

where the radiation pressure and the radiometer effect are reduced to single-parameter terms (ρ_{RP}, ρ_{RM}), while outgassing is represented by two parameters (ρ_{OG} and the activation temperature Θ_{OG}).

A recurrent approach to the analysis consists on approximating the outgassing term to a one parameter effect. Supposing the activation temperature is known ($\Theta_{\rm OG} \approx \Theta_{\rm OG}^{\rm est}$), the resulting Fisher matrix is defined as

$$\mathbf{I} = \frac{1}{\sigma_F^2}\begin{pmatrix} \sum_i^N f_{\mathrm{RP},i}^2 & \sum_i^N f_{\mathrm{RP},i} f_{\mathrm{RM},i} & \sum_i^N f_{\mathrm{RP},i} f_{\mathrm{OG},i} \\ \sum_i^N f_{\mathrm{RP},i} f_{\mathrm{RM},i} & \sum_i^N f_{\mathrm{RM},i}^2 & \sum_i^N f_{\mathrm{RM},i} f_{\mathrm{OG},i} \\ \sum_i^N f_{\mathrm{RP},i} f_{\mathrm{OG},i} & \sum_i^N f_{\mathrm{RM},i} f_{\mathrm{OG},i} & \sum_i^N f_{\mathrm{OG},i}^2 \end{pmatrix} \tag{4.27}$$

where the different f_{XX} are the specific temperature functions for each effect:

$$f_{\mathrm{RP},i} = T_i^3 \Delta T(t_i) \tag{4.28}$$

$$f_{\mathrm{RM},i} = \frac{1}{T_i} \Delta T(t_i) \tag{4.29}$$

$$f_{\mathrm{OG},i} = \frac{\exp\left(-\frac{\Theta_{\rm OG}^{\rm est}}{T_i}\right)}{T_i^2} \Delta T(t_i) \tag{4.30}$$

Following the same assumptions as in the single-parameter model, the Fisher matrix at a given absolute temperature T_0 is approximated to:

$$\mathbf{I}_{T_0} \approx \frac{\Delta T^2 N}{2\sigma_F^2}\begin{pmatrix} T_0^6 & T_0^2 & T_0 \exp\left(\frac{-2\Theta_{\rm OG}^{\rm est}}{T_0}\right) \\ T_0^2 & \frac{1}{T_0^2} & \frac{1}{T_0^3}\exp\left(\frac{-\Theta_{\rm OG}^{\rm est}}{T_0}\right) \\ T_0 \exp\left(\frac{-2\Theta_{\rm OG}^{\rm est}}{T_0}\right) & \frac{1}{T_0^3}\exp\left(\frac{-\Theta_{\rm OG}^{\rm est}}{T_0}\right) & \frac{1}{T_0^4}\exp\left(\frac{-2\Theta_{\rm OG}^{\rm est}}{T_0}\right) \end{pmatrix} = \frac{\Delta T^2 N}{2\sigma_F^2}\mathbf{M}_{T_0} \tag{4.31}$$

The resulting CRB is consequently the product of $\frac{2\sigma_F^2}{\Delta T^2 N}$ with the inverse of $\mathbf{M}_{T_0}$. As observed, ΔT^2 and σ_F^2 contribute as proportional weights to the final variances. On the other hand, the inversion of $\mathbf{M}_{T_0}$ is only possible when more than one absolute temperature T_0 is considered, i.e.

$$\mathbf{M}(\mathrm{T}) = \mathbf{M}_{T1} + \mathbf{M}_{T2} + \mathbf{M}_{T3} + \ldots \tag{4.32}$$

The result of its inversion is a complicated term not written here. At a numerical level, results for different absolute temperatures and temperature ranges are presented in Table 4.2, considering a sinusoidal temperature gradient amplitude ΔT of 50 mK, 1200 samples per temperature level and an estimated activation temperature of 9000 K. As in the previous case, the deviation in the estimation of the force is set to $1.6 \cdot 10^{-14}$ N.

$\mathbf{T_{abs}}$ **[K]**	**Temperature range [K]**	δ_{RP}	δ_{RM}	δ_{OG}
280	[0, 0.5, 1.5, 2]	96%	130%	5%
	[0, 1.5, 3.5, 5]	14%	19%	0.7%
	[0, 3, 6, 10]	3%	5%	0.1%
293	[0, 0.5, 1.5, 2]	110%	150%	2%
	[0, 1.5, 3.5, 5]	16%	21%	0.2%
	[0, 3, 6, 10]	4%	5%	0.05%
303	[0, 0.5, 1.5, 2]	120%	160%	0.8%
	[0, 1.5, 3.5, 5]	18%	24%	0.1%
	[0, 3, 6, 10]	4%	6%	0.02%

Table 4.2: Crámer-Rao bounds for the 3-parameter model under different thermal conditions. An activation temperature Θ_{OG} of 9000 K and a sinusoidal amplitude ΔT of 50 mK have been considered. The results correspond to measurements of 6000 s for each temperature level and the temperature ranges shown are applied starting from each T_{abs}.

The outgassing arises as the easiest effect to estimate due to its high variation with temperature. Since its contribution strongly increases with temperature, the estimation of the other effects is worse at high temperatures —even for the radiation pressure effect, whose contribution increases with temperature too.

Temperature ranges of ~5 K and ~10 K would be required to estimate all the effects within a 24% or 6% of precision, respectively. Unfortunately, the available temperature span may not be larger than 2−3 K due to power limitations, what challenges the success of the analysis. Here we have considered a case with high contribution of outgassing. However, eventual scenarios with small outgassing contributions like ones with activation temperatures higher than ≈22000 K would allow to neglect the outgassing effect and bound the contributions from the other effects with less than 50% of uncertainty.

Indeed, results in Table 4.2 may not be definitive since the impact of some effects is still uncertain and is not going to be revealed until first measurements take place in flight. In addition, the measured force noise may be lower [73] and longer experiments could eventually be planned —though the current timespan allocated for the Electrode Housing thermal experiment is ≈1.5 days.

As an alternative to the previous analysis, models including Θ_{OG} as an unknown parameter can also be assessed, though the implementation of the exponential term in the outgassing effect is troublesome and there is no effective benefit in the estimations of each individual effect. In order to get rid of the exponential term, the outgassing contribution can be approximated to a second order Taylor series —see Appendix C for more details on the parameters and the associated errors. The resulting expression is written as

$$\alpha_{\mathrm{OG},i} = \rho_{\mathrm{OG}} \frac{e^{-\frac{\rho_{\mathrm{OG}}}{T_i}}}{T_i^2} \approx \rho_{\mathrm{OG1}} + \rho_{\mathrm{OG2}} T_i + \rho_{\mathrm{OG3}} T_i^2 \tag{4.33}$$

As it is shown later in Chapter 5, such an approximation is useful in some specific experimental analysis on-ground. This approximation adds another parameter in the model, what actually increases the number of required temperature levels. However, concerning the CRB analysis done here there is no improvement in the estimation of the effects.

In any case, the identification of the outgassing effect is extremely dependent on the activation temperature Θ_{OG}, which can vary between 3000 to 30000 K [150]. For values higher than approximately 12000 K, its contribution could be directly neglected, while it may be the dominant effect if the activation temperature is lower than 10000 K. The final outgassing contribution will remain uncertain until the experiment takes place during the mission.

The identification of the radiometer effect contribution by means of a single experiment —that would eventually lead to an estimation of the pressure in the Electrode Housing— remains improbable under current expected levels of outgassing. Under these circumstances, a first step can be to subtract the theoretical estimation of the radiation pressure, thus reducing one strong temperature-dependent parameter and easing the estimation of an upper limit for the radiometer effect. Such a procedure has been applied in the experimental characterisation campaign by the torsion pendulum, as described in Chapter 5.

Finally, in such a scenario of strong outgassing, another possibility is to take advantage of its decreasing rate with time. So far we have only considered an experiment based on multiple modulations carried out during a single day. However, another approach to the problem would be to repeat different modulations at different points during the mission, in order to estimate the decay of the outgassing effect. Indeed, upper bounds for the remaining effects could be obtained by estimating the thermal coefficient periodically, i.e. in periods of weeks or months. The decay of the outgassing effect is experimentally studied in Chapter 5 though its implementation as an independent experiment is still under investigation.

4.4 Input definition

As a summary of the results of the previous sections, the input signal must be determined as a compromise between the following two objectives:

a) Induce a temperature gradient signal at the desired modulation frequency with a SNR as large as possible.

b) Perform the modulations in an absolute temperature range as wide as possible to attempt the estimation of the contributions of the temperature-dependant thermal effects.

Since the same heaters and heating system must be used to satisfy both points, the compromise arises from the fact that a maximum amplitude modulation (V_{AC} = 10V and V_{DC} = 0V) induces a maximum ΔT signal at a specific temperature. Any other absolute temperature level must be achieved by setting different AC/DC combinations with different averaged power. This actually implies to reduce the temperature gradient amplitudes.

A compromise input signal complying with the previous statements is proposed in Figure 4.4 consisting of series of modulations at four different amplitudes an applying two different temperature gradient amplitudes per temperature level to check the linearity of the system.

At each temperature level, series of pulses of 500 s are applied alternatively to H1 and H2, resulting into a 1 mHz modulated temperature gradient signal along the x axis. Each modulation level is preceded by a pre-heating step of 8000 s where high DC segments of heat are applied to shorten the transient time required between temperature levels. The levels achieved are separated as much as possible in the available power range. The different power amplitudes are presented in Table 4.3. The maximum power achieved —of 90 mW— is the maximum power available by the Electrode Housing heaters at temperatures close to 18°C. For colder temperatures, as for example 9°C, such a maximum available power is reduced, in this case to 60 mW.

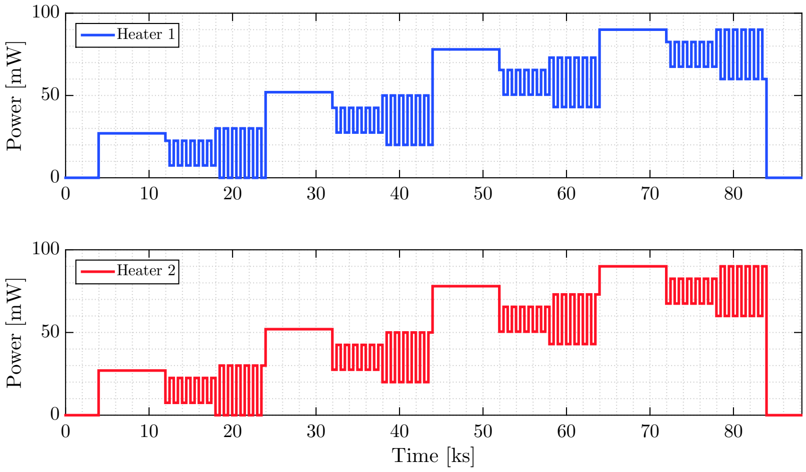

Figure 4.4: Signal proposed for heaters H1 and H2. As observed, the same modulation pattern is repeated with different DC levels and pre-heating steps.

A simulation by means of the ESATAN model implemented in Section 4.5 shows temperature gradient amplitudes of 100 mK and 200 mK for the smaller and larger amplitude modulations respectively. Regarding the absolute temperature levels between modulations, the range obtained is limited to a 2 K variation at a temperature ~293K. According to predictions in Table 4.2, such a maximum increment of temperature is in principle not enough to disentangle the effects.

Phase	DC power [mW]	AC power [mW]
DC1	27	0
MOD1A	7.5	22.5
MOD1B	0	30
DC2	52	0
MOD2A	27.5	42.5
MOD2B	20	50
DC3	78	0
MOD3A	50.5	65.5
MOD3B	43	73
DC4	90	0
MOD4A	67.5	82.5
MOD4B	60	0.09

Table 4.3: Proposed heating sequence for H1 and H2, the latter shifted half a modulation period with respect to H1 as shown in Figure 4.4. The corresponding voltages to be applied are calculated by the DMU at the beginning of each phase after measuring the temperature inside the Electrode Housing.

4.5 End-to-end simulation

A dedicated simulation of the experiment was performed at one of the major LTP simulation campaigns in order to validate the input signal proposed in this chapter and the data analysis tools associated. Namely, the 4th LPF Simulation Campaign took place in ESAC [1] in November 2013 and lasted for eight days, involving the whole LTP data analysis team. Every day, the telemetry corresponding to the experiments simulated the previous day was received and post-processed, and a different group of data analysts was responsible of the analysis.

During the day dedicated to the Electrode Housing thermal experiment, the signal proposed in Section 4.4 was applied. The simulator used was the OSE simulator located at the Science and Technology Operations Centre (STOC) in ESAC, emulating most of the spacecraft subsystems at a telecommand (TC) level. However, since at that time the algorithms to simulate the thermal effects had not yet been implemented in the OSE simulator, the thermal data was generated as it follows: the forces and torques were simulated by means of the LTPDA State-Space Models —see Chapter 3— and then applied to the OSE simulator as external, *out-of-loop*, direct forces and torques on the Test Masses. Meanwhile, the temperature sensor readouts were encapsulated as telemetry parameters and pushed to a database repository.

4.5.1 Data analysis

---

[1] ESAC: *European Space and Astronomy Centre*, Villanueva de la Cañada, Madrid, Spain

The data analysis steps leading to the estimation of the thermal coefficient on the x axis of a given heated Test Mass are summarized in the following procedures:

1. **Preprocess**. This point includes all the procedures that need to be applied to the telemetry data. For the specific case of temperature measurements, a conversion from counts to degrees as explained in Section 2.2.1.1 is required. The process of data cleaning from the spikes described in Section 2.2.1.3 is also part of this block. Finally, all the parameters involved —including OMS and temperature sensors— need to be resampled to a common sampling frequency and a common grid. In the simulation concerning this section, no count-to-temperature conversion and spike-cleaning processes were required.

2. **Build temperature signals**: In second place, both the temperature gradient and the absolute temperature are built from linear combinations of the different temperature sensor readouts. The temperature gradient signal is obtained from the difference of the average readouts at both x-sides, while the absolute temperature signal is the direct average between them —see Section 4.2.

3. **Estimate force**. The direct force F_x on the heated mass is estimated from the interferometer readouts, as described in Section 1.3.2.2. The final terms to be included in Equation 1.18 will be reconsidered after analysing the first acceleration noise measurements and identifying the most important noise sources and cross-talk terms.

4. **Demodulate**. Once ready, signals ΔT and F_x are demodulated at the applicable f_{mod} and then low-passed. A previous synchronisation between each signal and the demodulating sinusoid —as defined in Equation A.39— is required here. Such a synchronisation actually calculates the delays of the temperature gradient signal and the force with respect to the heater execution times. Such a calculation must be performed at each modulation segment corresponding to different telecommand execution, since expected delays up to 0.5 s can be introduced between telecommands.

5. **Estimate thermal coefficient**. At this point the thermal coefficients at each temperature level T_{abs} are calculated. The global thermal coefficient per temperature level is obtained by averaging all the thermal coefficients measured at a given temperature —two per temperature level in the proposed input signal.

6. **Identify thermal effects**. The identification of the different thermal effects should be performed by fitting the thermal coefficient curve with Equation 4.26 or an approximation to it. As discussed in Section 4.4, the success of this step is not guaranteed with the current expected conditions of noise and available temperature increments.

7. **Estimate Brownian noise**. This point is aimed to provide an upper limit to the pressure in the Electrode Housing cavity and to the Brownian noise contribution following the analysis explained in Section 2.1.1.2.

This data analysis procedure is performed by a dedicated pipeline to be executed in the LTPDA environment. A full description of the pipeline is found in Appendix B.

4.5.2 Results

The output data is presented in Figure 4.5, where a final absolute temperature increment of 2.5 K is achieved. Notice also that the modulation segments keep close to stable temperatures. As expected, the interferometer response is sensitive to the injection only on its differential channel x_{12}, the one that measures the relative distance between the Test Masses. The control loop that regulates the spacecraft position with respect to the primary Test Mass (x_1) has a high gain at 1 mHz, practically impeding the sensitivity of x_1 to the heat injections, while the control loop on x_{12} actuates on the x axis of the secondary mass with very low gain in the same band —see Section 1.3.2.

The temperature gradient signal shows an oscillating pattern with peak-to-peak amplitude levels of 100 and 200 mK as a consequence of the two different modulation amplitudes applied. Its shape is consistent with the force on the Test Mass. A delay of about 52 s between the temperature gradient and the force is attributed to intrinsic delays in the thermal model, since the surface nodes used to simulate the forces are in average geometrically further from the heaters than the thermistors used to measure the temperature gradient.

4.5.3 Thermal coefficients

Thermal coefficients in the order of $\sim 10^{-11}\,\mathrm{N\,K^{-1}}$ are obtained without observing any dependence on the amplitude of the temperature gradient —see Table 4.4 and Figure 4.6. The errors obtained, around $2.5 \cdot 10^{-14}\,\mathrm{N\,K^{-1}}$, are quite close to the theoretical prediction limit. Indeed, for a noise in the force measurement of $5 \cdot 10^{-14}\,\mathrm{N\,Hz^{-1/2}}$ and averaging for 6000 s, the theoretical error limit with temperature gradient amplitudes of $\Delta T_{A2} = 100\,\mathrm{mK}$ and $\Delta T_{A1} = 50\,\mathrm{mK}$ is $6.5 \cdot 10^{-15}\,\mathrm{N\,K^{-1}}$ and $1.3 \cdot 10^{-14}\,\mathrm{N\,K^{-1}}$ respectively. The difference between the theoretical limit and the errors obtained —between a factor 2–4 depending on the case— is mainly attributed to the residual transients caused by the low pass filter, that favour the dispersion of the demodulated points. These same transients also reduce the available timespan where to average the demodulated coefficients. This has an additional impact on the error. In second place, the absolute temperature drift keeps well below $1\,\mu\mathrm{K\,s^{-1}}$. This represents less than 0.01% of the error.

Figure 4.7 shows the dependence of the thermal coefficient with the absolute temperature. The clear temperature-dependence observed —much higher than radiation pressure, which is $\propto T^3$— suggests here an outgassing-dominated scenario, as expected.

As expected from Section 4.3.2, the reduced increment of absolute temperature available (around 2 K between modulation points) impedes the identification of the radiometer effect contribution, leaving only the option to set an upper limit to the Brownian effect. By considering the worst case of a totally radiometer-dominated environment at the lowest point, an upper limit to the pressure of $2.1\,\mu\mathrm{Pa}$ leads to an upper limit for

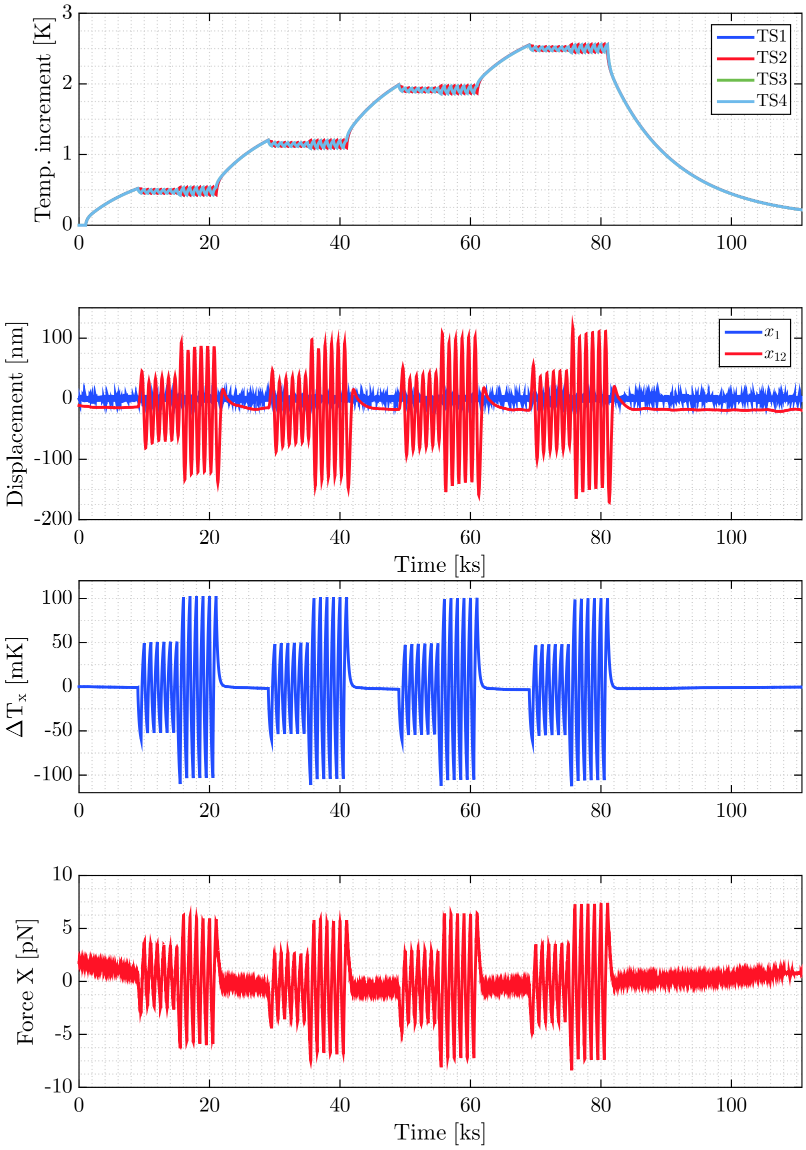

Figure 4.5: From top to bottom: 1. Electrode Housing temperature sensors readouts. 2. Interferometer measurements x_1 (*blue*) and x_{12} (*red*). 3. Temperature gradient ΔT on x axis of the Test Mass. 4. Force x induced on the Test Mass.

Temperature [K]	$\alpha_{\mathbf{x,A1}}$ [**pN K^{-1}**]	**Error** $\alpha_{\mathbf{x,A1}}$ [%]	$\alpha_{\mathbf{x,A2}}$ [**pN K^{-1}**]	**Error** $\alpha_{\mathbf{x,A2}}$ [%]
293.62	54.43	0.02	54.48	0.03
294.28	57.80	0.05	57.75	0.04
295.05	62.97	0.05	62.88	0.04
295.64	67.96	0.08	67.90	0.06

Table 4.4: Thermal coefficients estimated for the different temperature modulations. *A1* and *A2* correspond to the small and large modulation amplitudes respectively.

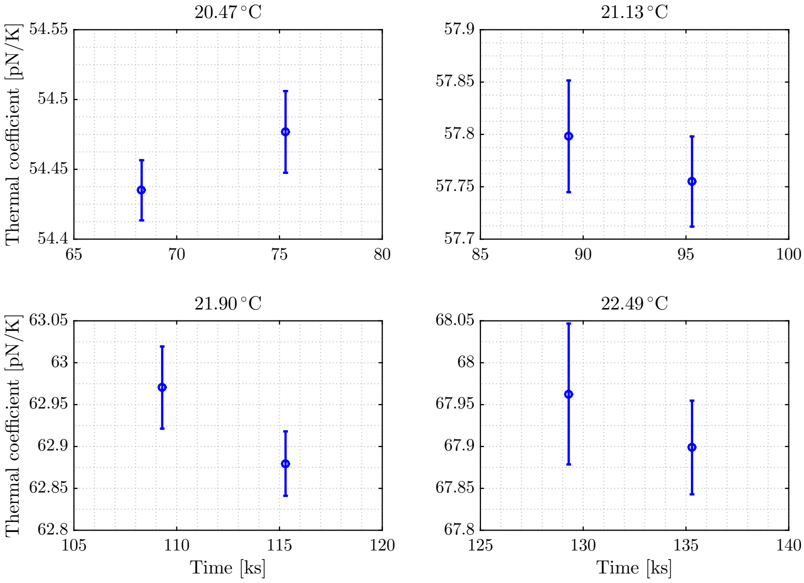

Figure 4.6: Average thermal coefficients α, classified in temperature levels. All the values present compatible coefficients at each temperature as expected, though the point at 21.90 °C is in the limit. This is attributed to the effects of the low pass filter.

the Brownian noise of $2.74 \cdot 10^{-15}\ \mathrm{m\,s^{-2}\,Hz^{-1/2}}$ at the lowest temperature.

4.5.4 Noise projection to the interferometer

It is also of interest to estimate the transfer functions between the temperature gradient and the force. Indeed, transfer functions estimates provide a tool to project the temperature noise to equivalent acceleration between the Test Masses —see Appendix A.3.1 for more details.

The temperature noise considered in the sensors is shown in Figure 4.8 (*left*). Uncorrelated instrumental noise is limiting the sensitivity above approximately 5 mHz, while below this frequency an increasing noise, partially correlated, represents some low fre-

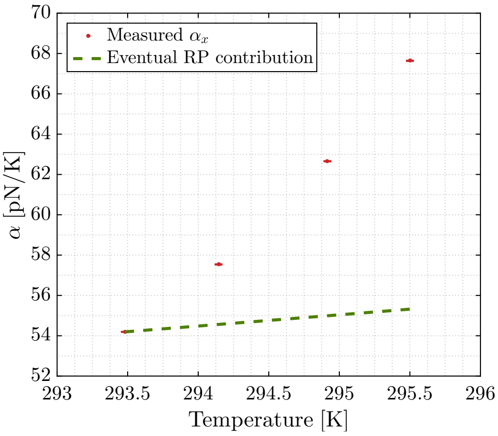

Figure 4.7: Thermal coefficient α_x vs. absolute temperature. The coefficients obtained (in *red*) are compared with the contribution associated to an eventual domination of the radiation pressure at the lowest temperature (*dashed* line). In the latter case, the radiation pressure contribution should increase with the third power of the temperature. The result points to an outgassing-dominated scenario.

quency real temperature noise.

Figure 4.8 (*right*) also shows the temperature noise projection to acceleration noise during a specific noise measurement with no thermal injections. As observed, the temperature noise contribution to the acceleration noise is kept about a factor 30 below the actual noise level. For $f > 0.02$ mHz the projection is no longer significant since the readout noise of the thermistors is dominant in this band.

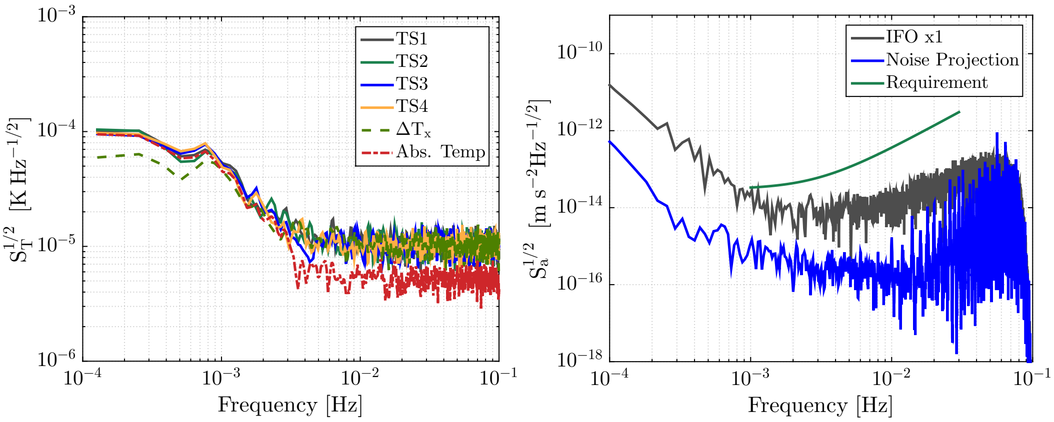

Figure 4.8: *Left*: Temperature noise applied to the temperature sensors. *Right*: Temperature noise projection on an acceleration noise measurement. The temperature gradient contribution keeps about a factor 30 below the noise level.

4.6 Summary

The basic constraints and minimum requirements that need to be considered for the Electrode Housing thermal experiment design have been assessed in this chapter. It has been shown that, given the expected conditions of noise and available power, the identification of the different thermal effects needs to follow alternatives rather than the direct fit of the whole model. This issue forces the analysis to look for other ways such as partial fitting of data —combining theoretical predictions with unknown parameters— to at least set limits and upper bounds to some parameters.

The final signal to be applied within the Electrode Housing thermal experiments is going to be decided in the immediate months preceding the operations under the criteria described here and considering also other factors like available time and estimated environmental, conditions in flight. There is still the possibility of repeating the thermal modulations with variations according to each of the specific objectives, i.e. (*a*) to perform the complete scheme to disentangle the effects and (*b*) to track time-dependence of the thermal coefficient by measuring it at different stages of the mission. The latter case would yield a time-variant outgassing effect contribution that may be of high interest in case Brownian noise arises as a LTP limiting sensitivity factor. Under this scenario, fitting the long-term outgassing rate variation would provide an estimation of the pressure inside the Electrode Housing.

Meanwhile, close-loop simulations of the LTP behaviour have been done to test the experiments designed. Such simulation exercises have been part of the simulation campaigns for the validation of the different LTP experiments and data analysis tools. The Electrode Housing thermal experiments have been simulated and analysed combining a global spacecraft simulator together with the SSM simulator of the thermal effects. Results show how the current procedure allows to estimate the global thermal coefficients with enough precision in an outgassing-dominated environment.

CHAPTER 5

On-ground testing of the Inertial Sensor thermal effects

Torsion pendulums are known to be very good dynamometers. With acceleration sensitivities down to $\sim 10^{-14}\,\mathrm{m\,s^{-2}\,Hz^{-1/2}}$ in the milli-Hertz frequency band, torsion pendulum setups have been for example extensively used in experiments to test the Equivalence Principle [151]. Since their sensitivity is comparable to the expected performance of LISA Pathfinder in the milli-Hertz band, these instruments are interesting platforms to characterise and set upper limits to force noise sources acting on the Test Masses.

Torsion pendulums are able to reproduce free-fall conditions on ground by suspending a single test mass or a system of masses by a thin fibre with very low stiffness and dissipations. Their performance is limited by an unavoidable noise source, the thermal noise dissipation of the fibre, that can be reduced by using fibre materials with high quality factor and working in vacuum conditions and magnetic/electric/thermal clean environments.

The University of Trento (UTN), Italy, has been extensively testing forces arising in the the LTP Inertial Sensors in two torsion pendulum facilities located at the *Laboratorio di Fisica della Gravitazione e delle Basse Temperature*: a single-mass pendulum setup and a 4-mass pendulum setup. They have been used to test many aspects of the LTP performance, such as the drift experiment, Test Mass charging by means of ultra-violet lamps, electrostatic sensing and actuation configurations, etc.

The single-mass pendulum basically consists on a prototype of LTP Test Mass suspended directly by a silica fibre, while in the 4-mass pendulum, a tungsten fibre suspends a cross-shaped, horizontal structure with masses at each edge, thus leaving the Test Masses separated ~10 cm with respect to the fibre. For the topic concerning this thesis, the latter is advantageous since it allows for a more representative measurement of the direct force induced by a thermal gradient across the Inertial Sensor.

5.1 The GRS prototype of the 4-mass torsion facility

The inertial member of the 4-mass torsion pendulum contains four cubic masses at the edge of its cross-shaped central structure —see Figures 5.1 and 5.2. One of these masses is a representative prototype of one LTP Test Mass —named here as GRS Test Mass— and is surrounded by a fully equipped prototype of the GRS, fixed with respect to the floor. The GRS Test Mass and its *opposed* mass, being part of electrostatic position sensors, need to be electrically isolated from the central structure, while the other two masses are grounded. All masses are hollow in order to reduce the total suspended mass.

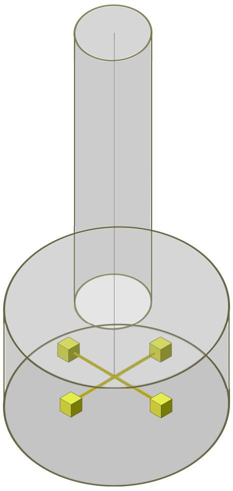

Figure 5.1: General scheme of the 4-mass torsion pendulum.

In terms of representativeness, the Electrode Housing prototype presents the same electrode configuration and geometry as the flight model case. It is made of the same material and has the same size and final surface coating, though the prototype followed a different mechanical implementation and presents a higher level of roughness. Regarding the Test Mass, it is externally the same as the flight model, with the spherical bumps at the corners and other features required by the caging system and release mechanism, though with less stringent tolerances. The most significant difference is that it is made of aluminium instead of a platinum-gold alloy, thus it is non-ferromagnetic. This prevents the pendulum from being sensitive to magnetic disturbances, focusing the instrument on the measurement of direct surface forces.

The Electrode Housing prototype lays on a three-DOF controlled plate that allows to center its position with respect to the Test Mass. On the top of the structure, the fibre is glued to the head of the pendulum, which is equipped with a mechanism to rotate the pendulum around its longitudinal axis to counteract the fibre natural unwinding —between 10 and 1000 μrad/day, mainly depending on the temperature.

The whole setup is located inside a dedicated vacuum chamber which is connected to a 400 L/s double-stage pumping system —see Figure 5.3. The pumping system consists of two turbo-molecular pumps that allow to achieve a working pressure inside down to 10^{-6} Pa. The pressure is measured by a Pfeiffer ion gauge (Compact FullRange$^{\text{TM}}$ BA Gauge PBR 260) within an accuracy of 15%, certified by the manufacturer. More details on how the pressure is calculated and the correction factors considered —including the system geometry and the gas composition— can be found in Appendix D.

The vacuum chamber is placed in a thermally insulated and stabilised room. Inside, a heat exchanger with up to six fans is connected to a Julabo thermal-control system that regulates the temperature in a range between 14°C and 35°C. This room is placed on a section of the floor isolated from the rest of the lab in order to reduce vibration

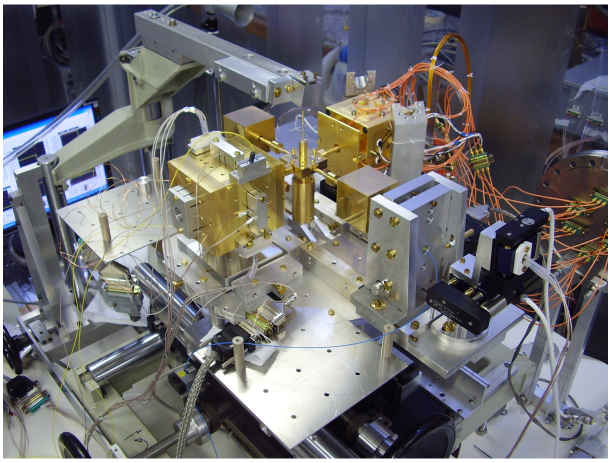

Figure 5.2: Picture of the cross-shaped structure with the four masses. The GRS prototype is the one at the top-left. Credits: UTN Experimental Gravitation group.

noise. The primary pump and the refrigeration system are kept on the main floor of the laboratory —Figure 5.4 provides a schematic of the facility.

5.1.1 Electrostatic sensing and actuating system

The motion of the GRS Test Mass on all its 6 DOF is measured by a representative prototype of the Inertial Sensor Front-End Electronics (IS-FEE). The actuation commands are generated in a LabView interface and then sent to the IS-FEE, allowing to apply forces on the Test Mass and to control the pendulum position. According to the notation in Figure 5.5, the main oscillation on η is sensed by the $\pm z$ electrodes, as shown in Figure 5.6.

5.1.2 Additional displacement sensors

Beside the GRS prototype, the 4-mass pendulum is also equipped with two auxiliary displacement sensors:

- The **Stiffness Compensator** (STC). The mass opposed to the GRS prototype is equipped with a second capacitive sensor, much simpler than the Electrode Housing prototype. Since it has just six electrodes —one per face—, it mainly provides a measurement of the displacement of its mass along x, when operating the pendulum in differential configuration. In such configuration, the x readouts of both the STC and the GRS prototype are combined in order to obtain a more sensitive measurement of the pendulum rotation.
- An external optical **autocollimator** (AC) is integrated to the setup providing an independent measurement of the pendulum rotation. It points directly to a mirror fixed on the torsional member. More details on its performance are shown in Section 5.2.

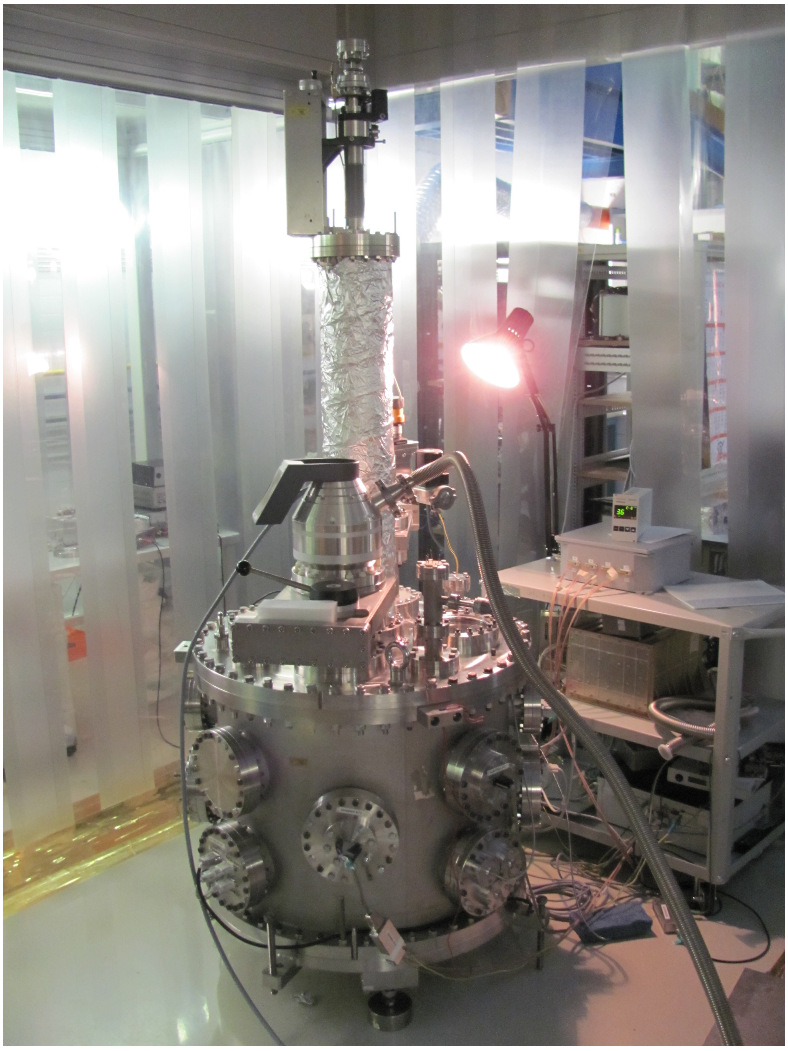

Figure 5.3: Global view of the 4-mass torsion pendulum vacuum chamber without the thermally insulated room. Credits: UTN Experimental Gravitation group.

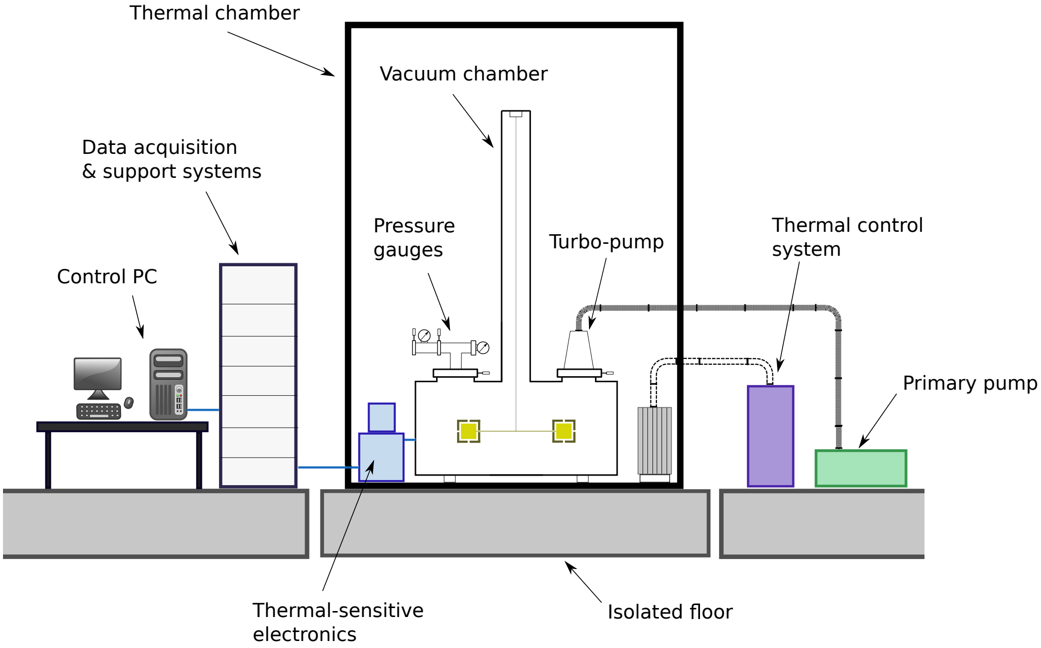

Figure 5.4: General schematic of the 4-mass torsion pendulum facility.

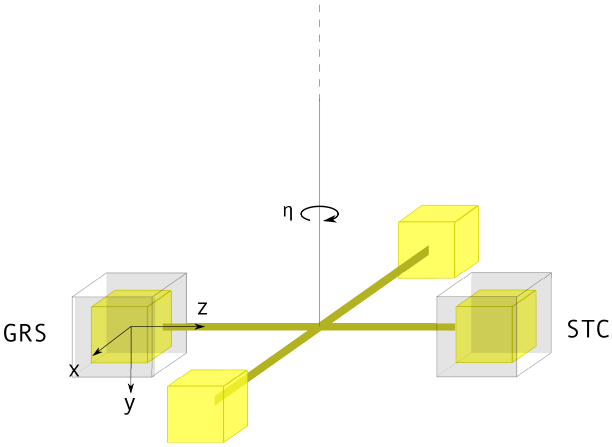

Figure 5.5: GRS prototype and STC sensor on the 4-mass torsion pendulum setup, with the main reference system centred on the GRS prototype.

5.1.3 Thermal items on the pendulum setup

The Electrode Housing prototype is equipped with series of LTP flight model NTC thermistors following the same layout of heaters and temperature sensors as in the satellite —see Figure 5.7. In addition, a set of additional temperature sensors (PT100) are placed in other locations of the Electrode Housing prototype and in different parts of the vacuum chamber for a better monitoring of the environment.

The temperature sensors are directly sampled at 83 mHz by a multichannel multi-

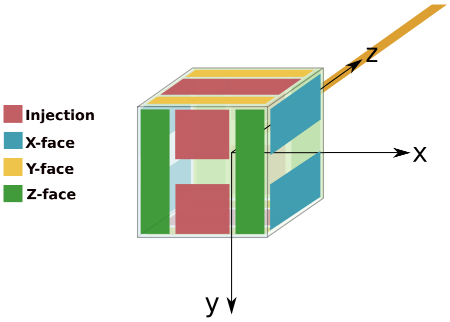

Figure 5.6: Electrodes configuration of the GRS prototype.

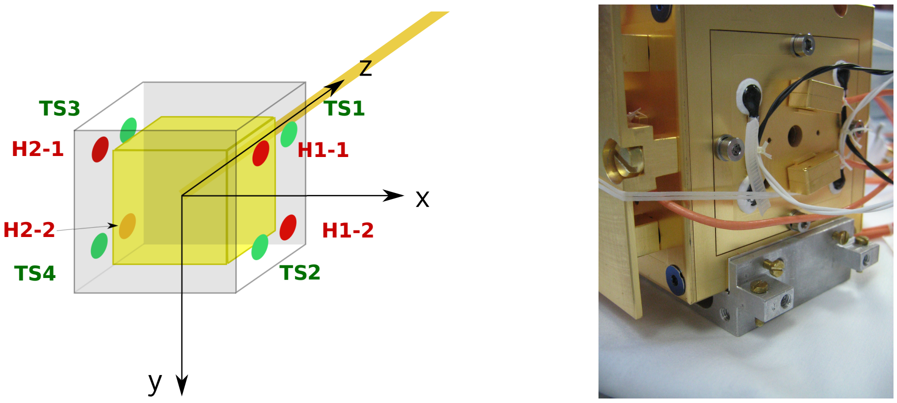

Figure 5.7: *Left:* Schematic of the diagnostics temperature sensors and heaters on the GRS prototype in the 4-mass torsion pendulum. *Right:* Partial view of the sensors installed on the Electrode Housing of the GRS prototype. Credits: UTN Experimental Gravitation group.

meter, so no DAU-DMU interface is used. Since the temperature range is not divided in different scale ranges, the temperature signals are continuous and no spikes are present in the measurements, simplifying the signal post-process. The associated loss of linearity [2] does not represent an inconvenient for the thermal experiments, since the analysis is generally focused on measuring large temperature perturbations rather than measuring the temperature noise.

Voltages are applied to the heaters through a DAC interface controlled by a LabView routine that allows to implement the heating scheme described in Section 2.2.2. Thus, the heat injection system is not fully representative at telecommand level but is able to apply the same signals as in the satellite.

5.2 Torsion pendulum performance

According to the reference system in Figure 5.5, the torsion pendulum angular displacement is indicated by η. The equation of motion around the fibre axis of the torsion pendulum is written as

$$I\ddot{\eta}(t) + \beta\dot{\eta}(t) + \Gamma\eta(t) = N(t) \tag{5.1}$$

where

- η is the angle of rotation around the fibre axis,
- I is the moment of inertia of the pendulum,
- β is the damping factor,
- Γ is the rotational stiffness and
- N is the total torque acting on the inertial member.

The torsional stiffness Γ is dominated by the fibre stiffness, as

$$\Gamma = \frac{\pi r^4}{2L}\left(F + \frac{mg}{\pi r^2}\right) \tag{5.2}$$

where L and r are the fibre length and radius respectively, F is the elastic modulus of the material, m the mass of the inertial member and g the gravitational field [152]. The diameter and material of the fibre is normally constrained by the total mass to be sustained. The natural frequency f_0 and the *underdamped* frequency of the pendulum are defined as

$$f_0 = \frac{1}{2\pi}\sqrt{\frac{\Gamma}{I}} \tag{5.3}$$

$$f_{ud} = \frac{1}{2\pi}\sqrt{\frac{\Gamma}{I} - \frac{\beta^2}{4I^2}} \tag{5.4}$$

The torsional stiffness Γ is $\sim 10^{-7}\,\mathrm{N\,m\,rad^{-1}}$ and the damping factor β is $\sim 10^{-9}\,\mathrm{N\,m\,s}$, while the momentum of inertia is $\approx 3.7 \cdot 10^{-3}\,\mathrm{kg\,m^2}$. Thus, the damping factor term is much smaller than the stiffness term, what leads to $f_{ud} \approx f_0 \approx 0.83\,\mathrm{mHz}$, resulting into a period of $\approx 1200\,\mathrm{s}$. On the other hand, the quality factor of the pendulum, Q, is defined as the ratio between the total energy and the energy lost at each cycle. For a simple damped harmonic oscillator, the quality factor Q and the *loss* angle δ are defined as

$$Q = \frac{\sqrt{I\Gamma}}{\beta} \tag{5.5}$$

$$\delta = \frac{1}{Q} \tag{5.6}$$

The quality factor Q is dominated by mechanical dissipation inside the fibre — assuming a low pressure environment. High values of Q are desired to lower the thermal noise dissipation of the fibre and hence to improve the performance of the instrument. Table 5.1 summarizes the main parameters of the 4-mass torsion pendulum.

Parameter	**Symbol**	**Value**	**Units**
Mass	m	0.46	kg
Fibre length	L	1.0	m
Fibre radius	r	25	μm
Arm-length	l	0.1057	m
Momentum of inertia	I	$3.7\cdot 10^{-3}$	kg m^2
Torsion stiffness	Γ	$1.0\cdot 10^{-7}$	N m rad^{-1}
Damping factor	β	$9\cdot 10^{-9}$	N m s
Quality factor	Q	2160	rad^{-1}
Resonant frequency	f_0	≈0.83	mHz
Natural period	T_0	≈1200	s

Table 5.1: Summary of the main parameters of the 4-mass torsion pendulum in nominal operating conditions. Uncertainties are of the order of the smallest digit.

The Laplace transform of Equation 5.1, under the assumption that all initial conditions are zero, leads to the torsion pendulum transfer function

$$\tilde{H}(s) = \frac{1}{I s^2 + \beta s + \Gamma} \tag{5.7}$$

that can also be written as a function of the parameters defined above:

$$\tilde{H}(\omega) = \frac{1}{\Gamma\left[1 - \left(\frac{\omega}{\omega_0}\right)^2 + \frac{j}{Q}\right]} \tag{5.8}$$

where s has been replaced by $j\omega$. Any torque applied to the inertial member induces an oscillation determined by

$$\tilde{\eta}(\omega) = \tilde{H}(\omega)\tilde{N}(\omega) \tag{5.9}$$

In the other way round, and what is of interest for the measurements of the thermal effects, the amplitude of the applied torque is deduced from the induced oscillation on η. However, the measured oscillation $\tilde{\eta}_m(\omega)$ presents a readout noise contribution $\tilde{\eta}_n(\omega)$ [152]

$$\tilde{\eta}_m(\omega) = \tilde{H}(\omega)\tilde{N}(\omega) + \tilde{\eta}_n(\omega) \tag{5.10}$$

In terms of PSD, this is written as

$$S_{\eta_m}(\omega) = S_{\eta,n}(\omega) + |\tilde{H}(\omega)|^2 \, S_N(\omega) \tag{5.11}$$

where the torque $S_N(\omega)$ includes any kind of external perturbation and the thermal dissipation of the fibre. If external perturbations are properly attenuated, the system is limited by the unavoidable thermal noise dissipation in the fibre, which is

$$S_{\text{therm}}(\omega) = 4K_B T \frac{\Gamma}{\omega Q} \tag{5.12}$$

where K_B is the Boltzmann constant and T the fibre temperature. Therefore, the pendulum performance is ultimately limited by the the thermal noise in the fibre, which increases with the torsional stiffness and decreases with the quality factor.

The torque on η is found by applying the inverse of the transfer function to the measured rotation, as

$$\tilde{N}_m(\omega) = \tilde{N}(\omega) + \frac{1}{\tilde{H}(\omega)} \tilde{\eta}_n(\omega) \tag{5.13}$$

and its associated PSD is

$$S_{N_m}(\omega) = S_N(\omega) + \frac{1}{|\tilde{H}(\omega)|^2} S_{\eta,n}(\omega) \tag{5.14}$$

Therefore, the sensitivity limit in the torque measurement is

$$S_{N_m,\text{limit}}(\omega) = S_{\text{therm}}(\omega) + \frac{1}{|\tilde{H}(\omega)|^2} S_{\eta,n}(\omega) \tag{5.15}$$

Figure 5.8 shows the PSD of the pendulum performance as measured by the GRS and by the autocollimator. The theoretical limits described above have been plotted according to the parameters in Table 5.1.

For frequencies higher than 5 mHz, the angular displacement noise —see Figure 5.8, on the *left*— is approximately constant at 0.5 μrad Hz$^{-1/2}$, while below this frequency the performance is dominated by environmental noise. On the other hand, the noise measured by the autocollimator confirms the FEE origin of the noise above 10 mHz. In addition, the GRS readout noise is consistent with an independent measurement, where the readout noise of the capacitive sensors is measured by applying zero bias voltage to the injection electrodes. Figure 5.8 (*left*) also shows the amplitude spectrum of one of these

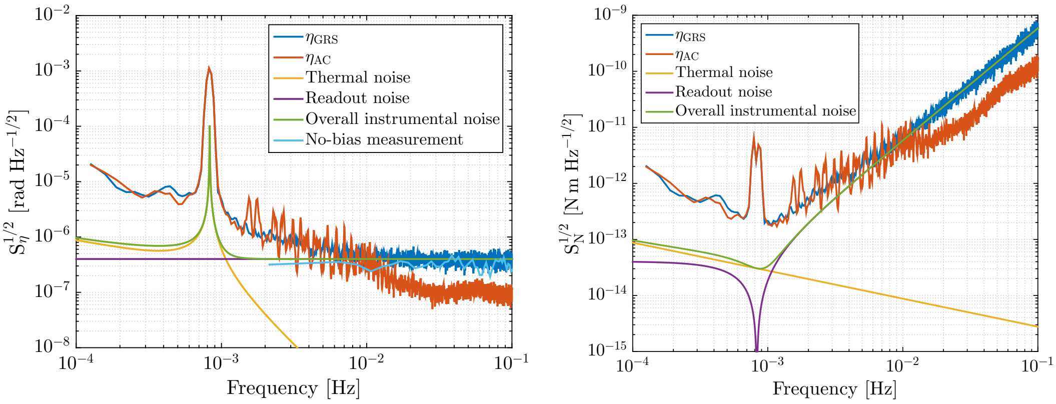

Figure 5.8: Performance plot of the pendulum for η (on the *left*) and for torque (on the *right*) as measured by the GRS prototype and by the autocollimator (AC). The theoretical thermal noise limit and the estimated readout noise of the GRS are also plotted, together with a no-bias measurement that confirms the readout noise floor level at $\approx 4 \cdot 10^{-7}$ rad Hz$^{-1/2}$, for frequencies higher than 10 mHz. As observed, at the range of interest between 1 – 10 mHz the GRS measurements present a better sensitivity than the autocollimator, which exhibits extra oscillations due to readout non-linearities.

measurements in High Resolution (HR) mode, labelled as *No-bias measurement*. Still, the GRS sensitivity in the range between 1 – 10 mHz during the measurement campaign was better than the AC sensitivity, so the former was still preferred for the measurement of the thermal coefficients.

Regarding the measured torque —see Figure 5.8, on the *right*—, the maximum sensitivity is found at both sides of the pendulum resonant frequency, 0.83 mHz, while at this specific frequency the noise is not completely suppressed by the transfer function and still presents a significant peak. In any case, a sensitivity of $2 \cdot 10^{-13}$ N m Hz$^{-1/2}$ is obtained at 1 mHz.

Following that, the estimation of the external net force applied on the GRS Test Mass requires some assumptions:

- The force distributions on the $\pm x$ faces of the GRS Test Mass can be considered homogeneous.
- The inertial member is kept horizontal, with negligible residual misalignments.
- The contribution of net forces on the other masses is negligible in comparison with the forces applied on the GRS Test Mass.

Under these conditions, we estimate the force as the measured torque divided by the nominal arm-length, defined by the distance l between the centre of mass of the whole inertial member and the centre of mass of the GRS Test Mass, as

$$\tilde{F}(\omega) = \frac{\tilde{N}(\omega)}{l} \tag{5.16}$$

5.3 Experiment design

The characterisation of the thermal effects is carried out by carefully measuring the total thermal coefficient α —as defined in Section 4.2— in several scenarios of pressure and temperature. Since each thermal effect presents a different dependence on absolute temperature and pressure, this procedure eventually allows to disentangle the different contributions and to assess their behaviour.

In order to define proper experiment inputs, it is required to previously analyse the temperature environment and characterise the temperature gradient measured as a function of frequency and absolute temperature. In addition, as in the case of the Electrode Housing thermal experiment design in Chapter 4, a set of stability requirements need to be derived to minimise the error of the measured coefficients.

5.3.1 Measurement of the thermal coefficient

The thermal coefficient is measured in a similar way as in the satellite: series of square-wave heating signals at a specific frequency f_{mod} are applied to both $\pm x$ sides of the Electrode Housing, what induces a modulation on the temperature gradient and to the pendulum motion on η. The temperature gradient is directly demodulated from the combined readout of the temperature sensors, and the motion observed needs to be converted to equivalent force. Such conversion is carried out after demodulating the motion on η, what is done in a similar way as explained in Section 4.2.

The demodulation process of the measured angle $\eta(t)$ —including the low pass filter, as described in Section A.5— yields a complex function $\eta_{\mathrm{het}}(t)$. The imaginary and real components of $\eta_{\mathrm{het}}(t)$ are disentangled and averaged as

$$\eta_{\mathrm{het,cos}} = \frac{1}{T}\int_0^T \mathrm{Re}\left\{\eta_{\mathrm{het}}(t)\right\} dt \tag{5.17}$$

$$\eta_{\mathrm{het,sin}} = \frac{1}{T}\int_0^T \mathrm{Im}\left\{\eta_{\mathrm{het}}(t)\right\} dt \tag{5.18}$$

Assuming that the pendulum parameters Q and T_0 are known, the force is measured by means of Equations 5.8 and 5.16, where the stiffness is estimated from the measured period as

$$\Gamma = I\left(\frac{2\pi}{T_0}\right)^2 \tag{5.19}$$

By applying a proper phase delay ψ in order to concentrate all the signal in the sine quadrature $\eta_{\rm het,\,sin}$ —see Section 4.2—, the relation between the demodulated η and te demodulated force is obtained by applying the pendulum transfer function and taking into account the arm-length l, as

$$F_{\rm het,\,sin} = \frac{1}{l}\frac{1}{\Gamma\left(1-\left(\frac{\omega_{\rm mod}}{\omega_0}\right)^2+\frac{j}{Q}\right)}\eta_{\rm het,\,sin} \tag{5.20}$$

By assuming that no other torque contributions are relevant with respect to the thermal-induced forces —i.e. neglecting thermal torques on the fibre, torques on the pendulum head and forces on all the other Test Masses—, the thermal coefficient is finally determined as

$$\alpha = \frac{F_{\rm het,\,sin}}{\Delta T_{\rm het,\,sin}} \tag{5.21}$$

where $\Delta T_{\rm het,\,sin}$ is again the sine quadrature of $\Delta T(t)$. Notice that different modulations may require different delays. This question is addressed in Section 5.4.4.

5.3.2 Modulation frequency

The modulation frequency envisaged for most of the LPF thermal experiments is 1 mHz. However, this frequency is considered too close to the pendulum's main natural mode around η, 0.83 mHz —see Figure 5.8—, so the modulations need to be performed at a slightly different frequency.

A first check on the temperature stability reported a constant noise around $10^{-4}\,{\rm K\,Hz^{-1/2}}$ across the whole milli-Hertz band —see Figure 5.9. The noise at lower frequencies is mainly dominated by the actuation noise from the room temperature control. The absolute temperature inside is controlled to $\Delta T_{\rm abs} < 0.01\,{\rm K}$ in an available temperature range of $15-35\,^\circ{\rm C}$ for measurements up to ~9 h. From this plot we first conclude that any modulation frequency above 5 mHz would allow to estimate the temperature gradient with similar errors.

In order to look for a proper alternative, it is of interest to review the low-pass thermal behaviour of the Electrode Housing prototype, which can be sampled applying series of heat input signals with equal amplitude and different frequencies. For this purpose, the square wave heating signal on heaters H1/H2 is applied here at different modulation frequencies. The applied power per heater is the maximum available at 26 °C, i.e. close to 133 mW, which is useful for the purpose of this chapter but actually infeasible in flight —the available power in flight is limited to 90 mW, as explained in Section 2.2.2.

Figure 5.10 shows the measured peak-to-peak temperature gradient amplitudes together with the predictions from the SSM —see Chapter 4. Since the amount of applied power is not available in the real satellite, the values presented here are scaled to equivalent peak-to-peak values at 90 mW. As expected, a low pass filter behaviour is observed with a cut-off frequency around 3 mHz. The model shows a similar pattern with larger amplitudes and factors varying from ~4 at 0.1 mHz, ~2 at 5 mHz and ~10 at 20 mHz. See

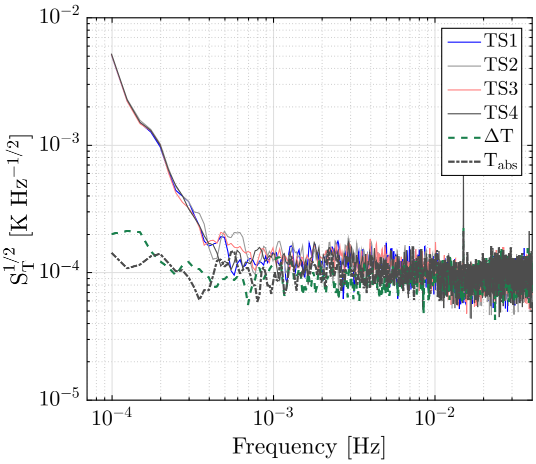

Figure 5.9: Temperature stability in the Electrode Housing including the noise in the temperature gradient and the absolute temperature. The milli-Hertz band is dominated by the system electronic noise.

Appendix E for an extended thermal characterisation of the Electrode Housing prototype.

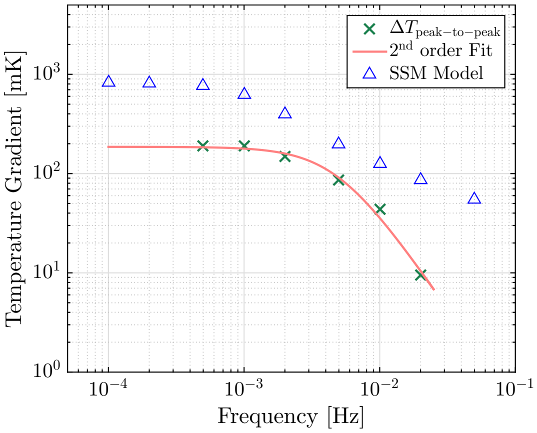

Figure 5.10: Peak-to-peak temperature gradient amplitudes as a function of the applied frequency of the square wave heating signal. The amplitude of the input signal is 90 mW for all cases. The SSM values are extracted from individual simulations at each frequency, while the measured amplitudes have been scaled from an actual applied power of 133 mW.

At 2 mHz, the temperature gradient signal amplitude is still around 80% of the amplitude at 1 mHz, while the effects of the natural oscillation on η do not exceed the band above 1 mHz, as shown in Figure 5.8. In consequence, a frequency of 2 mHz is selected as a compromise point between the natural resonance frequency and the fast temperature gradient roll-off at higher frequencies.

5.3.3 Measurement duration

We can express the minimum integration time required to achieve a certain precision in the estimation of the thermal coefficient α as a function of the measured torque noise S_{N_m}:

$$t_{\mathrm{exp}} \geq \frac{1}{\Delta T^2} \frac{1}{\sigma_\alpha^2} \frac{S_{N_m}}{l^2} \tag{5.22}$$

where ΔT is the amplitude of the signal at the modulation frequency, σ_α is the desired precision and l the arm-length. Therefore, considering a noise in the torque measurement of $S_{N_m}^{1/2} \approx 0.7\,\mathrm{pN\,Hz^{-1/2}}$ and an amplitude of 110 mK at 2 mHz, a minimum integration time of approximately 1 h is required to achieve a precision $\sigma_\alpha \approx 1\,\mathrm{pN\,K^{-1}}$. Such a precision is obtained by requesting a maximum 5% of error in the measurement in cases of low $\alpha \sim 20\,\mathrm{pN\,K^{-1}}$. Nevertheless, in circumstances with higher α values ($\sim$200 $\mathrm{pN\,K^{-1}}$), the measurement durations can be significantly reduced.

5.3.4 Environmental stability requirements

In addition to the errors associated to the sensitivity, the parameters of study —pressure and temperature— present residual fluctuations and drifts due to environmental perturbations that modify the value of the thermal coefficient itself. Such variations must be limited so as the induced change to the thermal coefficient is kept below the deviation σ_α. Regarding the pressure, we define a maximum accepted variation of absolute pressure ΔP^{max} during a measurement, for a desired $\sigma_{\alpha_{\mathrm{RM}}}$ and a *safety* factor 10, as

$$\frac{\partial \alpha_{\mathrm{RM}}}{\partial P} \Delta P^{\mathrm{max}} < \frac{1}{10} \sigma_{\alpha_{\mathrm{RM}}} \tag{5.23}$$

By requesting a $\sigma_{\alpha_{\mathrm{RM}}} \sim 1\%$ at in conditions of $\alpha_{\mathrm{RM}} = 30\,\mathrm{pN\,K^{-1}}$ and pressure of 5 μPa, the pressure variation limit is set to

$$\Delta P^{\mathrm{max}} < 5\ \mathrm{nPa} \tag{5.24}$$

Regarding the temperature variation, the same process described in Section 4.3.1.2 applies here, though a relaxed activation temperature value can be used. For a case with $\Theta_{\mathrm{OG}} \approx 10000\,\mathrm{K}$ and the lowest temperature available (14°C), we obtain a bound of $\Delta T_{\mathrm{abs}}^{\mathrm{max}} < 9$ mK.

Finally, the experiment campaign requires changing the temperature and the pressure several times, what induces strong transients and drifts to both the pressure and the temperature. In the worst cases of very low pressure and temperature conditions, a whole day is necessary to stabilise a new pressure while up to three days may be required to stabilise the temperature inside the Electrode Housing. Such long transients are reduced for conditions of higher pressure and temperature.

5.3.5 Experiment procedure

A plan is configured here to measure the thermal coefficient in a range of temperatures and pressures as wide as possible following the requirements derived in the previous sections. The available intervals of temperature and pressure are presented below:

- Temperature range: from 15°C to 35°C.
- Pressure range: from 3 to 50 μPa. Higher values of pressure are discarded due to a non-linearity in the measurement —see Appendix D.

The measurement campaign is divided in a series of measurements at different absolute temperature levels. At each of these levels, the thermal coefficient is measured at different pressures. The heat input signal is left oscillating all the time. Specifically, the procedure consists on:

1. Start a temperature gradient modulation.
2. Set the thermal control at a given absolute temperature.
    (a) Let it stabilise (2–3 days).
    (b) Set the turbo-molecular pump at a given speed and let the pressure stabilise (~12–24 h).
    (c) Correct the fibre unwinding if necessary and damp the free oscillation of the pendulum.
    (d) Capture a segment of modulated η and ΔT satisfying the experiment requirements with no other perturbations, like extra seismic noise from earthquakes.
    (e) Set a new turbo-molecular pump speed and repeat the process.
3. Set a new temperature level and repeat the process described in step 2.

At least four points of pressure should be obtained at each temperature for a proper characterisation of the pressure dependence. In the same way, an equivalent number of temperature levels should be addressed for the temperature dependence characterisation. Similar experiments have been already assessed in different publications such as [120, 153].

Still, it is desirable to previously check the linearity of the system to confirm that the thermal coefficient does not depend on the temperature gradient amplitude. This is easily checked by measuring the thermal coefficient obtained with different temperature gradient amplitudes at same conditions of pressure and absolute temperature.

Both results from the main experiments together with the linearity checks are presented in the following section.

5.4 Experimental results

The measurement campaign was carried out along different periods between late 2014 and July 2015. Figure 5.11 shows all the accepted thermal coefficient points measured as a function of pressure.

The applied heating signal is a square wave of 10 V, period of 500 s and 50% of duty cycle, with a 250 s delay between the applied signals on the heaters on one x side of the Electrode Housing prototype and the heaters on the other side. The temperature gradient induced in all cases is the maximum available at each absolute temperature, and varies from 61 mW at 14.1°C to 206 mW at 35.6°C.

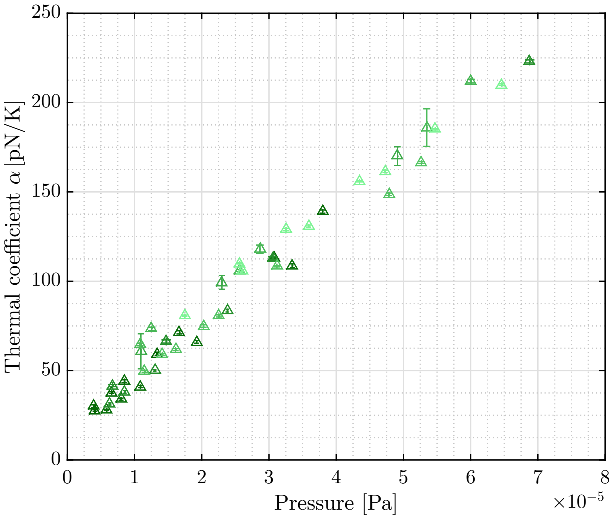

Figure 5.11: Accepted points for the thermal effects characterisation as a function of pressure. The color progression provides an approximated idea of the averaged temperature, from *dark green* for the colder points around 14°C to the *light green* for the hotter ones around 35°C. As observed, the lowest pressures can only be achieved at low temperatures. On the other hand, the clear dependence with pressure strongly indicates the contribution of the radiometer effect.

The analysis of the results is performed in the following way: in first place, the linearity in the measurement of the thermal coefficients is assessed. After that, an analysis over the pressure dependence allows to characterise the radiometer effect. Then, the combined contribution of the outgassing and the radiometer effects are disentangled from the global thermal coefficient. Finally, there is a short discussion on the dependence on pressure observed in the relative delay between the temperature gradient and the modulated η.

5.4.1 Linearity check test

The aim of this test is to verify that the force is linear with the temperature gradient amplitude. This is evaluated here by applying input heat modulations of

2 mHz with different voltage amplitudes. The environmental parameters are set to $P = (1.03 \pm 0.06) \cdot 10^{-5}$ Pa and $T_{\text{abs}} = (26 \pm 1)$°C. Figure 5.12 shows the results for the force with respect to the applied temperature gradient amplitude together with the residuals from the fit. Fit results with errors are presented in Table 5.2

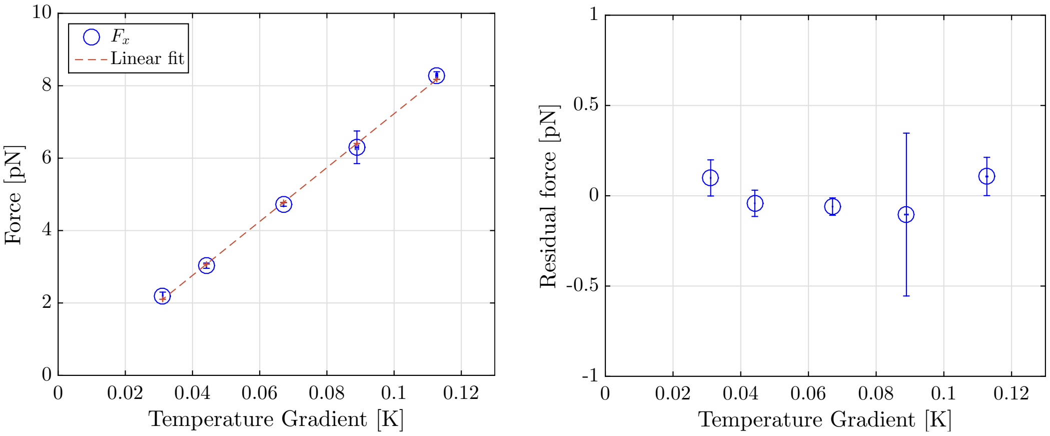

Figure 5.12: *Left:* Force amplitude with respect to the applied temperature gradient amplitude oscillating at 2 mHz. *Right:* Residual values of the fit.

Fit function	a	b
$F_x = a + b\Delta T$	-0.2 ± 0.4 [pN]	74 ± 5 [pN K^{-1}]

Table 5.2: Estimated values of the fit. A linear function $y = a + bx$ is applied to fit both plots in Figure 5.12. Coefficients within 95% confidence bounds.

As expected, both the force and the thermal coefficients are consistent with the hypothesis of linearity, which imposes no force at $\Delta T = 0$ and constant coefficient α. The errors observed in Figure 5.12 are dominated by environmental perturbations affecting the different measurements.

5.4.2 Pressure-dependent radiometer effect characterisation

The radiometer effect contribution has been modelled in Section 2.1.1.1 as

$$\alpha_{\text{RM}} = \frac{1}{4} k_{\text{RM}} A_{\text{TM}} \frac{P}{T} \tag{5.25}$$

where A_{TM} is the area of one face of the Test Mass, P the nominal pressure and T the absolute temperature. Under the pressure-controlled environment of the vacuum chamber, the contribution of the radiometer effect is estimated by measuring the thermal coefficient at different pressures keeping the absolute temperature stable. Since the radiometer effect is the only pressure-dependent term, it is found by

$$\alpha_{\mathrm{RM}} = \left(\frac{\partial \alpha_m}{\partial P}\right) P \tag{5.26}$$

where α_m is the measured coefficient.

Thus, the slope of the resulting thermal coefficient vs. pressure plot is directly the contribution of the radiometer effect at a given temperature. For this analysis, the measurement of the pressure itself is a critical step that can easily introduce errors in the estimation of the parameters. In this sense, some considerations including systematic effects and corrections due to the residual gas composition have been applied to the raw pressure measurement —for more details refer to Appendix D. Figure 5.13 shows the results of two series of thermal coefficient measurements at different pressures and at two different temperature levels. Notice the slope reduction and the increment of the $P = 0$ intercept at higher temperature, which is associated to a reduction of the radiometer effect —see also Figure 5.14– and to an increment of both outgassing and radiation pressure.

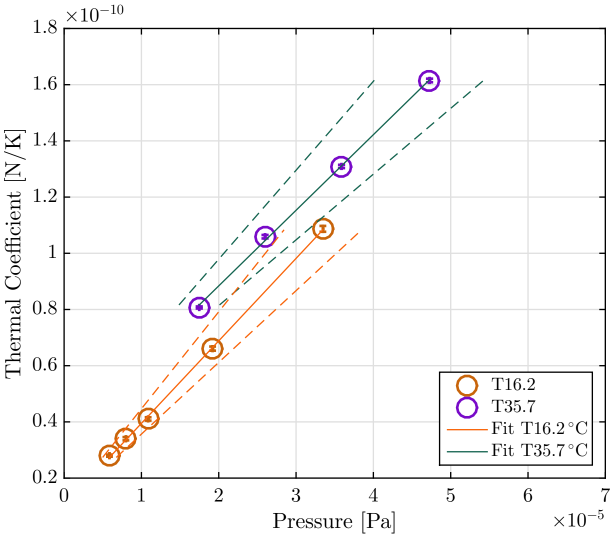

Figure 5.13: Thermal coefficient vs. pressure for two different temperatures, $T_{\mathrm{abs}} = 16.2°\mathrm{C}$ and $T_{\mathrm{abs}} = 35.7°\mathrm{C}$. The systematic errors are also represented (*dashed* lines). The slope reduction at high temperature —see also Figure 5.14— is consistent with a reduction of the radiometer effect, while the increment of the independent term at high temperature is associated to an increase of both outgassing and radiation pressure. The factor 4 between the lowest pressures achieved at each temperature corresponds to the vacuum chamber temperature-dependent outgassing, which forces the system to reach different equilibrium pressures though in both cases the turbo-pump is set to its maximum speed at 27000 rpm.

The term including the constant parameters in Equation 5.25 —i.e. the product $\frac{1}{4}k_{\mathrm{RM}}A_{\mathrm{TM}}$— is estimated by fitting the slopes obtained as a function of temperature. Since this slope is expected to be proportional to $1/T$, the fitted slopes are actually normalised by multiplying per T_{abs}. Figure 5.14 shows the measured and normalised slopes, where measurements at 12 different temperatures are considered with a minimum of 4 pressure points per temperature. Table 5.3 shows the coefficients of the fitted slopes.

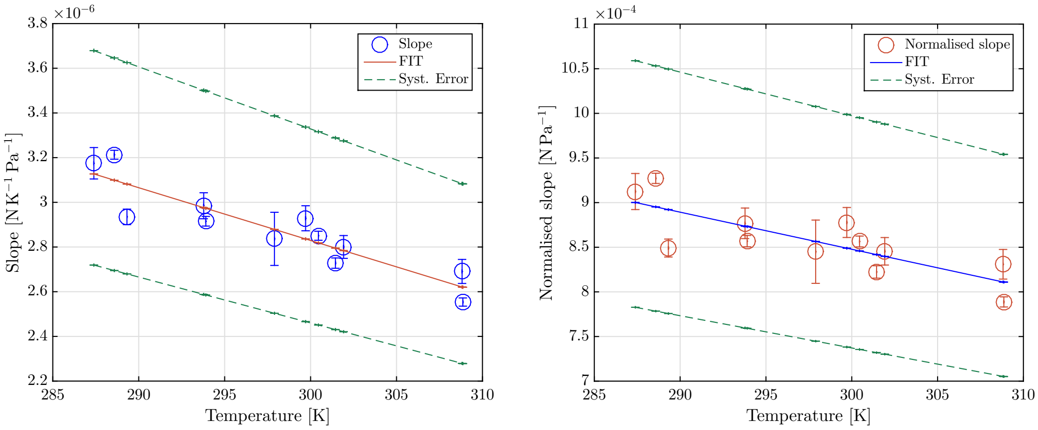

Figure 5.14: Radiometer effect measured slopes (*left*) and normalised slopes (*right*) including systematic errors (*dashed green* lines).

Fit function	a	b
$\frac{\partial\alpha}{\partial P} = a + bT$	$(1.1 \pm 0.3)\cdot 10^{-5}\,[\mathrm{N\,K^{-1}\,Pa^{-1}}]$	$(-2.8 \pm 0.8)\cdot 10^{-8}\,[\mathrm{N\,K^{-2}\,Pa^{-1}}]$
$\left(\frac{\partial\alpha}{\partial P}\right)_{\mathrm{norm}} = a + bT$	$(2.5 \pm 0.7)\cdot 10^{-3}\,[\mathrm{N\,Pa^{-1}}]$	$(-5.5 \pm 2.5)\cdot 10^{-6}\,[\mathrm{N\,K^{-1}\,Pa^{-1}}]$

Table 5.3: Estimated values obtained from fitting the measured and the normalised slopes in Figure 5.14. The fit function applied to both plots is $y = a + bx$. Coefficients within 95% confidence bounds.

The slope coefficient in Figure 5.14 (*left*) clearly decreases with temperature, though it slightly exceeds the expected value measured in former campaigns. Indeed, in previous campaigns, a leak in the chamber had been detected and reported contributions of $2.4\cdot 10^{-6}\,\mathrm{N\,K^{-1}\,Pa^{-1}}$ [154] at ≈25°C instead of the values around $2.8\cdot 10^{-6}\,\mathrm{N\,K^{-1}\,Pa^{-1}}$ measured here. Since a leak in the chamber leads to an atmosphere with less percentage of hydrogen, the pressure readout in presence of the leak is assumed to be more realistic than the pressure readout without the leak. Indeed, pressure measurements in atmospheres with significant percentages of hydrogen lead to pressure readouts lower than the actual pressure inside. Though the residual atmosphere composition in the chamber has been analysed in Appendix D in order to determine a proper correction factor to this effect, the slope reported here suggests that the pressure measurement still underestimates the percentage of hydrogen. *right*.

The normalised slope shown in Figure 5.14 (*right*) still presents a significant temperature component. As in the previous case, such an observed variation with temperature could be attributed to an effect of the residual composition inside the vacuum chamber leading to errors in the pressure readout. In this sense, recent investigation on how the pressure is measured in the facility indicate a possible hydrogen-composition dependence on the pumping speed.

5.4.3 Asymmetric outgassing vs. radiation pressure

The extrapolation of the different thermal coefficient fitted functions to zero pressure points leads to an estimation of the combined contribution of outgassing and radiation pressure by cancelling the radiometer contribution, since the latter is proportional to P. Figure 5.15 shows the $\alpha_{\mathrm{P=0}}(T)$ estimated points considered in the analysis, where the measurements are classified in two series depending on the period when they were taken: Winter-2014 and Summer-2015. The outgassing is clearly the dominating contribution in both since the thermal coefficient presents a temperature dependence greater than T^3. In addition, the decay in time observed between the two sequences, i.e. from Winter-2014 to Summer-2015, is attributed as well to a reduction of the outgassing effect. We remind here the model for the outgassing effect introduced in Chapter 2, in Equations 2.5 and 2.2:

$$\alpha_{\mathrm{OG}} = A_{\mathrm{TM}} \frac{Q_{\mathrm{rate}}}{C_{\mathrm{eff}}} \frac{\Theta_{\mathrm{OG}}}{T_0^2} \tag{5.27}$$

with

$$Q_{\mathrm{rate}} = Q_0 e^{-\frac{\Theta_{\mathrm{OG}}}{T_0}} \tag{5.28}$$

A direct fit with only the contribution of outgassing and radiation pressure should allow to identify their contributions. However, the fit by means of the outgassing expression in Equation 5.27 results infeasible due to the huge variability of the exponential term in Equation 5.28, which makes the fitting procedure impractical with the available temperature span. In order to proceed, a second order Taylor expansion is applied —see Appendix C for more details:

$$\alpha_{\mathrm{OG,FIT}} = K_1 \left(3 - \frac{\Theta_{\mathrm{OG}}}{T_0} + K_2\right) + \frac{K_1}{T_0}\left(\frac{\Theta_{\mathrm{OG}}}{T_0} - 2 - 2K_2\right) T + \frac{K_1 K_2}{T_0^2} T^2 \tag{5.29}$$

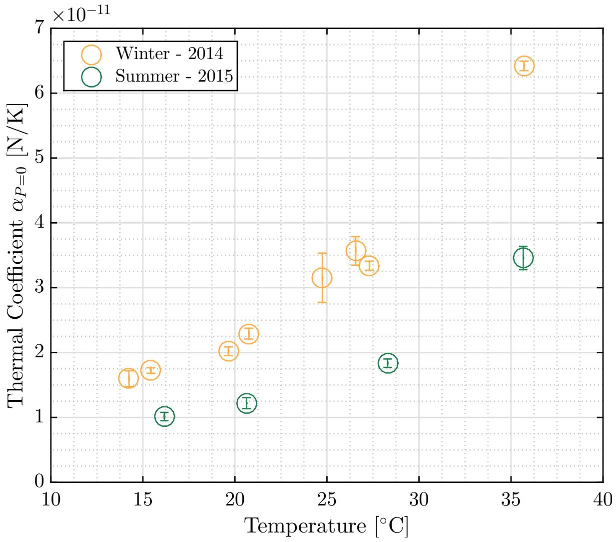

Figure 5.15: Distribution of $\alpha_{\mathrm{P=0}}$ points, classified in two series depending on the phase when they were measured. An exponential dependence on temperature, clearly greater than $\propto T^3$, is evident for both series. The reduction in the *Summer* series coefficients is attributed to a decrease of the outgassing rate with time.

where

$$K_1 = \frac{Q_0}{T_0^2} e^{-\left(\frac{\Theta_{\mathrm{OG}}}{T_0}\right)} \tag{5.30}$$

$$K_2 = \frac{1}{2}\left(6 - \frac{6\Theta_{\mathrm{OG}}}{T_0} + \frac{\Theta_{\mathrm{OG}}^2}{T_0^2}\right) \tag{5.31}$$

Such an approximation ends up with the following expression for the outgassing contribution:

$$\alpha_{\mathrm{OG,FIT}} = A + BT + CT^2 \tag{5.32}$$

Still, a fit using the expression in Equation 5.32 and an additional term DT^3 to account for the radiation pressure contribution provides inconsistent results. The alternative followed is to assume a given contribution of radiation pressure, considering that it is much more stable than the outgassing. The contribution is defined assuming $K_{\mathrm{RP}} = 0.32$, i.e. considering specular reflection on the EH/TM system [120]. The resulting contribution is subtracted from the thermal coefficients at $P = 0$ and the estimated outgassing is then fitted by means of Equation 5.32.

The results of the fit are plotted in Figure 5.16 for both sequences of points together with the assumed radiation pressure contribution, showing a good agreement with the distribution —see Table 5.4. The error propagation analysis associated to these results is detailed in Appendix C, Section C.2.

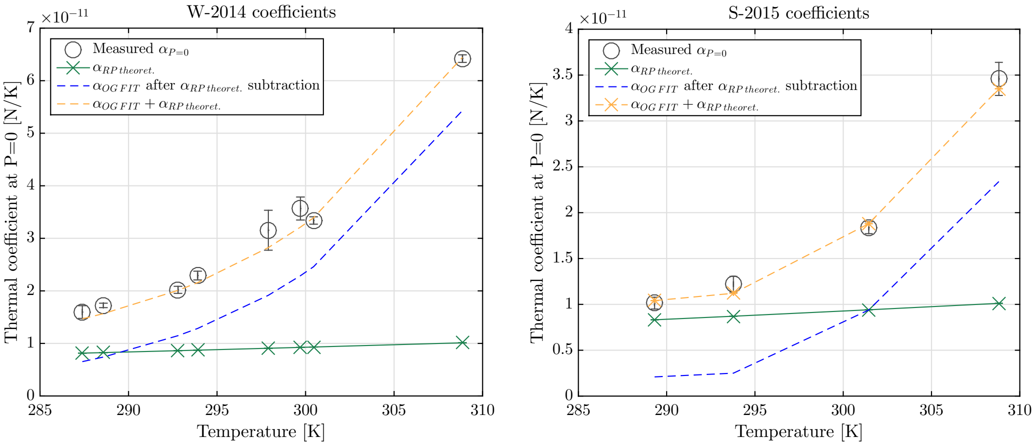

Figure 5.16: Fitted functions of the two sequences *Winter-2014* and *Summer-2015* (*W-2014* and *S-2015*, respectively) of $\alpha_{\mathrm{P}=0}$ estimated coefficients. In both cases the contribution of the radiation pressure is assumed from [120].

	W − 2014			**S − 2015**		
Parameter	**Value**	**Unit**	**Error**	**Value**	**Unit**	**Error**
A	$8.2 \cdot 10^{-9}$	$\mathrm{N\,K^{-1}}$	7%	$6 \cdot 10^{-9}$	$\mathrm{N\,K^{-1}}$	20%
B	$-5.7 \cdot 10^{-11}$	$\mathrm{N\,K^{-2}}$	7%	$-3.9 \cdot 10^{-11}$	$\mathrm{N\,K^{-2}}$	20%
C	$9.9 \cdot 10^{-14}$	$\mathrm{N\,K^{-3}}$	6%	$6.7 \cdot 10^{-14}$	$\mathrm{N\,K^{-3}}$	20%
Θ_{OG}	$1.11 \cdot 10^{4}$	K	4%	$1.72 \cdot 10^{4}$	K	20%
Q_{rate}	$2.3 \cdot 10^{-9}$	$\mathrm{J\,s^{-1}}$	9%	$3.15 \cdot 10^{-10}$	$\mathrm{J\,s^{-1}}$	50%

Table 5.4: Estimated outgassing parameters for both sequences *Winter-2014* and *Summer-2015* (**W-2014** and **S-2015**, respectively).

The decrease of the activation temperature with time, up to a factor two, is consistent with the decay of the outgassing between the two series. Indeed, each Θ_{OG} value is a kind of averaged $\Theta_{\mathrm{OG},k}$ corresponding to the k different species being outgassed from the surfaces. After some time —months, etc.—, the species with low activation temperature may have already vanished while other species with higher $\Theta_{\mathrm{OG},k}$ may keep still outgassing, increasing the averaged Θ_{OG} of the system. In the latter case, species with high activation temperatures are dominating the outgassing at that moment.

Finally, since the Electrode Housing prototype installed in the pendulum has not been as baked out as the flight model one, the outgassing contributions estimated here can be considered upper bounds for the outgassing level during the flight.

5.4.4 Phase delay in the thermal modulations

So far, the focus has been placed on the demodulated amplitude of the thermal coefficients at different pressures and temperatures, leaving aside other information such as the phase between modulated signals. Concerning the latter, two kind of delays are combined into the phase:

a) A delay between the heater activation signal and the temperature gradient measured by the sensors.

b) A delay between the temperature gradient measured by the sensors and the forces measured by the pendulum.

The delay in *(a)* is expected to be constant, since its origin is purely dependent on the thermal couplings between the location of the heaters and the location of the sensors. Across the range of the temperatures and pressures investigated, such links remain practically constant. Indeed, delays close to 70 s at the modulation frequency have been measured during the campaign, without significant variations.

The case *(b)* should be similar and present a constant delay between the temperature gradient signal —based on the thermistor readouts— and the actual temperature gradient inside the Electrode Housing. However, this is not the case. The differential phase between the modulated temperature and the force exhibits a clear dependence on the pressure at different temperatures. This is exposed in Figure 5.17, where the delays in some of the measurements including autocollimator readouts are plotted showing a clear correlation with the pressure. At first glance, such a delay can only be explained by a variation of the damping factor β with the pressure, i.e. the presence of a significant $\partial\beta/\partial P \neq 0$.

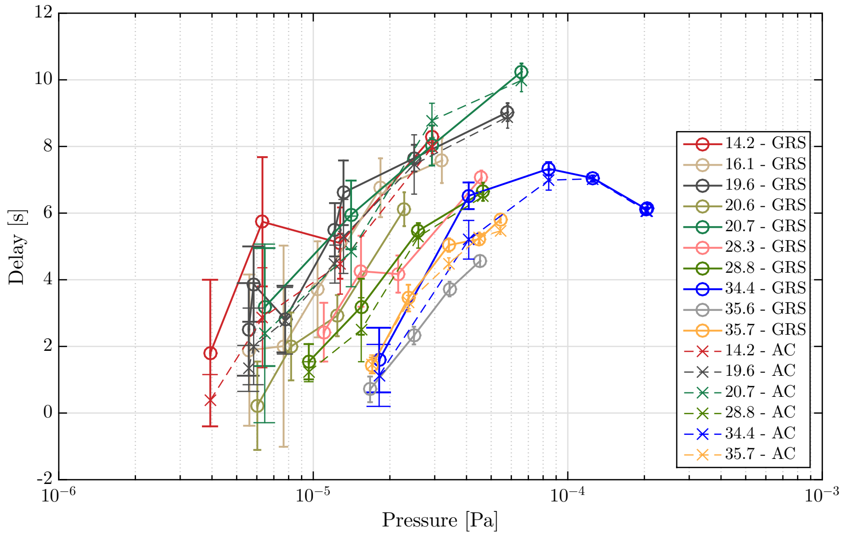

Figure 5.17: Relative delay between the temperature gradient and the force on the mass at 2 mHz for both GRS and autocollimator measurements, suggesting a dependence on the pressure.

The η-angle to x-force transfer function, derived from Equations 5.7 and 5.16 and represented in polar notation, provides the expression for the delay $\Phi(\omega)$ between the force —directly proportional to the temperature gradient— and the angle readout:

$$\begin{aligned} H_F(\omega) &= A(\omega)\underline{/\Phi(\omega)} \\ &= \frac{l}{\sqrt{\left(\Gamma-\omega^2 I\right)^2+\left(\omega\beta\right)^2}}\underline{/-\arctan\left(\frac{\omega\beta}{\Gamma-\omega^2 I}\right)} \end{aligned} \tag{5.33}$$

where the relative delay is $\Phi(\omega) = -\arctan\left(\frac{\omega\beta}{\Gamma-\omega^2 I}\right)$. A variation in the damping factor β induces a change of the phase at the same frequency as

$$\Delta\Phi(\omega) = \frac{\partial\Phi(\omega)}{\partial\beta}\Delta\beta \tag{5.34}$$

The coupling term $\partial\Phi/\partial\beta$ is found by differentiating the $\Phi(\omega)$ function as

$$\frac{\partial\Phi}{\partial\beta} = \left(\frac{\omega}{\omega^2 I-\Gamma}\right)\frac{1}{1+\left(\frac{\omega\beta}{\Gamma-\omega^2 I}\right)^2} \tag{5.35}$$

According to a $\partial\beta/\partial P = 9.4\pm0.2\cdot10^{-6}\,\mathrm{m}^3\,\mathrm{s}$ as reported in [98], the expected variation of β in front of a ΔP of 50 μPa is $\sim 5\cdot10^{-10}$ Nms. Delays of $\sim$1 ms are consequently obtained by evaluating this variation with Equation 5.34 at 2 mHz and a pendulum $Q = 2160$ and period 1210 s. Such a short delay clearly discards the damping term $\beta(P)$ as the mechanism inducing the observed delay, leaving as candidates other issues concerning the pendulum structure such as the fibre or the Electrode Housing venting holes. In any case, such an effect that could provide an alternative estimation of the pressure inside the Electrode Housing —if properly characterised— is not expected to appear in flight.

5.5 Conclusions and heritage to LISA Pathfinder

Torsion pendulums have experienced an intense development along the last decades, becoming nowadays extremely useful tools to study low-force effects in many fields and specially of interest in their implementation as inertial sensors. In this chapter, we have used a setup mimicking the nearly free-fall performance of one LPF Inertial Sensor in one of its degrees of freedom. Since the GRS prototype installed is equipped with the whole set of temperature diagnostics items, the setup allows the Electrode Housing thermal experiment to be tested.

As a result, the measurement campaign has allowed to estimate the contribution of the different thermal effects in different conditions of pressure and temperature. The radiometer effect has been characterised by estimating the thermal coefficient at different pressures, yielding the following relation for the slope of the radiation effect, i.e. for the radiation effect dependence on temperature

$$\frac{\partial \alpha}{\partial P} = (1.1 \pm 0.3) \cdot 10^{-5}\,\mathrm{N\,K^{-1}\,Pa^{-1}} - \left((2.8 \pm 0.8) \cdot 10^{-8}\,\mathrm{N\,K^{-2}\,Pa^{-1}}\right) T \tag{5.36}$$

where T is in [K] and the resulting units are [$\mathrm{N\,K^{-1}\,Pa^{-1}}$]. Such a dependence on temperature provides slope values around ~15% higher than expected, what has been attributed to an underestimation of the pressure readout. In this sense, a recent investigation points to a dependence of the hydrogen composition on the speed of the pump. Further analysis would provide more accurate pressure measurements.

On the other hand, the combined contribution of outgassing effect and the radiation pressure has been characterised by extrapolating to $P = 0$ the coefficients obtained at different temperatures. The individual weights of each of them remain difficult to disentangle due to the high outgassing contribution with respect to the radiation pressure effect, though approximated values for the outgassing effect have been estimated by assuming a nominal radiation pressure contribution.

Based on the results obtained here, it is of interest to figure out the different scenarios that can be met in flight. Three cases are to be considered:

- **Nominal case**: In conditions of nominal pressure (10^{-5} Pa), the total contribution varies between 40 and 60 pN $\mathrm{K^{-1}}$ depending on the temperature. The radiometer effect arises as the major contributor with ≈25 pN $\mathrm{K^{-1}}$ followed by the outgassing effect. The radiation pressure is expected to contribute with roughly 10 pN $\mathrm{K^{-1}}$.

- **Best case**: If the residual pressure is as low as current expectation (10^{-6} Pa), the contribution of the radiometer decreases down to <5 pN $\mathrm{K^{-1}}$. In such circumstances, the total coupling is 20–40 pN $\mathrm{K^{-1}}$, with a similar contribution of radiation pressure and outgassing effects.

- **Worst case**: In a given scenario with too high pressure associated to high outgassing fluxes in the vacuum enclosures (i.e. $5 \cdot 10^{-5}$ Pa), the total coupling achieves values ≈150–170 pN $\mathrm{K^{-1}}$ due to the linear dependence on pressure of the radiometer effect, which clearly dominates the contribution.

Nevertheless, for pressure conditions higher than 10^{-5} Pa, the Brownian noise arises as the major contributor. The final pressure value will remain unpredictable until the Test Masses are released by the Cage and Vent Mechanism.

In terms of noise contribution to the residual differential acceleration, for a nominal temperature gradient noise of $10^{-4}\,\mathrm{K\,Hz^{-1/2}}$, the corresponding total contributions in the previous cases would be $7 \cdot 10^{-15}\,\mathrm{m\,s^{2}\,Hz^{1/2}}$ (nominal case), $1.4 \cdot 10^{-15}\,\mathrm{m\,s^{2}\,Hz^{1/2}}$ (best case) and $2.3 \cdot 10^{-14}\,\mathrm{m\,s^{2}\,Hz^{1/2}}$ (worst case) —accounting for two masses with similar thermal contributions. All these noise levels would significantly benefit from the current expected temperature stability in the Electrode Housings, which is a factor 10 better, down to $10^{-5}\,\mathrm{K\,Hz^{-1/2}}$. If such a temperature gradient stability is achieved, all the cases considered here will remain inside the allocated noise budget.

Finally, a dependence between the pressure and the relative phase between the modulated temperature gradient and the motion induced to the pendulum has been detected. Though the driving mechanism has not yet been identified and it is presumably associated to the pendulum structure rather than to the GRS prototype, it is of interest to follow with its investigation. Indeed, any additional information with respect to the pressure inside the Test Masses cavity will be precious in the attempt to estimate the Brownian noise contribution.

CHAPTER 6

Thermo-elastic noise in the LISA Technology Package

The LTP Optical Metrology System (OMS) is exposed to thermo-elastic effects that can eventually induce phase noise to its different readouts. One characteristic of this kind of noise is that temperature fluctuations away from the bench can turn out into interferometer signals, in particular if they affect key parts of the structure that induce mechanical distortions to the Optical Bench (OB).

The procedure to identify the critical temperature fluctuation sources and to characterise their associated mechanical distortion modes requires to compare different temperature sensor readouts with the OMS main signals. Eventual high strong temperature variations on thermo-elastic sensitive locations will produce a pattern correlated with the OMS channels, but not necessarily correlated with the temperature sensors close to the Optical Bench.

The LTP noise budget document assigns a total of $3\,\mathrm{pm\,Hz^{-1/2}}$ to the thermo-elastic noise contribution to the OMS through Optical Bench distortion [75]. Such allocation is actually the correlated sum of the quantity designed for thermo-elastic distortions in the Optical Bench itself due to temperature fluctuations *inside* the same Optical Bench ($2\,\mathrm{pm\,Hz^{-1/2}}$) and thermo-elastic distortions of the Optical Bench due to temperature fluctuations *outside* the Optical Bench ($1\,\mathrm{pm\,Hz^{-1/2}}$). The case of temperature noise in the Optical Window, the only optical part located outside the Optical Bench, is considered apart and receives a special treatment —see Section 2.1.3 [127]. Therefore, the contribution of eventual thermo-elastic noise in the Optical Window is excluded from this noise budget and it is not going to be considered in this chapter.

The thermo-elastic noise affecting the Optical Bench is more likely to be dominated by temperature noise in the Suspension Struts. This is mainly due to:

- Temperature noise inside the Optical Bench is expected to be highly suppressed in comparison with temperature noise at the Suspension Struts. Indeed, the struts actuate as low-pass filters with a factor ~80 of attenuation at 1 mHz —see Appendix F. In front of an eventual scenario with temperature noise of $10^{-4}\,\mathrm{K\,Hz^{-1/2}}$ at the edge of a strut, its contribution at the other edge would remain $\leq 10^{-5}\,\mathrm{K\,Hz^{-1/2}}$. Such level is actually below the sensitivity limit of the measurement system —see Section 2.2.1.2.

- The Optical Bench is essentially composed of Zerodur® [155] with fused silica components attached through hydroxide-catalysis bonding [84]. This material presents a significantly lower thermal expansion coefficient than the struts (composed mainly of Titanium and CFRP). However, the fact that all of them present similar Young Modulus and size suggests that eventual thermal expansion of the struts may affect the Optical Bench. Some properties of interest regarding the different LCA structural materials are presented in Table 6.1.

Material	**Thermal Expansion** $[\mathrm{K}^{-1}]$	**Specific heat Conductivity** $[\mathrm{W\,m^{-1}\,K^{-1}}]$	**Thermal Capacity** $[\mathrm{J\,kg^{-1}\,K^{-1}}]$	**Young Modulus** [Pa]	**Density** $[\mathrm{kg\,m^{-3}}]$
Zerodur®	$5\cdot10^{-8}$	1.46	820	$9.1\cdot10^{10}$	2530
CFRP	$8.3\cdot10^{-7}$	~20–200	~700	$3.4\cdot10^{11}$	2000
Titanium	$8.6\cdot10^{-6}$	17	540	$1.1\cdot10^{11}$	4500

Table 6.1: Basic thermal and mechanical properties of the main structural materials in the LCA at ~$25^{\circ\mathrm{C}}$.

The subtraction of the *reference* readout to the different OMS motion channels as explained in Section 1.3.1.2 significantly cancels the effects from mechanical distortion outside the Optical Bench to the OMS motion readouts. However such cancellation does not include the mechanical distortion of the Optical Bench itself due to temperature fluctuations *outside* the Optical Bench, what can induce pathlength differences between the pairs of beams of each interferometer. Such a mechanism is going to be characterised in-flight by series of experiments injecting heat signals to the different struts that attach the LCA to the spacecraft structure. Figure 6.1 shows the Optical Bench with some of the different optical parts already assembled.

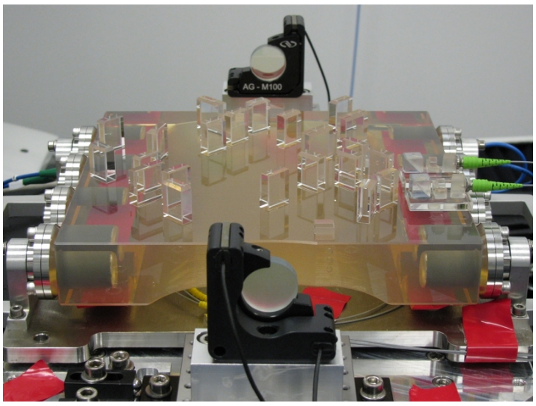

Figure 6.1: Flight Model of the Optical Bench before mounting the photodiodes. The structural material is Zerodur®. Credits: University of Glasgow [84].

Due to (1) the complexity of the mechanism describing these effects, together with (2) the possibility of performing on-ground validation tests, the procedure to design this experiment has followed an experimental approach. In this sense, spacecraft thermal-vacuum tests are the first realistic scenarios where these experiments can be tested. For the particular case of the struts experiments, the On-Station Thermal Test (OSTT) campaign that took place late in 2011 was an excellent opportunity to activate the strut heaters and measure the perturbation induced in the OMS. The results of such investigation are presented in this chapter, organised as follows: the relevant items are introduced and the experiment is reviewed in Section 6.1, then the available set-up during the campaign and the experiments performed are described in Section 6.2. Results are introduced in Section 6.3.1. Following to that, the thermo-elastic noise contribution to the optical metrology is presented in Section 6.4, to then finally discuss the conclusions in Section 6.5. Part of the work presented in this chapter has been published in [108].

6.1 Struts experiment design

The characterisation of thermo-elastic noise consequences on the LTP is performed by the heaters and sensors placed on six of the eight LCA struts. Heat pulses with power up to ∼2 W can be applied to each heater, inducing local temperature increments up to ≈10 K at the center of each strut. Such heating profile produces an expansion of the strut of the order ∼1 nm —under the same assumptions applied in Section 2.1.2—, representing a significant stress to the LCA structure clearly sensed by the interferometer [108]. In addition, the real phase shift observed also depends on factors like the components of the nominal optical pathlengths aligned with each DOF. Since a beam may circulate multiple times along the same direction x or y on the Optical Bench, the effect of an eventual Optical Bench bending can be amplified.

Since the LCA roughly presents three planes of symmetry, the same heat signal applied to the different struts induce similar stress to the LTP Core Assembly but with different directions. This eases the mechanism identification by observing the sign of the perturbed interferometer signals. Therefore, the main purpose of the struts experiments is to apply the same kinds of perturbations to different points of the LCA, i.e. to inject identical heat signals to each of the heaters on the struts individually. Series of pulses at frequencies close to 1 mHz with high power and low duty cycle are convenient options to maximise the strut elongation while remaining in the band of interest.

The measured coupling coefficient at a given strut is defined as

$$k_{\mathrm{m}}(\omega) = \frac{\Phi(\omega)}{T_{\mathrm{m}}(\omega)} \tag{6.1}$$

where $\Phi(\omega)$ is the Fourier transform of the time series of the OMS differential displacement, $T_{\mathrm{m}}(\omega)$ is the Fourier transforms of the measured temperature on the strut, and $k_{\mathrm{m}}(\omega)$ is the measured transfer function between them. As stated before, the heat pattern applied during the measurements induces strong signals on both the interferometer and the measured temperature on the heated strut. This allows to directly estimate the transfer function $k_{\mathrm{m}}(\omega)$ by doing —see Equation A.34 in Appendix A:

$$k_{\mathrm{m}}(\omega) = \frac{S_{T_{\mathrm{m}}\Phi}(\omega)}{S_{T_{\mathrm{m}}T_{\mathrm{m}}}(\omega)} \tag{6.2}$$

where $S_{T_{\mathrm{m}}\Phi}(\omega)$ and $S_{T_{\mathrm{m}}T_{\mathrm{m}}}(\omega)$ are the cross-power spectral density and the power spectral density of the measured signals.

With this transfer function we can already calculate a first noise projection of the temperature noise on a given strut to equivalent noise in the interferometer, as

$$S^{1/2}_{\Phi,T_{\mathrm{m}}}(\omega) = k_{\mathrm{m}}(\omega) S^{1/2}_{T_{\mathrm{m}}}(\omega) \tag{6.3}$$

However, the results of this transfer do not include the differences between the temperature distribution on the strut during the experiment and during a nominal noise run. Indeed, in order to obtain a more accurate noise projection it is necessary to analyse the differences between the strut temperature distribution when *measuring* the coupling and the temperature distribution when *projecting* the coupling on a certain measurement of noise.

As stated in Section 2.1.2, the constrained elongation of the strut is dependent on its spatially-averaged temperature T_{av}. In terms of noise, this is written as

$$S^{1/2}_{l,\mathrm{const.}}(\omega) = K\, L\, \alpha\, S^{1/2}_{T_{\mathrm{av}}}(\omega) \tag{6.4}$$

where α is the averaged thermal expansion coefficient of the strut, L the nominal length of the strut and K the factor accounting for the strut physical constrains with respect to its free elongation and estimated ~1/80. The spatially-averaged temperature of a given strut is defined as

$$T_{\mathrm{av}}(t) = \frac{1}{L}\int_0^L T(x,t)\,dx \tag{6.5}$$

where L is the nominal length of the strut and $T(x,t)$ the temperature distribution function along its length. So, the thermo-elastic perturbation depends on the temperature distribution function $T(x,t)$, but we *only* measure the temperature at the central part of the strut —where the sensor is located. During the heater activations, the temperature distribution function $T(x,t)$ presents a maximum in the middle of the strut, decreasing to the edges because the heaters are placed approximately in the central part of each strut. Since the strut temperature sensors are placed reasonably close to the heaters, their readouts during the thermal experiments mainly report the highest values of the temperature distribution function. An estimation of the thermal transfer function in Appendix F provides a 10% of attenuation between temperature fluctuations at the middle of the strut and temperature fluctuations at the edges at 1 mHz. Consequently, we approximate:

$$T_{\mathrm{av}} \approx \frac{1}{2} T_{\mathrm{m}} \tag{6.6}$$

where T_{m} is the measured temperature on the strut. Such a difference between the spatially-averaged temperature and the measured temperature already suggests a factor 2 in the correction of the measured coefficient k_{m} at 1 mHz.

Moreover, during nominal noise measurements, the measured temperature noise may be different from the spatially-averaged temperature noise of the strut. In the worst-case scenario, the sections with highest temperature noise may be located close to the spacecraft structure while the measured temperature noise may be lower due to the strut self-attenuation. This effect could lead to another underestimation of the averaged temperature of the strut and in consequence to an underestimation of *real* physical effect during normal noise measurements. In order to correct this deviation, we estimate a certain temperature noise at the edge $S_{T_{\mathrm{edge}}}$ that is progressively damped along the strut. At 1 mHz, the noise at the centre of the strut is about 10% of the noise at the edge, while the noise at the opposite edge —the edge in contact with the LCA— is about 1% of the noise at the external edge as calculated in Appendix F. According to these attenuation factors, and assuming noise totally correlated along the strut, the spatially-averaged temperature noise of the strut and the measured temperature noise are approximated as

$$S_{T_{\mathrm{av}}}^{1/2} \approx \frac{1}{4} S_{T_{\mathrm{edge}}}^{1/2} \tag{6.7}$$

$$S_{T_{\mathrm{m}}}^{1/2} \approx \frac{1}{10} S_{T_{\mathrm{edge}}}^{1/2} \tag{6.8}$$

These approximations allow to estimate the spatially-averaged temperature from the temperature measurement, leading to the approximation:

$$S_{T_{\mathrm{av}}}^{1/2} \approx \frac{5}{2} S_{T_{\mathrm{m}}}^{1/2} \tag{6.9}$$

Following to these observations, we obtain a correction factor ~5. This factor is only to be applied to the theoretical temperature noise projection in order to account for the differences between the spatially-averaged temperature and the measured temperature during nominal noise measurements. Notice that this approximation is only valid for the frequency 1 mHz.

In addition, the yield of the experiment, though being reported by transfer functions, must be consistent with a constant coupling across the LPF band for each combination of heated-strut and OMS readout. Indeed, since the frequency response in the milli-

Figure 6.2: IABG mbH space vacuum chamber with the satellite during the OSTT campaign. Credits: Airbus Defence and Space UK.

Hertz band can be approximated to a DC response due to the high stiffness of the LCA structure, the approximation $k_{\mathrm{m}}(\omega) \approx k_{\mathrm{m}}$ is considered. Any variations in the measured coefficient in the band close to 1 mHz may be attributed to the frequency dependence of the heat conduction across the strut.

6.2 The LISA Pathfinder Thermal Balance and Thermal Vacuum campaign

Thermal Balance and Thermal Vacuum tests are one of the most comprehensive series of checks that a spacecraft needs to overcome before launch. On one hand, the main purpose of Thermal Vacuum tests are to verify the satellite performance in its thermal design limits. This set of thermal data is required as well for correlation with the spacecraft thermal model. On the other hand, Thermal Balance tests check the performance of the spacecraft by operating all of its systems in the same simulated space conditions until thermal equilibrium is achieved.

For LISA Pathfinder, this represented an extensive campaign of tests conducted at the IABG mbH space simulator, in Ottobrun (Germany) in the framework of the On-Station Thermal Test campaign —see Figure 6.2. During the campaign, the spacecraft was operated in space conditions, i.e. with a nominal pressure below 10^{-4} Pa and powered up by means of a sun simulator, consisting of an array of high power lamps mimicking the radiation that will hit the spacecraft in orbit.

6.2.1 Subsystems in the LISA Pathfinder Core Assembly

The instrumentation on board the satellite during the campaign was almost the complete flight version. Most of the units were already integrated and operative. In the following lines we provide a brief description of the status of the LTP subsystems relevant to this analysis during the campaign:

Optical Metrology Subsystem The OMS was present and fully operative, including the Reference Laser Unit, the Laser Modulator, the Phasemeter [86], the Optical Bench [84] and the Data Management Unit (DMU) [88].

Gravitational Reference Sensor During the Thermal Balance and Thermal Vacuum campaign, the Electrode Housings and the Test Masses of the Inertial Sensors were not present and were replaced by piezoelectric driven mirrors located on dummy Inertial Sensors Housings and acting as end-mirrors of the interferometer [107].

Thermal Diagnostics The fact that the Inertial Sensors were not part of the campaign implied a relocation of some of the temperature items. Regarding the temperature sensors, 8 thermistors were relocated around the dummy Inertial Sensor Housing structures and 6 placed on the inner sides of the LCA support structure, leaving at their flight representative locations only the 6 Suspension Struts temperature sensors and the 4 sensors located on the Optical Bench —see Figure 6.3. Despite of these modifications, all the sensors composing the Temperature Measurement System (TMS) could perform correctly. With respect to the heaters, only the 6 Suspension Strut heaters were present and placed in their design locations. As a consequence, among the different heating experiments planned for the mission, only the thermistors and heaters concerning the Suspension Strut heating were available for test.

The LCA as during the campaign is shown in Figure 6.4

6.2.2 Thermal experiments during the campaign

The campaign was divided into two main parts, where experiments involving many different subsystems of the spacecraft were repeated at two different temperatures, i.e. the *hot case* at $30.5^\circ\,\mathrm{C} \pm 0.5^\circ\,\mathrm{C}$ and the *cold case* at $9.5^\circ\,\mathrm{C} \pm 0.5^\circ\,\mathrm{C}$, reaching temperatures of around 26° C and 12° C respectively in the LCA [107] —see Figure 6.5. In both of them, a series of experiments to verify system performance and to characterise different spacecraft subsystems were run and, as regards of the thermal diagnostics, the execution of different telecommand sequences of heater activations was included. These experiments were carried out during the *cold* case and were planned as follows:

- Phase 1: Continuous heat injection in Heaters 9 and 11 (14 h).
- Phase 2: Individual heater activations in series of pulses to all strut heaters (6×2 h).
- Phase 3: Combined heater activation for thermoelastic stress tests (10 h).
- Phase 4: Relaxation time (12 h).

Phase 1 experiment was aimed to test long-term heating system performance while *Phase 2* experiments were providing most of the information regarding the system response to local —at a single *Suspension Strut level*— temperature fluctuation. Following

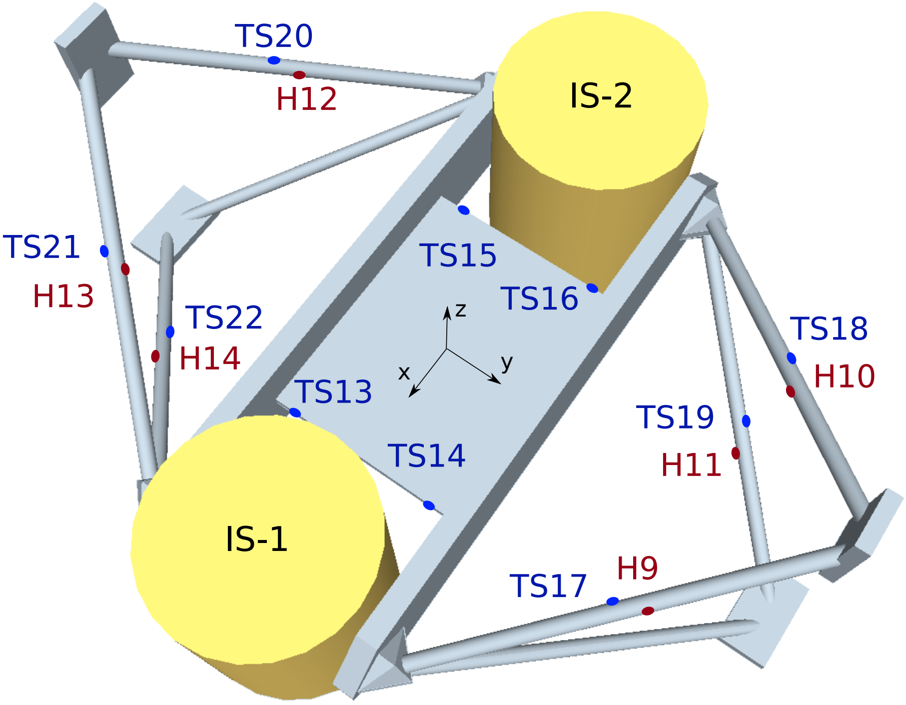

Figure 6.3: Schematic of the LCA and its series of diagnostics heaters H_i and temperature sensors TS_j on the different Suspension Struts and on the Optical Bench, as during the OSTT campaign.

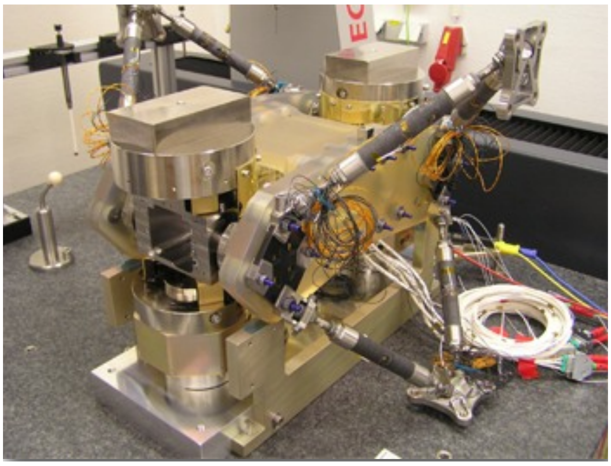

Figure 6.4: LTP Core Assembly (LCA) as during the OSTT campaigns. The missing GRS were replaced by thermal representative dummy Inertial Sensor Housing with piezoelectric-controlled mirrors in the Test Mass locations. Credits: Airbus Defence and Space UK.

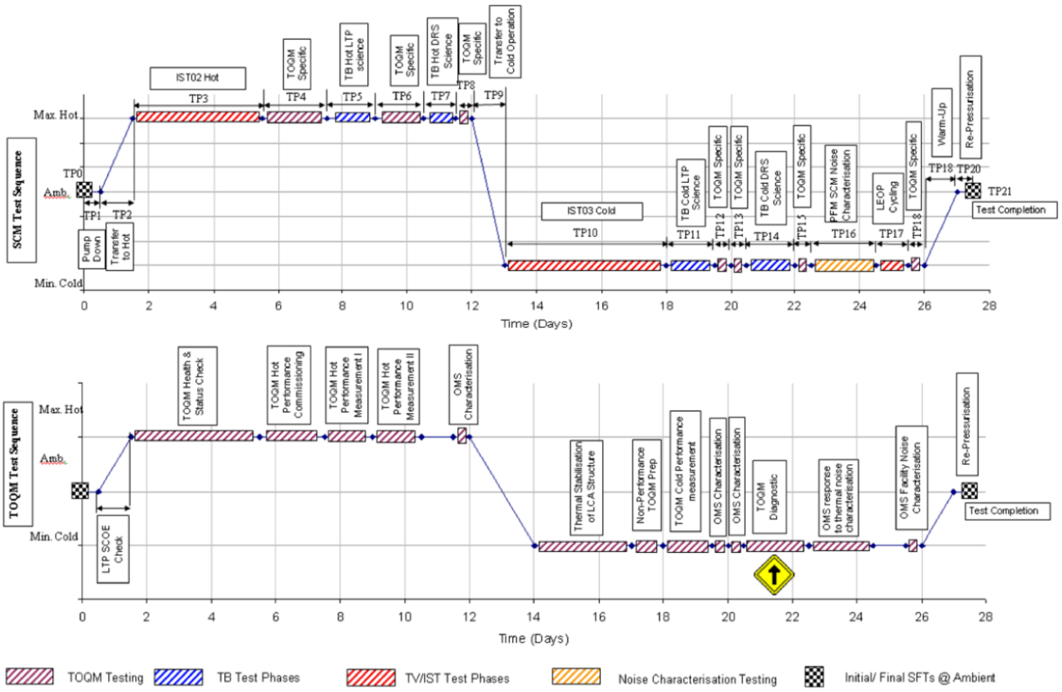

Figure 6.5: On-Station Thermal Test (OSTT) plan. The struts experiments (labelled as *TOQM Diagnostic*) were carried out between days 20–22 during the *cold* phase [156].

to that, *Phase 3* was intended to check the linearity of the incidence of the heater activations to the OMS readout. Finally, *Phase 4* provided a set of noise data used to analyse the temperature noise contribution during normal performance as well as information regarding the relaxation times needed to recover from heater-induced conditions.

The whole data communication chain between the spacecraft and the operations center was already through the flight model DMU and OBC, and the spacecraft kept being powered up from the solar-like radiation energy provided by an array of high power lamps in the vacuum chamber.

6.3 Thermo-optical characterisation of the LISA Pathfinder Core Assembly

The results of the campaign are presented here in the following way: first we review the temperature stability and evaluate the performance of the Temperature Measurement System and then the experiment results are analysed. This require to check not just the struts temperature and OMS motion channels but also the readouts of the static interferometers and the temperature on the Optical Bench. At the end of the section a plausible thermo-elastic mechanism consistent with the measurements is proposed.

6.3.1 Temperature environment characterisation

The Temperature Measurement System (TMS) kept active through all the tests of the campaign, allowing a complete characterisation of the environment whilst the different planned experiments were taking place. Before entering in the analysis of the data obtained through the set of temperature sensors, a careful cleaning of spikes as explained in Section 2.2.1.3 is required.

The best temperature stability during the OSTT campaign was found on a *relocated* sensor outside the LCA (case of TS9, labelled *Best case* in Figure 6.6, *left*), achieving a noise level of $10^{-5}\mathrm{K Hz}^{-1/2}$ through most of the frequency band, in practice reaching the electronic noise floor as expressed by the *reference* temperature measurements, i.e. measurements performed with high stability resistors instead of thermistors (labelled TMS noise in Figure 6.6, *left*).

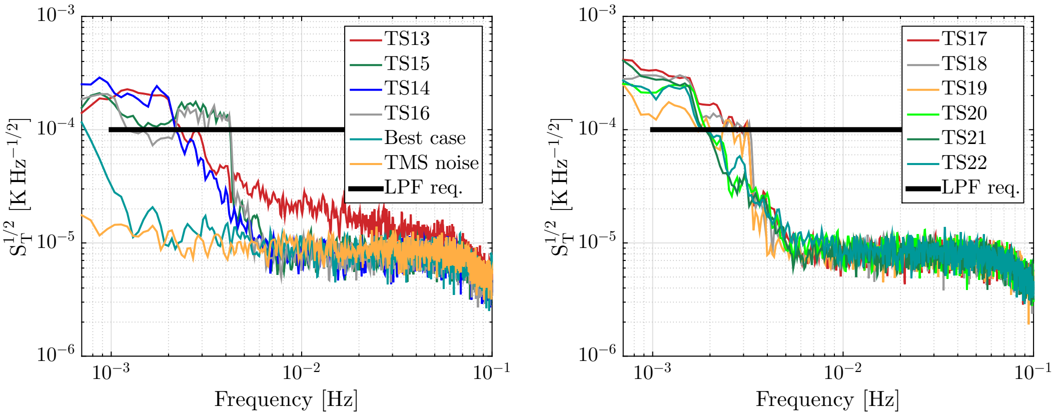

Figure 6.6: *Left*: Power Spectral Density (PSD) for the Optical Bench temperature sensors together with the best performance case of the temperature measurement subsystem during the campaign (labelled as *Best case*), obtained outside the LCA by a *relocated* sensor. The system reference noise (labelled as *TMS noise*) sets the floor for the temperature measurement. All these spectra correspond to temperature measurements taken some days before the thermal experiments, during the *hot* case of the campaign. *Right*: PSD of the different Suspension Strut temperature sensors for the same times as in the other plot. In both Figures, the sudden noise falls that can be observed for instance on TS15-19 are attributed to non-linear effects of the ADC, caused by the presence of too high temperature drifts during the campaign —see 2.2.1.3.

Such low levels were not achieved inside the LCA because of a high temperature drift that induced a feature in the spectrum of temperature fluctuations due to a cyclic error associated to Analog-to-Digital Converter (ADC) nonlinearity [157]. Such an error is related with imperfections at the quantization levels of the ADC. For more details on the error refer to Section 2.2.1.3.

Moreover, slightly different temperature noise levels at different sides of the Optical Bench caused sensors TS15 and TS16 to manifest higher noise levels than TS13 and TS14 though they had similar temperature drifts —see the bump affecting only TS15 and TS16 between 2 mHz and 4 mHz at Figure 6.6, *left*. This can be explained by the attenuation effect of the ADC non-linear error higher harmonics when the input signal combines a drift with certain levels of noise [133]. A higher temperature noise level on the $+x$ side —where TS13 and TS14 are located— can actually reduce the effect of this error, as it happens in Figure 6.6 (*left*) to TS15 and TS16. The same feature appears on the temperature stability plots of the struts (Figure 6.6, *right*), where a lower noise profile on the $+y$ side of the LCA between 2 mHz and 3 mHz induces high ADC non-linear noise while on the $-y$ side the error is attenuated.

The temperature drift causing the different bumps and sudden drops in Figure 6.6 appeared due to test schedule limitations, i.e. not allowing the instrument to achieve a complete steady state. The real drift during flight operations is thus expected to be smaller.

6.3.2 Response of the x_1 and x_{12} interferometers to heat inputs

During the *Phase 2* of the diagnostics experiments, a series of three pulses of 200 s in periods of 1000 s and a power of 2 W was applied individually to each heater, producing temperature increments in the respective struts around 8 K per pulse and inducing immediate observable consequences on the OMS channels with amplitudes around ±10 nm, as shown in Figure 6.7.

In order to better distinguish the effect, a 1st-order detrend is applied to all time series in the Figure 6.7.

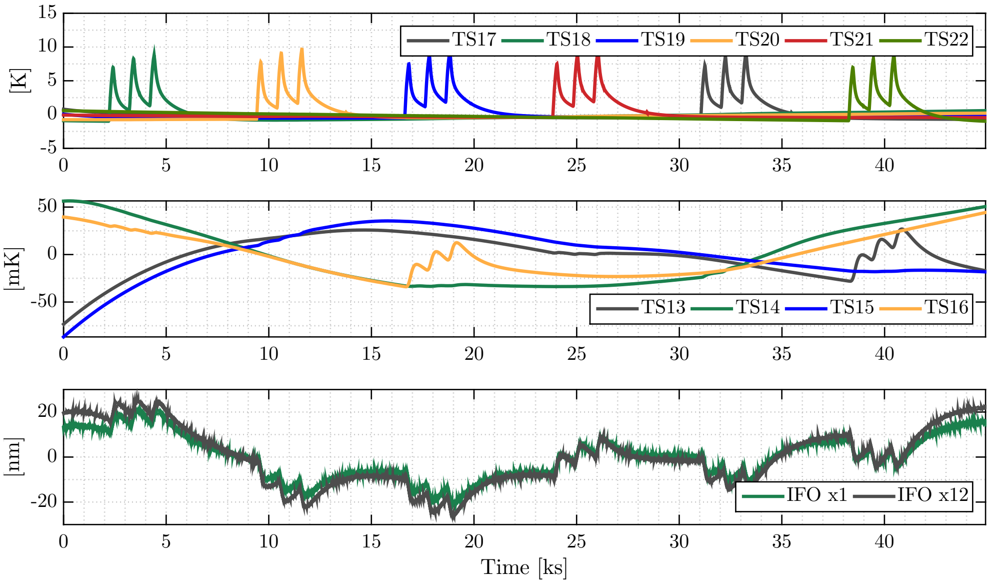

Figure 6.7: Temperature measurements at the different struts (*upper* plot), the Optical Bench temperatures (*centre* plot) and the displacements measured by the interferometer (IFO, *lower* plot), all of them detrended with a 1st-order polynomial.

Temperature increments at the Optical Bench clearly indicate that temperature variations in the lower struts (TS19, TS22) have a thermal impact on the Optical Bench much larger than the upper struts (TS17, TS18, TS20, TS21). Indeed, the central panel in Figure 6.7 shows how the temperature sensors in the Optical Bench have a significant response for the former and a negligible reaction —out of the environmental drift— for the latter.

The difference in the heat conduction through the parts between the upper and the lower struts to the Optical Bench cannot justify such an important difference of more than one order of magnitude (about a factor 13). On the other hand, none of the struts has visibility to the sensors which could create a direct radiative link.

An explanation of this effect may be sought in the fact that, opposite to the upper ($+z$) struts —see Figure 6.3—, the screws attaching the lower ($-z$) struts to the Optical Bench assembly present direct visibility to their closest Optical Bench sensor, establishing indeed a direct thermal radiative link. If we consider on one hand the screw temperature being increased at least up to 2 K through thermal conduction, a heated area of at least 20–22 mm^2 and a screw emissivity of around 0.5 and, on the other hand, a sensor area of around 10 mm^2 with high absorption ($\sim$0.9) and a thermal resistance to the Optical Bench of $\sim$100 K W$^{-1/2}$, increments of $\sim$10 mK should be expected in these Optical Bench sensors. This is already about one order of magnitude above the equivalent case with just conduction —which is the situation for the higher struts.

Nevertheless, the lower plot in Figure 6.7 shows how the OMS perturbation repeats the same pattern of signals for all the heater activations, regardless of the above discussed asymmetry on $+z$ and $-z$ struts. In order to further investigate this phenomenon, we computed the coherence function between the interferometer phase readout and the four temperature sensors involved in the $-z$ struts experiments.

As shown in Figure 6.8, the analysis confirms that the signal observed in the OMS is not coherent with temperature variations observed in the Optical Bench ($\simeq$ 8% coherence 10 mHz with sensors TS15 and TS16) and is strongly correlated with the temperature increase in the struts ($\simeq$ 92% coherence at 10 mHz with sensors TS19 and TS20). This suggests that, though the Zerodur® plate is being heated up through radiative effects when activating lower-strut heaters, the OMS sensitivity from this effect is negligible in comparison to the general strut heating effect, discarding the Zerodur® plate heating up as the mechanism describing the main perturbation and pointing to a global elastic distortion effect on the LCA.

6.3.3 Response of the static interferometers to heat inputs

The fact that the longitudinal motion signals x_{12} and x_1 present similar amplitudes no matter which strut is being heated (though the Φ_{12} optical path is a factor 2 longer than the Φ_1) suggests that the distortion mechanism does not involve the vacuum enclosures with the inertial sensors and must be sought on the Optical Bench itself.

In order to further investigate the origin of the response of the main OMS channels —x_1 and x_{12}—, we explore the readouts of the two remaining interferometers. The frequency and reference interferometers are *static* interferometers in the sense that, apart from the fibres, they do not have moving parts outside the bench.

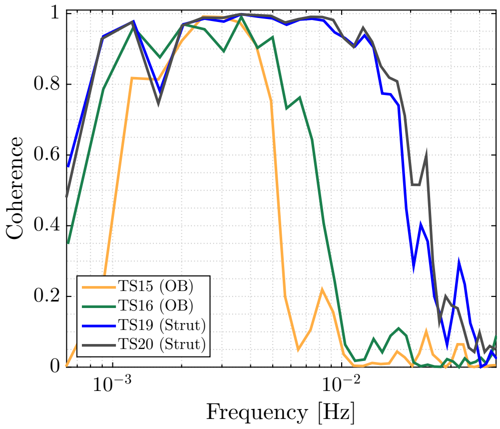

Figure 6.8: Coherences between different strut sensors (TS19 and TS20) and OMS's channel x_{12} together with the coherences from their closest Optical Bench (OB) sensors (TS15 and TS16 respectively) to the same OMS measurement.

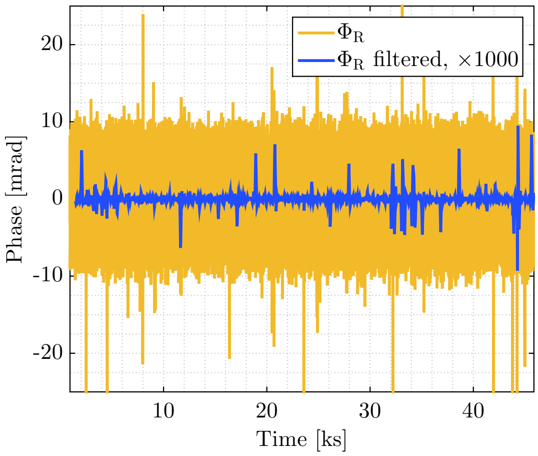

Figure 6.9: Readouts of the reference interferometer Φ_R and the same measurement filtered with a 4th order low-pass filter with a cut-off frequency of 5 mHz.

The reference interferometer readout (Figure 6.9) is roughly the phase measured at Φ_R and includes mainly all the optical pathlength fluctuations outside the Optical Bench —excepting eventual Test Masses motion. In addition, it is used to actively stabilize the Optical Pathlength Difference (OPD) between fibres [158] and, since its signal may be shaped by the noise, its relevant information is found on the control signal rather than on the signal itself. In Figure 6.10, the OPD control signal shows how the reference interferometer is sensitive to each of the heat injection series applied. As observed, the activation of Heater 9 (close to TS17) produces the largest response, followed by the activation of Heater 10 and, at third position, the activation of Heater 19, all of them at the $+y$ side of the LCA. However, the disturbance is significantly removed from the final reference interferometer readout and only fast optical pathlength corrections are

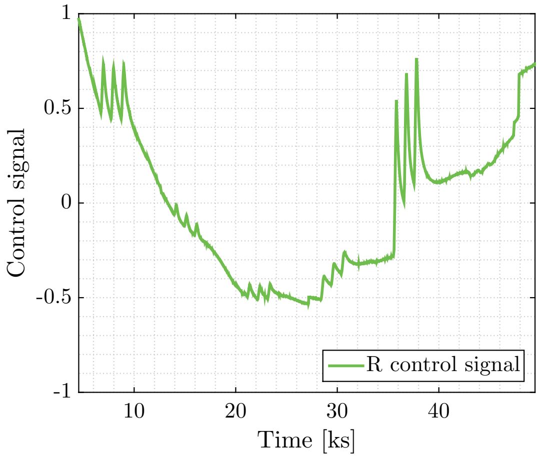

Figure 6.10: OPD control signal applied to the piezo actuator that controls the differential optical pathlengh fluctuations, labelled as *R control signal*.

observed, specifically ones from H9 activation. Due to the vicinity of this heater to the optical fibres, this suggests that a possible interaction with the optical fibres could cause this effect. However, the eventual consequences of this behaviour are cancelled in the common-mode rejection and do not explain the observations in Figure 6.7.

Regarding the other *static* interferometer, the frequency interferometer measurement (Figure 6.11) is used to control the frequency fluctuations in two different ways: a piezoelectric transducer stabilizes *high* frequency fluctuations and a thermal control loop regulates the low frequency oscillations by controlling the temperature at the laser head, being the *fast* controller nested inside the loop of the *slow* controller [158]. Since the final readout is the result of subtracting Φ_R to Φ_F, this interferometer is expected to present significantly less noise than the reference one, and actually a reduction factor of 10 is found between them —see Figure 6.11. After removing the reference measurement, the effect is much more homogeneous and, as expected, the proximity to the optical fibres no longer explain the effect. Regarding the control signals in Figure 6.12, quick kicks corresponding to corrections from the fast controller (obtained after low-pass filtering the whole signal) are combined with a quite smoother correction by the other controller. The signal amplitude of the *slow* controller presents approximately the same amplitude no matter the heater being injected, which is coherent with the observations in the main interferometers. Since the frequency interferometer can only be reporting disturbances from the Optical Bench, it is quite evident from Figure 6.12 that the Optical Bench must be distorted here following a unique deformation mode.

The DWS angles from the reference and frequency interferometers display interesting information about how the Optical Bench is being distorted. The vertical angle on the reference interferometer —labelled Φ_R *DWS-Vert* in Figure 6.13— is by far the most affected, followed by the one order of magnitude smaller vertical component of the frequency interferometer —labelled Φ_F *DWS-Vert*. Such an effect points to a mechanical deformation of the bench related to relative displacements on the z axis. In addition,

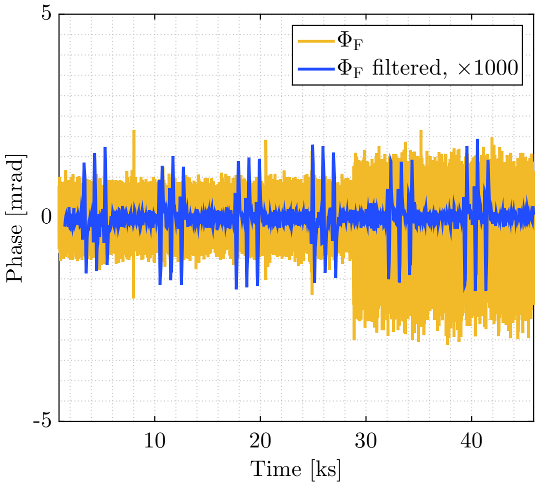

Figure 6.11: Readout of the frequency interferometer Φ_F and the same measurement filtered with a 4th order low-pass filter with a cut-off frequency of 5 mHz.

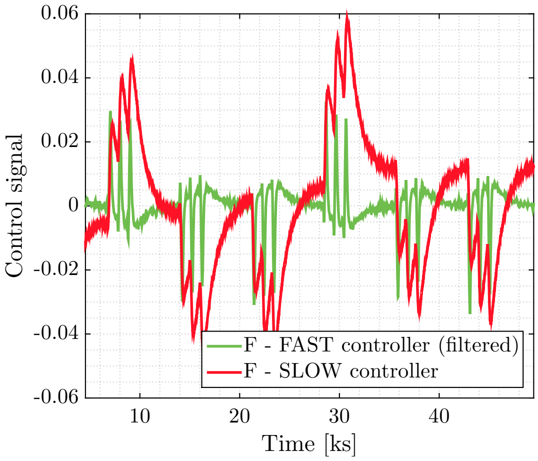

Figure 6.12: Control signals applied to the actuators for frequency noise stability. The fast controller —filtered here with the same filter than in Figure 6.11— is related to a piezoelectric transducer acting on the laser head while the slow control signal corresponds to a temperature control loop on the laser head as well. The slow control signal shows how a similar effect is affecting the Optical Bench no matter the heater being activated.

it is of interest to check the sign of the perturbations induced. By assigning the sign '+' to a perturbation leading to a *positive* angle increment and '−' to the opposite, we get a pattern of signs of $[- + + - + +]$. This is coherent with the relative displacement readouts observed in Figure 6.7, and it is also consistent with an eventual Optical Bench torsion along the y axis, induced by stresses on z caused by the z-component of the strut-elongation. Such torsion mode must expand/contract the optical path of the reference measurement more than the path of the other measurements and should bend the Optical Bench so its beams are tilt as observed. Under these circumstances, fluctuations affecting mainly the reference path on the Optical Bench would not be cancelled and therefore would be seen as a quite common distortion at all the other channels, as observed in Figure 6.7. Figure 6.14 shows the torsion mechanism proposed.

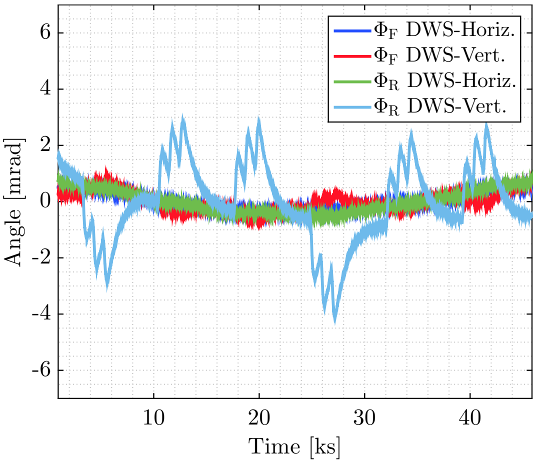

Figure 6.13: DWS angles of the vertical and horizontal incident beams on the reference and frequency interferometers, after a 1st order detrend.

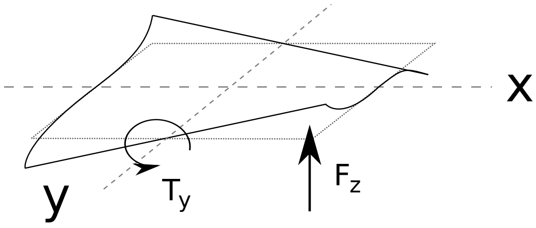

Figure 6.14: Schematic of the torsion mechanism on y produced by the vertical component of the force exerted by a heated strut. The case of the image would correspond to a lower strut heater activation such H11 or H14. This distortion mechanism is coherent with the observations.

The struts attaching the LCA to the spacecraft structure can be approximated to a 10 cm-length part of Carbon-fiber-reinforced polymer (CFRP) with 2.9 cm titanium end fittings at the edges [1] —see Apendix F. Assuming average temperature increments for the CFRP part and the titanium end fittings of 3.5 K and 1 K respectively, and the thermal expansion coefficients in Table 6.1, the projected free elongation on the z axis represents a vertical displacement of 0.7 μm. Since the LCA is a hyperstatic structure, it is reasonable to expect a real displacement of at least one order of magnitude smaller, i.e 0.07 μm, just a few times bigger than the measured ≈0.01 μm perturbation at the displacement channels. The total coefficient is consistent with the assumptions of Section 2.1.2.

---

[1] These values correspond to a -z strut at the OSTT campaign, while +z struts were a factor 1.1 longer.

Another first order approximation can be found by comparing the observations against a pure bending mechanism of the Optical Bench around the x axis [159]. In this sense, considering a beam path of $D \approx 30$ cm for the reference interferometer beams, the expected optical pathlength variation for a given beam angle θ at a photodiode can be expressed by

$$\Delta x = \theta^2 \frac{D}{2} \tag{6.10}$$

which turns to be $\Delta x \approx 0.6\ \mu$m for the DWS angle of $\theta \approx 2$ mrad measured by the reference interferometer. This value is much larger (about a factor of 60) than the observed longitudinal measurements in x_{12} and x_1. However, we would expect this simple model to give a significant overestimate of the coupling through two independent effects. The first is that the actual distortion is significantly more complicated than the simple model assumed, and the second is that the wavefront curvature of the optical beams will also significantly reduce the coupling factor.

6.4 Projection of thermo-elastic induced phase noise

Once the origin of OMS response has been traced, we can proceed to quantify its contribution to the noise budget. We start by computing the individual transfer functions from the the temperature signals to the OMS readouts, given by Equation 6.2. The transfer functions for each strut are shown in Figure 6.15. The thermo-elastic coupling between the struts and the OMS is $\sim 10^{-9}$ m K^{-1} throughout most of the LTP band. No significant differences between transfer functions are appreciated since the geometry of the LCA is symmetric regarding all the suspension struts and the OMS readouts. The noise at frequencies higher than 70 mHz corresponds to the band where the ambient noise is lower than the electronic noise and the signals become uncorrelated.

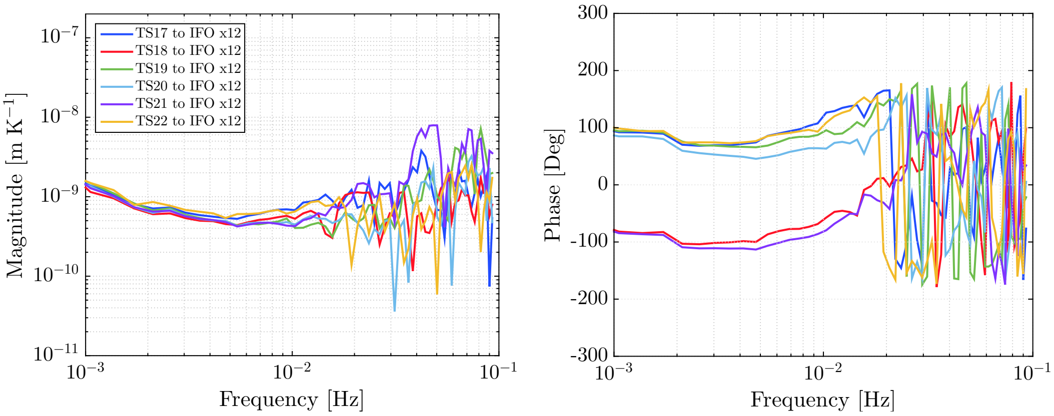

Figure 6.15: Transfer function gains (*left*) and phases (*right*) between the temperatures at the Suspension Struts and the interferometer readout x_{12}.

The system linearity in front of this distortion is checked by comparing such transfer functions with respect to data from *Phase 3*. In this phase, pulses of 500 s are applied

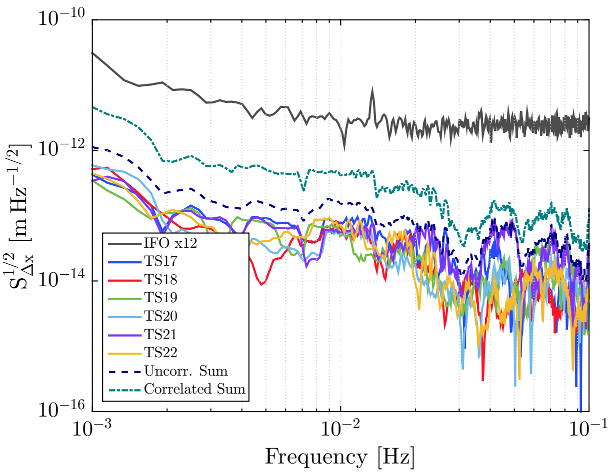

Figure 6.16: Noise projection of thermo-elastic induced phase noise on the OMS x_{12}. The contribution from each suspension strut is shown together with the uncorrelated sum of all.

simultaneously to TS17 and TS19 alternating with pulses to TS20 and TS22, producing a 2 mHz perturbation signal to the OMS. The global transfer function recovered in this experiment matches with the coherent sum of the individual transfer functions for all the temperature sensors involved, meaning that, as expected, the thermoelastic strain mechanism keeps within its linearity.

We now use a segment without heat injections, as the ones shown in Figure 6.6, to compute the direct noise projection. The results in Figure 6.16 display how the overall thermo-elastic phase noise contribution accounts approximately for 10^{-12} m Hz$^{-1/2}$ at 1 mHz, assuming that all contributions are added in an uncorrelated sum. Such assumption is feasible in the bandwidth of interest after discarding correlation through a coherence analysis between strut temperature sensors —see Figure 6.17. Although strong correlation dominates the band below 0.5 mHz and is present at some pairs of sensors (e.g. TS20 and TS21), the signals above 1 mHz are fairly enough uncorrelated. Still, Figure 6.16 also shows the worst-case contribution of a hypothetical completely-correlated temperature noise distribution, where the temperature noise pattern considered is built by selecting the highest level of noise at each frequency for all the sensors involved. On the other hand, no differences were appreciated between contributions to the different OMS readouts and also between the hot case and the cold case.

It is worth stressing that the obtained contribution is not representative of the flight operations since temperature stability is expected to be better in the Lagrange point L1 compared to the current experiment. However, the analysis reported here will be valid for the mission analysis.

Finally, the coefficient obtained has been considered constant across the bandwidth since at the low frequencies of interest the motion induced to the mechanical system keeps far from the eigenfrequencies of its characteristic modes. Nevertheless, the heat flux across the struts do present a low-pass frequency behaviour that favours the expan-

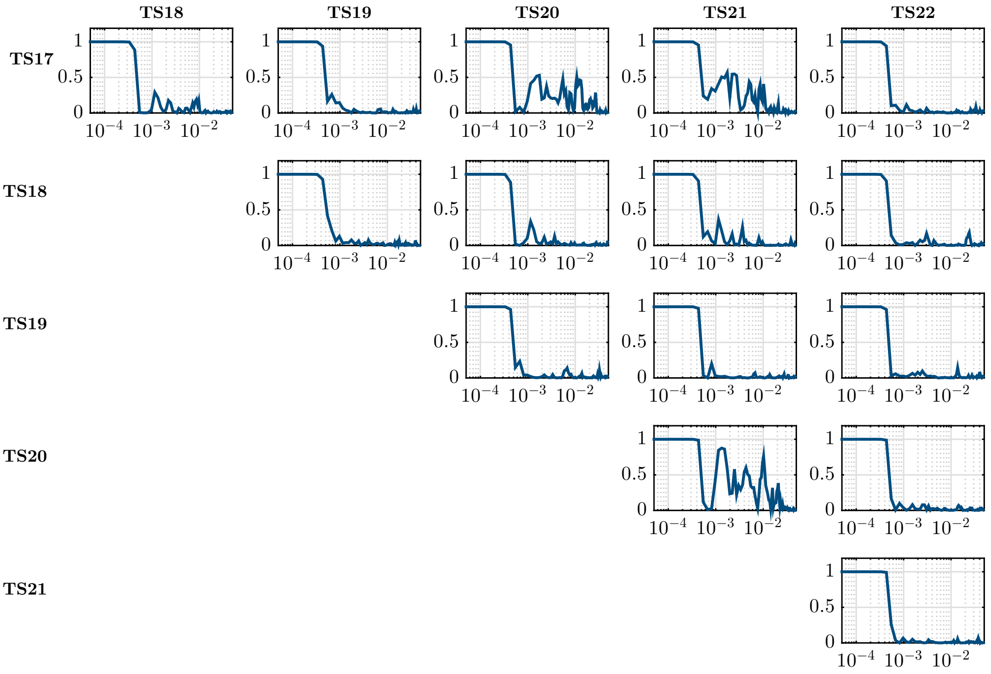

Figure 6.17: Coherences between the different temperature sensors on the struts in the same timespan used for the computation of the temperature noise projection. The units of the x axis are [Hz].

sion of low frequency components of the injected signal. Such a feature is responsible of the low-pass trend observed along the milli-Hertz band in Figure 6.15. In fact, in front of an eventual homogeneous temperature noise distribution along the strut, the most realistic coefficient to be applied is at least the one estimated in the lowest frequency at 1 mHz. Indeed, at such frequency the coefficient is estimated with a more homogeneous temperature distribution than those close to 5–10 mHz.

Back to the discussion raised at the end of Section 6.1, the thermal coupling measured here has been estimated inducing a high thermal stress at the centre of the strut, while under nominal performance the highest temperature fluctuation in the strut is expected to be at the edge close to the spacecraft's structure. If we assume an attenuation factor at 1 mHz of approximately 1/10 between one edge of the strut and its centre — consistent with the assumptions in Appendix F—, then a sensed noise of $10^{-4}\,\mathrm{KHz}^{-1/2}$ at the center of the heater where the sensors are located could actually imply a noise of $1\cdot 10^{-3}\,\mathrm{KHz}^{-1/2}$ at the edge close to the spacecraft. Considering that such a high noise affects just one side of the edge while in the experimental coefficient we heat up the central part of the strut, from the assumption in Section 6.1 we can set an upper limit on the effective thermal coupling up to $\sim 5\,\mathrm{nm\,K^{-1}}$.

6.5 Summary

The OSTT allowed to carry out a complete campaign of strut heating sequences in space-like conditions for the first time. Such a campaign provided a first estimation of the thermo-elastic coupling between temperature noise on the struts and the perturbation to the LTP. During the test, the temperature measuring system achieved an in-band sensitivity of $10^{-4}\,\mathrm{K\,Hz^{-1/2}}$ in those parts not exposed to temperature drifts higher than $10^{-5}\,\mathrm{K\,s^{-1}}$. The electronic noise of the measurement system kept the noise floor down to $10^{-5}\,\mathrm{K\,Hz^{-1/2}}$.

The set of heat injections applied at each Suspension Strut anchoring the LCA at the satellite's mechanical support structure for the LTP have allowed to predict the thermal functions between the sensed temperature at a given heated strut and the OMS motion readouts, estimating a nearly flat transfer function throughout the measuring bandwidth with magnitude $10^{-9}\,\mathrm{m\,K^{-1}}$.

At the same time, we have allocated the contribution arising from temperature fluctuations in the struts to be $10^{-12}\,\mathrm{m\,Hz^{-1/2}}$ at 1 mHz, around a factor 30 below the main OMS measurement floor noise, for the campaign conditions (which in turn was a factor of approximately 3 better than required for flight). Although the obtained results are related to the particular temperature environment of the campaign, the methodology described here is readily applicable to the in-flight case.

The origin of the coupling between temperature fluctuations and OMS response has been also investigated concluding that the effect has a thermo-elastic origin, discarding direct temperature gradients on the Optical Bench as the cause of the observed phase response. A thermo-elastic mechanism consisting of an Optical Bench torsion around the y axis is consistent with the observations. Such a distortion would be induced mainly by the vertical component of the stress caused by the thermal-expansion of the heated strut.

Still, the thermal coupling estimated has been obtained applying a large thermal load close to the sensor location in the middle of the strut. Since temperature fluctuations at 1 mHz are certainly attenuated by the strut thermal resistance, the assumption of homogeneous temperature along the strut is not realistic. In that case, the impact of different temperature distributions between the experiment case and the noise case — i.e. during a normal noise measurement— should be assessed separately. Here we have just set an upper bound of a factor 5 between the estimated spatially-averaged temperature during the experiment and the temperature during a normal run. Such a number would increment the measured contribution of the thermo-elastic noise. More accurate simulations of the temperature distribution along the strut could help to reduce this estimated upper bound.

CHAPTER 7

Summary and conclusions

In this work, we have contributed with further analytical and experimental analysis for the understanding of the effects of temperature noise in the LTP experiment. The noise budget allocates a contribution from temperature fluctuations to the LTP sensitivity of $6.7 \cdot 10^{-15}\,\mathrm{m\,s^2\,Hz^{-1/2}}$ at 1 mHz, as a shared contribution between mainly three kind of temperature noise sources: temperature gradient noise around the test masses, thermo-elastic noise in the structure of the LTP Core Assembly and thermo-optical noise in the optical parts outside the ultra-stable optical bench. This thesis presents a design for two experiments aimed to characterise the driving mechanisms for the first two sources: the Electrode Housing thermal experiment and the Suspension Struts thermal experiment, both to be carried out on board the LISA Pathfinder satellite by means of the Thermal Diagnostics subsystem. The analysis developed within this thesis has benefit from previous studies on the same topic and from various test campaigns concerning the satellite at different stages of integration, and it has allowed to provide series of bounds and criteria for the definition of the inputs for the two diagnostics experiments assessed here.

After introducing the experiment context in Chapter 1 and detailing the LISA Pathfinder Thermal Diagnostics subsystem in Chapter 2, the problem of temperature fluctuations inside the Electrode Housing has been addressed in Chapters 3 to 5 following different approaches.

In first place, we have adapted an existing ESATAN thermal model of the whole spacecraft into a State-Stace Model of the different heat fluxes of interest in the LTP. Such a model allows to simulate and understand the temperature responses in different areas of interest —mainly at the temperature sensor locations and at the inner surfaces of the Electrode Housing— when activating any diagnostics heater. Each coupling is represented by transfer functions converted to State-Space Models, that are later assembled altogether to a single model. Such a model has been cross-checked with data from different thermal campaigns, including tests at subsystem levels (the Inertial Sensor Housing EM thermal test) and at a whole satellite level (the On-Station Thermal test). Reasonable agreement between the model and test results has been found.

The implementation of this thermal model has been followed by the elaboration of an algorithm to simulate the thermal effects that show up in the Electrode Housing — the radiation pressure, the radiometer effect and the asymmetric outgassing. A specific radiative model of the different effects has been developed, allowing to represent both normal and shear effects induced by the molecules and photons that keep bouncing inside the Electrode Housing cavity with specific directions.

Following that, the thermal model has been used to derive a series of constraints bounding the experiment in order to estimate the thermal couplings with enough precision. Two cases have been considered here: (1) a model to estimate the global thermal coefficient and (2) a model to estimate the contribution of each thermal effect. Such a procedure has enabled to derive requirements for the different heat signals to be applied in terms of minimum length, amplitudes and modulation frequencies. Environmental stability requirements have also been derived.

The posterior integration of both thermal and radiative models of the Electrode Housing together with a model of the LTP close loop performance allows to carry out end-to-end simulations of the whole Electrode Housing experiment. These simulations have also been a convenient workbench where to test and validate the experiment and the data analysis tools prepared for the experiment analysis. In this sense, data analysis pipelines have been prepared for each of the experiments studied here, following the official LTPDA standards and being validated by the data analysis collaboration team. These pipelines are intended to provide a common workbench for the LTP data analysis community where to analyse each experiment.

This work has been complemented by an experimental campaign using a torsion pendulum facility at University of Trento equipped with an Electrode Housing prototype which includes the whole set of thermal diagnostics heaters and sensors. This facility has allowed to characterise the radiometer effect contribution by varying the pressure environment and to estimate the combined contribution of the outgassing effect and the radiation pressure at different absolute temperature. On the other side, the estimation of the pressure inside the Electrode Housing cavity has required a previous characterisation of the different cavities and conductances in the setup since any systematic error associated easily distorts the readout, hence the estimation of the thermal coefficient at any condition of pressure and absolute temperature.

All this work has yield some conclusions concerning the Electrode Housing experiment and the eventual scenarios:

- The torsion pendulum measurement campaign has allowed to bound the contributions of some of the effects depending on final conditions of pressure and temperature. Thus,
  - In conditions of nominal pressure (10^{-5} Pa), the radiometer effect is expected to be dominant with about half of the total contribution from the temperature gradient which is ~50 pN K^{-1}. Outgassing is following with a variable contribution of 10–30 pN K^{-1} depending on the absolute temperature, while radiation pressure is contributing with less than 10 pN K^{-1}.
  - In very good residual pressure conditions (10^{-6} Pa), the radiometer effect practically disappears (<5 pN K^{-1}) in an outgassing-dominated scenario with a total contribution of 20–30 pN K^{-1} depending on the absolute temperature.
  - The worst case scenario, set at $5{\cdot}10^{-5}$ Pa is clearly dominated by the radiometer effect contribution and the total coefficient is ~150 pN K^{-1}.
- The identification of the individual contributions in flight still remains infeasible with the current predictions of the maximum increments of temperature that can

be achieved. Under such conditions, alternative approaches need to be sought to at least set upper limits to certain effects. For instance, by assuming a maximum contribution of the radiation pressure effect —whose total contribution is much more constrained than for the other effects—, the number of unknown parameters is reduced from four to three. Alternatively, the repetition of the experiment at different stages of the mission could provide an estimate of the outgassing rate decay with time. Since such a decay has an impact to both radiometer and outgassing effects, a careful characterisation of the difference between them would report additional information of their individual contributions. The analysis of this approach is still under investigation.

- Since there is no way to directly measure the pressure in the LTP in flight, the estimation of the Brownian noise contribution remains subordinate to the estimation of the previous effects. Nevertheless, setting an upper limit to the radiometer effect through any of the cited approaches allows to quickly bound the Brownian noise apportionment. It is important to notice that with a residual pressure higher than 10^{-5} Pa, the contribution of this kind of noise to the LTP may be dominant, eventually exceeding the contributions from magnetic field noise and the actuation.

- A pressure dependence on the relative phase between temperature gradient and mass motion has been observed in the torsion pendulum setup. Though it is likely to be caused by a pendulum intrinsic effect rather than by a direct force on the mass, its origin has not been tracked and further investigation is required.

The thermo-elastic case has been studied following an experimental approach. The baseline experiment has been a thermal vacuum test campaign held in 2011 which involved a version of the satellite in an advanced level of integration. A series of strut heating sequences allows to derive a thermal coupling between the temperature of the struts and the interferometer of about $10^{-9}\,\mathrm{m\,K^{-1}}$ per strut. Still, this coefficient is obtained assuming a heating source close to the strut sensor and a temperature noise distribution decreasing towards the edges of the struts. When no heaters are switched on, the temperature noise distribution will differ from this one, being higher at the edge close to the spacecraft than in the center of the strut where the heater is located, leading to a possible underestimation of the real temperature noise in the strut. A factor 5 to be applied to the measured coefficient has been estimated here to account for this effect.

The results presented here for the thermo-elastic coupling and the thermal coefficient in the Electrode Housing allow to update the estimated temperature noise contribution in flight for the three kinds of temperature noise sources —the thermo-optical coupling from temperature noise in the Optical Window is extracted from [127]. Thus, at a nominal pressure of 10^{-5} Pa and a temperature noise of $10^{-4}\,\mathrm{K\,Hz^{-1/2}}$ at all the possible sources —assuming a worst-case scenario with correlated forces—, the contribution of temperature fluctuations to the LTP sensitivity is $7.2\cdot10^{-15}\,\mathrm{m\,s^{2}\,Hz^{-1/2}}$ at 1 mHz, clearly dominated by the contribution from thermal forces on the Electrode Housing. On the other side, the current best-case expectation is based on a residual pressure of

10^{-6} Pa and a temperature stability of 10^{-5} K Hz$^{-1/2}$ inside the LCA —leaving a stability of 10^{-4} K Hz$^{-1/2}$ at the edge of the struts. Such conditions would lead to a total contribution of $1.5 \cdot 10^{-16}$ m s^{2} Hz$^{-1/2}$, still dominated by temperature gradients in the Electrode Housing (~86%) but with a significant contribution of thermo-elastic noise (~13%).

Therefore, looking now to a future gravitational wave detector based on the classical LISA design, the work done within this thesis allows to state the following recommendations:

- The direct attenuation of the thermal effects in the Electrode Housing requires to achieve lower levels of pressure around the Test Masses. The Brownian noise would also strongly benefit from a pressure reduction. The residual pressure is actually a balance between the outgassing surfaces and the conductances with respect to the open space vacuum. In order to minimize it at least a factor 100 in a future LISA-based mission, larger conductances should be combined with stronger bake-outs of not only the Inertial Sensor parts but also the different nearby subsystems, such as the caging and grabbing mechanisms. On the other side, lowering the working temperature as much as possible would also have an important impact to the reduction of most of the effects, including Brownian noise. A short decrease of temperature (~ 10 K) could significantly damp the outgassing contribution, while cryogenic temperatures would be required to significantly reduce Brownian noise without changing the pressure.

- The contribution of the thermo-elastic noise to the LISA Pathfinder sensitivity cannot be directly extrapolated to a future eLISA spacecraft. This kind of noise is strongly related to the mechanical design of the instrumentation and an eLISA spacecraft would require a quite different disposition of the beams, actually including more optical components —thus being more exposed to thermo-elastic distortion. In this case, improving the ratio between ultra-stable materials like Zerodur® and other structural materials (Titanium, CFRP, etc) may help to reduce this kind of noise contribution. Furthermore, eLISA interferometers will require higher amounts of laser power, what will imply more concentration of heat at specific parts, though such an effect has not been critical in LISA Pathfinder.

Figure 7.1: LISA Pathfinder in the S5B building at the Centre Spatial Guyanais in Kourou, French Guiana, while filling the propulsion module with propellant (November 2015). Credits: ESA-CNES-Arianespace / Optique Vidéo du CSG - P. Baudon.

APPENDIX A

Data analysis tools for thermal systems

A.1 Introduction

The essential work of this thesis focuses on designing experiments aimed to evaluate couplings between temperature signals and relevant OMS signals. Since the ultimate goal of the LTP is to minimise any thermal coupling during acceleration noise measurements, the estimated coupling coefficients are of interest to project the temperature measurement noise to the OMS science readouts, i.e. to assess the impact of temperature fluctuations to the LTP.

It is therefore convenient to introduce at this point the tools required to operate with series of noise measurements. In this appendix, we also present the basic aspects of the Linear Time-Invariant (LTI) systems, which are of interest to model the different thermal distortion mechanisms, and the demodulation procedure used to estimate certain parameters in the thermal experiments.

All the tools presented in this appendix have been implemented in the LTPDA Toolbox.

A.2 Spectral Density

The noise to be measured by the different sensors in the LTP can be approximated to random stationary processes. Such kind of processes are characterised by their Power Spectral Density (PSD). The PSD of a stationary random process $x(t)$ is defined by the Fourier transform of its autocorrelation function $R_x(\tau) = \langle x(t)x(t+\tau)\rangle$:

$$S_x(\omega) = \int_{-\infty}^{+\infty} R_x(\tau) e^{-j\omega\tau}\, d\tau \tag{A.1}$$

For a discrete measurement x_n, the equivalent Discrete-Time Fourier transform is

$$S_x(\omega) = \sum_{n=-\infty}^{n=\infty} R_x(n) e^{-j\omega n} \qquad -\frac{1}{2} \leq \frac{\omega}{2\pi} \leq \frac{1}{2} \tag{A.2}$$

Sometimes it is of interest to compare the frequency content of two signals $x(t)$ and $y(t)$, what is addressed through the Cross-Power Spectral Density (CPSD):

$$S_{xy}(\omega) = \int_{-\infty}^{+\infty} R_{xy}(\tau) e^{-j\omega\tau} d\tau \tag{A.3}$$

where $R_{xy}(\tau)$ is the cross-correlation function defined as $R_{xy}(\tau) = \langle x(t) y(t+\tau) \rangle$. As in the previous case, the discrete case corresponding to signals x_n and y_n is

$$S_{xy}(\omega) = \sum_{n=-\infty}^{n=\infty} R_{xy}(n) e^{-j\omega n} \qquad -\frac{1}{2} \leq \frac{\omega}{2\pi} \leq \frac{1}{2} \tag{A.4}$$

Their implementation in the LTPDA environment is based on the Welch estimator [160] and allows to use a broad set of windows. The LTP Data Analysis collaboration has defined the Blackman-Harris of four terms (BH92) with 50% of overlap as the default windowing for the official LTP spectral analysis.

A.3 Thermal system modelling

Many physical systems are modelled as Linear Time-Invariant (LTI) systems. This kind of models are described by series of differential equations that, if the system is properly discretised in nodes, can be approximated to series of difference equations. LTI modelling allows to advantageously characterise and simulate many different environments including several inputs and outputs, different noise sources, etc.

Thermal systems are commonly described as LTI systems, what requires to define sets of heat flux equations describing the heat propagation across a given body properly discretised into a layout of iso-thermal, volume-finite nodes. Thermal couplings between nodes need to include the different types of heat transfer mechanisms applicable. In high vacuum or space environments like the LTP experiment case, LTI thermal models only need to include the heat transfer through conduction and a linearised approximation of heat transferred through radiation.

Here, we provide a generic approach to LTI systems stressing the qualities of interest concerning their modelling and analysis. Chapter 3 provides a more detailed description on the thermal model of LISA Pathfinder.

A.3.1 Transfer function of a LTI system

Transfer functions are commonly used to characterise the coupling between each input/output combination of a system described by series of LTI differential equations. In this sense, the transfer function of a LTI system is defined by the ratio of the Laplace transforms of the output signal over the input signal under the assumption that all initial conditions are zero [161]. For an input signal $x(t)$ and an output signal $y(t)$, the associated transfer function is

$$H(s) = \frac{\mathcal{L}\{y(t)\}}{\mathcal{L}\{x(t)\}} = \frac{Y(s)}{X(s)} \tag{A.5}$$

$X(s)$ and $Y(s)$ are polynomials whose order sets the order of the transfer function, usually written as

$$H(s) = \frac{c_0 s^N + c_1 s^{N-1} + ... + c_{N-1} s + c_N}{s^N + d_1 s^{N-1} + ... + d_{N-1} s + d_N} \tag{A.6}$$

where the different c_i and d_i are the coefficients of the characteristic polynomials of the transfer function. If $H(s)$ is known, the response of the system in front of a given input $x(t)$ is determined by the convolution function between the input $x(t)$ and the impulse response of $H(s)$, namely $h(t)$:

$$y(t) = h(t) * x(t) \tag{A.7}$$

Transfer functions can alternatively be expressed in series of partial fractions — namely their *partial fraction expansion*:

$$H(s) = \sum_{k=1}^{N} \frac{r_k}{s - p_k} \tag{A.8}$$

where r_k are the different *residues* and p_k the different *poles* of the transfer function $H(s)$.

A.3.2 Digital filtering

In order to deal with LTI systems and real measurements it is necessary to discretise the models to a sampling frequency of interest. In this sense, the Bilinear transform provides a method to convert continuous-time to discrete-time systems by using the Z-Transform [162]. In the classical LTI s-model representation, such a transform roughly consists on the substitution

$$z = e^{sT} \tag{A.9}$$

where s is the complex variable of the continuous model and z the variable in the discrete model, the later being implemented as z^{-1} representing the system unit delay in discrete models. Finally, T is the sampling period, actually the numerical integration step. The Bilinear transform approximates Equation A.9 to its first order. Thus, for the continuous to discrete case the conversion is

$$s \approx \frac{2}{T}\frac{z-1}{z+1} = \frac{2}{T}\frac{1-z^{-1}}{1+z^{-1}} \tag{A.10}$$

Such a conversion actually allows to derive **digital filters** $H[z]$ for each of the input/output combinations in a LTI system. The general representation of a digital filter is

$$H[z] = \frac{b_0 + b_1 z^{-1} + b_2 z^{-2} ... + b_N z^{-N}}{a_0 + a_1 z^{-1} + a_2 z^{-2} ... + a_N z^{-N}} \tag{A.11}$$

Still, as in the continuous case, $H[z]$ can be expressed in terms of an N^{th}-order transfer function or in series of N partial fractions:

$$H[z] = \sum_{k=1}^{N} \frac{r_{0,k}}{p_{0,k} + p_{1,k}\, z^{-1}} \tag{A.12}$$

Back to the time domain, the output $y[n]$ given an input $x[n]$ is finally found by

$$y[n] = \sum_{k=0}^{N} b_{0,k}\, x[n-k] - \sum_{k=1}^{N} a_{1,k}\, y[n-k] \tag{A.13}$$

Notice that the order N of a digital filter is also the number of N-last samples required to compute each new point.

A.3.3 State-Space Model representation

The State-Space Model (SSM) representation of a LTI model is a way to express LTI models in systems of first order differential equations grouped in a matrix form. The classical SSM representation is written as

$$\dot{\mathbf{x}}(t) = \mathbf{A}\mathbf{x}(t) + \mathbf{B}\mathbf{u}(t) \tag{A.14}$$

$$\dot{\mathbf{y}}(t) = \mathbf{C}\mathbf{x}(t) + \mathbf{D}\mathbf{u}(t) \tag{A.15}$$

where $\mathbf{x}(t)$ is the vector of *states* and $\dot{\mathbf{x}}(t)$ the time derivative of each state variable. $\mathbf{u}(t)$ is the vector of inputs and $\mathbf{y}(t)$ the vector of outputs. **A**, **B**, **C** and **D** are the different characteristic matrices that define the SSM system. **A** is the state matrix, **B** the input matrix, **C** the output matrix and **D** the feedthrough matrix.

SSMs are convenient tools to handle large systems with high number of states or internal variables.

SSM derivation from partial fraction representation

Starting from a given transfer function of order N written as in Equation A.6, the characteristic matrices of its associated SSM are defined as follows:

$$\mathbf{A} = \begin{bmatrix} 0 & 1 & 0 & \dots & 0 \\ 0 & 0 & 1 & \dots & 0 \\ \vdots & \vdots & \vdots & \ddots & \vdots \\ 0 & 0 & 0 & \dots & 1 \\ -d_N & -d_{N-1} & -d_{N-2} & \dots & -d_1 \end{bmatrix} \tag{A.16}$$

$$\mathbf{B} = \begin{bmatrix} 0 \\ 0 \\ \vdots \\ 0 \\ 1 \end{bmatrix} \tag{A.17}$$

$$\mathbf{C} = \begin{bmatrix} c_N - d_N c_0 & c_{N-1} - d_{N-1} c_0 & \dots & c_1 - d_1 c_0 \end{bmatrix} \tag{A.18}$$

$$\mathbf{D} = \begin{bmatrix} c_0 \end{bmatrix} \tag{A.19}$$

The opposite operation is directly found by

$$\mathbf{H}(s) = \mathbf{C}\left(s\mathbf{I} - \mathbf{A}\right)^{-1}\mathbf{B} + \mathbf{D} \tag{A.20}$$

Notice that a SSM can contain multiple transfer functions by assembling series of SSM matrices from different models, so $\mathbf{H}(s)$ can actually be a matrix. The size of $\mathbf{H}(s)$ is evidently defined by the total number of inputs and outputs.

SSM discretisation

When properly discretised, SSMs provide a fast tool to perform real time simulations. The equivalent discrete characteristic matrices are obtained from the continuous ones [163, 164]:

$$\mathbf{A_d} = e^{\mathbf{A}T} \tag{A.21}$$

$$\mathbf{B_d} = \int_0^T e^{\mathbf{A}\eta}\mathbf{B}d\eta \tag{A.22}$$

$$\mathbf{C_d} = \frac{\mathbf{C}}{2}\left(\mathbf{I} + \int_0^T e^{\mathbf{A}\eta}d\eta\right) \tag{A.23}$$

$$\mathbf{D_d} = \mathbf{D} + \frac{\mathbf{C}}{2}\int_0^T e^{\mathbf{A}\eta}d\eta\mathbf{B} \tag{A.24}$$

In order to numerically implement these expressions, the exponential terms are expanded in series, as

$$\mathbf{A_d} = e^{\mathbf{A}T} = \mathbf{I} + \mathbf{A}T + \frac{\mathbf{A}^2T^2}{2!} + \frac{\mathbf{A}^3T^3}{3!} + ... \tag{A.25}$$

what can be rewritten as

$$\mathbf{A_d} = \mathbf{I} + \mathbf{A}T\psi \tag{A.26}$$

where

$$\psi = \mathbf{I} + \frac{\mathbf{A}T}{2!} + \frac{\mathbf{A}^2T^2}{3!} + ... \tag{A.27}$$

By doing so, the integral in $\mathbf{B_d}$, which also appears in $\mathbf{C_d}$ and $\mathbf{D_d}$, can be expressed as

$$\mathbf{B_d} = \int_0^T e^{\mathbf{A}\eta}\mathbf{B}d\eta = \sum_{k=0}^{\infty}\frac{\mathbf{A}^kT^{k+1}}{(k+1)!}\mathbf{B} = \sum_{k=0}^{\infty}\frac{\mathbf{A}^kT^k}{(k+1)!}T\mathbf{B} = \psi T\mathbf{B} \tag{A.28}$$

Then, the only series expansion to compute is ψ, what can be done recursively as

$$\psi = \mathbf{I} + \frac{\mathbf{A}T}{2}\left(\mathbf{I} + \frac{\mathbf{A}T}{3}\left(...\frac{\mathbf{A}T}{N-1}\left(\mathbf{I} + \frac{\mathbf{A}T}{N}\right)\right)...\right) \tag{A.29}$$

From a numerical point of view, the conversion methodology presented is sometimes conflictive, inducing too high values in Equation A.27 if the time step is too large. Such a problem appears since the term $(\mathbf{A}\mathrm{T})^N/N!$ may become extremely big before it becomes small and the sequence converges. There is a typical solution to this problem, based on the property [163]:

$$\left(e^{\mathbf{A}T}\right)^2 = e^{\mathbf{A}T} e^{\mathbf{A}T} = e^{\mathbf{A}2T} \tag{A.30}$$

If T is too large, then it is possible to compute the series for $T/2$ and square the result, what can be applied recursively in order to reduce T enough to compute the series. Following to that, the resulting matrix is squared as many times as partitions have been applied to T. The criterion considered to determine the number of k partitions is the following:

$$k > \log_2\left(||\mathbf{A}T||\right) = \log_2\left(\max_j \sum_{i=1}^{n} |A_{ij}|T\right) \tag{A.31}$$

and the number selected is

$$k = \max\left(\lceil \log_2 ||\mathbf{A}T||, 0\right) \tag{A.32}$$

where $\lceil()$ stands for "*the smallest integer than* ()". Once the number of required partitions is calculated, the initial $\psi_i(T_i)$ is computed with an initial time step $T_i = T/2^k$. Then, the final ψ needed is determined by recursively applying k-times the following *time step doubling* expression

$$\psi(2T_k) = \left(\mathbf{I} + \frac{T_k\mathbf{A}}{2}\psi(T_k)\right)\psi(T_k) \tag{A.33}$$

until $T = 2^k T_i$ is reached.

The models used in the LTPDA environment to simulate the thermal behaviour of the LTP between points of interest are based on this last implementation. Details on that are provided in Chapter 3.

A.4 Data analysis tools for LTI systems

There are different tools of interest that provide an estimation of the relation between two measurements. In the following, we present an expression to estimate the transfer function between two signals, the coherence and the noise projection.

A.4.1 Transfer function estimate

The transfer function of a system can be directly estimated from its input and output signals. Under the assumptions of Linear Time-Invariant system, with zero initial conditions and zero-point equilibrium [165], the estimated transfer function between an input $x(t)$ and an output $y(t)$ is

$$H_{xy}(\omega) = \frac{S_{xy}(\omega)}{S_x(\omega)} \tag{A.34}$$

where $S_{xy}(\omega)$ and $S_x(\omega)$ are the cross-power spectral density and the power spectral density, respectively. At frequencies with high SNR, Equation A.34 provides an estimation of the complex coupling with reasonable low errors.

A.4.2 Coherence

Another quantity of interest to look for couplings between noisy signals without an apparent dependence is the coherence function, which quantifies the amount of correlation between two signals in each frequency bin:

$$\gamma^2_{xy}(\omega) = \frac{|S_{xy}(\omega)|^2}{S_x(\omega)S_y(\omega)} \tag{A.35}$$

A.4.3 Noise projection

Transfer functions can be used to estimate the contribution of a measured noise source $x(t)$ to a measurement of interest $y(t)$ by means of the noise *projection*

$$S_{x,\,y}(\omega) = |H_{xy}(\omega)|^2 S_x(\omega) \tag{A.36}$$

where $S_{x,\,y}(\omega)$ is the portion of noise in $S_y(\omega)$ due to the presence of a perturbing noise $S_x(\omega)$. Notice that under this notation the noise terms need to be represented in terms of amplitude spectral density.

This last expression is of great interest to ultimately assess the influence of temperature fluctuations during normal LTP acceleration measurements.

A.5 Demodulation process

During the Electrode Housing thermal experiments, significant amounts of heat with known frequency spectrum are applied to the Electrode Housing, yielding a response in the OMS with similar frequency content. As observed in the previous equations, transfer functions estimates provide a direct estimation of the coupling between signals without taking into consideration the input signal frequency. Nevertheless, there are alternative methods to look for specific coefficients at specific frequencies where the input signal is expected to be particularly strong. In this section, we present the demodulation method, which allows to recover the coupling coefficient at a specific frequency f_{mod}.

Given a times series measurement $g(t)$, the direct demodulation is a complex signal obtained from the product of $g(t)$ by a demodulating function $e^{j2\pi f_{\mathrm{mod}}(t-t')}$, where t' is a time delay. By doing so, any content in $g(t)$ at the modulation frequency f_{mod} is thus down-converted to a DC amplitude, while eventual DC components in $g(t)$ before the demodulation are up-converted to $2f_{\mathrm{mod}}$. The amplitude of the original component at f_{mod}, now in DC, is obtained by applying a low-pass filter to the demodulated function. The output of this filter leads to the demodulated, complex function $g_{\text{het}}(t)$, where the suffix *het* stands for *heterodyne*. The real and imaginary quantities of this term are renamed in the so called *quadratures*, as

$$g_{\text{het},\cos}(t) = \text{Re}\left\{g_{\text{het}}(t)\right\} \tag{A.37}$$

$$g_{\text{het},\sin}(t) = \text{Im}\left\{g_{\text{het}}(t)\right\} \tag{A.38}$$

Still, the component at f_{mod} in the original function $g(t)$ is likely to be *distributed* between the two quadratures depending on the phase relation between the demodulation function $e^{j2\pi f_{\text{mod}}}$ and the component of the same frequency in $g(t)$. Such a phase relation can be understood as a phase delay, determined by

$$t_{\text{delay}} = \frac{1}{T}\int_0^T \frac{-\arctan\left[\frac{g_{\text{het},\cos}(t)}{g_{\text{het},\sin}(t)})\right]}{2\pi f_{\text{mod}}} dt \tag{A.39}$$

Applying this delay to the demodulation function—i.e. using $e^{j2\pi f_{\text{mod}}(t+t_{\text{delay}})}$ instead of $e^{j2\pi f_{\text{mod}}(t)}$— allows all the signal in one quadrature to be centered. Figure A.1 shows the chain of steps of this method for a discrete signal $g(t_i)$.

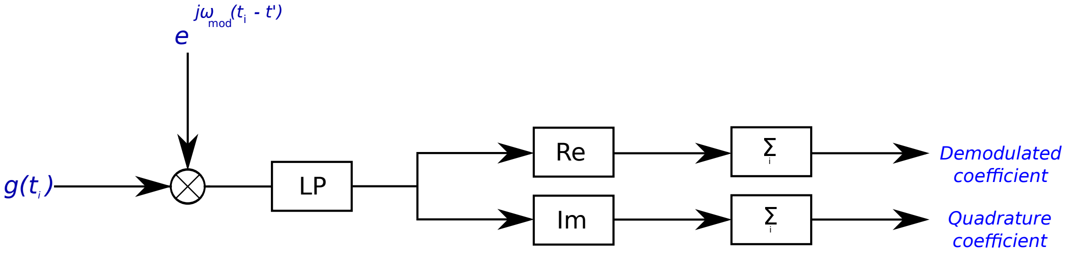

Figure A.1: Demodulation procedure for recovering the oscillation amplitude at f_{mod} from a given input function $g(t_i)$. The coefficient is estimated by averaging one quadrature of the mixed signal, after proper low-pass filtering (LP). The relative delay t' is previously estimated with Equation A.39.

APPENDIX B

Data analysis pipelines for the thermal experiments

This appendix contains the description of the analysis pipelines associated to the thermal experiments studied within this thesis. For each of them, dedicated pipelines have been developed and tested either in official simulation campaigns or using experimental data. The software framework is the LTPDA Toolbox environment running on MATLAB®.

The execution of each pipeline is organized following a common scheme defined by the LTP data analysis community:

1. Define the analysis *investigation*. In the LTPDA environment, an *investigation* object is a class that defines the essential parameters required for a full analysis of a LTP experiment. These parameters are the experiment timespans, the data bases to be used and the subset of telemetry objects required.
2. Define the pipeline class associated to the previous investigation. There is a pipeline class for each LTP experiment and for specific activities like instrument calibration and general performance quick-looks.
3. Download the minimal subset of data required.
4. Preprocess the raw data obtained. Such an action mainly includes correction of time-stamping issues like sample duplicates, uneven or missing samples, etc.
5. Resample post-processed data to the desired sampling frequency. Such a step is normally required since data from different instrumentation may present different sampling frequencies.
6. Perform the specific analysis associated to each experiment, sequentially organized in independent steps.
7. Finally, upload the results to an analysis repository.

During the mission, the execution of each pipeline will be complemented by the simultaneous filling of specific analysis procedure documents associated to the pipeline. The following sections present short descriptions of the steps and the content of the pipelines associated to the Electrode Housing and the struts thermal experiments.

B.1 Electrode Housing thermal experiment pipeline

The pipeline associated to the Electrode Housing thermal experiment is designed for an activation pattern like the sequence proposed in Section 4.4. The results provided by the pipeline allow to answer the operational questions of the experiment [166], summarized below:

1. Estimate the total $F_x/\Delta T$ coupling along x for different temperature gradients ΔT and at different absolute temperatures.
2. Given the estimated total $F_x/\Delta T$, what is the thermal contribution to the acceleration noise? Compare with the estimated/measured global acceleration by computing a noise projection.
3. Is it possible to disentangle the thermal effects and to estimate the pressure, or at least to put an upper limit to it?
4. With the estimated pressure value, or pressure upper limit, what is the contribution of Brownian noise to the acceleration noise?

Figure B.1 shows the list of steps associated to the pipeline, and Table B.1 provides a short summary of the actions performed a each step.

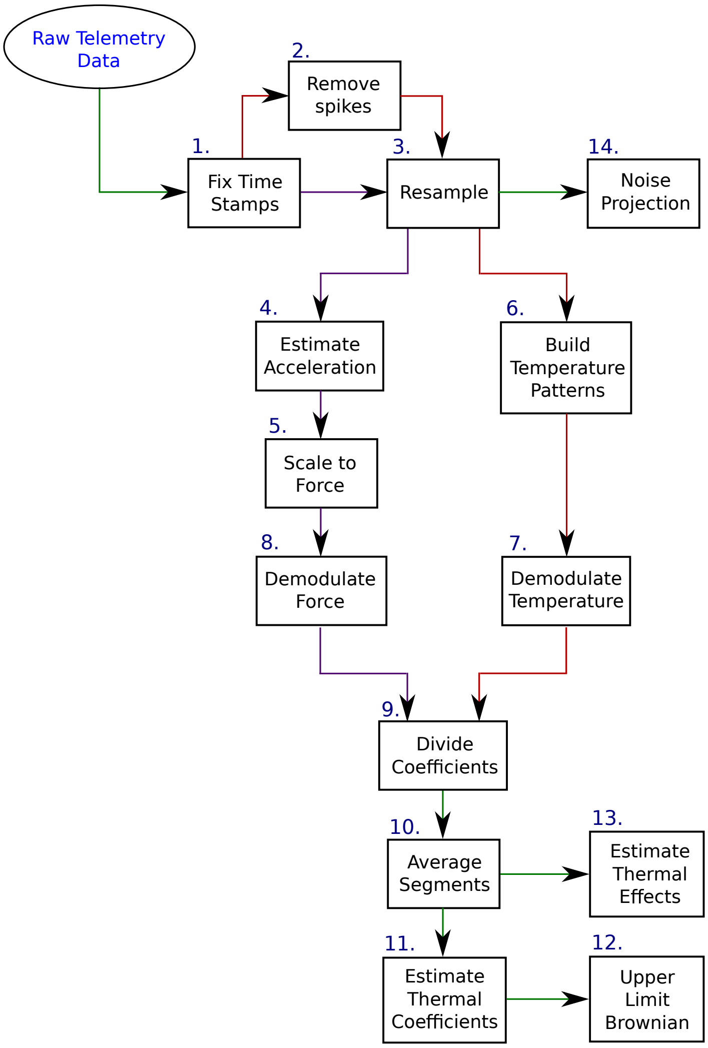

Figure B.1: Schematic of the pipeline implementing the analysis of the EH thermal experiment. The *red* lines refer to temperature sensor data and the *purple* ones to just interferometer and DFACS data. The *green* lines includes all of them.

Step	Action	Description
1	`Fix time stamps`	Corrects unequally spaced samples.
2	`Remove spikes`	Cleans temperature data from eventual spikes due to changes of scale.
3	`Resample`	Resamples both temperature and interferometer data to a same sampling frequency.
4	`Estimate acceleration`	Estimates acceleration on the test masses.
5	`Scale to force`	Converts estimated acceleration to estimated force on the heated test mass.
6	`Build temperature patterns`	Computes the temperature gradient and the absolute temperature signals from the different temperature sensor telemetry.
7	`Demodulate temperature`	Calculates the delay and demodulates the temperature gradient.
8	`Demodulate force`	Calculates the delay and demodulates the estimated force.
9	`Divide demodulated coefficients`	Divides the demodulated force over the demodulated temperature.
10	`Average segments`	Averages the resulting coefficients at each data segment with same input and absolute temperature.
11	`Estimate thermal coefficient`	Estimates the thermal coefficient at each absolute temperature level.
12	`Upper limit Brownian`	Sets an upper limit for Brownian noise.
13	`Estimate thermal effects`	Estimates the contribution of the different thermal effects.
14	`Noise projection`	Calculates the transfer function between temperature gradient and the interferometer displacement and projects the temperature gradient noise contribution on an interferometer noise segment.

Table B.1: Actions performed at each step of the Electrode Housing thermal experiment pipeline.

B.2 Strut thermal experiment pipeline

The purpose of this pipeline is twofold:

- First, investigate unexpected couplings between the strut heater activation and many readouts of interest. This is achieved through an extensive coherence analysis.
- Secondly, estimate the coefficients of the main couplings in order to project their contribution to the main interferometer readouts.

The experiment itself mainly consists on the application of a series of pulses to one of the 6 heaters on the struts. A nominal case of injection consists on a 3-pulses signal of 2 W at 1 mHz and duty cycle of 5%, for a total time of 3000 s —3 full cycles— followed by a relaxation time of 4200 s [167]. The data analysis of this experiment as implemented in the pipeline requires the following steps:

- Look for coherence between temperature in the heated struts and other signals of interest, such as temperature at other sensors and different interferometer channels.
- Estimate transfer functions between the temperatures in the heated struts and the different eventually perturbed readouts, i.e. in the cases with clear coherence between signals.
- A noise projection step to assess the strut temperature noise contribution for the situations with clear coherence between signals.

The pipeline is mainly composed of the steps shown in Figure B.2. Table B.2 provides short descriptions for each of the steps. Since the different heat injections to the struts may be applied one after the other during the mission, the analysis pipeline is already prepared to cope with data from all the injections. Other possible heating combinations, such as heating two different heaters at the same time to stress specific distortion modes of the structure have not been included in this version of the pipeline.

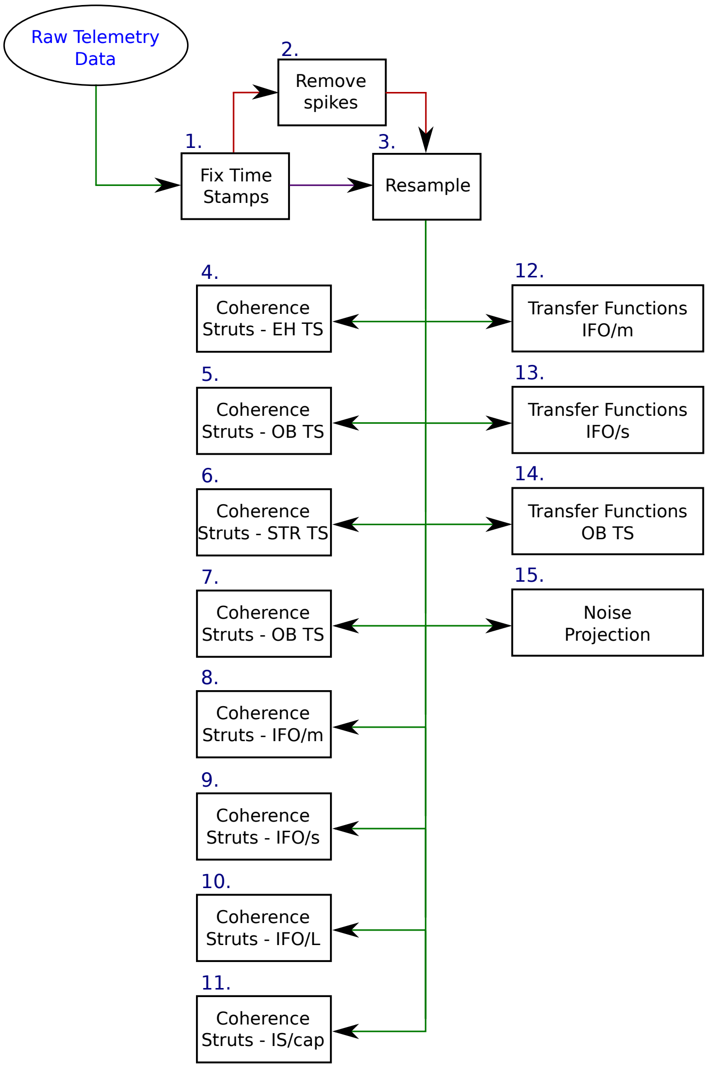

Figure B.2: Schematic of the pipeline implementing the analysis of the struts thermal experiment. The data links in *green* refer to all data, in *red* to just temperature sensor data and in *purple* to just interferometer and DFACS data. *IFO/m*, *IFO/s* and *IFO/L* stand for *IFO-motion*, *IFO-static* and *IFO control loop* parameters, while *IS/cap* refers to the Inertial Sensor capacitive readouts.

Step	Action	Description
1	`Fix time stamps`	Corrects unequally spaced samples.
2	`Remove spikes`	Cleans temperature sensor data from spikes.
3	`Resample`	Resamples to a common sampling frequency.
4	`Coherence Struts/EH`	Computes the coherence between struts and EH TS.
5	`Coherence Struts/OW`	Computes the coherence between struts and OW TS.
6	`Coherence Struts/STR`	Computes the coherence between struts and STR TS.
7	`Coherence Struts/OB`	Computes the coherence between struts and OB TS.
8	`Coherence Struts /IFO motion`	Computes the coherence between struts and IFO motion channels.
9	`Coherence Struts /IFO static`	Computes the coherence between struts and IFO static channels.
10	`Coherence Struts /IFO loops`	Computes the coherence between struts and IFO loops.
11	`Coherence Struts /IS capac`	Computes the coherence between struts and IS capacitive measurements.
12	`Transfer functions IFO motion`	Computes the Transfer functions between struts and IFO motion.
13	`Transfer functions IFO static`	Computes the Transfer functions between struts and IFO static.
14	`Transfer functions OB sensors`	Computes the Transfer functions between struts and OB sensors.
15	`Noise projection`	Computes the Temperature noise projection to IFO motion channels.

Table B.2: Pipeline steps for the Strut heating experiment.

APPENDIX C

Outgassing fit: expressions of interest

C.1 Asymmetric outgassing approximation to second order Taylor expansion

The fit to be applied in order to identify the different parameters in Equation 2.5 is inconvenient due to the huge variability of the exponential term in the outgassing expression, which makes the fitting procedure infeasible with the reduced amount of temperature points available. In order to proceed, Equation 2.5 is approximated to a second order polynomial. Starting from:

$$\alpha_{\mathrm{OG}} = \frac{Q_{\mathrm{OG}}}{T^2} e^{-\left(\frac{\Theta_{\mathrm{OG}}}{T}\right)} \tag{C.1}$$

with

$$Q_{\mathrm{OG}} = \frac{Q_0 \Theta_{\mathrm{OG}} A_{\mathrm{TM}}}{C_{\mathrm{eff}}} \tag{C.2}$$

The second order Taylor expansion is written as

$$P_{\alpha_{\mathrm{OG}}}(T) = \alpha_{\mathrm{OG}}|_{T=T_0} + \frac{\partial \alpha_{\mathrm{OG}}}{\partial T}|_{T=T_0}(T-T_0) + \frac{\partial^2 \alpha_{\mathrm{OG}}}{\partial T^2}|_{T=T_0}\frac{(T-T_0)^2}{2!} \tag{C.3}$$

with the terms:

$$\begin{aligned}\frac{\partial \alpha_{\mathrm{OG}}}{\partial T} &= -\frac{2Q_{\mathrm{OG}}}{T^3} e^{-\left(\frac{\Theta_{\mathrm{OG}}}{T}\right)} + \frac{Q_{\mathrm{OG}}\Theta_{\mathrm{OG}}}{T^4} e^{-\left(\frac{\Theta_{\mathrm{OG}}}{T}\right)} \\ &= \frac{Q_{\mathrm{OG}}}{T^3} e^{-\left(\frac{\Theta_{\mathrm{OG}}}{T}\right)} \left(\frac{\Theta_{\mathrm{OG}}}{T} - 2\right)\end{aligned} \tag{C.4}$$

$$\begin{aligned}\frac{\partial^2 \alpha_{\mathrm{OG}}}{\partial T^2} &= \frac{6Q_{\mathrm{OG}}}{T^4}e^{-\left(\frac{\Theta_{\mathrm{OG}}}{T}\right)} - \frac{2Q_{\mathrm{OG}}\Theta_{\mathrm{OG}}}{T^5}e^{-\left(\frac{\Theta_{\mathrm{OG}}}{T}\right)} - \frac{4Q_{\mathrm{OG}}\Theta_{\mathrm{OG}}}{T^5}e^{-\left(\frac{\Theta_{\mathrm{OG}}}{T}\right)} + \frac{Q_{\mathrm{OG}}\Theta_{\mathrm{OG}}^2}{T^6}e^{-\left(\frac{\Theta_{\mathrm{OG}}}{T}\right)} \\ &= \frac{Q_{\mathrm{OG}}}{T^4}e^{-\left(\frac{\Theta_{\mathrm{OG}}}{T}\right)}\left(6 - \frac{6\Theta_{\mathrm{OG}}}{T} + \frac{\Theta_{\mathrm{OG}}^2}{T^2}\right) \qquad \text{(C.5)}\end{aligned}$$

Replacing and simplifying, we get

$$\begin{aligned}P_{\alpha_{\mathrm{OG}}}(T) &= \frac{Q_{\mathrm{OG}}}{T_0^2}e^{-\left(\frac{\Theta_{\mathrm{OG}}}{T_0}\right)} + \frac{Q_{\mathrm{OG}}}{T_0^3}e^{-\left(\frac{\Theta_{\mathrm{OG}}}{T_0}\right)}\left(\frac{\Theta_{\mathrm{OG}}T_0}{-}2\right)(T-T_0) \\ &\quad + \frac{Q_{\mathrm{OG}}}{T_0^4}e^{-\left(\frac{\Theta_{\mathrm{OG}}}{T_0}\right)}\left[6 - \frac{6\Theta_{\mathrm{OG}}}{T_0} + \frac{\Theta_{\mathrm{OG}}^2}{T_0^2}\right]\frac{(T-T_0)^2}{2} \\ &= \frac{Q_{\mathrm{OG}}}{T_0^2}e^{-\left(\frac{\Theta_{\mathrm{OG}}}{T_0}\right)}\left[1 + \left(\frac{\Theta_{\mathrm{OG}}}{T_0} - 2\right)\frac{(T-T_0)}{T_0} + \left(6 - \frac{6\Theta_{\mathrm{OG}}}{T_0} + \frac{\Theta_{\mathrm{OG}}^2}{T_0^2}\right)\frac{(T-T_0)^2}{2T_0^2}\right] \\ &\qquad \text{(C.6)}\end{aligned}$$

At this point we define two intermediate variables, as

$$K_1 = \frac{Q_{\mathrm{OG}}}{T_0^2}e^{-\left(\frac{\Theta_{\mathrm{OG}}}{T_0}\right)} \qquad \text{(C.7)}$$

$$K_2 = \frac{1}{2}\left(6 - \frac{6\Theta_{\mathrm{OG}}}{T_0} + \frac{\Theta_{\mathrm{OG}}^2}{T_0^2}\right) \qquad \text{(C.8)}$$

Hence,

$$\begin{aligned}P_{\alpha_{\mathrm{OG}}}(T) &= K_1\left[3 - \frac{\Theta_{\mathrm{OG}}}{T_0} + K_2 + \left(\frac{\Theta_{\mathrm{OG}}}{T_0^2} - \frac{2}{T_0} - \frac{2K_2}{T_0}\right)T + \frac{K_2}{T_0^2}T^2\right] \\ &= A + BT + CT^2 \qquad \text{(C.9)}\end{aligned}$$

where

$$A = K_1\left(3 - \frac{\Theta_{\mathrm{OG}}}{T_0} + K_2\right) \qquad \text{(C.10)}$$

$$B = \frac{K_1}{T_0}\left[\frac{\Theta_{\rm OG}}{T_0} - 2 - 2K_2\right] \tag{C.11}$$

$$C = \frac{K_1 K_2}{T_0^2} \tag{C.12}$$

After fitting, the original parameters are progressively found by

$$K_1 = A + BT_0 + CT_0^2 \tag{C.13}$$

$$K_2 = \frac{CT_0^2}{K_1} \tag{C.14}$$

$$\Theta_{\rm OG} = T_0\left(3 + \sqrt{3 + 2K_2}\right) \tag{C.15}$$

$$Q_{\rm rate} = \frac{K_1 C_{\rm eff} T_0^2}{\Theta_{\rm OG} A_{\rm TM}} \tag{C.16}$$

C.2 Propagation of errors in outgassing fit curve

The propagation of errors in the previous expressions must take into account the covariance between parameters. Given a generic system of estimated parameters $\mathbf{x} = [x_1, x_2, ..., x_N]$ that depend on known parameters $\mathbf{y} = [y_1, y_2, ..., y_M]$ with a known estimated covariance matrix $\mathrm{cov}(\mathbf{y})$, we distinguish two cases:

- **Linear system** case: if the dependence of $\mathbf{x}$ with respect to $\mathbf{y}$ can be expressed as $\mathbf{x} = A\mathbf{y}$ by means of a matrix of coefficients, then the covariance matrix is directly found by:

$$\mathrm{cov}(\mathbf{x}) = A\,\mathrm{cov}(\mathbf{y})\,A^T \tag{C.17}$$

  where A^T is the transposed matrix of A.

- **Non-linear system** case: if the dependence is not linear and the system can only be expressed as a series of non-linear equations $\mathbf{x} = f(\mathbf{y})$, then the covariance matrix is written as

$$\mathrm{cov}(\mathbf{x}) = J\,\mathrm{cov}(\mathbf{y})\,J^T \tag{C.18}$$

where J and J^T are the Jacobi matrix and its transposed, defined as

$$J = \begin{bmatrix} \frac{\partial x_1}{\partial y_1} & \frac{\partial x_1}{\partial y_2} & \cdots & \frac{\partial x_1}{\partial y_M} \\ \vdots & \vdots & & \vdots \\ \frac{\partial x_N}{\partial y_1} & \frac{\partial x_N}{\partial y_2} & \cdots & \frac{\partial x_N}{\partial y_M} \end{bmatrix} \tag{C.19}$$

The errors associated to the coefficients obtained in Equations C.16 are traced by means of Equation C.17 or Equation C.18 depending on each function. The starting point is the covariance matrix associated to the vector of parameters $\mathbf{p} = [A, B, C]$ as reported by the fitting method, say

$$\operatorname{cov}(\mathbf{p}) = \begin{pmatrix} \sigma_A^2 & \sigma_{AB} & \sigma_{AC} \\ \sigma_{AB} & \sigma_B^2 & \sigma_{BC} \\ \sigma_{AC} & \sigma_{BC} & \sigma_C^2 \end{pmatrix} \tag{C.20}$$

Thus,

$$\sigma_{K_1}^2 = \sigma_A^2 + \sigma_B^2 T_0^2 + \sigma_C^2 T_0^4 + 2T_0\sigma_{AB} + 2T_0^2\sigma_{AC} + 2T_0^3\sigma_{CB} \tag{C.21}$$

$$\sigma_{K_2}^2 = K_2^2\left(\frac{\sigma_C^2}{C^2} + \frac{\sigma_{K_1}^2}{K_1^2} - 2\frac{\sigma_{CK_1}}{CK_1}\right) \tag{C.22}$$

where the covariance σ_{CK_1} is

$$\sigma_{CK_1} = \sigma_{AC} + \sigma_{BC}T_0 + \sigma_C^2 T_0^2 \tag{C.23}$$

Finally, the errors associated to the final parameters Θ_{OG} and Q_{rate}:

$$\sigma^2_{\Theta_{\mathrm{OG}}} = \frac{T_0^2\sigma^2_{K_2}}{3+2K_2} \tag{C.24}$$

$$\sigma^2_{Q_{\mathrm{rate}}} = \left(\frac{C_{\mathrm{eff}}T_0^2}{\Theta_{\mathrm{OG}}A_{\mathrm{TM}}}\right)^2\left[\sigma^2_{K_1} - \frac{2K_1}{\Theta_{\mathrm{OG}}}\sigma_{K_1\Theta_{\mathrm{OG}}} + \frac{K_1^2}{\Theta^2_{\mathrm{OG}}}\sigma^2_{\Theta_{\mathrm{OG}}}\right] \tag{C.25}$$

where the covariance $\sigma_{K_1\Theta_{\mathrm{OG}}}$ is

$$\sigma_{K_1C} = P\sigma_{AC} + Q\sigma_{AK_1} + T_0P\sigma_{BC} + T_0Q\sigma_{BK_1} + T_0^2P\sigma^2_C + \left(P + T_0^2Q\right)\sigma_{CK_1} + Q\sigma^2_{K_1} \tag{C.26}$$

with

$$P = \frac{T_0^3}{K_1}\left(3+\frac{2CT_0}{K_1}\right)^{-1/2} \tag{C.27}$$

$$Q = -\frac{CT_0^3}{K_1^2}\left(3+\frac{2CT_0}{K_1}\right)^{-1/2} \tag{C.28}$$

$$\sigma_{AK_1} = \sigma^2_A + T_0\sigma_{AB} + T_0^2\sigma_{AC} \tag{C.29}$$

$$\sigma_{BK_1} = \sigma_{AB} + T_0\sigma^2_B + T_0^2\sigma_{BC} \tag{C.30}$$

APPENDIX D

Measurement of pressure in the 4-mass vacuum chamber

Far from being trivial, the measurement of the absolute pressure in high vacuum (down to 10^{-9} mbar or 10^{-7} Pa) is clearly one of the most delicate steps in the measurement of the thermal coefficient, where any kind of error in the pressure measurement leads to deviations in the estimation of the thermal effects. In such conditions of vacuum, ionization gauges arise as the most convenient pressure sensors in terms of sensitivity but, however, they present some important drawbacks: the accuracy error up to 15% of the readout and other factors can still distort the measurement with accumulated errors up to 100%. Therefore, it is of high importance to evaluate the environment and the performance of the gauge in order to reduce as much as possible the measurement errors.

In this appendix, we first analyse the particular case of the pressure measurements in the 4-mass torsion pendulum from the University of Trento in order to obtain correction factors related with the residual gas composition. After that, further discussion on the gauge location allows us to estimate the pressure inside the Electrode Housing cavity. Finally, some non-linearities observed in the readout are analysed by cross-checking them with an independent readout.

D.1 Residual gas composition

The principle of measurement of the ionization gauges is to indirectly measure the pressure by detecting the quantity of ions in the environment after radiating a small volume of the gas with electrons. The ions are attracted to a charged electrode that collects them, inducing a current in the electrode proportional to the number of particles, and thus to the pressure, assuming that all the particles have a same ionization rate. However, different particles do have different ionization rates, so eventual concentrations of particles with different ionization rates may lead to a systematic error in the pressure measurement.

In fact, most particles in normal atmosphere have quite similar ionization rates and the error should be pretty small —see Table D.1. However, at high vacuums the concentration of other species like hydrogen can easily induce a non-negligible error in the measurement.

In order to scan the gas composition, a residual gas analyser was installed in the vacuum chamber for some days and some pressure cycles. Figure D.1 shows the evolution

Molecule	Correction factor
H_2	0.42–0.53
He	0.18
H_2O	0.9
N_2	1
CO	1.05–1.1
O_2	0.8–0.9

Table D.1: Gauge correction factors for Bayard-Alpert ionization gauges calibrated according to a full nitrogen atmosphere [168]. The coefficients indicated are directly the sensitivity of the gauge to a relative pressure of each chemical specie.

of the composition during 8 days. Since the only relevant chemical specie with a ionization rate far enough from nitrogen is hydrogen, according to its proportion of ~30% including both H_2 and ions H^+, a correction factor of 1.15 must be applied to all the pressure measurements carried out during the thermal measurement campaign, assuming no significant variations in composition.

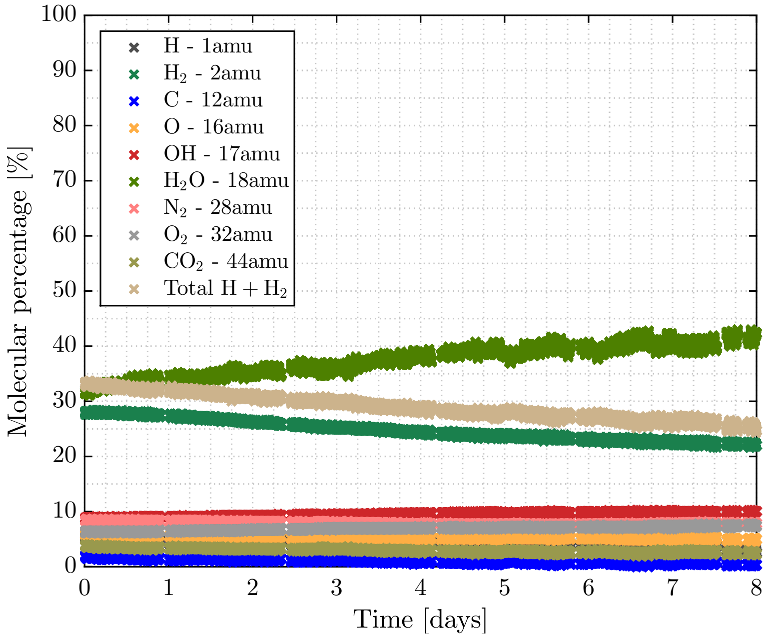

Figure D.1: Residual gas composition in the vacuum chamber during 8 days including some pressure cycles, all around 10^{-5} Pa. Water remains as the most frequent molecule and the total proportion of hydrogen molecules —both H_2 and H^+— is close to 30%. Since the gauge is calibrated in a way that is sensitive to just *half* of the hydrogen molecules, the real pressure is 15% larger than the value reported by the gauge.

D.2 Pressure system schematic

In addition to the residual gas correction, the presence of local pressure differences between the location of the gauge with respect to the experimental point of interest must be assessed. The schematic in Figure D.2 shows the particle flux in the facility.

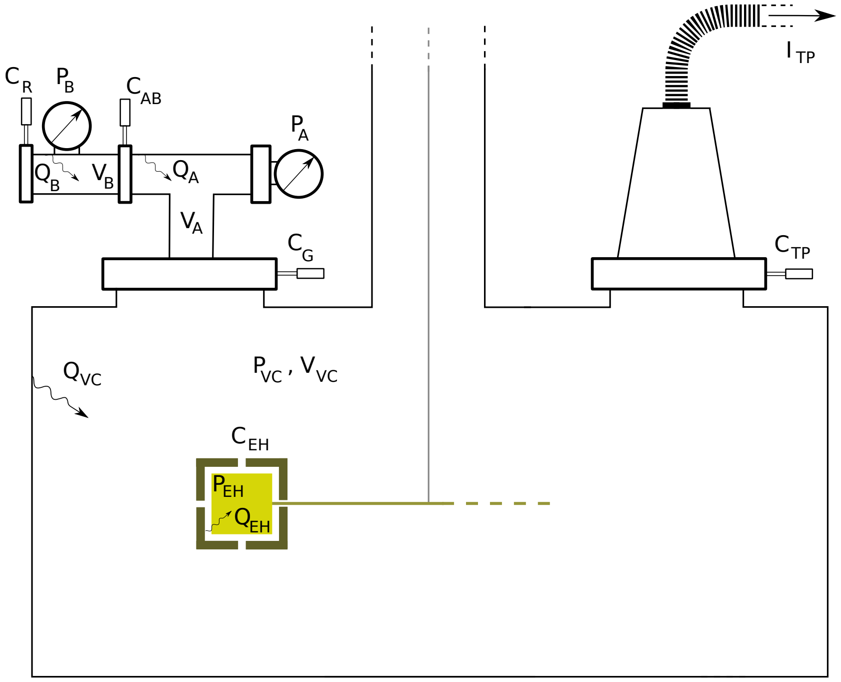

Figure D.2: Particle flux in the 4-mass vacuum chamber.

In normal conditions, the valve at C_{AB} is closed and the main gauge P_A is sensitive to the pressure in the cavity V_A, which differs from the pressure in the main cavity V_{VC} because of the local outgassing Q_A and conductance C_G. This is written as

$$P_A = P_{\mathrm{VC}} + \frac{Q_A}{C_G} \tag{D.1}$$

where P_{VC} is the limit pressure that is nominally achieved by running the turbo pump at a specific speed. The nominal case considered is a pumping speed of 27000 rpm achieving a pressure of $\sim 5 \cdot 10^{-6}$ Pa with temperature stabilized around 20°C. The conductance at the output C_{TP} is $\approx 7000\,\mathrm{L\,s^{-1}}$.

An estimation of the outgassing rate Q_A is obtained by measuring the increment of pressure in the cavity A after closing the metallic gate at C_G once in high vacuum. Under the assumption of no loses and low outgassing rates, immediately after closing the valve the pressure in the cavity increases linearly with time as

$$\Delta P_A = \frac{Q_A}{V_A} t \tag{D.2}$$

A quick test with an estimated $C_G \approx 4\,\mathrm{L\,s^{-1}}$ leads to a ΔP between P_A and P_{VC} of $4.5 \cdot 10^{-7}\,\mathrm{Pa}$. Since the lowest pressure obtained in the thermal experiments rarely underpasses the $5 \cdot 10^{-6}\,\mathrm{Pa}$, this difference is considered negligible.

On the other hand, some residual outgassing is expected as well in the Electrode Housing. Its eventual contribution as an additional ΔP_{EH} with respect to the pressure in the vacuum chamber is addressed by estimating the conductance C_{EH}. Since the particle flow is clearly in the molecular regime (Kn > 1), the conductance of a part is obtained from the calculated probability of a particle to get the proper direction to pass by. From [168], the conductances of a *tube* and an orifice are approximated to (in $[\mathrm{L\,s^{-1}}]$):

$$C_{TUBE} = 12.1\,\frac{D^3}{L} \tag{D.3}$$

$$C_{ORIFICE} = 11.6\,A \tag{D.4}$$

where L, A, and D stand for longitude, area and diameter, respectively, all of them in [cm]. The combined conductance of a cylindrical *hole*, composed by and orifice and a tube is defined as

$$\frac{1}{C_{\mathrm{TOTAL}}} = \frac{1}{C_{\mathrm{TUBE}}} + \frac{1}{C_{\mathrm{ORIFICE}}} \tag{D.5}$$

The resulting conductance of each Electrode Housing *holes* is $2.15\,\mathrm{L\,s^{-1}}$. In the torsion pendulum EH prototype, only three of the six holes are not blocked. Therefore, the final conductance can be estimated to

$$C_{\mathrm{EH}} \approx 6.5\,\mathrm{L\,s^{-1}} \tag{D.6}$$

With such a high conductance, and assuming that Q_{EH} is much smaller than Q_A since the Electrode Housing inner parts and the Test Mass are highly polished, the resulting pressure difference between P_{EH} and P_{VC} is also neglected.

D.3 Pressure gas non linearities

Apparent reduction of the thermal coefficient at pressures higher than $5\text{–}6 \cdot 10^{-5}\,\mathrm{Pa}$ is observed affecting the measurements at any temperature. At this pressure, the Knudsen number is ≈20 (at $T \approx 35°\mathrm{C}$), and therefore the flux is still fully molecular and the behaviour should still be linear. Therefore, this effect can not be attributed to the transition between molecular and continuous regimes, so an alternative explanation could be a non-linearity in the pressure measurement.

In order to investigate the effect, a second pressure gauge was added to the setup —see P_B in Figure D.2— to crosscheck the readout of P_A. After opening the valve in C_{AB}, the pressure at P_A increased $\approx 10^{-5}$ Pa, what is assumed to be the impact of adding the outgassing from cavity V_B to the whole chamber and must be subtracted for all the pressure measurements in same conditions. Amongst the different parts in such cavity, a rubber-based valve C_R, opposite to the valve C_{AB} in Figure D.2, is identified as the major outgassing part.

Figure D.3 shows the readouts of one gauge against the other. A clear tendency change at around $P \approx 6 \cdot 10^{-5}$ Pa suggests a non-linearity at some of the gauges, what is consistent with the observations.

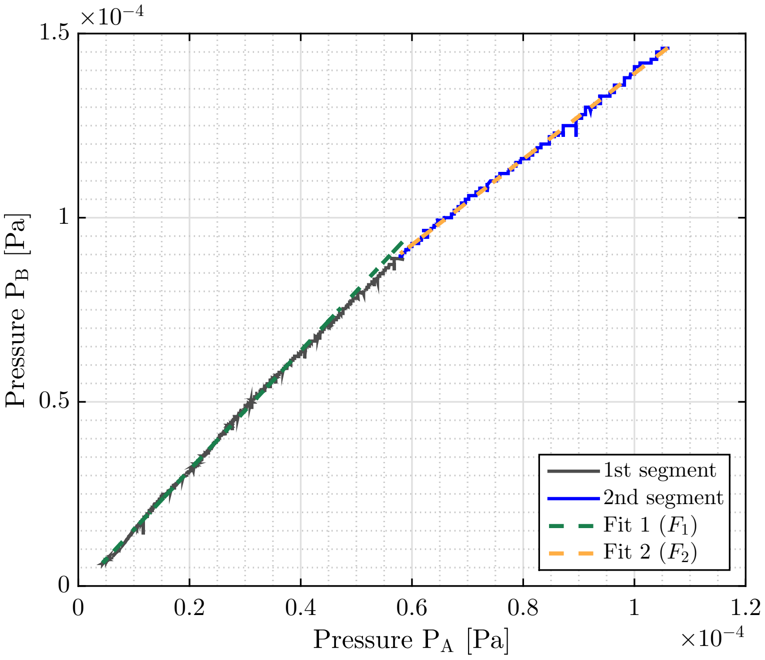

Figure D.3: Calibration plot between the two pressure gauges installed. A non-linearity is observed close to $6 \cdot 10^{-5}$ Pa.

When fitting both lines with the function $P_B = m P_A + k$, different patterns are obtained for the data stretches below and above $P \approx 6 \cdot 10^{-5}$ Pa, as shown in Table D.2. The independent term in line F_1 ($P < 6 \cdot 10^{-5}$ Pa) is consistent with predictions in Section D.2, $\Delta P_{AB} \sim 10^{-7}$ Pa. The change in the slope around a pressure value of $6 \cdot 10^{-5}$ Pa confirms a non linear behaviour that suggests to restrict the pressure measurement range below $5 \cdot 10^{-5}$ Pa. We notice that the disagreement between the two gauges readout at low pressure is significantly bigger than the expected circa 30% due to declared possible gauges miscalibration, pointing again to possible gas composition dependent effects.

Function	**m**	$\sigma_{\mathbf{m}}$	**k** [**Pa**]	$\sigma_{\mathbf{k}}$ [**Pa**]
F_1	1.617	10^{-4}	$-8.39 \cdot 10^{-7}$	$2 \cdot 10^{-9}$
F_2	1.163	10^{-3}	$2.29 \cdot 10^{-5}$	10^{-7}

Table D.2: Fit coefficients for the two functions in Figure D.3.

D.4 Conclusions

As a consequence of the analysis carried out in this Appendix, the following criteria are decided for the estimation of the pressure:

- A proportional correction factor of 1.15 must be applied to the pressure readout. Such a factor is coherent with the 30 % of hydrogen measured inside the vacuum chamber.
- Due to detected readout non-linearities, the available pressure range for the thermal modulations is reduced to a maximum working pressure of $5 \cdot 10^{-5}$ Pa.

A recent investigation has pointed to dependence of the hydrogen composition on the pumping speed. Further analysis of this effect in future measurements would provide a more accurate pressure readout.

APPENDIX E

Thermal characterisation of the pendulum EH prototype

The Electrode Housing (EH) prototype installed in the 4-mass torsion pendulum facility is slightly different from the final flight model Electrode Housing. Such an issue can induce to different heating patterns when applying the same input signals to the heaters. The similarity between the SSM and the measured amplitudes in the Electrode Housing prototype is analysed in this appendix following two approaches: (1) a direct sampling of the gains at two specific frequencies in the milli-Hertz band by applying sinusoid signals to the heaters and (2) an analysis of the temperature gradients obtained in front of a standard heat modulation pattern. In both cases, the heat signal applied to the *real* heaters needs to be post-processed in order to correct the temperature dependence of the NTC thermistors being used as heaters.

The results reported here complement Figure 5.10 presented in Section 5.3.2.

E.1 Single heater transfer functions

The heaters in the Electrode Housing prototype are commanded at a *physical* heater level instead of the *logical* heater scheme implemented in the satellite. This particularity actually allows to individually activate each of the two heaters at the same side of the Electrode Housing. Consequently, this setup turns out to be an ideal platform where to directly sample the thermal transfer functions reported in Chapter 3.

The test is organised as follows: sinusoids signals of $f = 2\,\mathrm{mHz}$ and 5 V are applied to each *physical* heater with minimum offsets to avoid negative voltages, leading to a final voltage function of $v(t) = 5\sin\left(2\pi f t\right) + 5\,\mathrm{V}$. As a result, the power applied presents two strong components at 2 and 4 mHz due to the unavoidable offset term.

The amplitudes measured are shown in Table E.1 together with the gains from the thermal model [140]. The experimental gains have been obtained by normalizing the temperature amplitudes with respect to the power applied at each frequency taking into account NTC thermistors dependence on temperature.

Some divergences are clearly identified. First, the gain at the opposite face of the Electrode Housing is ~4 times larger in the pendulum than in the model, suggesting a higher conduction between faces than expected by the model. Second, while the model is nearly perfectly symmetric between sensors and heaters on the same face, clear differences are observed in the measurements, pointing to a significant asymmetric distributions of items. However, since both heaters on the same face are going to be activated simultaneously, this effect is less important —though non-representative temperature

		TS1		**TS2**		**TS3**		**TS4**	
		2 mHz	**4 mHz**	**2 mHz**	**4 mHz**	**2 mHz**	**4 mHz**	**2 mHz**	**4 mHz**
H1-1	G_p	1.12	0.94	0.73	0.57	0.082	0.040	0.085	0.041
	G_m	1.34	0.80	1.36	0.81	0.018	0.002	0.018	0.002
H1-2	G_p	0.70	0.51	0.63	0.49	0.076	0.031	0.078	0.027
	G_m	1.36	0.81	1.34	0.79	0.018	0.002	0.018	0.002
H2-1	G_p	0.077	0.026	0.081	0.030	0.73	0.62	0.62	0.51
	G_m	0.018	0.002	0.018	0.002	1.34	0.79	1.36	0.81
H2-2	G_p	0.738	0.023	0.786	0.027	0.61	0.48	0.64	0.52
	G_m	0.018	0.002	0.018	0.002	1.34	0.81	1.36	0.79

Table E.1: Comparison between the ESATAN thermal model gains (G_m) and the measurements on the Electrode Housing replica installed in the pendulum facility (G_p), all of them in [K W^{-1}]. The pendulum gains are the measured amplitudes normalised by the estimated power applied.

responses lead to non-representative temperature gradients. Third, a cut-off frequency effect is observed between the two frequencies clearly affecting the model but not so much the measurements. Finally, the responses between adjacent heater-sensor pairs present higher amplitudes in the model than in the system, actually a factor 2. Such a feature could be associated to the simplicity of the Electrode Housing discretisation in the thermal model —see Figure E.1—, where the nodes associated to the heaters are directly in contact to the nodes associated to the temperature sensors on the same face.

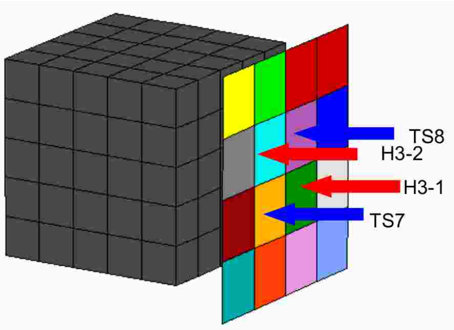

Figure E.1: Location of the heaters (H_i), temperature sensors (TS_j) on one side of the EH2, and the thermal nodes where they are attached in the thermal model [140]. Credits: CGS S.p.A.

E.2 Temperature gradient transfer function from direct measurements

It is also of interest to directly compare the time series from both the SSM and the data from the pendulum in front of the same heat modulation pattern. With such a purpose, a 10 V, 2 mHz-squared signal is applied to the H1/H2 heaters, producing the temperature gradient responses shown in Figure E.2. The power applied has been normalised considering a room temperature of 19.7 °C, what is equivalent to pulses of 40.2 mW per heater.

A factor of ≈ 2.33 between the peak-to-peak amplitudes is found. The high frequencies of the measured temperature gradient are significantly much more attenuated compared to the simulated temperature gradient. These observations are also seen by the estimated transfer function between the two signals, which reports a gain of 1.84 at 2 mHz, increasing with frequency. These results are consistent with those obtained in the previous section and are coherent with the idea that the Electrode Housing prototype presents a higher thermal conduction between its $\pm x$ faces than the model, which in fact reduces the amplitude of the sensed temperature gradient. Such a high thermal conduction could be attributed to differences in the subjection of the Electrode Housing with respect to its base.

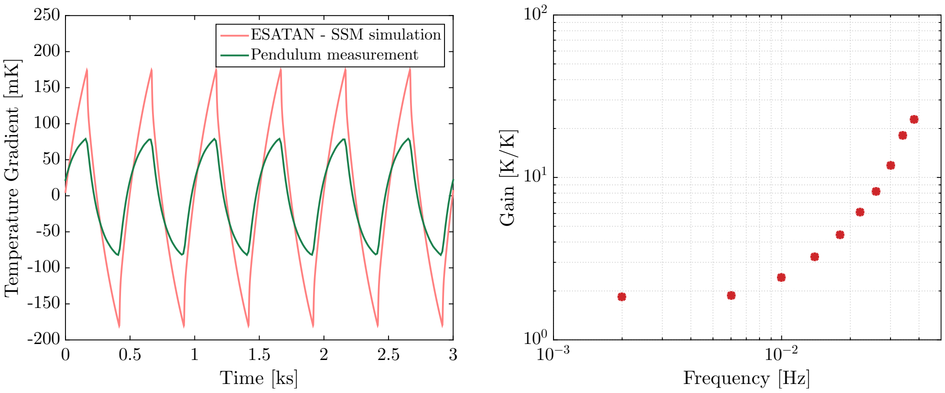

Figure E.2: On the *left*, the time series associated to a same heat input for both the pendulum (*green*) and a SSM simulation (*red*) at 2 mHz. On the *right*, an estimation of the transfer function between the measurement the simulation yields a factor 1.84 at 2 mHz. Only the frequency bins with high signal have been plotted —the immediate harmonics of a 2 mHz sinusoid. The high frequencies appear to be much more attenuated in the pendulum readout than in the simulation.

APPENDIX F

Thermal transfer function of the LCA struts

This appendix introduces the transfer function that estimates the thermal attenuation between edges of the Suspension Struts that attach the LTP Core Assembly (LCA) to the structure of the satellite. Beyond the mechanical application of these parts, these struts also provide an additional thermal isolation layer to the LCA.

Each strut is roughly a cylinder composed of three parts: a central part of Carbon-fiber-reinforced polymer (CFRP) of 9.95 cm and two Titanium end fittings of 2.9 cm at the edges. Following the analogy between thermal systems and electronic circuits, each strut can be modelled as shown in Figure F.1. Assuming that heat is only transferred by conduction and that the flux is unidirectional, the system is approximated to a three-stage block with four temperature nodes.

Each part —the CFRP central part and each Titanium end fitting— is modelled by equivalent thermal resistances (θ_{CFRP} and θ_{Ti}) and total thermal capacitances (C_{CFRP} and C_{Ti}). Values for the resistances are obtained from a dedicated campaign by ASD [169], while the capacitances are calculated assuming the properties in Table 6.1 and diameters for each part $d = 2.4\,\mathrm{cm}$. Table F.1 shows the thermal properties of each part.

Part	**Thermal resistance** [$\mathbf{K\,W^{-1}}$]	**Thermal capacitance** [$\mathbf{J\,K^{-1}}$]
CFRP central	26	63.3
Ti end fitting	7	30.5
Total	40	124

Table F.1: Thermal properties of the Titanium and CFRP blocks composing the struts. The total amount already includes the two pieces of Titanium.

The transfer functions linking the temperatures between edges of each block are

$$H_{\mathrm{Ti}}(s) = \frac{\tilde{T}_{\mathrm{A}}(s)}{\tilde{T}_{\mathrm{S/C}}(s)} \tag{F.1}$$

$$H_{\mathrm{CFRP}}(s) = \frac{\tilde{T}_{\mathrm{B}}(s)}{\tilde{T}_{\mathrm{A}}(s)} \tag{F.2}$$

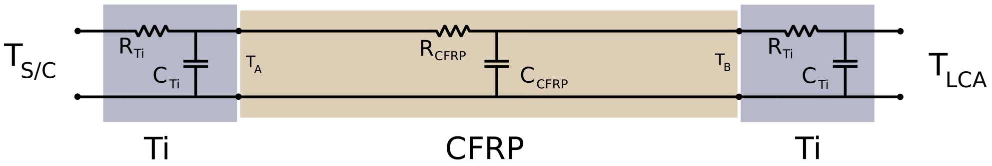

Figure F.1: Thermal model for the Suspension Struts.

where the different $\tilde{T}_i(s)$ are the Laplace transforms of the temperature at each node in Figure F.1. Solving each block separately, single-pole first order transfer functions are obtained:

$$H_{\mathrm{Ti}}(s) \quad = \quad = \frac{1}{1+s\,C_{\mathrm{Ti}}\,\theta_{\mathrm{Ti}}} \tag{F.3}$$

$$H_{\mathrm{CFRP}}(s) \quad = \quad \frac{1}{1+s\,C_{\mathrm{CFRP}}\,\theta_{\mathrm{CFRP}}} \tag{F.4}$$

Finally, an approximation to the transfer function of the whole strut is found by

$$H_{\mathrm{str}}(s) \quad = \quad H_{\mathrm{Ti}}(s)\,H_{\mathrm{CFRP}}(s)\,H_{\mathrm{Ti}}(s) \tag{F.5}$$

$$H_{\mathrm{str}}(s) \quad = \quad \frac{1}{\left(1+s\,C_{\mathrm{CFRP}}\,\theta_{\mathrm{CFRP}}\right)\left(1+s\,C_{\mathrm{Ti}}\,\theta_{\mathrm{Ti}}\right)^2} \tag{F.6}$$

Table F.2 shows the amplitudes of the attenuation factors calculated as the gains of the transfer functions when replacing the complex variable s by $j\omega$.

Transfer function	**Gain**	
	1 mHz	**30 mHz**
$\lvert H_{\mathrm{Ti}}(\omega)\rvert$	0.197	0.007
$\lvert H_{\mathrm{CFRP}}(\omega)\rvert$	0.338	0.012
$\lvert H_{\mathrm{str}}(\omega)\rvert$	0.013	$5.3\cdot 10^{-7}$

Table F.2: Transfer function gains of the different stages of the strut model.

References

[1] M. Nofrarias. *Thermal Diagnostics in the LISA Technology Package Experiment*. PhD thesis, Universitat de Barcelona, 2007. vi, 21, 22, 23, 38, 41, 44, 46, 58

[2] J. Sanjuán. *Development and validation of the thermal diagnostics instrumentation in LISA Pathfinder*. PhD thesis, Universitat Politècnica de Catalunya, 2009. vi, 2, 11, 23, 28, 29, 47, 48, 49, 50, 52, 56, 60, 61, 100, 102, 122

[3] M. Díaz-Aguiló. *Magnetic diagnostics algorithms for LISA Pathfinder: system identification and data analysis*. PhD thesis, Universitat Politècnica de Catalunya, 2011. vi, 6, 22, 23, 33

[4] P. Amaro-Seoane et al. The Gravitational Universe. 2013. Document submitted to the European Space Agency for the L2/L3 selection of ESA's Cosmic Vision program. URL. 1, 4, 9, 12

[5] P. Bender et al. LISA for the detection and observation of gravitational waves. Prephase A. Technical Report 244, Max Plank für Quantenoptik, 1998. 1, 9, 12

[6] A. Einstein. Über Gravitationswellen. *Sitzungsberichte der Königlich Preußischen Akademie der Wissenschaften (Berlin)*, pages 154–167, 1918. 1

[7] R.A. Hulse and J.H. Taylor. Discovery of a pulsar in a binary system. *Astrophys.J.*, 195:L51–L53, 1975. 2

[8] Ch.W. Misner, K.S. Thorne, and J.A. Wheeler. *Gravitation*. W. Freeman, 1973. 3

[9] S. A. Hughes. Listening to the universe with gravitational-wave astronomy. *Annals of Physics*, 303(1):142 – 178, 2003. 3, 4

[10] B. F. Schutz. Gravitational waves on the back of an envelope. *American Journal of Physics*, 52(5):412–419, 1984. 3, 4

[11] O. D. Aguiar. Past, present and future of the Resonant-Mass gravitational wave detectors. *Research in Astronomy and Astrophysics*, 11(1):1, 2011. 4, 5

[12] F. Acernese et al. The Advanced Virgo detector. *Journal of Physics: Conference Series*, 610(1):012014, 2015. 4, 7

[13] S. Dwyer and LIGO Scientific Collaboration. Advanced LIGO status. *Journal of Physics: Conference Series*, 610(1):012013, 2015. 4, 7

[14] R. et al. van Haasteren. Placing limits on the stochastic gravitational-wave background using European Pulsar Timing Array data. *Monthly Notices of the Royal Astronomical Society*, 414(4):3117–3128, 2011. 4, 8

[15] X.-J. Zhu et al. An all-sky search for continuous gravitational waves in the Parkes Pulsar Timing Array data set. *Monthly Notices of the Royal Astronomical Society*, 444(4):3709–3720, 2014. 4, 8

[16] R. D. Ferdman et al. The European Pulsar Timing Array: current efforts and a LEAP toward the future. *Classical and Quantum Gravity*, 27(8):084014, 2010. 4, 8

[17] P. A. R. et al. Ade. Joint Analysis of BICEP2 Keck Array and Planck Data. *Phys. Rev. Lett.*, 114:101301, Mar 2015. 4, 8

[18] C. J. Moore, R. H. Cole, and C. P. L. Berry. *Gravitational Wave Sensitivity Curve Plotter*. 2014. 5

[19] C. J. Moore, R. H. Cole, and C. P. L. Berry. Gravitational-wave sensitivity curves. *Classical and Quantum Gravity*, 32(1):015014, 2015. 5

[20] J. Weber. Detection and Generation of Gravitational Waves. *Phys. Rev.*, 117:306–313, Jan 1960. 4

[21] R. L. Garwin and J. L. Levine. Single Gravity-Wave Detector Results Contrasted with Previous Coincidence Detections. *Phys. Rev. Lett.*, 31:176–180, Jul 1973. 5

[22] J. Weber. Evidence for Discovery of Gravitational Radiation. *Phys. Rev. Lett.*, 22:1320–1324, Jun 1969. 5

[23] J. Weber. Anisotropy and Polarization in the Gravitational-Radiation Experiments. *Phys. Rev. Lett.*, 25:180–184, Jul 1970. 5

[24] E. Mauceli, Z. K. Geng, W. O. Hamilton, W. W. Johnson, S. Merkowitz, A. Morse, B. Price, and N. Solomonson. The Allegro gravitational wave detector: Data acquisition and analysis. *Phys. Rev. D*, 54:1264–1275, Jul 1996. 5

[25] M. P. McHugh et al. Calibration of the ALLEGRO resonant detector. *Classical and Quantum Gravity*, 22(18):S965, 2005. 5

[26] M. Bonaldi, M. Cerdonio, L. Conti, M. Pinard, G. A. Prodi, L. Taffarello, and J. P. Zendri. Selective readout and back-action reduction for wideband acoustic gravitational wave detectors. *Phys. Rev. D*, 68:102004, Nov 2003. 5

[27] M. Cerdonio et al. The ultracryogenic gravitational-wave detector AURIGA. *Classical and Quantum Gravity*, 14(6):1491, 1997. 5

[28] P. Astone, M. Bassan, E. Coccia, S. D'Antonio, V. Fafone, G. Giordano, A. Marini, Y. Minenkov, I. Modena, A. Moleti, G. V. Pallottino, G. Pizzella, A. Rocchi, F. Ronga, R. Terenzi, and M. Visco. Analysis of 3 years of data from the gravitational wave detectors EXPLORER and NAUTILUS. *Phys. Rev. D*, 87:082002, Apr 2013. 5

[29] D. G. Blair, E. N. Ivanov, M. E. Tobar, P. J. Turner, F. van Kann, and I. S. Heng. High Sensitivity Gravitational Wave Antenna with Parametric Transducer Readout. *Phys. Rev. Lett.*, 74:1908–1911, Mar 1995. 5

[30] P. Astone et al. The next science run of the gravitational wave detector NAUTILUS. *Classical and Quantum Gravity*, 19(7):1911, 2002. 5

[31] A. De Waard et al. MiniGRAIL progress report 2004. *Classical and Quantum Gravity*, 22(10):S215, 2005. 5

[32] S. M. Merkowitz and W. W. Johnson. Spherical gravitational wave antennas and the truncated icosahedral arrangement. *Phys. Rev. D*, 51:2546–2558, Mar 1995. 5

[33] O.D. Aguiar et al. The gravitational wave detector Mario Schenberg: status of the project. *Brazilian Journal of Physics*, 32:866 – 868, 12 2002. 5

[34] A. Lobo. Effect of a weak plane GW on a light beam. *Classical and Quantum Gravity*, 9(5):1385, 1992. 6

[35] C. Affeldt et al. Advanced techniques in GEO 600. *Classical and Quantum Gravity*, 31(22):224002, 2014. 7

[36] H. Grote and the LIGO Scientific Collaboration. The GEO 600 status. *Classical and Quantum Gravity*, 27(8):084003, 2010. 7

[37] R. Takahashi and the TAMA Collaboration. Status of TAMA300. *Classical and Quantum Gravity*, 21(5):S403, 2004. 7

[38] F. Acernese, P. Amico, M. Alshourbagy, F. Antonucci, S. Aoudia, et al. Status of Virgo detector. *Classical and Quantum Gravity*, 24:S381–S388, 2007. 7

[39] D. Sigg. Status of the LIGO detectors. *Classical and Quantum Gravity*, 25:114041, 2008. 7

[40] S. Hild. Advanced ligo: Next steps and future improvements. In *13th Marcel Grossmann Meeting*, 2012. 7

[41] M. Abernathy et al. Einstein gravitational wave Telescope conceptual design study. Technical Report ET-0106C-10, 2011. 7

[42] J. Aasi et al. Improved Upper Limits on the Stochastic Gravitational-Wave Background from 2009–2010 LIGO and Virgo Data. *Phys. Rev. Lett.*, 113:231101, Dec 2014. 7

[43] M. H. Gregory and the LIGO Scientific Collaboration. Advanced LIGO: the next generation of gravitational wave detectors. *Classical and Quantum Gravity*, 27(8):084006, 2010. 7

[44] F. Acernese et al. Advanced Virgo: a 2nd generation interferometric gravitational wave detector. *Classical and Quantum Gravity*, 32:024001, 2015. 7

[45] *IndIGO*. Indian Initiative in Gravitational-wave Observations, 2015. IndIGO web. 7

[46] R. Gouaty. Status of the Advanced Virgo Gravitational Wave Detector. In *50th Rencontres de Moriond - Gravitation*, 2015. 8

[47] A. Witze. Physics: Wave of the future. *Nature*, 511(7509):278–281, July 2015. DOC. 8

[48] K. Somiya. Detector configuration of KAGRA —the Japanese cryogenic gravitational wave detector. *Classical and Quantum Gravity*, 29(12):124007, 2012. 8

[49] M. Punturo et al. The Einstein Telescope: a third-generation gravitational wave observatory. *Classical and Quantum Gravity*, 27(19):194002, 2010. 8

[50] Z. Arzoumanian and NANOGrav Collaboration. Gravitational Waves from Individual Supermassive Black Hole Binaries in Circular Orbits: Limits from the North American Nanohertz Observatory for Gravitational Waves. *The Astrophysical Journal*, 794(2):141, 2014. 8

[51] G. Hobbs et al. The International Pulsar Timing Array project: using pulsars as a gravitational wave detector. *Classical and Quantum Gravity*, 27(8):084013, 2010. 8

[52] The North American Nanohertz Observatory for Gravitational Waves (NANOGrav). 2015. URL. 8

[53] S. T. McWilliams, J. P. Ostriker, and F. Pretorius. The imminent detection of gravitational waves from massive black-hole binaries with pulsar timing arrays. *ArXiv e-prints*, November 2012. 8

[54] D. Barkats et al. Degree-scale Cosmic Microwave Background Polarization Measurements from Three Years of BICEP1 Data. *The Astrophysical Journal*, 783(2):67, 2014. 8

[55] I.V. Ogburn et al. The BICEP2 CMB polarization experiment, 2010. 8

[56] P. A. R. Ade et al. Detection of B-Mode Polarization at Degree Angular Scales by BICEP2. *Phys. Rev. Lett.*, 112:241101, Jun 2014. 8

[57] R. Adam et al. Planck 2015 results. I. Overview of products and scientific results. 2015. 8

[58] C. D. Sheehy et al. The Keck Array: a pulse tube cooled CMB polarimeter, 2010. 8

[59] Z. Ahmed et al. BICEP3: a 95GHz refracting telescope for degree-scale CMB polarization , 2014. 8

[60] N. Seto, S. Kawamura, and T. Nakamura. Possibility of direct measurement of the acceleration of the universe using 0.1 hz band laser interferometer gravitational wave antenna in space. *Phys. Rev. Lett.*, 87:221103, Nov 2001. 9

[61] K. Yagi and N. Seto. Detector configuration of DECIGO/BBO and identification of cosmological neutron-star binaries. *Phys. Rev. D*, 83:044011, Feb 2011. 9

[62] ESA announcement on L3 slot. November 2013. URL. 9

[63] M. Armano et al. The LISA Pathfinder Mission. *Journal of Physics: Conference Series*, 610(1):012005, 2015. 9

[64] M. Ando et al. DECIGO pathfinder. *Classical and Quantum Gravity*, 26(9):094019, 2009. 9

[65] K. Yagi. Gravitational wave observations of galactic intermediate-mass black hole binaries with DECIGO path finder. *Classical and Quantum Gravity*, 29(7):075005, 2012. 9

[66] C. Cutler and J. Harms. Big Bang Observer and the neutron-star-binary subtraction problem. *Phys. Rev. D*, 73:042001, 2006. 9

[67] M. Tinto and S. V. Dhurandhar. Time-Delay Interferometry. *Living Reviews in Relativity*, 17(6), 2014. 11

[68] P. Amaro-Seoane et al. eLISA/NGO: Astrophysics and cosmology in the gravitational-wave millihertz regime. *GW Notes*, 6:4–110, 2013. Arxiv. 12

[69] Gravitational-Wave Core Team Gravitational-Wave Community Science Team and Gravitational-Wave Science Task Force. Gravitational-Wave Mission Concept Study Final Report. Technical report, National Aeronautics and Space Administration (NASA), August 2012. URL. 12

[70] P. Amaro-Seoane et al. Low-frequency gravitational-wave science with eLISA/NGO. *Classical and Quantum Gravity*, 29(12):124016, 2012. URL. 13

[71] S. Vitale. Space-borne gravitational wave observatories. *General Relativity and Gravitation*, 46(5), 2014. Arxiv. 13

[72] S. Anza, M. Armano, E. Balaguer, M. Benedetti, C. Boatella, et al. The LTP experiment on the LISA Pathfinder mission. *Classical and Quantum Gravity*, 22:S125–S138, 2005. 13

[73] M. Armano et al. Free-flight experiments in LISA Pathfinder. *Journal of Physics: Conference Series*, 610(1):012006, 2015. URL. 13, 15, 30, 32, 33, 107

[74] A. Carmain, C. Dunn, J. Ziemer, V. Hruby, D. Spence, N. Demmons, T. Roy, R. McCormick, E. Ehrbar, J. Zwahlen, W. Connolly, J. O'Donnell, F. Markley, P. Maghami, and O. Hsu. Space Technology 7 – Micropropulsion and Mass Distribution. In *Aerospace Conference, 2007 IEEE*, pages 1–10, March 2007. 13

[75] N. Brandt et al. Experiment Performance Budget. Technical Report S2-ASD-RP-3036, Airbus Defence and Space GmbH, 2007. 15, 23, 46, 143

[76] M. Nofrarias, F. Gibert, N. Karnesis, A.F. Garcia, M. Hewitson, et al. Subtraction of temperature induced phase noise in the LISA frequency band. *Phys.Rev.*, D87(10):102003, 2013. 16

[77] P. Cañizares, A. Conchillo, E. García-Berro, L. Gesa, C. Grimani, et al. The Diagnostics subsystem on board LISA PathFinder and LISA. *Classical and Quantum Gravity*, 26:094005, 2009. 16, 22

[78] D. Mance. *Development of Electronic System for Sensing and Actuation of Test Mass of the Inertial Sensor LISA*. PhD thesis, University of Split, 2012. URL. 17, 19

[79] J. Weber. Actuators: ISS-FEE, February 2012. *Slides for the LPF School in ESTEC, 2012.02.28*. 20

[80] J. Weber. Sensors: ISS-FEE, February 2012. *Slides for the LPF School in ESTEC, 2012.02.28*. 20

[81] T. Ziegler, W. Fichter, M. Schulte, and S. Vitale. Principles, operations, and expected performance of the LISA Pathfinder charge management system. *Journal of Physics: Conference Series*, 154(1):012009, 2009. 20

[82] C. Zanoni, D. Bortoluzzi, J. W. Conklin, I. Köker, B. Seutchat, and S. Vitale. Summary of the results of the LISA Pathfinder Test Mass release. *Journal of Physics: Conference Series*, 610(1):012022, 2015. 20

[83] B. Zahnd, M. Zimmermann, and R. Sporri. LISA Pathfinder Cage and Vent Mechanism: Development and Qualification. *Proceedings 15th European Space Mechanism and Tribology Symposium (ESMATS)*, 2013. URL. 21

[84] D.I. Robertson, E.D. Fitzsimons, C.J. Killow, M. Perreur-Lloyd, H. Ward, et al. Construction and testing of the optical bench for LISA pathfinder. *Classical and Quantum Gravity*, 30:085006, 2013. 21, 22, 143, 144, 149

[85] F. Guzmán Cervantes. LPF OMS Sensors, February 2012. *Slides for the LPF School in ESTEC, 2012.02.28*. 22

[86] G. Heinzel, V. Wand, A. Garcia, O. Jennrich, C. Braxmaier, et al. The LTP interferometer and phasemeter. *Classical and Quantum Gravity*, 21:S581–S587, 2004. 22, 149

[87] G. Wanner, G. Heinzel, E. Kochkina, C. Mahrdt, B. S. Sheard, S. Schuster, and K. Danzmann. Methods for simulating the readout of lengths and angles in laser interferometers with Gaussian beams. *Optics Communications*, 285(24):4831 – 4839, 2012. 22

[88] P. Cañizares, A. Conchillo, M. Díaz-Aguiló, E. García-Berro, Ll. Gesa, et al. The LISA PathFinder DMU and Radiation Monitor. *Classical and Quantum Gravity*, 28:094004, 2011. 22, 24, 149

[89] P. J. Wass, H. Araújo, C. Boatella, M. Chmeissani, W. Hajdas, A. Lobo, C. Puigdengoles, and T. Sumner. The LISA Pathfinder Radiation Monitor. *AIP Conference Proceedings*, 873(1):225–229, 2006. 24

[90] I. Mateos, M. Díaz-Aguiló, F. Gibert, C. Grimani, D. Hollington, et al. LISA PathFinder radiation monitor proton irradiation test results. *Journal of Physics: Conference Series*, 363:012050, 2012. URL. 24, 35

[91] A. Schleicher. DFACS Requirement Specification. Technical Note S2-ASD-RS-2001, Astrium Space Germany, 2013. 26

[92] M. Armano. DFACS structure, February 2012. *Slides for the LPF School in ESTEC, 2012.02.28*. 28

[93] P. McNamara. Autonomouse Star-Tracker, February 2012. *Slides for the LPF School in ESTEC, 2012.02.28*. 26

[94] G. E. Morris and C. Edwards. Design of a Cold-Gas Micropropulsion system for LISA Pathfinder. *49th AIAA/ASME/SAE/ASEE Joint Propulsion Conference*, Jul 2013. 26

[95] LISA Pathfinder progress. ESA Bulletin 160, 2014. p68 URL. 26

[96] S. Vitale. Measurement of differential acceleration noise on LISA Pathfinder. Technical Note S2-UTN-TN-3053, University of Trento, 2007. 28

[97] F. Antonucci, M. Armano, H. Audley, G. Auger, M. Benedetti, et al. From laboratory experiments to LISA Pathfinder: achieving LISA geodesic motion. *Classical and Quantum Gravity*, 28:094002, 2011. URL. 30, 32

[98] A. Cavalleri, G. Ciani, R. Dolesi, A. Heptonstall, M. Hueller, D. Nicolodi, S. Rowan, D. Tombolato, S. Vitale, P. J. Wass, and W. J. Weber. Increased Brownian Force Noise from Molecular Impacts in a Constrained Volume. *Phys. Rev. Lett.*, 103:140601, Sep 2009. 30, 43, 44, 140

[99] F. Antonucci, M. Armano, H. Audley, G. Auger, M. Benedetti, et al. LISA Pathfinder data analysis. *Classical and Quantum Gravity*, 28:094006, 2011. 32

[100] N. Karnesis, M. Nofrarias, C. F. Sopuerta, F. Gibert, M. Armano, et al. Bayesian Model Selection for LISA Pathfinder. *Phys.Rev.*, D89(6):062001, 2014. 32

[101] M. Nofrarias, L. Ferraioli, G. Congedo, M. Hueller, M. Armano, et al. Parameter estimation in LISA Pathfinder operational exercises. *Journal of Physics: Conference Series*, 363:012053, 2012. 32

[102] S. Vitale, G. Congedo, R. Dolesi, V. Ferroni, M. Hueller, et al. Data series subtraction with unknown and unmodeled background noise. *Phys.Rev.*, D90(4):042003, 2014. URL. 32

[103] A. Grynagier, W. Fichter, and Vitale. The LISA Pathfinder drift mode: implementation solutions for a robust algorithm. *Classical and Quantum Gravity*, 26(9):094007, 2009. URL. 33

[104] D. N. A. Shaul, H. M. Araújo, G. K. Rochester, M. Schulte, T. J. Sumner, C. Trenkel, and P. Wass. Charge management for LISA and LISA Pathfinder. *International Journal of Modern Physics D*, 17(07):993–1003, 2008. 33

[105] MATLAB. v. R2012a - R2014a. The MathWorks Inc., Natick, Massachusetts, 2014. URL. 33

[106] M. Nofrarias, F. Antonucci, M. Armano, H. Audley, G. Auger, et al. State space modelling and data analysis exercises in LISA Pathfinder. *ASP Conf. Ser.*, 467:161, 2013. 33

[107] F. Guzmán Cervantes, R. Flatscher, D. Gerardi, J. Burkhardt, R. Gerndt, M. Nofrarias, J. Reiche, G. Heinzel, K. Danzmann, L. G. Boté, V. Martín, I. Mateos, and A. Lobo. LISA Technology Package Flight Hardware Test Campaign. In G. Auger, P. Binétruy, and E. Plagnol, editors, *9th LISA Symposium*, volume 467 of *ASP Conf. Ser.*, page 141, January 2013. 34, 35, 149

[108] F. Gibert et al. Thermo-elastic induced phase noise in the LISA Pathfinder spacecraft. *Classical and Quantum Gravity*, 32(4):045014, 2015. 35, 46, 53, 98, 145

[109] F. Gibert and Ll. Gesa. DDS performance report at LPF ISH-EQM test. Technical Note S2-IEC-TR-3129, Institut de Ciències de l'Espai (ICE-IEEC/CSIC), 2013. 35, 71

[110] M. Armano et al. In-flight thermal experiments for LISA Pathfinder: Simulating temperature noise at the Inertial Sensors. *Journal of Physics: Conference Series*, 610(1):012023, 2015. URL. 35

[111] A.M. Nobili, D. Bramanti, G. Comandi, R. Toncelli, E. Polacco, et al. Radiometer effect in space missions to test the equivalence principle. *Phys.Rev.*, D63:101101, 2001. 37

[112] A. M. Nobili et al. Galileo Galilei (GG) a small satellite to test the equivalence principle of Galileo, Newton and Einstein. *Experimental Astronomy*, 23(2):689–710, 2009. 37

[113] P. Touboul, G. Metris, V. Lebat, and A. Robert. The MICROSCOPE experiment, ready for the in-orbit test of the equivalence principle. *Classical and Quantum Gravity*, 29:184010, 2012. 37

[114] A.M. Nobili, D. Bramanti, G.L. Comandi, R. Toncelli, and E. Polacco. Radiometer effect in the μSCOPE space mission. *New Astronomy*, 7(8):521 – 529, 2002. 37

[115] T.J. Sumner et al. STEP (satellite test of the equivalence principle). *Advances in Space Research*, 39(2):254 – 258, 2007. 37

[116] C. W. F. Everitt et al. Gravity Probe B: Final Results of a Space Experiment to Test General Relativity. *Phys. Rev. Lett.*, 106:221101, May 2011. 37

[117] R. Rummel, T. Gruber, J. Flury, and A. Schlicht. ESA's Gravity Field and Steady-State Ocean Circulation Explorer GOCE. *zfv - Zeitschrift für Geodäsie, Geoinformation und Landmanagement*, 134(3):125–130, 05 2009. 37

[118] R. Stanton et al. Gravity Recovery and Climate Experiment (GRACE) Science and Miqssion Requirements Document. Technical Report 327 - 200, Jet Propulsion Laboratory and University of Texas, 1998. 37

[119] B. Sheard, G. Heinzel, K. Danzmann, D. A. Shaddock, W. M. Klipstein, and W. M. Folkner. Intersatellite laser ranging instrument for the GRACE follow-on mission. *Journal of Geodesy*, 86(12):1083–1095, 2012. 37

[120] L. Carbone, A. Cavalleri, G. Ciani, R. Dolesi, M. Hueller, et al. Thermal gradient-induced forces on geodetic reference masses for LISA. *Phys.Rev.*, D76:102003, 2007. 39, 40, 41, 42, 79, 104, 131, 137, 138

[121] W. Crookes. On Attraction and Repulsion Resulting from Radiation. *Philosophical Transactions of the Royal Society of London*, 164(0):501–527, Jan 1874. 41

[122] J. C. Maxwell. On Stresses in Rarified Gases Arising from Inequalities of Temperature. *Philosophical Transactions of the Royal Society of London*, 170(0):231–256, Jan 1879. 41

[123] O. Reynolds. On Certain Dimensional Properties of Matter in the Gaseous State. Part I. Experimental Researches on Thermal Transpiration of Gases through Porous Plates and on the Laws of Transpiration and Impulsion, Including an Experimental Proof That Gas is Not a Continuous Plenum. Part II. On an Extension of the Dynamical Theory of Gas, Which Includes the Stresses, Tangential and Normal, Caused by a Varying Condition of Gas, and Affords an Explanation of the Phenomena of Transpiration and Impulsion. *Philosophical Transactions of the Royal Society of London*, 170(0):727–845, Jan 1879. 41

[124] P. Gibbs. How does a light-mill work? 1996. URL. 41

[125] B. M. Cornella, A. D. Ketsdever, N. E. Gimelshein, and S.F. Gimelshein. Analysis of Multivane Radiometer Arrays in High-Altitude Propulsion. *Journal of Propulsion and Power*, 28(4):831–839, Jul 2012. 41

[126] H. B. Callen and R. F. Greene. On a Theorem of Irreversible Thermodynamics. *Phys. Rev.*, 86:702–710, 1952. 43

[127] M. Nofrarias, A.F. Garcia Marin, A. Lobo, G. Heinzel, J. Ramos-Castro, et al. Thermal diagnostic of the optical window on board LISA pathfinder. *Classical and Quantum Gravity*, 24:5103–5122, 2007. 46, 58, 143, 165

[128] Betatherm G10K4D453 Datasheet. Technical report, Betatherm Ireland ltd. Ballybrit Business Park, Galway, Ireland., 2008. URL. 48

[129] J. S. Steinhart and S. R. Hart. Calibration curves for thermistors. *Deep Sea Research and Oceanographic Abstracts*, 15(4):497 – 503, 1968. 49

[130] J. Sanjuán. Calibration of FM NTC Thermistors. Technical Note S2-IEC-TN-3072, Institut de Ciències de l'Espai (ICE-IEEC/CSIC), 2010. 49, 62

[131] F. Gibert et al. Report on OSTT data. Technical Report S2-IEC-RP-3222, Institut de Ciències de l'Espai (ICE-IEEC/CSIC), 2013. 50

[132] I. Mateos and I. Lloro. DMU Temperature Data Conversion. Technical Note S2-IEC-TN-3091, Institut de Ciències de l'Espai (ICE-IEEC/CSIC), 2011. 50

[133] J. Sanjuán, A. Lobo, and J. Ramos-Castro. Analog-to-digital converters nonlinear errors correction in thermal diagnostics for the laser interferometer space antenna mission. *Review of Scientific Instruments*, 80(11), 2009. 53, 153

[134] M. F. Wagdy. Effect of additive dither on the resolution of ADC's with single-bit or multibit errors. 45(2):610–615, 1996. 53

[135] Betatherm G2K7D411 Datasheet. Technical report, Betatherm Ireland ltd. Ballybrit Business Park, Galway, Ireland., 2008. URL. 55, 62

[136] L. Gesa et al. DMU Software ICD. Interface Control Document S2-NTE-ICD-3004 v7.8, Institut de Ciències de l'Espai (ICE-IEEC/CSIC), 2014. 55

[137] A. Lobo and A. Conchillo. LTP Electrode Housing Heaters commanding. Technical Note S2-IEC-TN-3080, Institut de Ciències de l'Espai (ICE-IEEC/CSIC), 2011. 55, 56, 61

[138] F. Gibert. Study of the mechanical response of the LTP's test masses due to the action of control heaters in LISA Pathfinder. Master thesis (pre-Bologna period), Universitat Politècnica de Catalunya, January 2011. URL. 61, 64

[139] ESATAN Thermal Modelling Suite. ITP Engines UK Ltd, Whetstone, Leicester, UK., 2015. URL. 63

[140] A. Franzoso. LISA Core Assembly Thermal Model Description. Technical Report S2-CGS-TN-3031 v6, Compagnia Generale per lo Spazio (CGS SpA), 2007. 63, 75, 199, 200

[141] B. Gustavsen. The Vector Fitting Web. 2015. URL. 64

[142] B. Gustavsen and A. Semlyen. Rational approximation of frequency domain responses by vector fitting . *Power Delivery, IEEE Transactions on*, 14(3):1052–1061, Jul 1999. 64

[143] L. Gesa, F. Gibert, I. Lloro, and Martín V. Report on NCRs S2-ASD-NC-0205 and S2-ASD-NC-0206. Tehnical Report S2-IEC-RP-3223, Institut de Ciències de l'Espai (ICE-IEEC/CSIC), 2013. 76

[144] ESARAD Kernel Algorithms Document v7.3. Technical report, ALSTOM Power Technology Centre, 2004. 79, 80

[145] F. Gibert, M. Nofrarias, and A Lobo. Algorithm Specification for the Thermal Diagnostics on board LPF. Technical Report S2-IEC-TN-3088 v1, Institut de Ciències de l'Espai (ICE-IEEC/CSIC), 2012. 79, 84, 85, 89

[146] J.A Clark and M. E. Korybalski. Algebraic methods for the calculation of radiation exchange in an enclosure. *Wärme - und Stoffübertragung*, 7(1):31–44, 1974. 80

[147] B. Gebhart. Surface temperature calculations in radiant surroundings of arbitrary complexity –for gray, diffuse radiation. *International Journal of Heat and Mass Transfer*, 3(4):341 – 346, 1961. 80

[148] G. Kahl. DDS Subsystem Specification. Requirements Specification S2-ASD-RS-3004 v4.6, Airbus Defence and Space GmbH, 2010. 98

[149] S. M. Kay. *Fundamentals of Statistical Signal Processing: Estimation Theory*. Prentice-Hall, Inc., Upper Saddle River, NJ, USA, 1993. 100, 101

[150] R. Dolesi, D. Bortoluzzi, P. Bosetti, L. Carbone, A. Cavalleri, et al. Gravitational sensor for LISA and its technology demonstration mission. *Classical and Quantum Gravity*, 20:S99–S108, 2003. 108

[151] S. Schlamminger, K.-Y. Choi, T. A. Wagner, J. H. Gundlach, and E. G. Adelberger. Test of the Equivalence Principle Using a Rotating Torsion Balance. *Phys. Rev. Lett.*, 100:041101, Jan 2008. 117

[152] G. Ciani. *Free-fall of LISA test masses: a new torsion pendulum facility to test linear motion*. Phd thesis, University of Trento, 2008. 123, 124

[153] A. Cavalleri et al. A new torsion pendulum for testing the limits of free-fall for LISA test masses. *Classical and Quantum Gravity*, 26(9):094017, 2009. 131

[154] F. Antonucci, A. Cavalleri, A. Cesarini, G. Ciani, R. Dolesi, M. Hueller, P. Pivato, G. Russano, W. Shyang, D. Tombolato, S. Vitale, P. Wass, and W.J. Weber. Summary of GRS Electrode Housing test activities at the University of Trento. Tehnical Report S2-UTN-RP-3020, University of Trento, 2015. 135

[155] D. Gerlich and M. Wolf. Thermoelastic properties of Zerodur$^{\circledR}$ glass-ceramic. *Journal of Non-Crystalline Solids*, 27(2):209 – 214, 1978. 143

[156] J. Burkhardt and R. Flatscher. LTP LCA Thermal Test during the OSTT Campaign. Technical Note S2-ASD-TR-3173, Astrium Space Germany, 2012. 151

[157] J. Sanjuán, A. Lobo, J. Ramos-Castro, N. Mateos, and M. Díaz-Aguiló. ADC non-linear error corrections for low-noise temperature measurements in the LISA band. *Journal of Physics: Conference Series*, 228:012041, 2010. 152

[158] G. Hechenblaikner, V. Wand, M. Kersten, K. Danzmann, A. Garcia, et al. Digital laser frequency control and phase stabilization loops for a high precision space-borne metrology system. *IEEE J.Quant.Electron.*, 47:651, 2011. 155, 156

[159] D. Robertson. DC beam positions and baseplate bending. LISA Pathfinder Technical Report S2-UGL-OTH-3018, University of Glasgow, 2012. 159

[160] P. D. Welch. The use of fast Fourier transform for the estimation of power spectra: A method based on time averaging over short, modified periodograms. *Audio and Electroacoustics, IEEE Transactions on*, 15(2):70–73, Jun 1967. 170

[161] A. Bazoune. Transfer function approach to modelling dynamic systems. *Notes from ME 413 Systems Dynamics and Control, Chapter 4. King Fahd University of Petroleum and Minerals, Saudi Arabia.* 170

[162] J. R. Ragazzini and L. A. Zadeh. The analysis of sampled-data systems. *American Institute of Electrical Engineers, Part II: Applications and Industry, Transactions of the*, 71(5):225–234, Nov 1952. 171

[163] G. F. Franklin, M. L. Workman, and D. Powell. *Digital Control of Dynamic Systems.* Addison-Wesley Longman Publishing Co., Inc., Boston, MA, USA, 3rd edition, 1997. 173, 174

[164] M. Hewitson, A. Grynagier, and M. Díaz-Aguiló. A linear MIMO model of LPF implemented in LTPDA. Technical note, Albert-Einstein-Institut, September 2010. 173

[165] J. S. Bendat and A. G. Piersol. *Engineering applications of correlation and spectral analysis.* Wiley, New York, NY [u.a.], 1980. 175

[166] F. Gibert, M. Nofrarias, and N. Karnesis. Design for a pipeline implementing the Electrode Housing Thermal Experiment. Technical Note S2-IEC-TR-3097, Institut de Ciències de l'Espai (ICE-IEEC/CSIC), 2015. 180

[167] F. Gibert and M. Nofrarias. Design for a pipeline implementing the Struts Thermal Experiment data analysis. Technical Note S2-IEC-TR-3101, Institut de Ciències de l'Espai (ICE-IEEC/CSIC), 2015. 183

[168] J.F. O'Hanlon. *A User's Guide to Vacuum Technology.* John Wiley & Sons, 2003. 194, 196

[169] J. Burkhardt. LCA Struts Thermal Conductance Test Report. Technical Note S2-ASD-TR-3173, Astrium Space Germany, 2013. 203